A HYBRID ELECTROMAGNETIC IMAGING SYSTEM FOR NDE AND BIOMEDICAL APPLICATIONS

By

Saptarshi Mukherjee

A DISSERTATION

Submitted to
Michigan State University
in partial fulfillment of the requirements
for the degree of

Electrical and Computer Engineering–Doctor of Philosophy

2018

ABSTRACT

A HYBRID ELECTROMAGNETIC IMAGING SYSTEM FOR NDE AND BIOMEDICAL APPLICATIONS

By

Saptarshi Mukherjee

Microwave imaging techniques are well suited for NDE of dielectric materials such as composites because of the ability of microwaves to propagate through and interact with these materials. The scattered field provides information about the discontinuity in dielectric properties and hence structural integrity of these materials. While far field electromagnetic inspection systems have the capability of rapid, large area inspection because of large stand-off measurement capability, near field techniques enable higher resolution and imaging of anomalies. Moreover, the wide range of the electromagnetic spectrum allows greater penetration using lower frequencies and better resolution at higher frequencies. A synergistic integration of far field and near field techniques into a hybrid monitoring system is therefore promising.

This research aims at developing a novel, hybrid electromagnetic imaging system (HEMIS) that combines benefits of both near field and far field electromagnetic systems. The development of a new system that will utilize novel antenna design and sensors, coupled with time reversal imaging is proposed for imaging in NDE and biomedical applications. The first part of the research deals with the design of a time reversal (TR) imaging system. Unlike iterative approaches that provide a complete solution to the inverse problem, the TR based approach is non-iterative and provides a partial solution. Main advantages of the approach include faster computation time, super-resolution and selective focusing capabilities. The contribution of this research include:

- Development of a model based TR algorithm for efficient target imaging without prior knowledge of background Green's function,
- Design of a passive microstrip TR mirror for efficient breast tissue imaging application,
- Development of a robust experimental system demonstrating its feasibility for rapid NDE of large areas of composites and breast tumor imaging.

The second part of the research investigates use of probes and metamaterials for sub-wavelength imaging applications. The unique properties of metamaterials such as negative refractive index offer several benefits such as sub-wavelength nature, compact design and super-resolution and sub-wavelength imaging. A metamaterial lens is configured into the experimental setup to provide higher sensitivity to subwavelength defects and larger sensor to sample distance. Metamaterial inspired sensors and probes are also utilized for high resolution near field imaging of sub-wavelength features. The far field approach allows rapid scanning of large areas to detect regions of interest (ROI) with potential flaws and near field sensors are then used for scanning the ROIs to yield detailed imaging of sub-wavelength defects.

ACKNOWLEDGMENTS

I want to express my sincere gratitude to all those, who have been there for me and have supported me through out my graduate life. I am grateful to all those who have kept an open mind to my ideas, helped me identify and focus on my goals and open-heartedly assisted me during my research.

I would like to thank Michigan State University for giving me the opportunity to do my graduate studies in the U.S. There is an innate warmth in the environment surrounding MSU that makes international students feel at home promptly.

To Professor Lalita Udpa, you have been a parent to me away from home. I am thankful to you for accepting me as your PhD student and including me in the extremely talented and dynamic NDE group. You have not only been an academic advisor to me, but also a true mentor in all other fronts. Your kindness and supportive nature inspires and motivates me and my fellow lab mates. Your optimism, faith and confidence in me helped me achieve my goals during my PhD. You gave me the flexibility and independence to try out numerous ideas during my research.

To Professor Antonello Tamburino, you have taught me innumerable qualities of research, which are fundamental to my academic and professional development. You have motivated me to master the art of perfection and to gain a deep understanding of the fundamentals. Your meticulous nature has helped me to improve my research and make it more accurate and elegant.

I am thankful to Professor Satish Udpa to always find time to meet with me and provide guidance, despite being extremely engaged in administrative duties. Your visionary thinking has invoked many important questions and novel ideas in my mind that have helped me to

shape my research towards practical applications.

I am thankful to Professor Edward Rothwell for being the perfect teacher for me. I feel lucky to have attended the electromagnetics courses that you taught and to have worked with you. I am fascinated by your communication skills and your capability to explain even the most difficult formulas with such ease. You have always positively encouraged me on several fronts such as professional writing, teaching and research ethics.

To Professor Yiming Deng, you have supported me a lot during the latter stages of my research. You have been a perfect role model for me, assisting me in understanding what I really want after my PhD. I am especially thankful to you for your invaluable help in finding job opportunities and my career development.

To Professor Mahmoodul Haq, I am extremely thankful to you for your insights and practical ideas in the field of composites. You have helped me understand both the benefits and limitations of my research and implement it for practical applications. I am thankful to Professor Prem Chahal for his invaluable help and practical insights in the field of microwave devices and antenna design.

I am thankful to Brian Wright for his help with the development of my experimental setups and fabrication of several RF devices. I am thankful to Professor Patrick Kwon for his help with the fabrication of the additive manufacturing sample and the Composite Vehicle Research Center for its help with the fabrication of the GFRP composite sample.

I feel proud to have been affiliated with one of the most diverse, dynamic and renowned groups at MSU, NDE Lab. Being an active member of multiple projects involving cross-cultural teams, the friendly environment of the lab has developed my interpersonal and communication skills. I am thankful to the whole group and specifically Dr. Naiguang Lei, Michael Saybolt and Xiaodong Shi to assist me directly with my research.

Finally, I would like to express my deepest gratitude to my family who are responsible for making me the person I am today. After each exam, my late grandma would ask me seriously, "Did you pass?". I want to reply to her: "Now, I have passed ". My father, mother and sister have sacrificed a lot for me to accomplish this achievement. I am inspired by the strength, commitment and integrity of my father and the infinite love, selflessness and warmth of my mother. My loving big sister has forever supported and cared for me more than anyone in this world.

To my best friend and partner in crime, Portia, I want to thank you for being there with me through out these years. We set out with a goal five years ago and I am proud to say we completed this chapter. Cheers to the happy and sad times spent together and I am extremely excited about the next phase of our lives.

TABLE OF CONTENTS

LIST OF TABLES . . . . **xi**

LIST OF FIGURES . . . . **xii**

Chapter 1 Introduction **1**
1.1 Motivation 1
1.2 Scope of the research 5

Chapter 2 Time reversal **7**
2.1 Microwave imaging 7
2.2 Benefits of microwave imaging 8
2.2.1 Operational principles of microwave imaging 10
2.3 TR literature review 12
2.4 Theory of TR 15
2.5 Numerical formulation 18
2.5.1 Maxwell's equations 18
2.5.2 FDTD formulation 19
2.5.3 Boundary conditions 21
2.5.4 Source 23
2.6 Development of TR algorithm for imaging 25
2.7 Localization techniques 27

Chapter 3 Target localization by time reversal **32**
3.1 Introduction 32
3.2 Time reversal algorithm and simulations 33
3.2.1 Quantitative metrics 34
3.2.2 Source localization 35
3.2.3 Target localization 36
3.2.3.1 Iterative model based technique for target sizing 38
3.2.4 Parametric studies 40
3.2.4.1 Target size 40
3.2.4.2 Angular coverage 41
3.2.4.3 Effect of noise 42
3.3 Experimental studies 43
3.3.1 Experiment details 45
3.3.2 Experimental results 47
3.3.2.1 Case I 47
3.3.2.2 Cases II and III 49
3.3.2.3 Case IV 49
3.3.2.4 Cases V and VI 50
3.3.2.5 Case VII 52

3.3.3 Discussion of results . . . 53
3.4 Conclusion . . . 56

Chapter 4 Design of a microwave time reversal mirror for imaging applications . . . 58
4.1 Introduction . . . 58
4.2 Design of an antenna system for time reversal . . . 59
4.3 Transmitting antenna . . . 60
4.3.1 Design parameters . . . 61
4.3.1.1 SE APV antenna . . . 63
4.3.2 Antenna characteristics in the UWB range . . . 63
4.3.2.1 Far field radiation patterns . . . 64
4.3.2.2 Near field radiation patterns . . . 66
4.4 Receiving antenna . . . 67
4.5 Breast tumor simulation . . . 71
4.6 Time domain characterization . . . 72
4.6.1 Group delay . . . 72
4.6.2 Time domain response . . . 72
4.7 Experimental results . . . 74
4.8 Conclusion . . . 77

Chapter 5 Breast tumor imaging and hyperthermia by time reversal . . . 78
5.1 Introduction . . . 78
5.2 Theory and principles . . . 81
5.2.1 FDTD modeling . . . 81
5.2.2 Hyperthermia study via TR . . . 82
5.2.3 Quantitative metrics . . . 83
5.3 Simulation studies . . . 83
5.3.1 Breast phantom model . . . 83
5.3.2 Feasibility study . . . 85
5.3.3 Signal processing algorithm . . . 86
5.3.4 Imaging results . . . 89
5.3.5 Parametric studies . . . 91
5.3.5.1 Tissue heterogeneity . . . 92
5.3.5.2 Tumor spacing . . . 96
5.3.5.3 Material contrast ratio . . . 98
5.3.5.4 Bandwidth . . . 99
5.3.5.5 Effect of noise . . . 99
5.4 Experimental studies . . . 100
5.4.1 Experiment details . . . 101
5.4.2 Breast phantom experiment . . . 102
5.4.3 Experimental results . . . 105
5.4.3.1 Single tumor . . . 105
5.4.3.2 Multiple tumors . . . 107
5.5 Conclusion . . . 108

Chapter 6 Microwave imaging of composites **110**
6.1 Introduction 110
6.2 Composite materials 112
6.3 NDE of composites 113
6.4 Prior work in microwave NDE 116
6.5 Time reversal algorithm for far field NDE 117
6.5.1 Theory of TR for NDE 117
6.5.2 NDE algorithm 119
6.5.3 Quantitative metrics 121
6.6 Far field simulation studies 122
6.6.1 Multiple defects 124
6.6.2 Extended defects 125
6.6.3 Noise injection 126
6.7 Parametric analysis 127
6.7.1 Defect size 127
6.7.2 Receiver array aperture 127
6.7.3 Transmit-receive distance 128
6.8 Experimental analysis 129
6.8.1 Far field experimental setup 129
6.8.2 Near field experimental setup 132
6.8.2.1 Open ended waveguide probe 132
6.8.2.2 Extended coaxial probe 133
6.8.3 Experimental results 137
6.8.3.1 Prototype samples: I, II 137
6.8.3.2 Real composite samples: III, IV 140
6.9 Conclusion 148

Chapter 7 Enhancement of time reversal imaging using a metamaterial lens **150**
7.1 Wave equation in metamaterials 152
7.1.1 Electromagnetic properties of the metamaterial 154
7.1.2 Misconceptions surrounding metamaterials 156
7.1.2.1 Assumptions 156
7.1.3 Misconceptions 156
7.1.4 Numerical modeling of the DNG layer 158
7.2 Focusing of fields using the lens 161
7.2.1 Focusing of the lens in free space 161
7.2.2 Focusing in presence of a composite 163
7.2.2.1 Resolution of focal spot 164
7.2.2.2 Location of focal spot inside the sample 165
7.3 Time reversal with metamaterial lens 167
7.3.1 Source detection in air 168
7.3.2 Target detection in air 169
7.3.3 Defect detection in composites 170
7.3.3.1 Cross range separated defects 170

7.3.3.2 Down range separated defects . . . 173
7.4 Geometrical optics formulation for focusing in composites . . . 175
7.4.0.1 Determination of P_t . . . 176
7.4.0.2 Determination of d_{22}^1 . . . 178
7.4.0.3 Determination of the power density function . . . 179
7.4.0.4 Determination of δz . . . 179
7.5 Conclusion . . . 181

Chapter 8 Design of a SRR sensor for near field microwave imaging . . . 183
8.1 Introduction . . . 183
8.2 Theory and operation . . . 185
8.2.1 Parametric sweeps . . . 186
8.2.1.1 Ring radius . . . 187
8.2.1.2 Ring thickness . . . 188
8.2.1.3 Split gap . . . 188
8.2.1.4 Ring separation . . . 188
8.3 Modified sensor . . . 189
8.4 Simulation studies . . . 193
8.4.1 Parametric analysis for imaging . . . 193
8.4.1.1 Dielectric constant . . . 194
8.4.1.2 Sample lift-off . . . 195
8.4.2 Imaging studies . . . 196
8.4.2.1 Target imaging . . . 197
8.4.2.2 Defect detection . . . 197
8.5 Measurement results . . . 199
8.5.1 Performance of the sensor . . . 200
8.5.2 Microwave imaging experiments . . . 201
8.5.2.1 Experimental setup . . . 201
8.5.2.2 Metal detection . . . 202
8.5.2.3 NDE of additive manufactured metals . . . 202
8.5.2.4 NDE of composites . . . 204
8.6 Conclusion . . . 206

Chapter 9 Conclusion . . . 208
9.1 Key contributions . . . 208
9.2 Future work . . . 209

APPENDICES . . . 213
Appendix A Inverse scattering problem . . . 214
Appendix B Far field experimental system and measurements . . . 217
Appendix C Breast phantoms . . . 222

BIBLIOGRAPHY . . . 226

LIST OF TABLES

Table 3.1: Target detection experiments . . . 43

Table 3.2: Detection error and imaging quality . . . 55

Table 5.1: Simulation cases . . . 92

Table 6.1: Materal Properties . . . 122

Table 6.2: Experiments . . . 137

Table 6.3: Detection error and imaging quality . . . 148

Table 8.1: Sensor dimensions . . . 192

Table B.1: Equipment used for time domain measurements . . . 218

Table B.2: Beamwidth of the arch range system . . . 219

Table C.1: Properties of various phantoms . . . 225

LIST OF FIGURES

Figure 1.1: Model based inverse problem : Iterative approach 2

Figure 1.2: Overall approach of the proposed hybrid electromagnetic imaging 4

Figure 2.1: Typical active microwave imaging setup 7

Figure 2.2: Electromagnetic imaging applications (a) Through wall radar imaging, (b) Millimeter wave concealed weapon detection 8

Figure 2.3: Plane wave reflection and transmission on a dielectric sample 10

Figure 2.4: Focal spot of the TR wave: (a) Interference of convergent and divergent waves, (b) Theoretical focal Spot 18

Figure 2.5: Staggered E,H fields on an Yee cell 20

Figure 2.6: Source: Individual pulses in (a) time domain, (c) frequency domain, Modulated pulse in (b) time domain, (d) frequency domain 24

Figure 2.7: Plane wave incident on free space and a scatterer 25

Figure 2.8: Schematic of TR approach (a) Flowchart, (b) Demonstration 27

Figure 2.9: Problem geometry 28

Figure 3.1: Schematic of the FDTD simulation model 34

Figure 3.2: Source localization simulations: (a) TR Entropy plot, (b) TR Energy image, (c) Electric fields focused at metal plate at time instant A, (d) Electric fields focused at source at time instant B 36

Figure 3.3: Target localization simulations:(a) TR Entropy plot, (b) Electric fields focused at target at time instant A, (c) Integrated energy image 37

Figure 3.4: (a) CR Resolution, (b) DR Resolution 37

Figure 3.5: Cost function reaches minimum near the actual target size 39

Figure 3.6: TR Energy image vs target size 40

Figure 3.7: TR Energy peak vs : (a) target size, (b) target dielectric constant 41

Figure 3.8: TR energy peak vs angular coverage and number of sensors 42

Figure 3.9: Effect of noise: (a)5 dB noise addition, (b) TR Energy image 43

Figure 3.10: Time domain scattering measurement configuration 44

Figure 3.11: (a) UWB pulse generated by the pulse generating network,(b) Frequency spectrum of the pulse 44

Figure 3.12: Experimental setup (laser highlights the locations), ... 45

Figure 3.13: Source localization experiments (Case I): (a) Reflected fields measured by the receiver antenna array, (b) TR entropy plot, (c) Electric fields focused at metal plate at time instant A, (d) Electric fields focused at source at time instant B, (e) FWHM of cross-range signal estimates source's size . 47

Figure 3.14: Source localization experiments without background subtraction: (a) TR entropy plot, (b)Electric fields inefficiently focused at source at time instant B 48

Figure 3.15: Target localization for angular coverage of 40° and 80° (Cases II and III): (a),(c) and (e)- Stretched focal spot for Case II (a) Entropy, (c) Fields focused at target, (e) Energy image, (b),(d) and (f)- Tight focal spot for Case III (b) Entropy, (d) Fields focused at target, (f) Energy image, . . . 50

Figure 3.16: (Case IV): (a) Electric fields focused at entropy minima, (b) Integrated energy image and (c) Cross-range energy signal distinctly shows two peaks corresponding to the targets 51

Figure 3.17: Localization of targets separated along DR: (a),(c) and (e)- Case V : (a) fields focused at targets, (c) energy image, (e) DR signal shows extended energy image for separation of 0.08 m; (b),(d),(f) Case VI: (b) fields focused at target, (d) energy image, (f) DR signal shows distinct peaks for separation of 0.16 m 52

Figure 3.18: Localization of source and all targets (Case VII): (a) TR Entropy plot, (b) Focused electric fields around both targets at instant A, (c) Focused electric fields at metal sheet at instant B, (d) Focused electric fields near source at instant C 53

Figure 4.1: Design of the proposed transmitting antenna. (a) Vivaldi design (mm). (b) Fabricated antenna (US quarter dollar shown for comparison). 61

Figure 4.2: Current density for APV vivaldi (Units in A/m): (a) 4 GHz, (c) 8 GHz, SE APV antenna: (b) 4 GHz, (d) 8 GHz. 63

Figure 4.3: Transmitting antenna performance. (a) Reflection coefficients comparison. (b) Maximum realized gain comparison. 64

Figure 4.4: Transmitting antenna far field realized gain radiation pattern. (a) E Plane: 4 GHz. (b) E Plane: 6 GHz. (c) E Plane: 8 GHz 65

Figure 4.5: Other tried vivaldi antenna designs 66

Figure 4.6: Performance of various designs: (a) Simulated reflection coefficients (b) Simulated E Plane radiation pattern at 6 GHz 66

Figure 4.7: Transmitting antenna near E-field pattern. (a) E plane near field radiation pattern. (b) Electric field: 6 GHz. (c) Electric field: 10 GHz. 67

Figure 4.8: Monopole antenna design and its evolution. 68

Figure 4.9: Receiving antenna. (a) Monopole design (mm). (b) Fabricated monopole antenna. 69

Figure 4.10: Proposed receiving antenna and its performance. (a) Reflection coefficients comparison. (b) Radiation pattern: 4 GHz. (c) Radiation pattern: 6 GHz. (d) Radiation pattern: 10 GHz. 70

Figure 4.11: Antenna performance : (a) Radiation efficiency of the antennas, (b) Table 1. Comparison of different antennas 71

Figure 4.12: HFSS Simulation : S21 changes due to presence of tumor 71

Figure 4.13: Time-domain analysis for the TRA. (a) TRA configuration. (b) Group delay of the TRA. (c) TRA time-domain transient response 73

Figure 4.14: Time domain compact imaging setup 75

Figure 4.15: Time reversal imaging results (a) Focused field, (b) Measured TR energy, (c) Simulated TR energy, (d) Comparison between simulated and measured TR signals 76

Figure 5.1: Schematic of the TRI system 80

Figure 5.2: Simulation schematic with breast and antenna positions 84

Figure 5.3: Typical microwave imaging setup (Patient interface table, patient getting her breast scanned) [1] 85

Figure 5.4: TR for breast tumor detection feasibility study: (a) fields scattered from breast, (b) entropy plot, (c) electric fields at A, (d) integrated energy . . 86

Figure 5.5: Major modules of the signal processing algorithm: (a) Background subtraction, (b) Early time content removal, (c) TOA based time gating, (d) Gaussian windowing 87

Figure 5.6: Entropy method used for temporal localization: (a) Entropy plot, (b) Electric fields at time instant A, (c) Electric fields at time instant B, (d) Electric fields at time instant C, (e) Electric fields at time instant D, (f) Electric fields at time instant E 90

Figure 5.7: Modified TR for tumor detection simulation study: (a) Case I: Integrated energy, (b) Case I: Cross, down range signals, (c) Case II: Integrated energy, (d) Case III: Integrated energy 91

Figure 5.8: Results of parametric studies: mE and mSAR with (a) tissue dielectric variance, (b) tumor spacing (NDT: non detectable tumor) 93

Figure 5.9: Case I- TR imaging results for variation of tissue. (a, d): 20 % heterogeneity (a) Energy (mE=5.2) (d) Absorption (mSAR=18); (b, e): 40 % heterogeneity (b) Energy (mE=4.6) (e) Absorption (mSAR=13); (c, f): 80 % heterogeneity (c) Energy (mE=2.5) (f) Absorption (mSAR=9.5) . . 94

Figure 5.10: Case I- TR imaging results in presence of inhomogeneity. (a, d): 1 ellipse major axis 6 cm (a) Energy (mE=3.2) (d) Absorption (mSAR=12); (b, e): 2 ellipsis major axis 5 cm (b) Energy (mE=3.4) (e) Absorption (mSAR=15); (c, f): unknown scatterer (ellipse major axis 6 cm) (c) Energy (mE=0.5) (f) Absorption (mSAR=8) 95

Figure 5.11: Case II- TR imaging results for varying gap between tumors. (a, d): 2 tumors gap=2.8 cm (a) Energy (mE=1) (d) Absorption (mSAR=7); (b, e): 2 tumors gap=1.4 cm (b) Energy (mE=0.6) (e) Absorption (mSAR=5.5); (c, f): 3 tumors gap=5 cm and 8 cm (c) Energy (mE=1) (f) Absorption (mSAR=9) 97

Figure 5.12: Results of parametric studies: mE and mSAR with (a) tissue contrast, (b) input pulse bandwidth 98

Figure 5.13: (a) Addition of 5 dB noise to the simulated signals, (b) Integrated energy image still detects tumor 100

Figure 5.14: Experimental setup for imaging : (a) Time domain experimental system, (b) Breast phantom 102

Figure 5.15: Experimental results for breast phantom with a 1 cm radius tumor (a) Energy: raw fields (mE=1.5), (b) Tumor contribution, (c) TR entropy plot, (d) Electric fields at A, (e) Electric fields at B, (f) Electric fields at C, (g) Energy: processed fields, (h) Energy: scattered fields, (i) SAR of processed fields 106

Figure 5.16: Experimental results for breast phantom with (a,c) a 0.5 cm radius tumor (a) Energy: processed fields, (c) SAR (mSAR=23), (b,d) two tumors (b) Energy: processed fields,(d) SAR (mSAR=20) 107

Figure 6.1: Applications of composite materials 113

Figure 6.2: Summary of common defects in composites 114

Figure 6.3: Wave incident on healthy and defective samples 118

Figure 6.4: Model-based defect imaging : Iterative approach 119

Figure 6.5: Time Reversal for NDE (a) Algorithm, (b) Example (c) TR processing . 120

Figure 6.6: Time Reversal Simulation Schematic 121

Figure 6.7: Simulation signals (a) Healthy and unhealthy signals, (b) Defect contribution 123

Figure 6.8: TR Simulation Results for NDE of composites (a) Entropy plot, (b)Electric fields at minimum entropy instant, (c) Integrated energy image, (d) Cross range signal 123

Figure 6.9: TR images for multiple defects (a) Equal disbonds, (b) Unequal disbonds 124

Figure 6.10: Energy image for extended disbond 125

Figure 6.11: Extended disbonds: (a) Disbond signal, (b)Estimation accuracy 125

Figure 6.12: TR imaging in presence of noise (a) AWGN distribution used as noise for time reversal with SNR 5 dB, (b) Noisy TR image 126

Figure 6.13: Parametric analysis (a) TR peak with defect size, (b) TR peak with receiver aperture 128

Figure 6.14: Experimental schematic 130

Figure 6.15: Far field experimental setup 131

Figure 6.16: Near field experimental setup 131

Figure 6.17: Open ended waveguide simulation results (a) Cross section of radiated near E field at 10 GHz, (b) Radiation pattern of the probe, (c) Near E field radiation pattern of the probe, (d) Reflection coefficients for the probe in presence of circular metal targets of different radius, (e) Reflection coefficients for the probe in presence of healthy and defective samples . . 134

Figure 6.18: Coaxial probe results (a) Probe, (b) Simulated reflection coefficients for the coaxial probe with varying tip extensions, (c) Simulated reflection coefficients for the coaxial probe with varying tip extensions, (d) Measured reflection coefficients for the coaxial probe, (e) Cross section of radiated near E field, (f) Near E field radiation pattern of the probe 136

Figure 6.19: Prototype samples: (a) Prototype sample schematic, (b) Sample I dimensions, (c) Sample II dimensions 137

Figure 6.20: TR experimental results: prototype sample (a) Entropy: Sample I, (b) Entropy: Sample II, (c) Energy: Sample I, (d) Energy: Sample II, (e) Cross Range Signal : Sample I, (f) Cross Range Signal : Sample II . . . 139

Figure 6.21: Near field experimental results: prototype sample (a) Magnitude 10 GHz: Sample I, (b) Phase 10 GHz: Sample I, (c) Magnitude 10 GHz: Sample II, (d) Phase 10 GHz: Sample II 140

Figure 6.22: Real GFRP sample damage modes (Red dashed lines indicate the healthy region of the samples) (a) Drilled holes, (b) Impact damage 141

Figure 6.23: Experimental signals of one receiver element for Sample III 142

Figure 6.24: Experimental results: Sample III (a) Sample, (b) TR Energy, (b) CR Signal142

Figure 6.25: Near field experimental results: Sample III (a) Magnitude: 8 GHz, (b) Magnitude: 10 GHz, (c) Magnitude: 12 GHz, (d) Phase: 8 GHz, (e) Phase: 10 GHz, (f) Phase: 12 GHz 144

Figure 6.26: Experimental signals of one receiver element for Sample IV 145

Figure 6.27: Experimental results: Sample IV (a) Sample, (b) TR Energy, (b) CR Signal146

Figure 6.28: Near field experimental results: Sample IV (a) Magnitude: 10 GHz, (b) Phase: 10 GHz 146

Figure 6.29: Coax probe results (a) Sample III Phase: 8 GHz, (b) Sample IV Phase: 8 GHz 147

Figure 7.1: A ray passing through a metamaterial region and the image of a straw dipped in a metamaterial region 150

Figure 7.2: Refractive index of metamaterial, (a)Drude model of refractive index for DNG medium, (b) Zoomed in plot shows n=-1 and zero crossover point . 155

Figure 7.3: Focusing of the metamaterial lens in free space, (a) Simulation schematic, (b) Wave propagation 160

Figure 7.4: Ray diagram of metamaterial lens in free space 161

Figure 7.5: Focusing of the metamaterial lens in free space, (a) Focused fields with lens (d_1= 3.5 λ_0; d_2= 4.4 λ_0; t=8λ_0), (b) Focused fields with lens (d_1= 2.4 λ_0; d_2= 5.5 λ_0; t=8λ_0 163

Figure 7.6: Focusing of the metamaterial lens in composites : (a) Focused wave impinges composite with lens, (b) Near plane wave impinges composite without lens 163

Figure 7.7: Focusing resolution of the lens, (a) Free Space, (b) Composite 164

Figure 7.8: Ray diagram of metamaterial lens in the presence of (a) air, (b) composite half space 165

Figure 7.9: Comparison of focal point between simulated and approximated geometrical optics results 167

Figure 7.10: TR with metamaterial lens shows enhancement of microwave imaging for source imaging, (a) Schematic of test geometry, (b) TR energy without metamaterial lens, (c) TR energy with lens 169

Figure 7.11: TR with metamaterial lens shows enhancement of microwave imaging for sub-wavelength target imaging, (a)Schematic of test geometry, (b) TR energy without metamaterial lens, (c) TR energy with lens 169

Figure 7.12: Cross range signal of target with and without lens 170

Figure 7.13: TR with metamaterial lens shows enhancement of microwave imaging for sub-wavelength cross range separated sub-wavelength defects in a composite slab, (a) Schematic of test geometry, (b) TR energy comparison . 171

Figure 7.14: TR with metamaterial lens shows enhancement of microwave imaging for sub-wavelength cross range separated sub-wavelength defects in a composite slab, (a) Schematic of test geometry, (b) TR energy comparison . 172

Figure 7.15: TR with metamaterial lens shows enhancement of microwave imaging for a sub-wavelength defects in a composite slab for different source positions, (a) Schematic of test geometry, (b) TR energy comparison 173

Figure 7.16: TR with metamaterial lens shows enhancement of microwave imaging for sub-wavelength cross range separated sub-wavelength defects in a composite slab, (a) Schematic of test geometry, (b) TR energy comparison . 174

Figure 7.17: TR with metamaterial lens shows enhancement of microwave imaging for sub-wavelength down range separated sub-wavelength defects in a composite slab, (a) Schematic of test geometry, (b) TR energy comparison . 175

Figure 7.18: Ray diagram of a wave packet of incident angle θ_1 and angular spread dθ in the composite 175

Figure 7.19: Ray diagram of metamaterial lens in the presence of (a) air, (b) composite half space 178

Figure 7.20: Focusing spread of power for varying d_{21} (a) p(z), (b) δz 180

Figure 7.21: Focusing spread of power for varying d_1 (a) p(z), (b) δz 181

Figure 7.22: Focusing spread of power for varying d_{21} (a) p(z), (b) δz 181

Figure 8.1: Simple microstrip line coupled SRR sensor (a) Sensor design, (b) SRR unit cell 184

Figure 8.2: Insertion loss of the SRR sensor (a) Magnitude, (b) Phase 186

Figure 8.3: Parametric analysis of the sensor (a) Variation of f_0 and Q of the sensor with ring radius, (b) Variation of f_0 of the sensor with ring thickness, (c) Variation of f_0 of the sensor with split ring gap, (d) Variation of f_0 of the sensor with ring separation 187

Figure 8.4: Extended tip sensor (a) Configuration 1: Sample placed parallel to surface of ring, (b) Configuration 2: Sample placed perpendicular to surface of ring, (c) Overall structure, (d) Extended ring 190

Figure 8.5: Insertion loss, field distribution and induced electric field of the extended tip sensor (a) Magnitude of Insertion loss, (b) Electric fields decay slower in the extended tip SRR sensor than the general SRR sensor, (c) Induced electric field: f_r, (d) Induced electric field: f_s 191

Figure 8.6: Insertion loss magnitude of the sensors with and without extended tip for target detection (a) Insertion loss of sensor without tip extension in presence of target, (b) Insertion loss of sensor with tip extension in presence of target . . . 192

Figure 8.7: Final Sensor (a) Design, Resonant frequency obtained from Insertion loss (b) Magnitude, (c) Phase difference . . . 192

Figure 8.8: Evolution of the proposed sensor, (a) Design modifications, (b) Performance of the designs (Addition of equivalent reference ring shifts resonance to the left; Extension of tip of S results in two separate resonant frequencies for R and S; 3 resonant frequencies for R, S1 and S2) . . . 194

Figure 8.9: Relationship of resonance with dielectric constant (a) Magnitude of insertion loss vs ε_r, (b) Resonant frequency shift vs ε_r . . . 195

Figure 8.10: Relationship of resonance with lift-off (a) Magnitude of insertion loss vs lift-off, (b) Resonant frequency shift vs lift-off, (c) Electric field at f_{s1}, (d) Electric field at f_{s2} . . . 196

Figure 8.11: Schematic of 2 simulation geometries (a) Target detection, (b) Defect detection . . . 197

Figure 8.12: Simulation results of target imaging (a) Insertion loss for 3 positions: S2 detects target at position 2, (b) Phase change at resonant frequencies provides an estimate of the target size . . . 198

Figure 8.13: Simulation results of defect imaging (a) Insertion loss for 3 positions: S2 detects defect at position 2, (b) Phase change at resonant frequencies provides an estimate of the defect size . . . 198

Figure 8.14: Different sensors fabricated (US quarter for size comparison) . . . 199

Figure 8.15: Fabricated sensors: Microscope image of (a) extended tip sensing ring, (b) reference ring . . . 199

Figure 8.16: Performance of the sensor (a) Measured Insertion loss, (b) Resonance shift 200

Figure 8.17: Experimental setup for imaging . . . 201

Figure 8.18: Detection of metal using sensor (a) Resonance shift, (b) Shift of S_{12} magnitude at resonance, (c) Shift of S_{12} phase at resonance . . . 202

Figure 8.19: Imaging of different shaped defects in a AMM sample (a) Sample, (b) S_{12} magnitude at resonance, (c) S_{12} phase at resonance . . . 203

Figure 8.20: Imaging of different sized defects in a AMM sample (a) Sample, (b) S_{12} magnitude at resonance, (c) S_{12} phase at resonance 204

Figure 8.21: GFRP Sample with defects 205

Figure 8.22: Imaging of different sized defects in a GFRP sample (red box indicates delamination area) (a) S_{12} magnitude at resonance, (b) S_{12} phase at resonance, (c) Line scan signal detects all defects 205

Figure 9.1: Full time domain DORT Technique for well resolved point-like scatterers 210

Figure B.1: Far field experimental setup 217

Chapter 1

Introduction

1.1 Motivation

Microwave imaging is emerging as an important technology in order to evaluate hidden or embedded objects in a structure. The wide range of applications encompasses activities such as full body scanning technologies at airport screening areas to detection of biomolecules and DNA sensing. The huge thrust in wireless engineering and demands for remote sensing have led to the development of ultra-wideband microwave (300 MHz to 30 GHz) imaging systems that provide higher detection ranges in complicated environments than other existing technologies, since they can provide both greater penetration using lower frequencies and better resolution using higher frequencies [2]. The fact that electromagnetic waves can travel through vacuum enables their propagation in the absence of a coupling medium. Hence, microwave imaging can serve as an effective, rapid non-contact method for inspection of large areas of interest. The two primary focus areas of microwave imaging is development of novel sensors and development of novel inverse scattering algorithms.

The imaging principle is based on an inverse scattering problem, which can be solved using direct or indirect inversion methods [3, 4]. The main objective of the inverse scattering algorithm is to reconstruct or estimate the spatial distribution of the scatterer's electrical properties or the scattering potential from scattered field measurements. These inverse

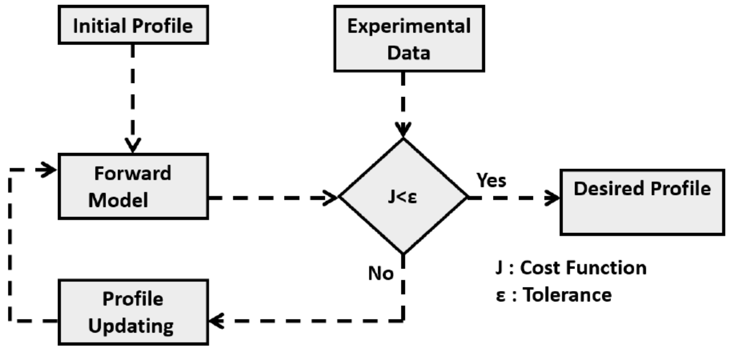

Figure 1.1: Model based inverse problem : Iterative approach

problems are in general ill-posed, where the solutions are non unique and discontinuous. Conventional inverse problem solutions, based on error minimization or regularization algorithms have been developed to tackle the ill-posedness [5]. However they are generally iterative, which can converge to local minima or have slow convergence rates, thus making them computationally intensive. A model based inverse problem is shown in Fig. 1.1. It relies heavily on an accurate forward model, typically based on a numerical technique, which makes it computationally intensive. These factors motivate the development of a non-iterative model-based direct imaging method for solving the inverse problem [6].

The main objective of the sensor is to transmit and receive efficiently signals such that maximum information about the imaging domain is known. For example in far field ultra-wide band imaging, the gain of an antenna needs to be large throughout the spectrum in order to obtain better signal-to-noise ratio. If closely spaced targets need to be imaged, the antenna needs to have a focused beam with a relatively narrow beamwidth. For near field imaging, capacitive or inductive sensors with narrow tip size can be used for obtaining high resolution. Research in both areas is necessary in order to obtain high imaging quality with a low detection error.

Microwave imaging can be performed at both far field and near field ranges. Each technique has its own advantages and limitations. Far field imaging is relatively fast and has large stand-off distances. However, the imaging resolution is dictated by the diffraction limits ($O(\lambda)$) and is not sufficient to image tiny scatterers. Especially in the field of NDE, there are several types of practical defects in composites such as disbonds and fiber delaminations (< 1 mm), that are smaller than diffraction limits at GHz ranges ($\sim$1.5 cm at 10 GHz). In contrast, near field sensors provide high resolution images with the resolution primarily dependent on the sensor tip size. However, performing near field scanning of large sample areas is typically time-consuming. The above mentioned factors motivate the development of a novel imaging method. The first part of the research involves setting up the framework of TR imaging for radar and biomedical applications. The second part involves the development of a hybrid electromagnetic imaging system (HEMIS) for NDE applications. An overall schematic of the proposed approach is shown in Fig. 1.2. In order to reduce the total scan time, in the first step, a rapid scan using time reversal on far field microwave data is used for detecting potential anomalies in the sample. In the next step, novel near field sensors such as the split-ring resonators (SRRs), open-ended waveguides and coaxial probes are used to scan the localized regions to accurately image the anomalies with high resolution. The hybrid approach will create a synergy between different techniques to eliminate the limitations of each technique while harnessing their benefits, thus making the entire system cost-effective.

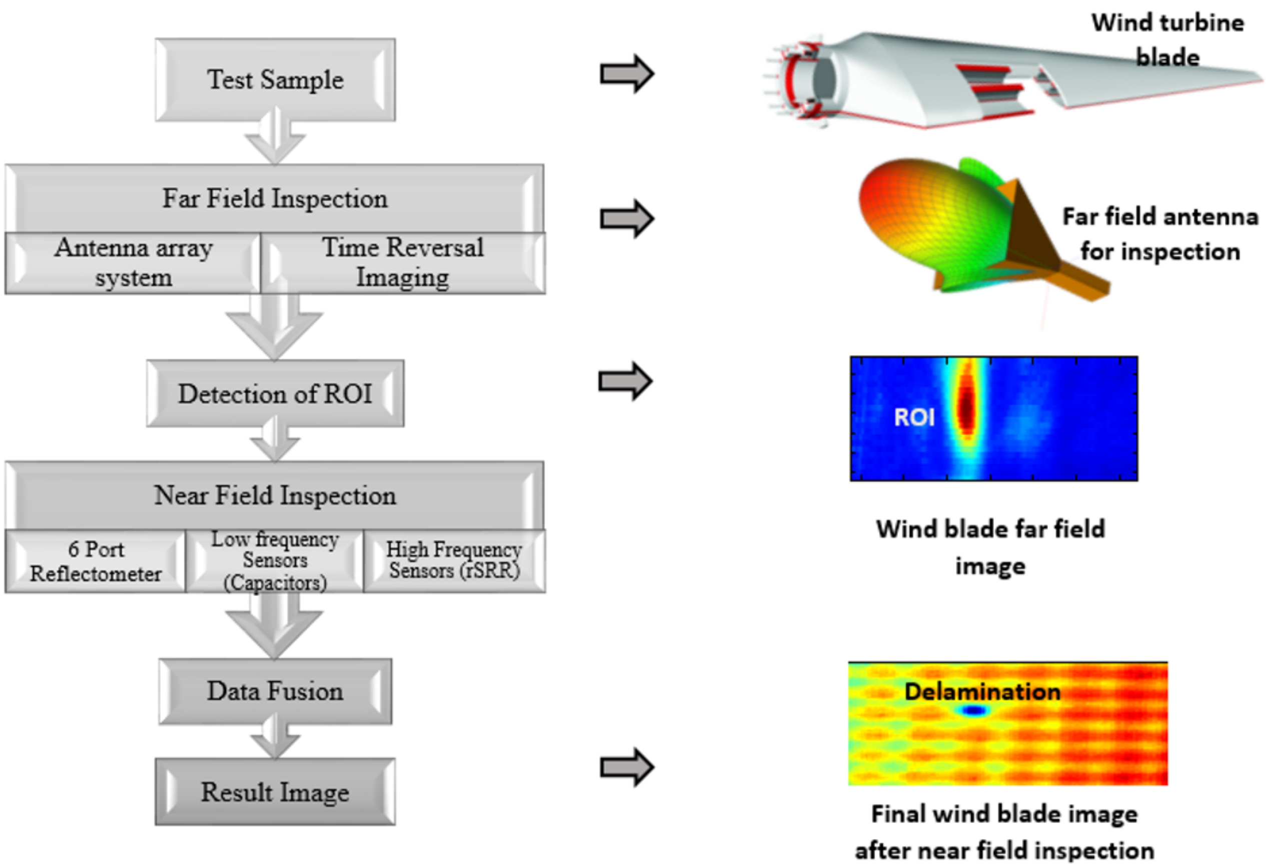

Figure 1.2: Overall approach of the proposed hybrid electromagnetic imaging

1.2 Scope of the research

This research investigates a variety of applications, each posing its unique set of challenges. The first part deals with the development of a non-iterative microwave TR algorithm for back-propagation of waves and imaging. The theory of TR is established, followed by the development of the back-propagation algorithm for spatio-temporal focusing of the waves. Simulation results and parametric analysis help in determining the limits and demonstrates the efficacy of the algorithm. A pulsed time domain experimental system (2-18 GHz) with standard horn antennas positioned in a far field reflectivity arch range is utilized for obtaining the scattered fields for different types of targets. The scattered fields are processed using TR for detecting the excitation source and closely spaced targets. Next the system is modified for compact imaging applications such as breast tissue imaging. The microwave time reversal mirror (TRM) is designed in accordance with the theory of TR based wide band imaging. The antennas are integrated into the experimental system and utilized for imaging metallic targets and finally utilized for detection of tumors in multi-layered breast phantoms. The second part of the research deals with NDE of composites. The TR algorithm is modified in order to use TR for NDE. The modified TR algorithm is coupled to the existing experimental setup to image realistic defects such as impact damages and disbonds on Glass fiber reinforced polymer (GFRP) composites. A near field microwave imaging system with coaxial and open-ended waveguide probe is set up. The near field imaging results serve as a reference for comparison with far field results and helps identifying its limitations. These limitations are tackled by designing a metamaterial lens is modeled and coupled with TR in order to achieve sub-wavelength resolution. The lens provides perfect focusing and amplification of evanescent waves, thus leading to enhanced detection capabilities. Finally, a novel near field sensor based on SRR is developed for detecting tiny defects (sub-mm) in composites. The design and development of the sensor system along with experimental results demonstrating the feasibility of the approach for detection of sub-wavelength defects in composites and additive manufactured metals (AMMs). The near field microwave imaging system, metamaterial lens and the SRR sensor serves as the second step of the hybrid imaging system.

The dissertation consists of the following chapters. Chapter 2 describes the principles, theory and previous research on TR, followed by the algorithm, numerical modeling and localization techniques. Chapter 3 describes radar detection application for imaging source and targets in reflection mode, encompassing both simulation and experimental results. The development of a microstrip TRM for compact imaging applications is discussed in Chapter 4. The development of a non-conventional TR algorithm for detection of breast tumors and the feasibility of a hyperthermia treatment of breast tissues are presented in Chapter 5. Chapter 6 describes the application of TR imaging for NDE of composite structures. Simulation and experimental studies for disbond detection in metal-composite joints and other practical defects on real composite samples are presented. Chapter 7 couples the concept of TR with a metamaterial lens for enhanced detection and sub-wavelength microwave imaging. Chapter 8 deals with the design of a novel microstrip SRR sensor for sub-millimeter, near field microwave imaging. Simulation studies as well as imaging experiments elucidate the efficiency of the sensor system. The concluding remarks and potential future research work are presented in Chapter 9.

Chapter 2

Time reversal

2.1 Microwave imaging

Microwave imaging is a science which has evolved from older localization techniques (e.g., radar) in order to evaluate hidden or embedded objects in structured media using electromagnetic (EM) waves. Microwave imaging methods can be broadly classified into passive, hybrid and active methods. In passive methods, microwave radiometers measure the temperature distribution inside the sample to be imaged [7]. Microwave radiometry has long been explored as a replacement for X-ray mammogram due to lack of radiation risk [8]. In hybrid methods, microwave is used in complement with other modalities to enhance the imaging quality of the modality. For example, in microwave induced thermo-acoustic imaging, microwave energy is focused in the medium to generate energy, that results in expansion and contraction of the medium. This results in omni-directional acoustic wave emission that is utilized for imaging the medium. The active microwave imaging methods belong to the

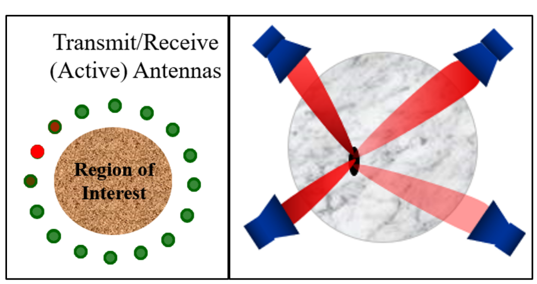

Figure 2.1: Typical active microwave imaging setup

class of an inverse scattering problem in which, microwaves illuminate the sample and the scattered fields measured at different locations surrounding the sample are used to image it [9]. A typical active microwave imaging setup is shown in Fig. 2.1. The transmitting and receiving antennas surround the region of interest that needs to be imaged. The scattered field from the antennas are processed and used in an inverse scattering algorithm in order to image the region. In this research, we deal with an active microwave imaging method.

2.2 Benefits of microwave imaging

The demands for remote sensing have led to the development of ultra-wideband microwave systems that provide higher detection ranges, better imaging capabilities of complicated environments, since they can provide both greater penetration at lower frequencies and better resolution at higher frequencies. Moreover, since electromagnetic waves can travel through vacuum, experiments can be conducted by rapid scanning of the whole area with the help of the antenna array with large stand-off distances, which is difficult to be achieved using ultrasonic systems. Some recent electromagnetic imaging applications [10] are shown in Fig. 2.2. The physics governing electromagnetic imaging is different from other physics

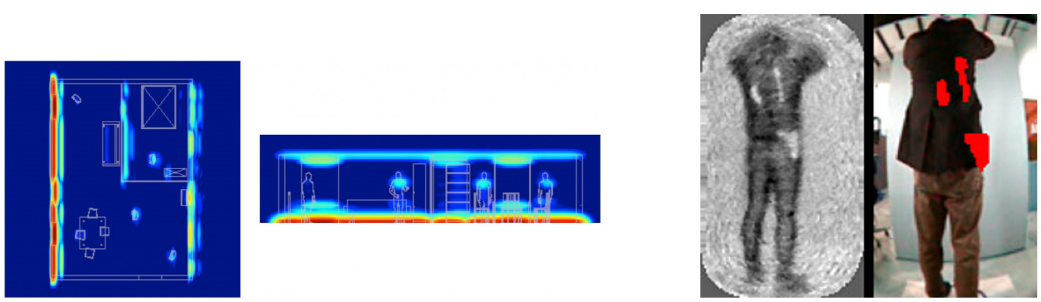

(a) (b)

Figure 2.2: Electromagnetic imaging applications (a) Through wall radar imaging, (b) Millimeter wave concealed weapon detection

based systems as follows:

- Ultra-wideband microwave systems that provide higher detection ranges and better imaging capabilities of complicated environments than other existing, since they can provide both greater penetration using lower frequencies as well as better resolution using higher frequencies.

- Electromagnetic waves can travel through vacuum. They do not require a coupling medium for propagation, and hence can serve as an effective non-contact method. In contrast, ultrasonic waves require a propagation medium between the transceiver and the target. This requirement leads to two primary restrictions:

  - Rapid scans of large areas using ultrasonics are not possible.

  - Ultrasonic experiments cannot be conducted at large stand-off distances.

- Electromagnetic waves are transverse waves and hence can be polarized. This can be utilized to achieve improved detection and focusing capabilities. In contrast, acoustic waves are longitudinal waves, and hence cannot be polarized.

The electromagnetic theory necessary to understand the inverse scattering problem is briefly explained in the following sections.

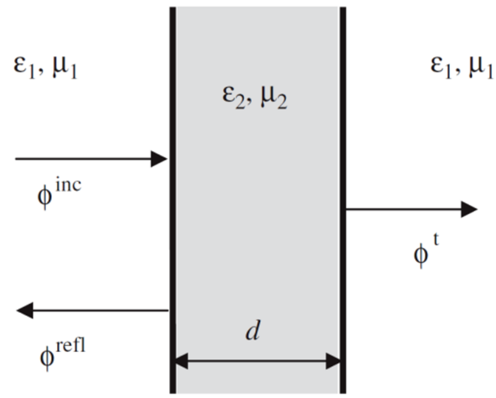

Figure 2.3: Plane wave reflection and transmission on a dielectric sample

2.2.1 Operational principles of microwave imaging

Consider a plane wave traveling in medium 1 and incident on medium 2 as shown in Fig. 2.3. The following equations govern the behavior of EM waves [11].

$$\begin{gathered} T_d = T\frac{1-\tau^2}{1-\tau^2 T^2}, \\ \tau_d = \tau\frac{1-\tau^2}{1-\tau^2 T^2}, \\ \tau = \frac{\eta_2-\eta_1}{\eta_2+\eta_1}, \qquad T_d = e^{-jk_2 d} \qquad k_2 = \frac{2\pi}{\lambda_2} \\ \eta_1 = \sqrt{\frac{\mu_1}{\varepsilon_1}} \qquad \eta_2 = \sqrt{\frac{\mu_2}{\varepsilon_2}}. \end{gathered} \tag{2.1}$$

where T_d, τ_d are the total transmission coefficient and the reflection coefficient showing the fraction of total power that is transmitted and reflected, T, τ are the transmission coefficient and the reflection coefficient at the medium interfaces, η_1, η_2 are the refractive index of the two mediums, k_2, λ_2 and d are the wave number, wavelength and thickness of medium 2. From the measurement point of view, scattering parameters, or S-parameters are used to characterize real and imaginary data parts of reflected and transmitted power. The return loss, known as S_{11}, is the power reflected back from port one when power is applied to port one. This is equivalent to the reflection coefficient, τ. A detailed study and derivation of S parameters is done in [12]. Since (2.1) is dependent on the permittivity and permeability of the material, a change in the material property will result in a change in the reflection coefficient, which is the fundamental basis for microwave imaging.

In the microwave regime as the size of the objects are comparable to the wavelength, the waves no longer travel in a straight path. At these frequencies, the waves undergo diffraction and the straight ray tomography as in X-rays is no longer valid. The wave object interaction at microwave frequencies are governed by wave propagation and diffraction phenomenon depending on the scatterer size relative to wavelength of the source. The EM waves satisfy Maxwell's and continuity equations and fields are related to the material property via the constitutive equations [13, 14]. An EM wave impinging on a penetrable object undergoes diffraction and multiple scattering within the object resulting in a nonlinear relationship between the measured field and electrical property of the object at the incident frequency [15].

Inverse scattering problems aims to reconstruct the spatial distribution of the scatterer's electrical property or the scattering potential of the obstacle from scattered field measurements. The mathematical background of the inverse scattering problem is well-established and demonstrated in Appendix A. As explained in the appendix, the object function $O(\overrightarrow{r}, \omega)$ needs to be solved using an imaging technique. This is an inverse problem that can be solved using direct or indirect inversion methods. More details about inverse problems and its different techniques can be found in the literature [16, 17, 5]. In this research, a direct imaging method TR has been used to solve for $O(\overrightarrow{r}, \omega)$.

2.3 TR literature review

The first introduction to "time reversal", was in a paper by B. P. Bogert of Bell Labs [18] in the year 1957 in the IRE Transactions on Communications Systems. The idea was to compensate for phase distortion using a time reversal technique for transmitting pictures and slow television signals on telephone lines. Picture-quality enhancement was achieved by applying the time-reversal procedure. A paper similar to Bogert's paper was published in the IBM journal in 1965 [19], dealing with automatic distortion correction for efficient pulse transmission over telephone networks. Since the late 1950s time reversal was established as a well-known technique in electrical engineering, as a means to compensate for phase distortions of linear systems. The idea of time reversal was used to design non causal digital filters with zero phase shifts. Many researchers are currently trying to use this technology in personal wireless communications. While they have introduced it as a new technology that originated in acoustics in the early 1990s, almost no recent papers give credit to the earlier time reversal work, such as Bogert's work [18].

The basic principles of TR for focusing fields, were demonstrated by Mathias Fink in 1992 using ultrasonic fields through inhomogeneous media on reflective targets[20]. Robust TR ultrasonic experiments were first conducted by Fink et al. in 1992 and later applied to detect kidney stones [21, 22]. The TRM is an array that has wideband spatial-processing capability. The mirror received most of the propagated fields and retransmitted them along the same directions from which they were received, achieving both spatial and temporal focusing.

Twelve years after Fink's papers, TR was extended to the realm of electromagnetics [23, 24], with several applications. Initial electromagnetic TR experiments were performed for focusing wideband microwaves at a central frequency of 2.45 GHz, in a closed reverberant chamber. Since then, a lot of research has been conducted to utilize electromagnetic TR in several applications. TR was applied in wireless communications to solve issues caused by multipath fading [25]. Kosmas et. al showed promising simulation results using microwave TR algorithm for detection of breast tumors as small as 3 mm in diameter [26]. TR has also been applied to microwave nondestructive evaluation data to solve the inverse problem of defect detection in dielectric materials [27, 28]. Another application of TR is radar and imaging problems to detect targets in complicated environments [29, 30].

Time reversal started to be viewed as a backward-propagation mechanism, by giving the time-reversal procedure all the credit for spatial and temporal focusing, without considering either the medium or the structure of the TRM itself. Thus, there are two views of time reversal. One view deals with the subject as a signal- processing technique, which has some useful effects in some situations. This view was presented mainly in the work of Bogert [18] and his followers during the period from the late 1950s to the early 1990s. The other view defines time reversal as the backward propagation of the waves converging back to their source. The latter view started roughly in 2004, and dominates the current work on time reversal. Most of the available papers in which time reversal is applied to electromagnetics can be broadly categorized into four classes, as follows.

- **Introductory Work** : These papers include the interesting work and initial papers by Fink and related researchers, demonstrating the theory of TR for ultrasonic fields. The ultrasonic work reinitiated the work on time reversal in electromagnetics in 2004 [23] which ended with the 2010 paper in the IEEE Transactions on Antennas and Propagation demonstrating the theory of the electromagnetic TRM [24].

- **Wireless communications** : This category involves research dealing with the application of time reversal to the problem of multipath wireless communications. The main aim of the work was to apply Fink's successful experiments to the field of wireless communications [31]. The efficient spatial and temporal focusing capabilities of time reversal [31] was proposed as a promising technology to solve the distortions caused by multipath fading [31].

- **UWB communications** : TR based ultra-wideband communications in indoor and reverberant environments form the third category of papers [30]. Most of these papers were published by research groups from French universities and labs, drawing inspiration from Fink's work.

- **Radar and Imaging** : The last category includes most of the work applying time reversal to radar and imaging problems [29, 25, 28]. The pulse-compression capabilities of TR is utilized to detect targets in densely cluttered environments. The work is closely related to the concept of matched filters in conventional radars. One of the main limitation facing those techniques is the necessity of the deconvolution of the detector responses. This means that antenna responses in time-domain may affect the focusing performance of the system and hence need to be thoroughly studied before application.

There are several advantages of using TR [30] over conventional radar or microwave tomographic systems [32]. Besides its easy implementation procedure, TR is capable of utilizing multipath components in a highly cluttered environment for super-resolution focusing [25]. Its selective focusing capability [29] can determine a number of well-separated targets, producing higher signal-to-noise ratio (SNR) and faster convergence by restricting the inverse problem to a smaller domain.

2.4 Theory of TR

The scalar wave equation is invariant w.r.t. time-reflection in a lossless, passive medium due to the reciprocity theorem. This means that if $\varphi(r,t)$ is solution of the scalar wave equation:

$$(\nabla^2 - \frac{n^2(r)}{c^2}\frac{\partial^2}{\partial t^2})\varphi(r,t) = 0, \tag{2.2}$$

where c is the speed of light in vacuum and n is the refractive index of the medium, then $\varphi(r,-t)$ is solution of the wave equation too. If $\varphi(r,t)$ is a diverging wave from a source, then $\varphi(r,-t)$ is a wave converging on the source. The corresponding Green's function for (2.2) is given by

$$(\nabla^2 - \frac{n^2(r)}{c^2}\frac{\partial^2}{\partial t^2})G(r,t) = -\delta(r)\delta(t). \tag{2.3}$$

Hereafter, the time-reversal operator is indicated as T, i.e. $\varphi(r,-t) = T\varphi(r,t)$ [23]. When considering the electromagnetic field, Maxwell equations in a lossless medium are invariant w.r.t. time-reflection, assuming that the electromagnetic field is reflected (in time) as follows [23]:

$$\begin{aligned}
T\mathbf{E}(r,t) &= \mathbf{E}(r,-t),\\
T\mathbf{D}(r,t) &= \mathbf{D}(r,-t),\\
T\mathbf{H}(r,t) &= -\mathbf{H}(r,-t),\\
T\mathbf{B}(r,t) &= -\mathbf{B}(r,-t).
\end{aligned} \tag{2.4}$$

Thus, the electric field **E** and the electric flux density **D** are even, while the magnetic field **H** and the magnetic flux density **B** are odd, under a time reversal transformation. It can be easily shown from (2.4) that the four Maxwell's equations are time-symmetric. If **E**, **D**, **H** and **B** are solutions of Maxwell's equations, T**E**, T**D**, T**H** and T**B** are solutions to the same equations. Back propagation of the time reversed fields in a reversible medium results in proper spatial and temporal focusing of the waves on the source [23].

Phase conjugation is a term used in the frequency domain for monochromatic waves. The link between time reversal and phase conjugation can be easily understood. Expressing the equations in frequency domain, it is observed that time reversal in time domain is equivalent to phase conjugation in frequency domain. The Fourier transform $\varphi(r, \omega)$ of the field $\varphi(r, t)$ is given by

$$\varphi(r, \omega) = \int_{-\infty}^{\infty} \varphi(r, t) e^{-j\omega t} \tag{2.5}$$

Consequently, it can be seen that the fourier transform of the field $T\varphi(r, \omega)$ is $\pm\varphi^*(r, t)$, depending on the nature of the physical field. Thus, under an odd transformation time reversing a monochromatic field is not equal to phase conjugating it. Thus, the term 'time-reversal' is preferred rather than the term 'phase-conjugation'.

The pulse width of the excitation source should be ideally infinitesimally small. When the initial short pulse is a delta function, it has been shown that the time reversed field $\psi(r, t)$ is given by the interference of the divergent and convergent Green's function, given by :

$$\psi(r, t) \propto G(r, -t) - G(r, t) \tag{2.6}$$

where $G(r, t)$ is the causal Green's function ($G(r, t) = 0$ for $t < 0$) and $G(r, -t)$ is the anticausal Green's function ($G(r, -t) = 0$ for $t > 0$). For an infinite bandwidth signal, the focal spot would be a point. However in practical, signals are band-limited. For a band limited source, the interference of the converging and diverging wave leads to a focal spot [24].The spot can be determined by taking the Fourier transform of (2.6) as follows:

$$\psi(r,\omega) \propto G(r,\omega)^* - G(r,\omega) \propto \mathbf{Im}\ G(r,\omega). \tag{2.7}$$

Thus, the focal spot of the time reversed wave is governed by he imaginary component of the Green's function [24]. In the case of an isotropic 3D homogeneous medium, we know that the Green's function is given by

$$G(r,\omega) = \frac{e^{-jk|r|}}{4\pi|r|}. \tag{2.8}$$

If the source is located at r_0, 2.8 is changed to

$$G(r,\omega) = \frac{e^{-jk|r-r_0|}}{4\pi|r-r_0|}. \tag{2.9}$$

While the real part of the Green's function has a singularity at $r - r_0$, the imaginary part is continuous and proportional to $\sin(k|r-r_0|)/|r-r_0|$. The expression for the imaginary part electric-electric of the electric-electric Green's function when the wave polarization is parallel to $\hat{z}$ is given by

$$\mathbf{Im} = \hat{z}G_{EE}(r\hat{x})\hat{z} = \frac{\eta}{4\pi}\left[\frac{cos(kr)}{r^2} - sin(kr)(\frac{1}{kr^3} - k)\right]. \tag{2.10}$$

The typical fluctuation length scale is given by $1/k$ [24]. The typical focal spot governed by (2.10) is plotted in Fig. 2.4 and is of the order of wavelength.

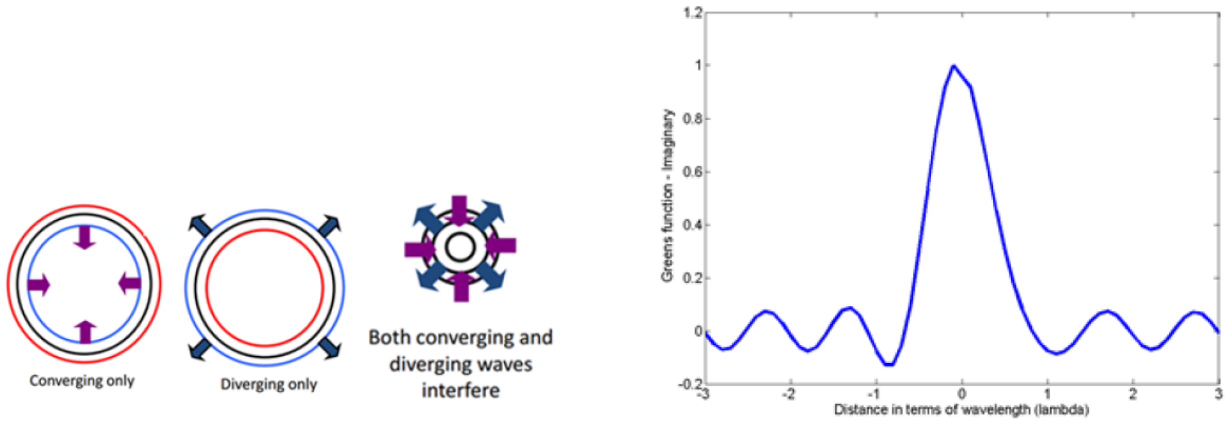

(a) (b)

Figure 2.4: Focal spot of the TR wave: (a) Interference of convergent and divergent waves, (b) Theoretical focal Spot

2.5 Numerical formulation

In this Section, we summarize the numerical model used for simulating the forward propagation simulation of EM waves through various media for generating the scattered fields. The same model is used for conducting TR back-propagations. A brief description of Maxwell's equations, numerical model based on finite difference time domain (FDTD) method, boundary conditions and excitation source is presented next.

2.5.1 Maxwell's equations

The governing equation describing the underlying physics are Maxwell equations:

$$\begin{aligned} \nabla \times \mathbf{E} &= -\frac{\partial \boldsymbol{\mu} \mathbf{H}}{\partial t} \\ \nabla \times \mathbf{H} &= \mathbf{J_s} + \boldsymbol{\sigma}\mathbf{E} + \frac{\partial \boldsymbol{\varepsilon}\mathbf{E}}{\partial t} \\ \nabla \cdot \boldsymbol{\mu}\mathbf{H} &= 0 \\ \nabla \cdot \boldsymbol{\varepsilon}\mathbf{E} &= \boldsymbol{\rho} \end{aligned} \tag{2.11}$$

where $\boldsymbol{\varepsilon}$, $\boldsymbol{\mu}$ and $\boldsymbol{\sigma}$ are the dielectric permittivity, the magnetic permeability and the electrical conductivity of the medium, respectively, $\boldsymbol{\rho}$ is the electric charge density and $\mathbf{J_s}$ is the source current density that produces electromagnetic waves. $\boldsymbol{\epsilon}$, $\boldsymbol{\mu}$ and $\boldsymbol{\sigma}$ are defined as tensors.

$$\boldsymbol{\sigma} = \begin{bmatrix} \sigma_{xx} & \sigma_{xy} & \sigma_{xz} \\ \sigma_{yx} & \sigma_{yy} & \sigma_{yz} \\ \sigma_{zx} & \sigma_{zy} & \sigma_{zz} \end{bmatrix}, \ \boldsymbol{\varepsilon} = \begin{bmatrix} \varepsilon_{xx} & \varepsilon_{xy} & \varepsilon_{xz} \\ \varepsilon_{yx} & \varepsilon_{yy} & \varepsilon_{yz} \\ \varepsilon_{zx} & \varepsilon_{zy} & \varepsilon_{zz} \end{bmatrix}, \ \boldsymbol{\mu} = \begin{bmatrix} \mu_{xx} & \mu_{xy} & \mu_{xz} \\ \mu_{yx} & \mu_{yy} & \mu_{yz} \\ \mu_{zx} & \mu_{zy} & \mu_{zz} \end{bmatrix}. \tag{2.12}$$

In linear, isotropic, time-invariant, non-dispersive media, the fluxes $\mathbf{D}, \mathbf{B}$ and the field strengths $\mathbf{E}, \mathbf{H}$ are related by material parameters.

$$\begin{aligned} \mathbf{D} &= \varepsilon \cdot \mathbf{E} \\ \mathbf{B} &= \mu \cdot \mathbf{H}. \end{aligned} \tag{2.13}$$

The variables are as follows

$\mathbf{E}$: Electric Field Intensity (V/m) ; $\mathbf{H}$: Magnetic Field Intensity (A/m)

$\mathbf{D}$: Electric Flux Density (C/m^2) ; $\mathbf{B}$: Magnetic Flux Density (T)

$\mathbf{J}$: Electric Current Density (A/m^3) ; ρ : Electric Charge Density (C/m^3)

ε : Dielectric Permittivity(F/m) ; μ : Magnetic Permeability(F/m)

σ : Electrical Conductivity(S/m)

2.5.2 FDTD formulation

The Finite Difference Time Domain (FDTD) method has become the state-of-the-art method for solving Maxwell's equations in complex geometries [33]. It is a fully vectorial method that naturally gives both time domain and frequency domain information to the user, offering unique insight into all types of problems and applications such as in electromagnetics and photonics. The technique is discrete in both space and time. The electromagnetic fields and structural materials of interest are described on a discrete mesh made up of Yee cells [34]. A basic FDTD Yee cell with staggered E and H fields is shown in Fig. 2.5. Maxwell's equations are solved discretely in time, where the time step used is related to the mesh size through the speed of light. This technique is an exact representation of Maxwell's equations in the limit that the mesh cell size goes to zero.

The numerical model used in this research is based on a two-dimensional TMz mode. Since there is no transverse magnetic field component, H_z, E_x and E_y are vanishing. The standard Leap Frog scheme is adopted to solve the FDTD Equations [34]. The FDTD equations for the electric and magnetic fields are given by

$$\begin{aligned}
E_z^{n+1}[i,j] &= \frac{1-\frac{\sigma\Delta t}{2\varepsilon}}{1+\frac{\sigma\Delta t}{2\varepsilon}} E_z^n[i,j] - \frac{1}{1+\frac{\sigma\Delta t}{2\varepsilon}}\Big(\frac{\Delta t}{\varepsilon\Delta x}\big(H_y^{n+\frac{1}{2}}[i+\frac{1}{2},j] \\
&\quad -H_y^{n-\frac{1}{2}}[i-\frac{1}{2},j]\big) - \frac{\Delta t}{\varepsilon\Delta x}\big(H_x^{n+\frac{1}{2}}[i,j+\frac{1}{2}] - H_x^{n-\frac{1}{2}}[i,j-\frac{1}{2}]\big)\Big); \\
H_x^{n+\frac{1}{2}}[i,j+\frac{1}{2}] &= H_x^n[i,j+\frac{1}{2}] - \frac{\Delta t}{\mu\Delta x}(E_z^n[i,j+1] - E_z^n[i,j]; \\
H_y^{n+\frac{1}{2}}[i+\frac{1}{2},j] &= H_y^n[i+\frac{1}{2},j] - \frac{\Delta t}{\mu\Delta x}(E_z^n[i+1,j] - E_z^n[i,j];
\end{aligned} \tag{2.14}$$

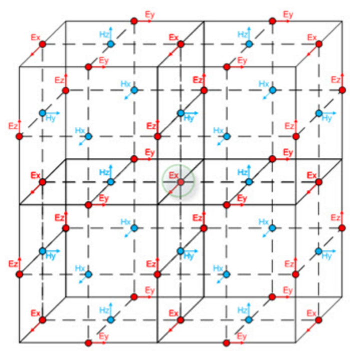

Figure 2.5: Staggered E,H fields on an Yee cell

where σ and ε are the material conductivity and dielectric constant, Δt and Δx are the FDTD time steps and cell size respectively. The spatial step sizes in the modelis chosen to be equal in both x and y directions and satisfy Courant's stability conditions : $c\Delta t \leq \frac{\Delta x}{\sqrt{2}}$. Additionally, in order to avoid significant changes in the fields, $\Delta x = \Delta y \leq \lambda/10$.

2.5.3 Boundary conditions

Since FDTD is used for solving the electromagnetic waves in an open space, efficient boundary conditions need to be imposed to truncate the domain and reduce the computational costs. Proper boundary conditions need to be implemented in order to avoid field reflections at the outer boundary interfaces. Although there have been numerous boundary condition schemes in place, MUR's Absorbing boundary Conditions (ABCs) have been employed in this model [35]. Absorbing boundary conditions are imposed as boundary conditions in order to avoid field reflections at the outer boundary interfaces. The outgoing first order condition is given by :

$$\left(\partial_x - c_0^{-1}\left(1-(c_0 s_y)^2-(c_0 s_z)^2\right)^{\frac{1}{2}}\partial_t\right)W_{x=0} = 0, \tag{2.15}$$

where s_y, s_z are the inverse velocity components of the wave and W is H_x or H_y for TM to z. This equation solves for W on the outer surface, so that it is consistent with an outgoing wave. The finite difference approximation equations implementing absorbing boundary conditions for the H field are given by:

$$\begin{aligned} H_y^{n+\frac{1}{2}}[i,0] &= H_y^{n-\frac{1}{2}}[i,1] - \frac{c\Delta t - x}{c\Delta t + x}\left(H_y^{n+\frac{1}{2}}[i,1] - H_y^{n-\frac{1}{2}}[i,0]\right) \\ H_x^{n+\frac{1}{2}}[0,j] &= H_x^{n-\frac{1}{2}}[1,j] - \frac{c\Delta t - x}{c\Delta t + x}\left(H_x^{n+\frac{1}{2}}[1,j] - H_x^{n-\frac{1}{2}}[0,j]\right) \end{aligned} \tag{2.16}$$

While MUR boundaries are utilized in several simulations for this research, the MUR boundaries are inaccurate in certain cases such as oblique incidences and when the source is placed close to the boundaries. As a result, Perfectly Matched Layers (PMLs) were invented by Berenger in [36] to tackle this issue, which could absorb waves at all angles. A detailed derivation of the mathematics involving PML boundaries can be found in [36]. PML boundaries have been utilized in simulations where source is placed close to the boundary for this research. Although PMLs work efficiently for lossy, dielectric media, it is inefficient for complicated mediums such as metamaterials. Moreover, PML is derived from a non-physical field splitting method of Maxwells equations. This generates significant discretization error while implementing FDTD, especially when the source is placed close to the boundaries. Various advancements to tackle this problem have resulted in novel boundary conditions such as uniaxial PML [37]. However in 2000, Roden and Gedney invented the Convolution PML (CPML) which is entirely independent of the medium properties such as inhomogeneity, loss, dispersiveness, nonlinearity and anisotropy while implementing the splitting field technique and efficiently absorbs evanescent fields. A detailed derivation of the mathematics involving CPML boundaries can be found in [38]. The final electric field components can be expressed as:

$$
\begin{aligned}
E_z^{n+1}(i,j) &= E_z^n(i,j) + \frac{\Delta t}{\Delta x \varepsilon_0 \kappa_{ex}(i,j)} \left[H_y^{n+1/2}(i,j) - H_y^{n+1/2}(i-1,j) \right] \\
&\quad - \frac{\Delta t}{\Delta y \varepsilon_0 \kappa_{ey}(i,j)} \left[H_x^{n+1/2}(i,j) - H_x^{n+1/2}(i,j-1) \right] \\
&\quad + \frac{\Delta t}{\varepsilon_0} \varphi_{ezx}^{n+1/2}(i,j) - \frac{\Delta t}{\varepsilon_0} \varphi_{ezy}^{n+1/2}(i,j) \\
\varphi_{ezx}^{n+1/2}(i,j) &= b_{ex} \varphi_{ezx}^{n-1/2}(i,j) + a_{ex} \Big(H_y^{n+1/2}(i,j) - H_y^{n+1/2}(i-1,j) \Big) \\
\varphi_{ezy}^{n+1/2}(i,j) &= b_{ey} \varphi_{ezy}^{n-1/2}(i,j) + a_{ey} \Big(H_x^{n+1/2}(i,j) - H_x^{n+1/2}(i,j-1) \Big) \\
a_{ey} &= \frac{\sigma_{pey}[b_{ey} - 1]}{\Delta y(\sigma_{pey}\kappa_{ey} + \alpha_e y \kappa_{ey}^2)} \quad ; \quad b_{ey} = \frac{\Delta t}{\varepsilon_0} e^{-\frac{\sigma_{pey}}{\kappa_{ey}} + \alpha_{ey}}
\end{aligned} \tag{2.17}
$$

where κ, σ, α are the parameters corresponding to the complex stretched coordinate metrics. σ, α are assumed to be real and positive, while κ is real and $\geq$1. CPML boundary conditions have been utilized in this research for conducting simulations related to metamaterials.

2.5.4 Source

The excitation source is a modulated UWB Gaussian pulse having a modulating frequency f_c=2 GHz

$$
s(t) = e^{-\frac{(t-t_0)^2)}{2\sigma^2}} cos(2\pi f_c t), \tag{2.18}
$$

where the Gaussian pulse is centered at t_0 and $\sigma = 20/(2\sqrt{2\log(2)})\Delta t$, which determines the bandwidth of the pulse. The center wavelength (λ) of the pulse is 15 cm (corresponding to f_c). As shown in Fig. 2.6, the pulse has a narrow width of 120 picoseconds, corresponding to a half power bandwidth of 5.5 GHz. The sinusoidal part of the signal shifts the center frequency of the gaussian signal by f_c. While the resolution is determined from the central wavelength and other factors as mentioned before in the previous chapter, the range resolution is governed by pulse width, with smaller pulse width leading to better detection. The narrow pulse provides a large frequency spectrum (ultra-wide band), which is desirable for TR. The equation that is used in the FDTD algorithm to apply the source is

$$
\begin{aligned}
E_z^{n+1}[i,j] = \frac{1-\frac{\sigma\Delta t}{2\varepsilon}}{1+\frac{\sigma\Delta t}{2\varepsilon}} E_z^{n}[i,j] - \frac{1}{1+\frac{\sigma\Delta t}{2\varepsilon}} \Bigg(\frac{\Delta t}{\varepsilon\Delta x}\big(H_y^{n+\frac{1}{2}}[i+\tfrac{1}{2},j] - H_y^{n-\frac{1}{2}}[i-\tfrac{1}{2},j]\big) \\
- \frac{\Delta t}{\varepsilon\Delta x}\big(H_x^{n+\frac{1}{2}}[i,j+\tfrac{1}{2}] - H_x^{n-\frac{1}{2}}[i,j-\tfrac{1}{2}]\big)\Bigg) - \frac{\Delta t}{\varepsilon} J_z^{n+\frac{1}{2}}[i,j]
\end{aligned}
\tag{2.19}
$$

where J_z is the input current density due to the pulse.

The region was modeled using the above numerical model. Electromagnetic fields recorded at sensor locations in the geometry were time reversed and back-propagated in the same model to obtain focusing.

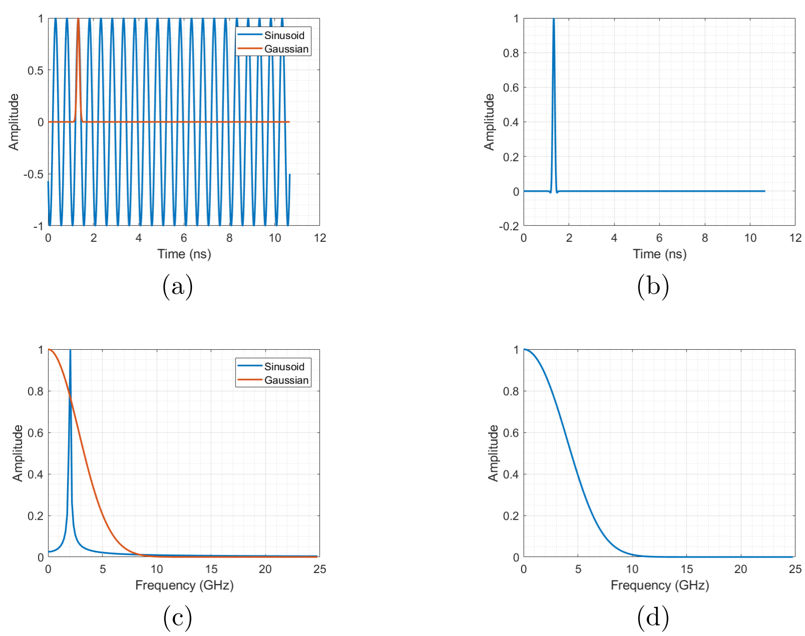

Figure 2.6: Source: Individual pulses in (a) time domain, (c) frequency domain, Modulated pulse in (b) time domain, (d) frequency domain

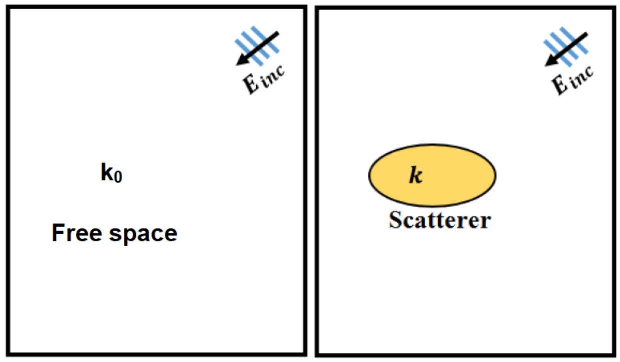

Figure 2.7: Plane wave incident on free space and a scatterer

2.6 Development of TR algorithm for imaging

The time reversal algorithm involves back-propagation of the perturbed signal in free space, which is the difference between the signals from free space and scatterer. The back-propagated signal focuses on the scatterer location since the perturbation signal satisfies the Helmholtz equation. This can be theoretically proved by considering a scenario shown in Fig. 2.7, showing a plane wave incident on free space and a scatterer. The free space total electric field (φ_0) satisfies the scalar Helmholtz equation :

$$\nabla^2\varphi_0 - \frac{1}{c^2}\frac{\partial^2\varphi_0}{\partial t^2} = 0. \tag{2.20}$$

The total electric field in the presence of the scatterer (φ) also satisfies the scalar Helmholtz equation:

$$\nabla^2\varphi - \frac{n^2(r)}{c^2}\frac{\partial^2\varphi}{\partial t^2} = 0. \tag{2.21}$$

The perturbation due to the scatterer given by ($\widetilde{\varphi} = \varphi - \varphi_0$) is obtained by subtracting 2.10 from Equation 2.21. Subtracting the two equations, we obtain

$$\nabla^2\widetilde{\varphi} - \frac{1}{c^2}(\frac{n^2(r)\partial^2\varphi}{\partial t^2} - \frac{\partial^2\varphi_0}{\partial t^2}) = 0. \tag{2.22}$$

Expressing $n = \sqrt{1+f}$, we can rewrite 2.22 as

$$\nabla^2 \widetilde{\varphi} - \frac{1}{c^2}\left(\frac{f\partial^2 \varphi_0}{\partial t^2} + \frac{(1+f)\partial^2 \widetilde{\varphi}}{\partial t^2}\right) = 0. \tag{2.23}$$

Simplifying Equation 2.23, we obtain the expression for the perturbed field in the form of Helmholtz equation.

$$\nabla^2 \widetilde{\varphi} - \frac{n^2(r)}{c^2}\frac{\partial^2 \widetilde{\varphi}}{\partial t^2} = \frac{f}{c^2}\frac{\partial^2 \varphi_0}{\partial t^2}. \tag{2.24}$$

Thus, the perturbation field due to the scatterer satisfies the Helmholtz equation due to a source which depends on free space field, wave number and refraction index of the material. Thus, back-propagating the perturbed field in free space focuses the wave back at the scatterer.

Conventional inverse imaging problems are iterative algorithms based on error minimization with regularization algorithms to determine the location of a target. Such iterative procedures typically suffer from slow and can converge to local minima and thus can be computationally intensive [16, 17, 5]. The proposed time reversal algorithm uses a non-iterative approach as shown in Fig. 2.8 [39, 6].

The basic time reversal process is given by the following steps:

- a short pulse is transmitted from an antenna to the region of interest where the sample is positioned;
- scattered signals due to the background and scatterer are measured by the receivers;
- the two signals are subtracted from each other in order to obtain the perturbation signal;

(a) (b)

Figure 2.8: Schematic of TR approach (a) Flowchart, (b) Demonstration

- the perturbation signal waveform is reversed in time and back-propagated in free space using a numerical model;
- localization techniques are applied to obtain spatio-temporal focusing.

To summarize, the scattered fields collected by the receiver antenna array are time reversed and back propagated using simulation model in free space to focus back at the target or source location. Localization techniques are capable of providing information on both spatial and temporal focusing.

2.7 Localization techniques

Assuming that a transmitter at a location $\overrightarrow{r}_0$ sends a pulse $s(t)$,the signal measured at a receiver located at $\overrightarrow{r}_i$ (shown in Fig. 2.9) can be expressed in terms of the convolution

$$f_i(t) = s(t) * h_{\overrightarrow{r}_0 \overrightarrow{r}_i}(t), \tag{2.25}$$

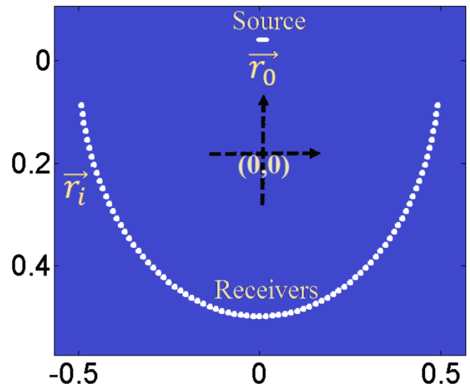

Figure 2.9: Problem geometry

where $h_{\overrightarrow{r}_0\overrightarrow{r}_i}(t)$ is the impulse response between $\overrightarrow{r}_0$ and $\overrightarrow{r}_i$. From the reciprocity theorem, $h_{\overrightarrow{r}_0\overrightarrow{r}_i}(t)$=$h_{\overrightarrow{r}_i\overrightarrow{r}_0}(t)$=$h_{\overrightarrow{r_i}}(t)$. Thus, the time-reversed retransmitted signal at $\overrightarrow{r}_0$ due to a source at $\overrightarrow{r}_i$ is given by

$$p_i(t) = s(-t) * h_{\overrightarrow{r_i}}(-t) * h_{\overrightarrow{r_i}}(t). \tag{2.26}$$

For a time reversal array with N receivers, the received signal is given by

$$p(\overrightarrow{r}_0, t) = \sum_{i=1}^{N} s(-t) * h_{\overrightarrow{r_i}}(-t) * h_{\overrightarrow{r_i}}(t). \tag{2.27}$$

As mentioned in step 5 of the Time Reversal method, different localization techniques are employed in order to find the proper temporal instant and spatial extents of the defect. The proper focusing instant can be found out using several techniques.

- **Maximum electric field**: At the exact focusing instant, the electric fields are tightly concentrated around the target region. Thus, the E-field magnitude is maximum during this time frame. As reported by Zheng et al. [40], in this method the maximum E-field amplitude of the imaging domain is found at each time frame and it is plotted along the time axis. The time at which the back-propagated wave is in focus corresponds to the maximum of this plot, given by :

$$t_{opt} = \{ \ \ t' : E_{max}(t') \geq E_{max}(t), t_0 < t < t_1 \ \ \& \ \ t \neq t' \ \ \} \tag{2.28}$$

- **Minimum Entropy**: The first method involves an entropy regularization technique, based on finding the maximum of the inverse of the normalized variance of the fields, also known an inverse varimax norm [41, 42]. The back-propagated wave focuses at the defect and after a time lag, starts diverging from it, due to the spatio-temporal matched filter property of time reversal. The time instant corresponding to this convergence-divergence transition is determined from the local minimum entropy criterion **(R)**. The entropy can be defined using multiple ways. We have used two different definitions in this context. The first definition is given by:

$$R(n) = -\frac{\sum_i \sum_j p_{ij}(n)\ \ln(p_{ij}(n))}{\max(p_{ij}(n))}, \tag{2.29}$$

where $p_{ij}(n) = \frac{E_n^2(i,j)}{\sum_i \sum_j E_n^2(i,j))}$. In the above equations,n refers to the number of time steps, while $p_{ij}(n)$ is the normalized square amplitude of the electric field. The second definition for entropy is given by:

$$\mathbf{R}(n) = \frac{\left[\sum_i \sum_j E_n^2(i,j)) \right]^2}{\sum_i \sum_j E_n^4(i,j)}. \tag{2.30}$$

Equation 2.30 represents the entropy of the electric fields, and is based on finding the maximum of the inverse of the normalized variance of the fields. Hence, it is also known an an inverse varimax norm. The derivation of the varimax norm is shown below: Let

x_{ij} be our signals, where $i = 1 : N_s$ and $j = 1 : N_t$. Let $y_{ij} = \sum_i^(N_u) f_k x_{i,j-k}$. The varimax norm is given by :

$$V = \sum V_i$$
$$V_i = \frac{\sum_j y_{ij}^4}{(\sum_j y_{ij}^2)^2}. \tag{2.31}$$

V_i is the sum of the normalized squares of the variance. The minimum of V corresponds to the maximum of its minimum. Such an approach maximizes the order or equivalently minimizes the entropy of the system. The minimum entropy instant corresponds to the maximum energy instant of the time-reversed fields. Thus, the electric fields computed at this time frame provide a tightly focused image around the defect.

- **Integrated energy method**: The second method involves calculation of the integrated energy image of the back-propagated fields. Since time-reversal focusing is similar to matched filter techniques in signal processing, a sharp peak is produced when the time-reversed signal correlates with the medium response [**?**]. The time reversed, back-propagated signal at the source is given by

$$\varphi(r,t) = \sum_{r=1}^{M} h_r(t) * h_r(-t), \tag{2.32}$$

where $h(t)$ is the impulse response function and M is the number of receivers. Each signal in the convolution sum add constructively, while uncorrelated contributions that occur at a different time will interfere destructively. The result of this convolution will reach its maximum at time t = 0. The maximum is equal to the energy of the TR signals (Θ) given by

$$\Theta(i,j) = \sum_{t=1}^{N} E_n^2(i,j)\Delta t, \tag{2.33}$$

where N is the total number of time steps and Δt is the time step.

Chapter 3

Target localization by time reversal

3.1 Introduction

Target detection is the first step of an imaging experiment. The detection sensitivity and the resolution limits determine the imaging capability of the system. This chapter demonstrates use of TR technique for for target detection and localization applications using far-field microwave measurements in reflection mode. Simulation results investigate the feasibility and robustness of this approach and determine the limits of this technique. Experimental results based on reflection mode measurements validate the approach for the detection of source and closely spaced multiple dielectric targets.

Previously, the TR technique was successfully applied for source focusing in transmission mode. In this part, we attempt to utilize a microwave TRM for localizing source and targets using reflection mode measurements. Reflection mode based measurements are crucial in experiments having only single side access, such as through-the-wall target detection for civilian and military applications [43], NDE of metal-composite joints, surface penetrating radar [44] and biomedical applications such as breast tumor detection. Metallic targets are often easier to detect in reflection mode due to their strong backscatter fields, but it is difficult to detect weak dielectric targets in reflection mode. Thus, it is important to study the capabilities of reflection mode TR to see if it is appropriate for the many scenarios that require single-side access.

Theoretically, a contrast in the dielectric properties would lead to a contrast in the scattered fields, leading to detection. Since dielectric targets behave as weak scatterers, detection becomes difficult with decreasing dielectric constant, especially in the reflection configuration. Although a single target with low dielectric constant might be detected, it is more difficult to detect these weak targets close to strong metal targets. However, in practice factors such as accuracy, signal to noise ratio, and hardware limitations should affect the detection capability. Hence the capabilities of reflection mode TR need to be studied.

Scattered electromagnetic fields from targets at long distances are received by an antenna array system. Back-propagation of the time reversed fields focuses back at the target locations. Initial simulations and parametric analysis demonstrate the feasibility of this technique to detect and localize targets. The simulations are validated by far field experimental results using a pulsed time domain laboratory setup. Time reversed images show efficient localization of excitation sources, single and multiple dielectric and metal targets in free space. Accurate results and high imaging quality achieved from the parametric limits obtained from robust simulation studies demonstrate the efficacy of this work. The focusing resolution of the time reversed image is studied particularly with regard to rapid inspection of large areas.

3.2 Time reversal algorithm and simulations

Simulation studies are conducted to understand the feasibility of time reversal for target detection. TR simulations were conducted to detect source and dielectric targets in reflection mode. A metal sheet of length 1.27 m and dielectric target of radius 5 cm and dielectric

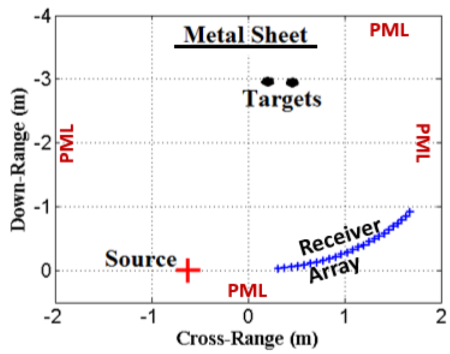

Figure 3.1: Schematic of the FDTD simulation model

constant (ε_r) =4 were used as reflection targets. The reflected or back-scattered fields from the targets were time reversed and back-propagated. The schematic for the simulations is shown in Fig. 3.1. The transmitter is modeled as a point source, and a circular array of sensors is used to collect the back-scattered fields. The fields are time-reversed and back-propagated in the same model.

3.2.1 Quantitative metrics

Two quantitative metrics have been studied in this research in order to evaluate the accuracy and quality of the imaging algorithm.

- Detection Error: Using the localization techniques as mentioned before, the time reversed wave focuses on the target location with the energy peak localized at the center of the target. Hence, the center of the target is assumed as the maximum intensity point of the localized energy images. The detection error is defined as the relative difference between the actual and predicted locations of the target ξ :

$$\xi = \frac{|\overrightarrow{\rho}_m - \overrightarrow{\rho}_a|}{R} \tag{3.1}$$

where ρ_m and ρ_a are the predicted and actual locations of the target and R is the region of interest.

- Imaging Quality: The signal to noise ratio or the resolution of the time reversed image is expressed in terms of imaging quality (IQ):

$$\mathrm{IQ} = 20\log_{10}\left\{\frac{X - X_s}{X_s}\frac{\sum_{i=1}^{X_s} E_s^2}{\sum_{j=1}^{X-X_s} E_r^2}\right\}, \tag{3.2}$$

where X is the total number of pixels of the image, X_s is the total number of pixels containing the peak 5% of the total energy,, E_s is the electric field magnitude of the X_s pixels and E_r is the electric field magnitude of the rest of the pixels of the imaging domain. This value is used as a quantitative comparison of the image resolution for different simulations and experiments.

3.2.2 Source localization

The detection of source is determined from the entropy localization criterion. The spatio-temporal focusing instant is calculated according to (3.2) and shown in Fig. 3.2(a). A sharp minimum is observed at an early time instant A. Electric fields corresponding to this instant are focused at the metal sheet location (Fig. 3.2(c)). A second local minimum is observed at time instant B. Electric fields, corresponding to this instant, are localized around the source region (Fig. 3.2(d)). The location corresponding to the peak value of electric field image is estimated as the source location. The energy image according to the integrated energy image technique, is shown in Fig. 3.2(b).

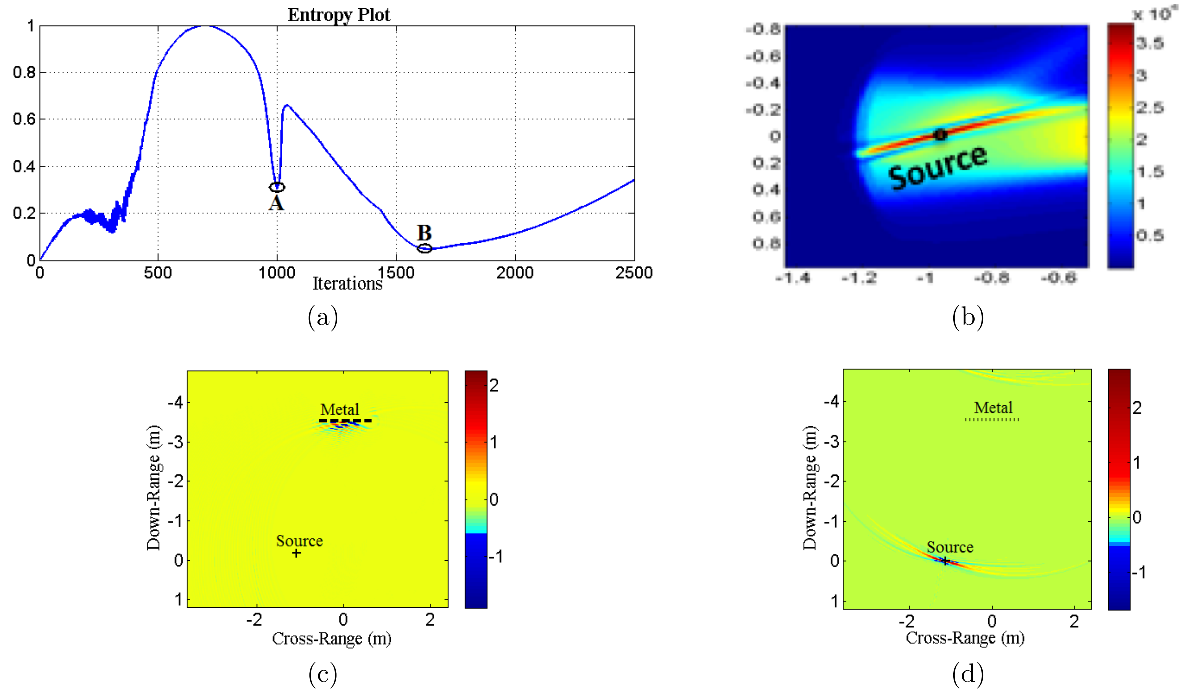

(a) (b) (c) (d)

Figure 3.2: Source localization simulations: (a) TR Entropy plot, (b) TR Energy image, (c) Electric fields focused at metal plate at time instant A, (d) Electric fields focused at source at time instant B

3.2.3 Target localization

The next objective is to demonstrate the feasibility of the reflection mode time reversal setup for detecting dielectric targets. The visualization of the back-scattered time reversed electric fields shows them starting to converge, focusing near the target location, and diverging away from the target. The spatio-temporal focusing instant, A obtained from the entropy localization is shown in Fig. 3.3 (a). The electric field image corresponding to A shows the localized fields very close to the actual target location, as seen in Fig. 3.3(b), while the integrated energy image shows the energy localized around the target location, given by Fig. 3.3(c).

Thus while the minimum entropy criterion is capable of determining the exact focusing instant at which the waves are localized around the target, the integrated energy is capable of

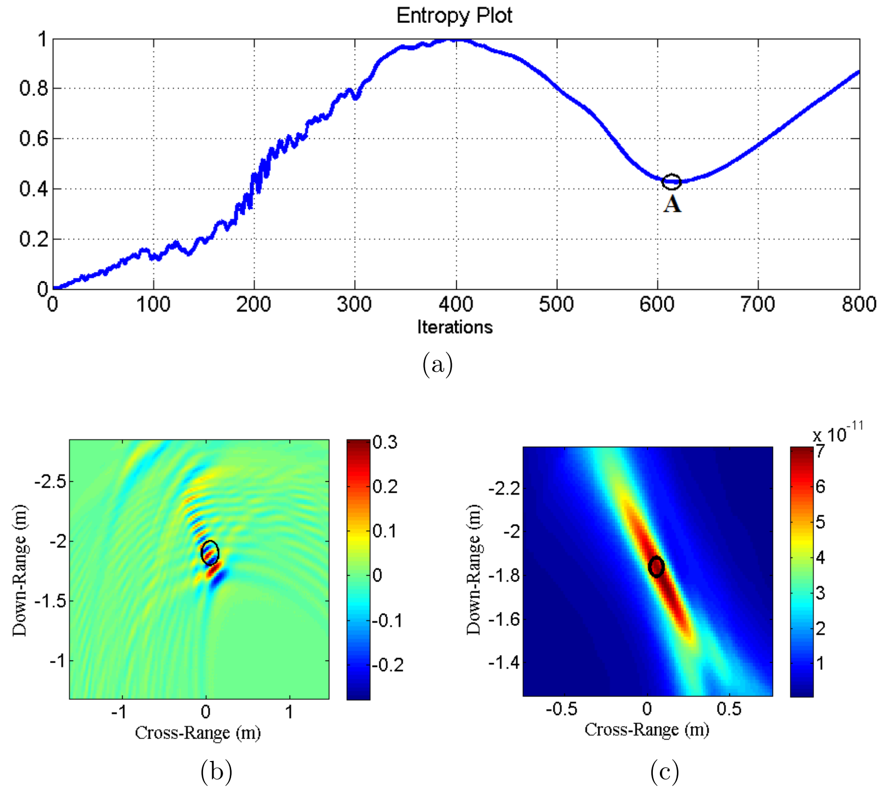

Figure 3.3: Target localization simulations:(a) TR Entropy plot, (b) Electric fields focused at target at time instant A, (c) Integrated energy image

providing a focal spot around the target. The time reversed focusing resolution is diffraction limited in both down-range (DR) and cross-range (CR), as described in [45]. The CR and DR resolutions are limited to $\lambda\frac{L}{a}$ and $\lambda(\frac{L}{a})^2$ respectively, where L is the distance of the

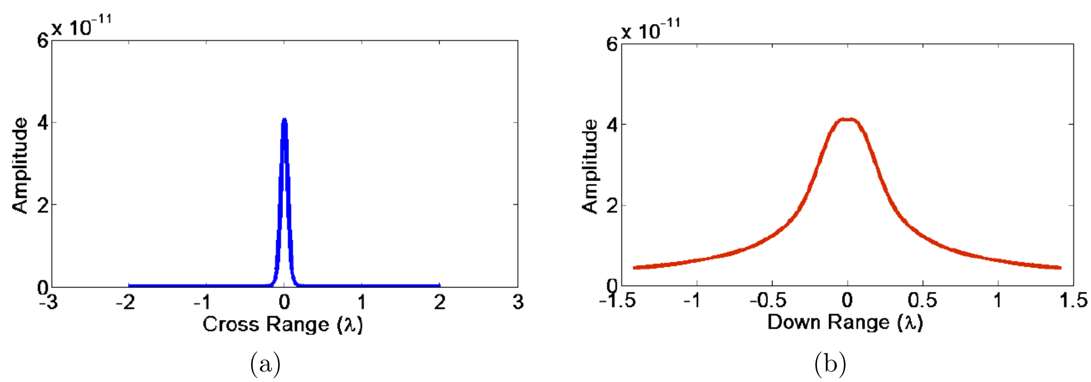

Figure 3.4: (a) CR Resolution, (b) DR Resolution

target from the source and a is the length of the time reversal array [46]. An example of the resolution is shown by choosing $L > a$ so that the ration $\frac{L}{a} > 1$. Thus the CR resolution should be better than the DR resolution. The CR and DR focusing for a point source in such a case is shown in Fig. 3.4. We observe that the CR resolution is indeed better than the DR resolution. Although a target having smaller dimensions ($\sim \lambda/2$) can be detected, the focal spot will be limited to the resolution limits. A tightly focused image is obtained if we have a receiver array that provides full $360°$ coverage surrounding the target. But, since the access is restricted to one side, with a limited angular coverage of only $40°$, the energy image is stretched out (along the down range).

Although, the full width at half maxima of the energy signals give an approximate length of the target, advanced algorithms such as space time based signal processing can be efficiently utilized to extract the exact properties of the target. Techniques such as space-time based signal processing and statistical techniques based on maximum likelihood [30], MUSIC [47] and DORT [29] should be able to provide further information such as the shape and material properties of the target.

3.2.3.1 Iterative model based technique for target sizing

Once the target is located using TR algorithm, very often it is necessary to determine target size. This section describes an iterative model based approach, where an initial profile is assumed, and simulated to predict the scattered signal. The error between measured and predicted signal is computed. The target profile is iteratively update to minimize this error. When the achieved cost function is less than a specified threshold, the desired target profile is achieved.

The maximum intensity point of the energy image is assumed to be the center of the target. The sizing algorithm is summarized in the steps below:

- Input the data $Di, i = 1, 2, \ldots, N$ to TRM.

- Determine location (x_a, y_a) from energy image.

- Initial target size L at (x_a, y_a).

- Use forward propagation model to generate data array signal $M_i, i = 1, \ldots, N$.

- Calculate the cost function : $J = \|D_i - M_i\|^2$

- Update $L_i = L_{i-1} + \Delta L$

- go to step 4

  else

- If $J > \epsilon - -L$ is reconstructed size of target $\longleftrightarrow$ Stop

The algorithm was implemented for a target of radius 5 cm. The cost function was calculated at each iteration, and is displayed in Fig. 3.5. It is seen that the cost function achieves a global minimum when the target radius is iteratively updated to its actual value. Hence the algorithm can be used to determine both the location and the spatial dimensions of the target.

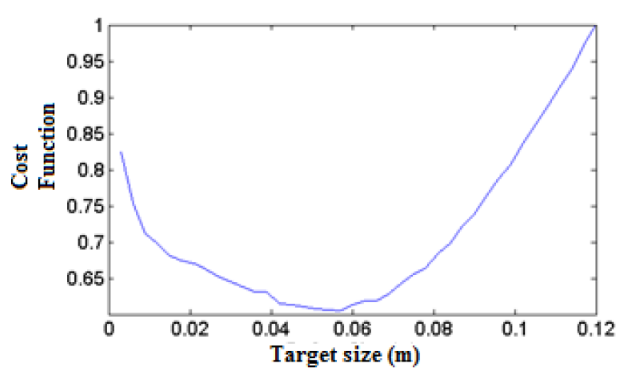

Figure 3.5: Cost function reaches minimum near the actual target size

3.2.4 Parametric studies

A parametric analysis of the TR algorithm for target detection is done to determine its robustness with respect to the target size, receiver array angular coverage, number of sensors and noise. For each of these parameters, the time reversed energy peak value was examined, which can be used as a measure of the quality or resolution of the time reversed image. The parameter limits obtained from the simulations are later used in the experiments.

3.2.4.1 Target size

The time reversed wave focuses back with an amplitude proportional to the reflection coefficient and size of the targets. Hence, the TR energy peak at the target increases with increasing target size, as shown in Fig. 3.6. Fig. 3.7 shows the parametric variation of the

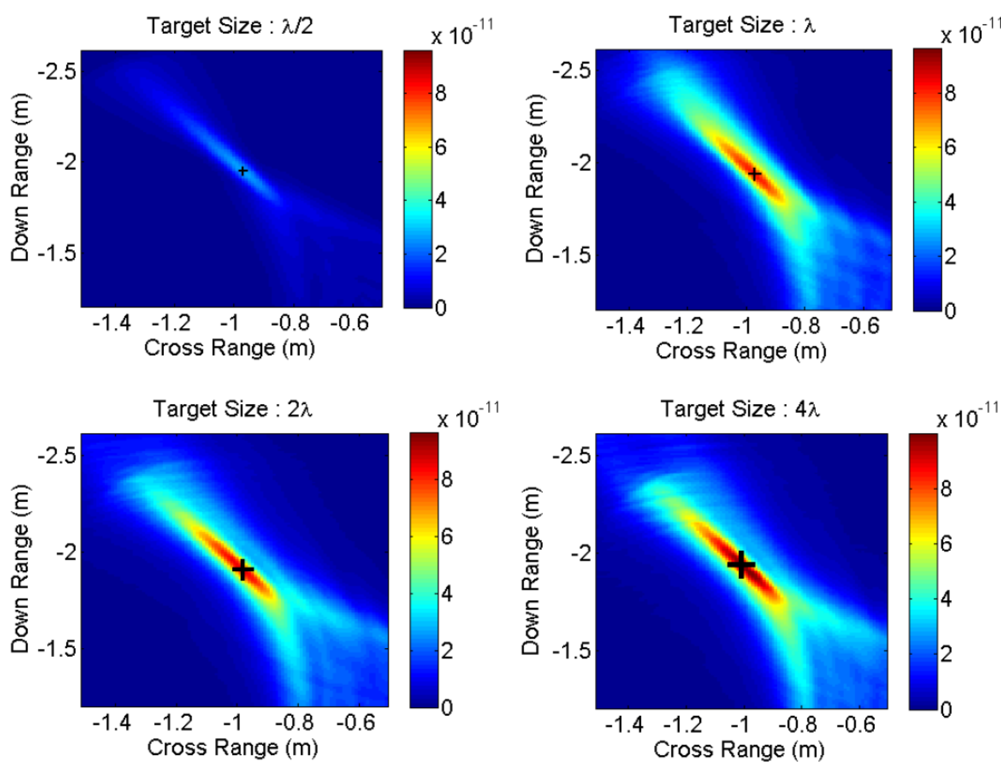

Figure 3.6: TR Energy image vs target size

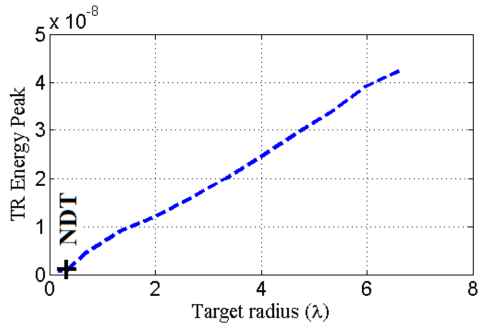

(a)

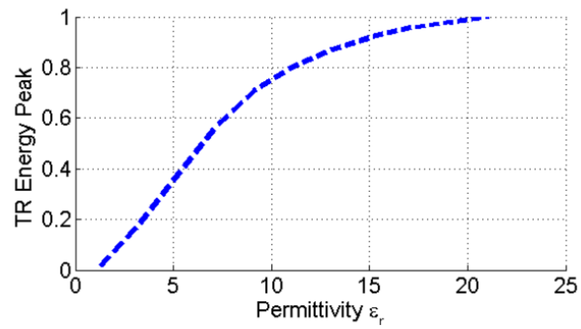

(b)

Figure 3.7: TR Energy peak vs : (a) target size, (b) target dielectric constant

time reversed energy peak with respect to the size and dielectric constant of the target. The time reversal technique follows the classical diffraction limits, producing a focal spot of the order of a wavelength [24]. The time reversal technique follows the classical diffraction limits, producing a focal spot of the order of wavelength. The minimum target that can be detected has a radius of 0.06 m (0.4λ). Scatterers smaller than (0.4λ) are non detectable targets (NDT) in the energy image.

3.2.4.2 Angular coverage

A parametric study of the minimum number of array elements and angular coverage of the receiving antenna array is described in this section. The greater the angular coverage, and smaller the inter-element spacing (larger number of elements) of the receiving antenna array, the more enhanced the information in the scattered fields is, leading to a higher lateral resolution of the energy image. Thus, the TR energy peak at the target location increases with angular coverage and number of array elements of the receiver, as depicted in Fig. 3.8. However, with limited angular coverage and number of sensors, the TR method is still able to image the target location. As shown in Fig. 3.8, for the target radius of 0.4λ and an angular coverage of $40°$, a minimum of 20 sensors are required for detection.

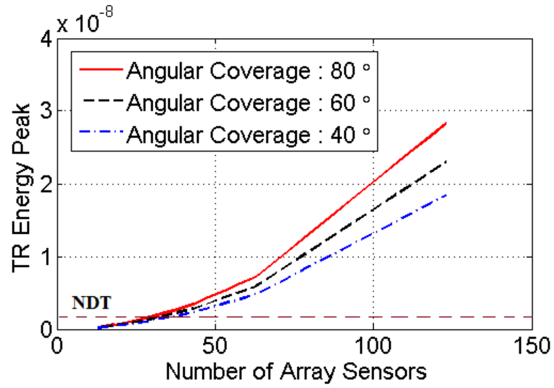

Figure 3.8: TR energy peak vs angular coverage and number of sensors

3.2.4.3 Effect of noise

In order to evaluate the robustness of the time reversal algorithm, its performance was evaluated with noisy data. Consider noisy time reversed measurements expressed as $h_r(-t)+n_r(t)$, the back propagated signal is given by

$$\mathrm{S}_{\mathrm{TR}}(t) = \sum_{t=1}^{N} h_r(t) * h_r(-t) + \sum_{t=1}^{N} h_r(t) * n_r(t) \tag{3.3}$$

The random background noise $n_r(t)$ is uncorrelated with the medium's impulse response. Hence the phase differences between relative array elements are not hampered by the addition of uncorrelated noise and time reversal focusing is achieved efficiently, even for very low SNRs. Additive white Gaussian noise with SNR of 10 dB is added to the individual receiver antenna signals, as shown in Fig. 3.9(a). The back propagated noisy time-reversed fields still show good target localization ability and the integrated energy image highlights the target location in Fig. 3.9(b). The simulated SNR threshold for detection is found out to be as low as 5 dB.

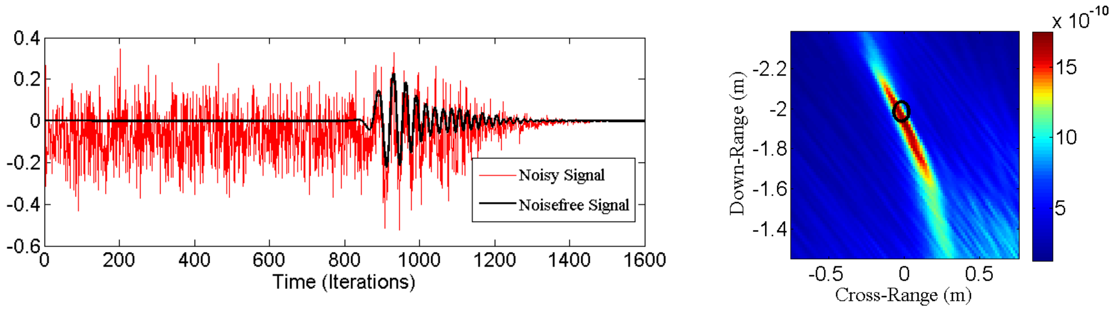

(a) (b)

Figure 3.9: Effect of noise: (a)5 dB noise addition, (b) TR Energy image

Table 3.1: Target detection experiments

Case	Details	Size (m)	Coverage
I	Source	0.125	40°
II	Single Target	0.016	40°
III	Single Target	0.016	80°
IV	Two cross-range separated targets (0.05 m)	0.02	40°
V	Two down-range separated targets (0.08 m)	0.02	40°
VI	Two down-range separated targets (0.16 m)	0.02	40°
VII	Metal and two cross-range separated targets (0.3 m)	0.02	40°

3.3 Experimental studies

Passive time reversal experiments were conducted with the help of a time domain laboratory setup and a back-propagation code for detecting source, single and multiple targets in reflection mode. Seven different experimental scenarios are outlined in Table 3.1, and corresponding results are presented in the next sections. A detailed description of the experimental setup and measurement procedure is provided in Appendix B.

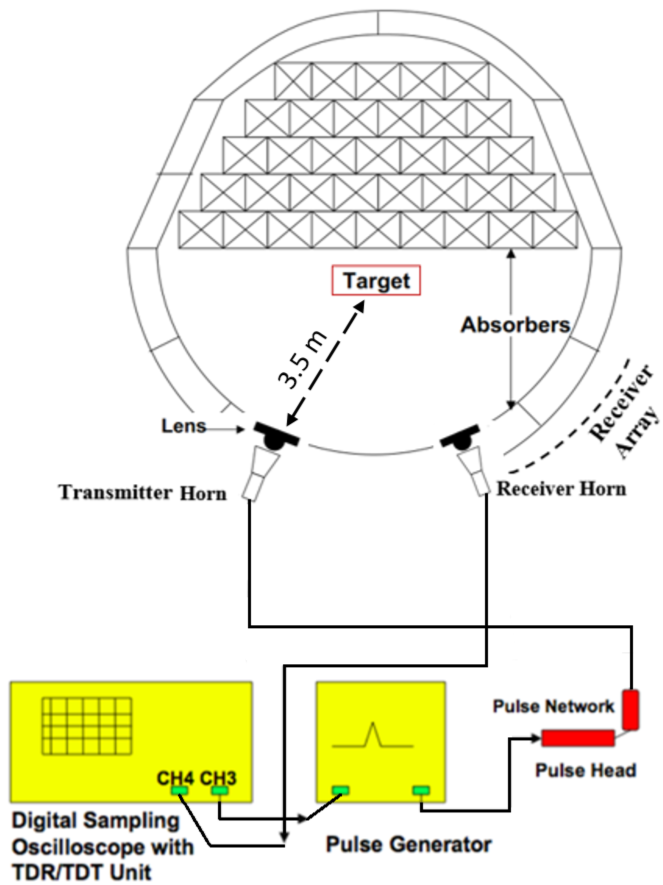

Figure 3.10: Time domain scattering measurement configuration

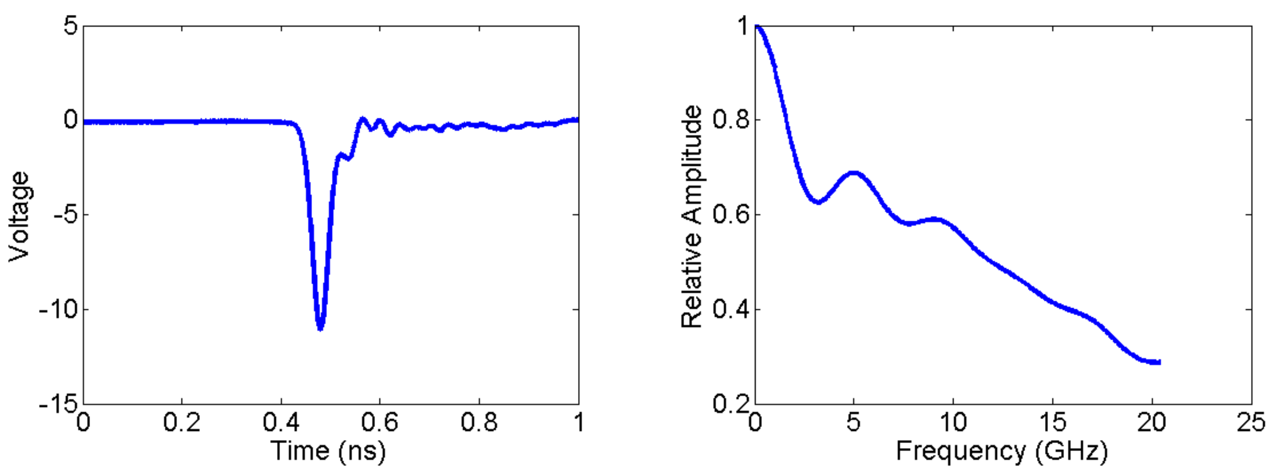

(a)

(b)

Figure 3.11: (a) UWB pulse generated by the pulse generating network,(b) Frequency spectrum of the pulse

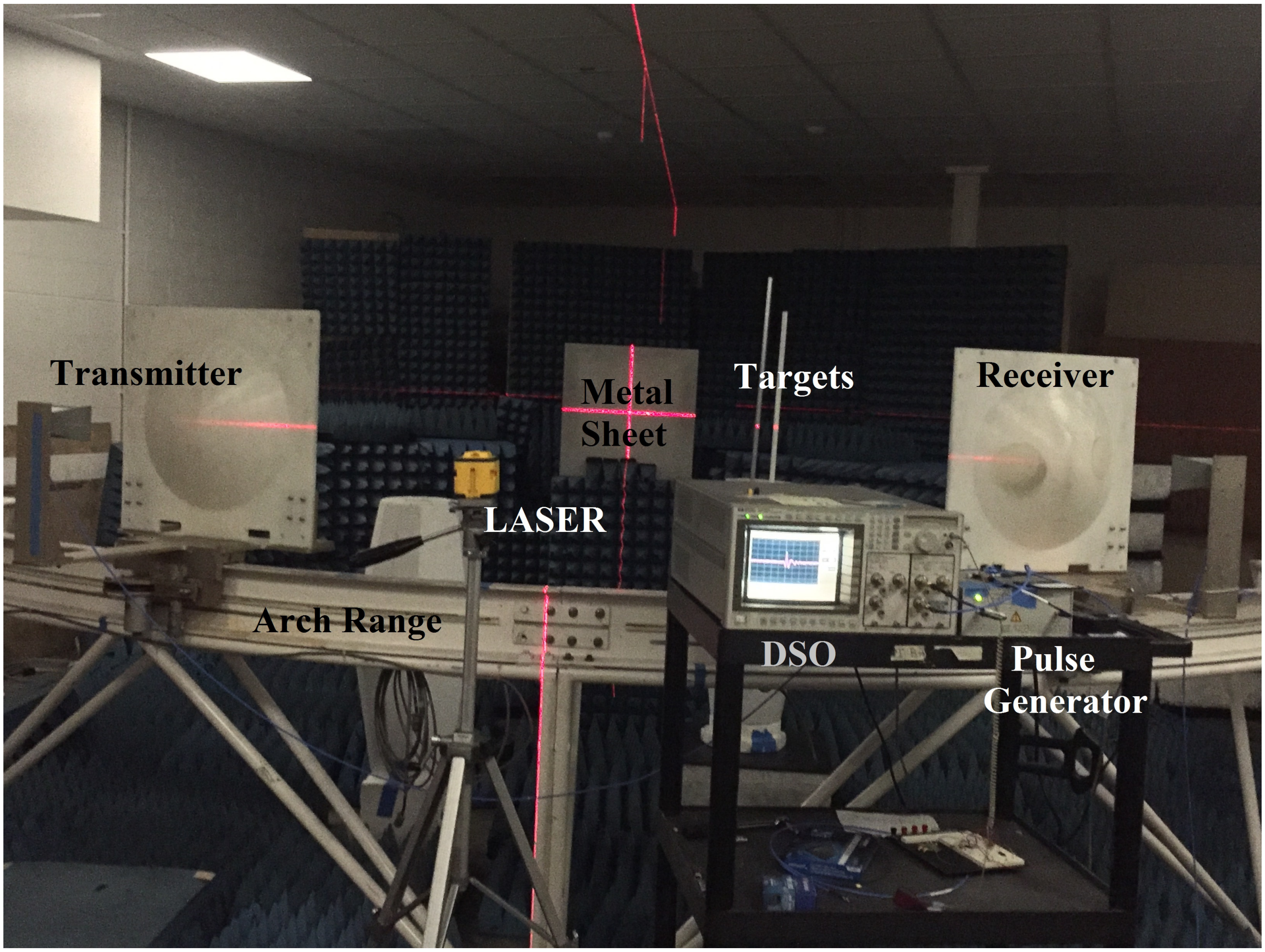

Figure 3.12: Experimental setup (laser highlights the locations),

3.3.1 Experiment details

The experiment configuration and setup is shown in Figs. 3.10 and 3.12. A metal sheet of length and width 0.3 m was chosen as the reflection target for source detection. An acetron (T1) cylinder of relative dielectric constant $\varepsilon_r = 3.8$ and a metal (T2) cylinder were chosen for target localization. The size of these targets are provided in Table 3.1. They were placed at the center of the arch range, where the beam of the transmitter antenna is focused.

The transmitting and receiving antennas are American Electronic Laboratories H-1498 TEM horns each with a bandwidth of 2 to 18 GHz. The source horn antenna is kept stationary while moving the receiver antenna in order to emulate the receiver array system. A Hewlett Packard digital sampling oscilloscope (DSO) model HP54750A is used to display and measure the back-scattered fields. It has a time-domain-reflectometer/time-domain-transmission (TDR/TDT) plug-in module, model HP54753A, which provides 20 GHz and 10 GHz channels for the oscilloscope. This TDR/TDT device has an integrated step generator, which sends steps from channel 3 with a rise time of 45 ps and an amplitude of 200 mV. This unit triggers a step generator made by Picosecond Pulse Labs (PSPL), model number 4015B. A remote pulse head (PSPL 4015RPH) follows the pulse generator and creates another step. The step signal is sent into a PSPL 5208-DC pulse generating network where a pseudo-Gaussian pulse signal is generated. This pulse, shown in Fig. 3.11(a), is applied to the transmitter horn antenna. The Fourier transform of the generated pulse gives its ultra-wideband frequency spectrum, shown in Fig. 3.11(b), having a central frequency at 2 GHz, with a high bandwidth of 18 GHz [2]. The time-domain pulsed system can be replaced by an equivalent ultra-wide band frequency domain system to yield similar results. [48]. The free space wavelength (λ) corresponding to 10 GHz (center of frequency band) is 0.03 m. Clutter is eliminated by measuring the background signal with no target present and subsequently subtracting it from the target signal. We use the target data for 20 equally spaced antenna positions obtained from the parametric limits conducted in the previous section, with 2° increments spread over an angular coverage of 40°.

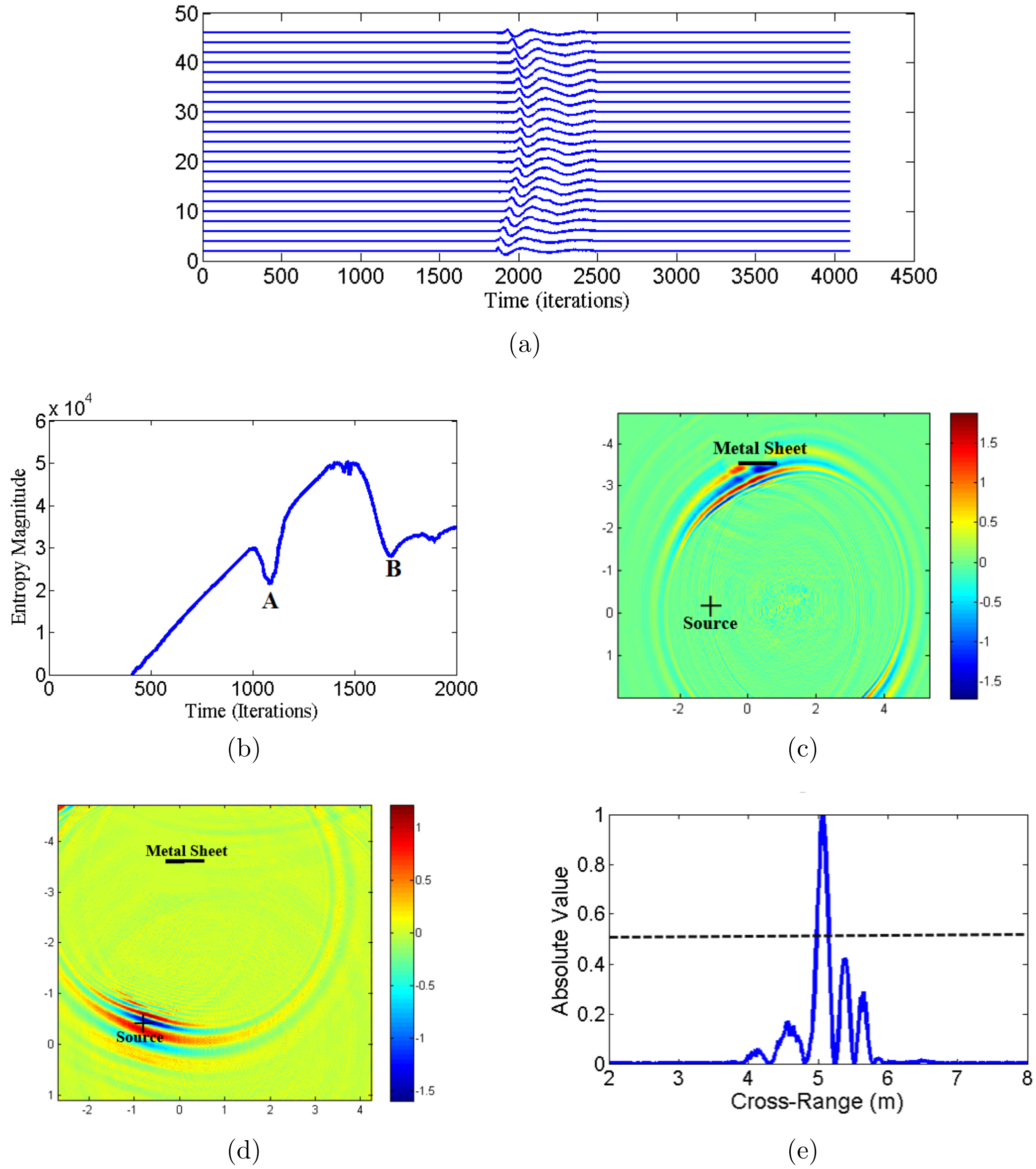

Figure 3.13: Source localization experiments (Case I): (a) Reflected fields measured by the receiver antenna array, (b) TR entropy plot, (c) Electric fields focused at metal plate at time instant A, (d) Electric fields focused at source at time instant B, (e) FWHM of cross-range signal estimates source's size

3.3.2 Experimental results

3.3.2.1 Case I

Far field experiments using the setup described above, were conducted to detect the source.

Reflected fields from the metal sheet were recorded by the receiver horn antenna array (as shown in Fig. 3.13 (a)) and back-propagated using the simulation model. The entropy localization technique was utilized to determine the exact focusing instants, as shown in Fig. 3.13(b). A sharp minimum is observed at a time instant A followed by a second local minimum at B. The electric fields plotted at time A shows the focusing at the metal reflector, as displayed in Fig. 3.13(c), while at time instant B the electric fields are focused at the source location, as shown in Fig. 3.13(d). The row of the energy image corresponding to the peak value is named as the cross-range energy signal and shown in Fig. 3.13(e). The full width at half maximum (FWHM) of the signal (0.15 m) is almost equal to the length of the source horn antenna (0.125 m). Hence the signal can be utilized to determine the approximate spatial dimensions of the source.

For the sake of completeness, additional imaging results are obtained without reference subtraction. The scattered field has lot of perturbations due to background clutter. We observe that the entropy has a local minima when the wave converges. However, the minima is not small enough to determine the focusing instant. Thus the electric fields are focused inefficiently at the source location without reference or background subtraction as shown in Fig. 3.14.

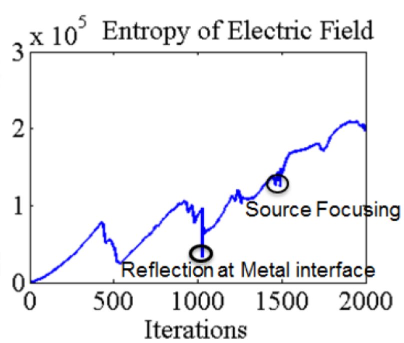

(a)

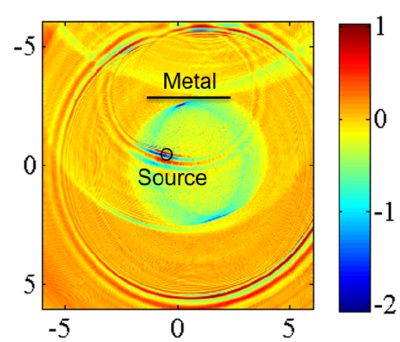

(b)

Figure 3.14: Source localization experiments without background subtraction: (a) TR entropy plot, (b)Electric fields inefficiently focused at source at time instant B

3.3.2.2 Cases II and III

Conforming to the principles of time reversal and the prior simulation results, the minimum target size that was experimentally detected is of radius 0.016 m ($\sim \lambda/2$). Fig. 3.15 shows TR experimental results for single target localization for small (40°) and large (80°) angular coverage. Better temporal focusing is obtained for Case III, since the time reversed wave entropy for has a sharper minimum (almost 3 times deeper than Case II), as seen in Fig. 3.15(a) and Fig. 3.15(b). Although the target is detectable for small angular coverage, there is a loss in both DR and CR resolutions, resulting in a stretched out focal spot, as seen in Figs. 3.15(c) and 3.15(e). A tighter focal spot is obtained for large angular coverage, leading to better resolution in both cross-range and down-range and smaller position error, as seen in Figs. 3.15(d) and 3.15(f).

3.3.2.3 Case IV

Case IV involves T1 and T2 of radius 0.02 m placed at the center of the arch-range, separated along the cross range by 0.05 m (CR resolution). The time-reversed electric field image corresponding to the spatio-temporal focusing instant shows the localized fields very close to both the target locations, as seen in Fig. 3.16 (a). The integrated energy image of the region also shows two distinct peaks around the two target locations, as seen in Fig. 3.16(b). The cross range signal distinctly shows the location of the two targets, as seen in Fig. 3.16(c). The FWHM of the signal at the two target locations (0.015 m) correlates with the radius of the actual targets.

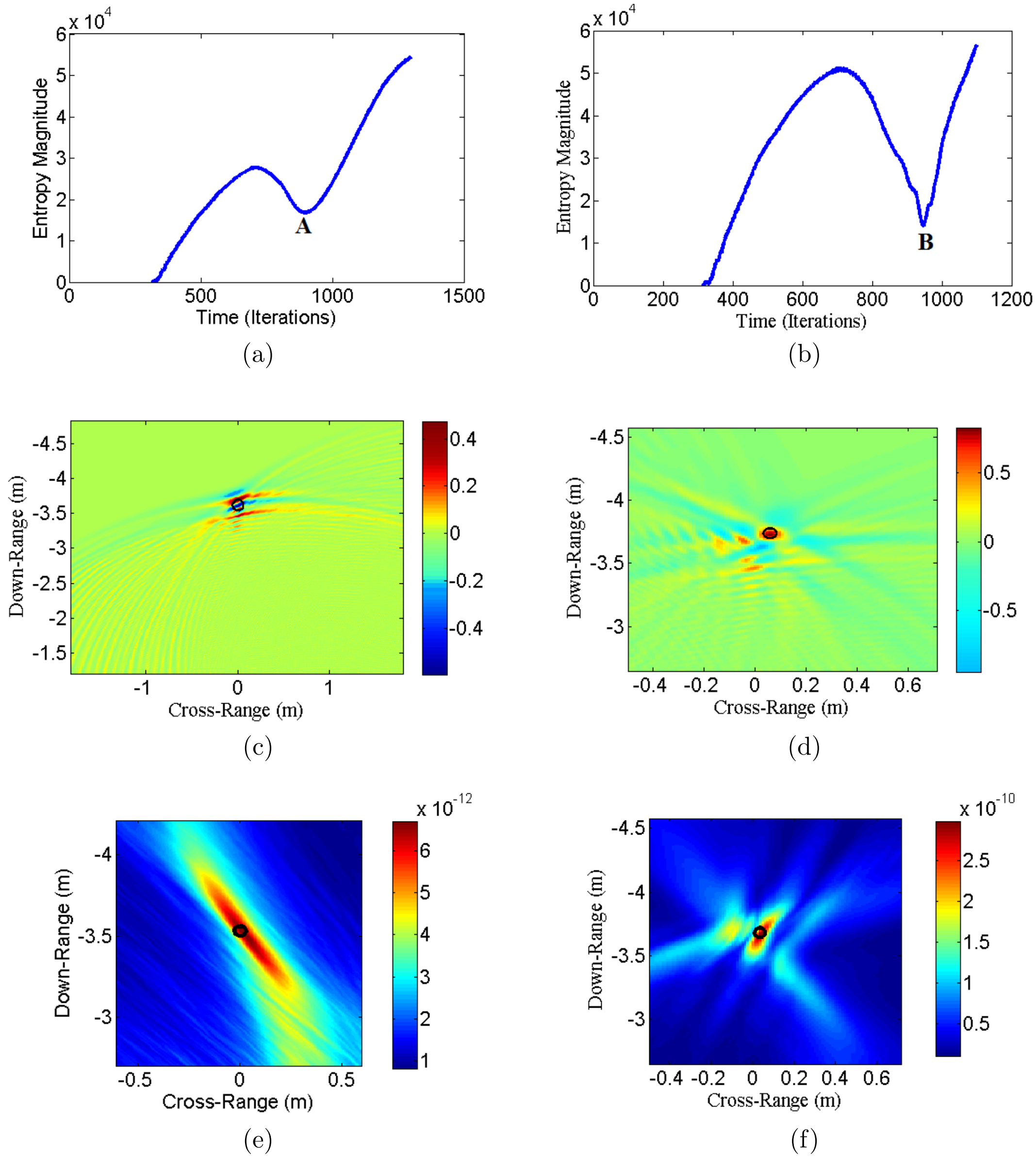

Figure 3.15: Target localization for angular coverage of 40° and 80° (Cases II and III): (a),(c) and (e)- Stretched focal spot for Case II (a) Entropy, (c) Fields focused at target, (e) Energy image, (b),(d) and (f)- Tight focal spot for Case III (b) Entropy, (d) Fields focused at target, (f) Energy image,

3.3.2.4 Cases V and VI

The next experiments involve T1 and T2 placed at the center of the arch-range, separated along the down-range by 0.08 m (DR resolution) and 0.16 m (twice the DR resolution). The time reversed electric field images corresponding to the spatio-temporal focusing instants are

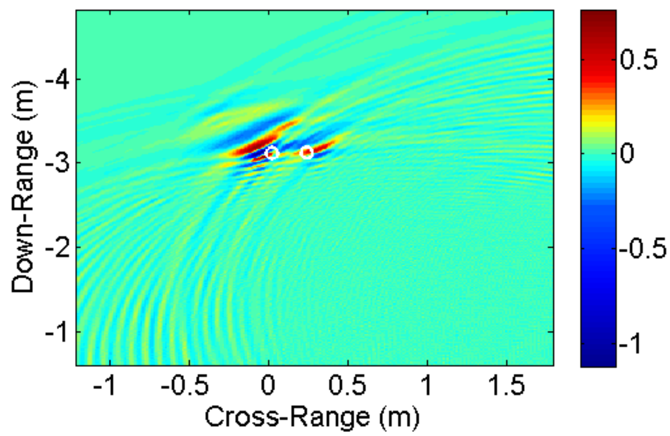

(a)

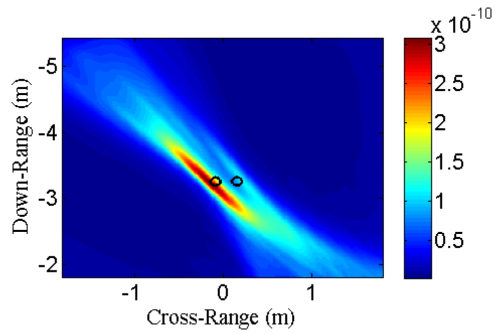

(b) Energy Image

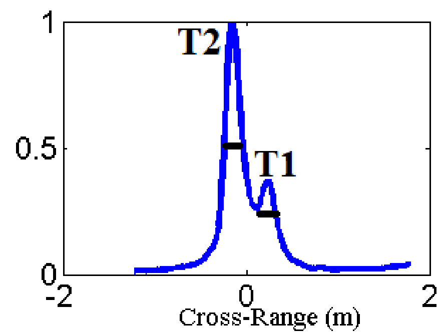

(c) caption

Figure 3.16: (Case IV): (a) Electric fields focused at entropy minima, (b) Integrated energy image and (c) Cross-range energy signal distinctly shows two peaks corresponding to the targets

shown in Figs. 3.17(a) and 3.17(b). The integrated energy images of the region are shown in Figs. 3.17(c), 3.17(d), while the down-range energy signals (column of the energy image corresponding to the peak value) are shown in Figs. 3.17(e) and 3.17(f). Case V shows an extended focal spot, making it difficult to localize the two targets, as seen in Figs. 3.17(c) and 3.17(e). However, case VI shows that both entropy and energy techniques are able to successfully detect and localize the target locations, as seen in Figs. 3.17(b) and 3.17(d). The down range signal distinctly shows the location of the two targets and the FWHM of the signal at the two target locations (0.018 m) correlates with the radius of the actual targets.

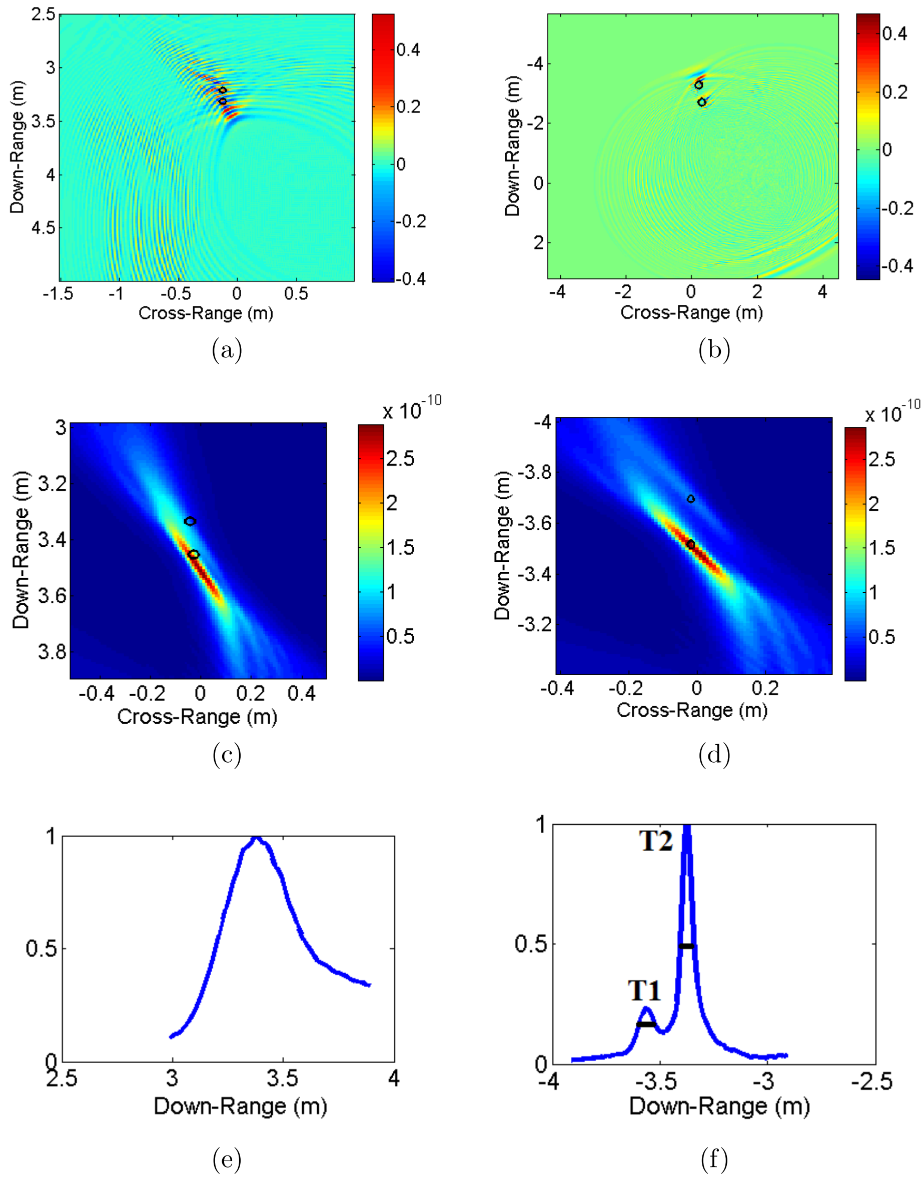

Figure 3.17: Localization of targets separated along DR: (a),(c) and (e)- Case V : (a) fields focused at targets, (c) energy image, (e) DR signal shows extended energy image for separation of 0.08 m; (b),(d),(f) Case VI: (b) fields focused at target, (d) energy image, (f) DR signal shows distinct peaks for separation of 0.16 m

3.3.2.5 Case VII

The final experiment involves detection in presence of all the targets mentioned in the above experiments. The experimental schematic is similar to the setup shown in Fig. **??**. The metal sheet is placed at the arch range center, along with the metal and dielectric targets on the receiver side, separated along the cross range by 0.3 m. The spatio-temporal focusing instant of the time-reversed fields shown in Fig. 3.18(a) shows three minima observed at time instants A, B and C. The electric field images corresponding to the time instants A,B and C show the electric fields localized at the 2 targets, metal sheet and the source antenna, as seen in Figs. 3.18(b), 3.18(c) and 3.18(d) respectively. The results demonstrate detection capabilities (both source and targets) using TR for complicated experiments.

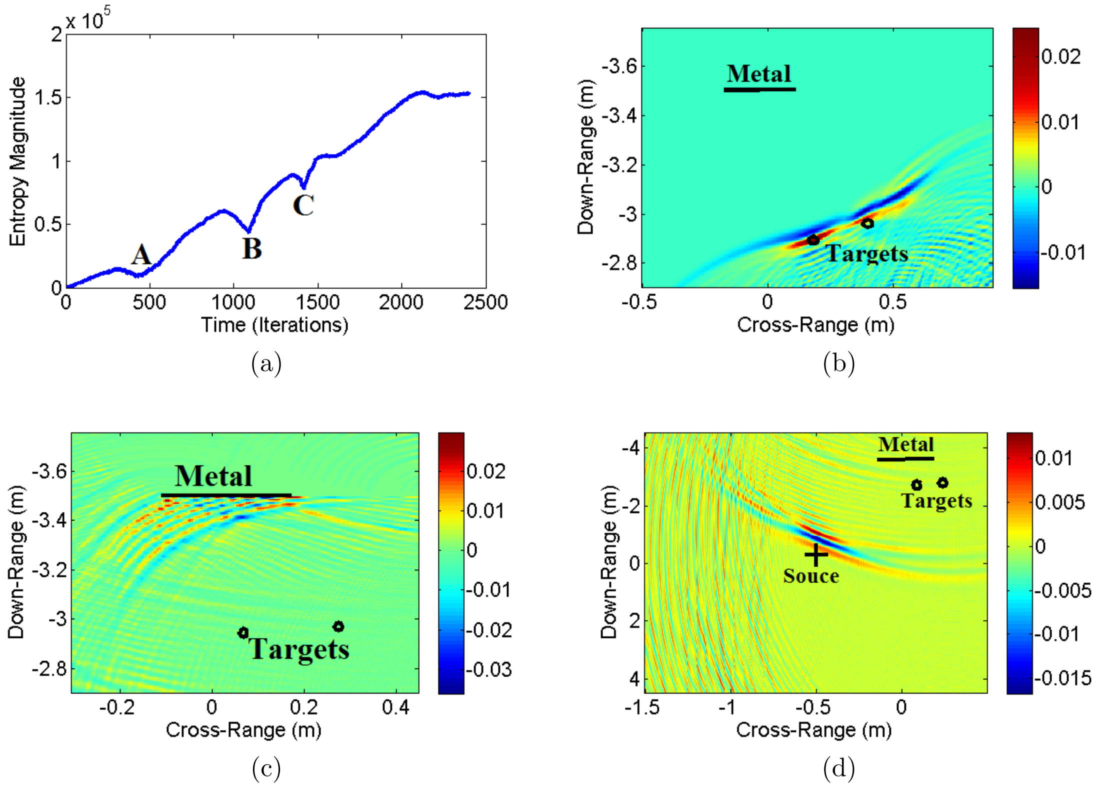

Figure 3.18: Localization of source and all targets (Case VII): (a) TR Entropy plot, (b) Focused electric fields around both targets at instant A, (c) Focused electric fields at metal sheet at instant B, (d) Focused electric fields near source at instant C

3.3.3 Discussion of results

In accordance with the experimental results obtained in this paper, we observe that precise detection of targets depends on several factors. It should be noted that it is impossible to focus back ideally at the source, since the time reversal array is finite and limited. Moreover, source focusing in reflection mode by time reversal is non-trivial due to several factors. Since the source and receiver array in reflection mode are quite close to each other, a lot of energy is focused near the receiver array, compared to the time reversed energy peak focused at the source. Moreover, the receiver array, which actually consists of horn antenna is assumed to be point sources in the 2-D simulation model. A consequence of this assumption is that the integrated energy image localization technique is incapable of providing effective results, since the forward and backward media are not exactly reversible. However, the entropy based localization technique is able to determine both the location and focusing time instants quite accurately. The computational error along with the above factors involved in modeling the problem are responsible for the error in position of the actual source location.

Targets can be efficiently detected by time reversal using both localization techniques, provided we have sufficient angular coverage, receiver array elements and the targets well-separated. Also, targets located along the down-range were harder to locate than along the cross-range in our experiments, since the CR resolution (0.05 m) was better than the DR resolution (0.08 m) and the receiver array was also located mostly along the cross-range. Detection also depends on the target properties such as its size and reflection coefficient. Although the TR algorithm has the ability to detect multiple targets, focal resolutions limit the ability of this technique in the presence of two closely spaced targets. From a mathematical point of view, the time reversed signals for two well resolved targets correspond to the linear combination of two non-null orthogonal eigenvectors. However, when the targets are not well separated, the eigenvectors are no longer orthogonal due to the cross-coupling between the targets. Thus, the image fields interfere with each other resulting in poor image quality. Additionally, since the amplitude of the back-propagated fields is proportional to the

Table 3.2: Detection error and imaging quality

Case	Error				IQ
	ρ_a(m,m)	ρ_e(m,m)	Distance (m)	ξ (%)	(dB)
I					
Simulation	(-1.2,0)	(1.15,-0.06)	0.078	2.2	25
Experiment	(-0.7,-0.4)	(-0.6,-0.5)	0.14	4	20
II					
Simulation	(0,-2.1)	(0.01,-1.92)	0.081	2.3	38
Experiment	(0,-3.5)	(-0.05,-3.53)	0.058	3.7	25
III	(0,-3.5)	(-0.05,-3.53)	0.021	0.57	33
IV					
Target 1	(-0.025,-3.3)	(-0.02,-3.2)	0.10	2.9	
Target 2	(0.025,-3.3)	(0.10,-3.2)	0.125	3.6	12
V	NDT				-
VI					
Target 1	(0.05,-3.30)	(0.10,-3.45)	0.16	4.57	
Target 2	(0.05,-3.35)	(0.10,-3.26)	0.103	2.94	20
VII					
Target 1	(0.05,-3.30)	(0.10,-3.24)	0.08	2.29	
Target 2	(0.05,-3.35)	(0.10,-3.23)	0.16	4.57	16
Source	(0.00,-3.50)	(-0.05,-3.53)	0.14	4.04	21

target reflection coefficients, it is difficult to detect weak dielectric targets adjacent to metal targets [21, 49]. The electric field reaches a higher value at the location of the metal target (T2) whose scattering cross section is larger than the dielectric target. Thus T2 produces much stronger energy peaks in comparison to T1, as shown in the energy images.

The detection error (ξ) and imaging quality (IQ), as has been defined before are calculated for all the different cases and summarized in Table 3.2. As interpreted from the table, the highest (ξ) of 5%, and lowest IQ of 12 dB is achieved in Case IV, since the experiment uses the theoretical cross range resolution limit. The lowest (ξ) of 0.57%, and highest IQ of 33 dB as seen in Case III, since larger coverage enables better focusing resolution and accuracy.

3.4 Conclusion

Previously, the TR technique had been successfully applied for source focusing in transmission mode. However many practical applications involve detection with both the transmitter and receiver on the same side, with limited angular coverage. This paper presents feasibility of using TR for far field reflection mode measurements. It first presents a simulation model for target detection, along with parametric performance of the overall system. The simulations are validated with experimental results using a pulsed time domain microwave system. The TR performance has been quantitatively evaluated using the detection error and imaging quality. Detection of source, single and closely spaced multiple targets at long ranges (~ 3.5 m), with a highest detection error of 5% and lowest imaging quality of 16 dB have been achieved. Experiments are also performed to estimate the time reversed down-range and cross-range resolutions. A limited angular coverage of 40° and 20 sensor elements are used in the experiments. Complicated time-reversal selective focusing methods such as the DORT can be employed to focus on individual targets selectively, in case of multiple targets. However, they are either time-consuming or expensive, since they require design of automated RF switching circuits for recording multiple projections of the antenna array system.

While the results shown in this paper appear promising, several future topics could be explored. These include development of an efficient ultra-wideband MUSIC algorithm for detection of closely spaced targets as well as conducting time reversal experiments for through wall imaging and target detection in the presence of cluttered media to investigate the super resolution capabilities of the algorithm. A shortcoming of the time reversal technique is that targets need to be well separated in order to be detected, since time reversal follows diffraction limits. Moreover, iterative time reversal results in the fields converging to the strongest target. Thus, it might be complicated and difficult to resolve two targets that are close to each other. However, techniques such as MUSIC that utilize the rank-deficient nature of time reversal data and use subspace rather than signal space of time reversal data might be helpful in detection of closely spaced targets. As mentioned in the final section, the MUSIC algorithm is currently being investigated for application in detection of closely spaced targets. Some potential applications of this technique are complicated long range radar imaging and rapid non destructive inspection of large composite structures.

Chapter 4

Design of a microwave time reversal mirror for imaging applications

4.1 Introduction

Numerous microstrip antennas have been proposed to cover the UWB frequency band between 3.1 and 10.6 GHz released by the Federal Communications Commission for short-range wireless applications. Designing UWB antennas for imaging applications is challenging since unlike narrow-band antennas, UWB antennas must exhibit near-uniform radiation characteristics such as high gain, return losses and low cross-polarization, over large bandwidths. Moreover, the design of UWB time reversal antennas (TRAs) is particularly challenging, since the antennas need to comply with the unique properties of time reversal. The TRA needs to illuminate most of the the region of interest effectively and detect potential anomalies in presence of other significant scatterers. A lot of different UWB antennas proposed recently do not satisfy these requirements. For example, UWB antenna presented in [50], though having small size, lacks both reasonable gain and return losses. Additionally, previous research on microstrip TRA designs have proposed using the same transmitting and receiving antenna [51], which is not desirable for time reversal.

This research proposes a novel design of a time reversal mirror (TRM) for imaging applications. The final objective of using them for breast tissue imaging is kept in mind while designing them, since the antennas need to satisfy distinct requirements for breast tissue imaging [2]. Separate UWB transmitting and receiving antennas operating between 3 to 10 GHz are designed, keeping in consideration the unique features of TR imaging. Comparison between simulation and measurement results show good correlation. The proposed TRM has been validated by performing an imaging experiment using a pulsed time domain laboratory setup, coupled with a back-propagation 2D FDTD code. Experimental results validate the system's efficiency and lay the foundation for potential imaging applications.

4.2 Design of an antenna system for time reversal

The design of the TRA is non-trivial due to several reasons. The contributing factors are as follows

- Bandwidth. TR is similar to phase conjugation in optics. The range resolution is governed by the pulse width, with smaller pulse width leading to better detection. A short time-domain pulse has a half-amplitude bandwidth given by the following relation [52]:

  $$\Omega = \frac{1}{\pi\tau} 4\ln(2) \tag{4.1}$$

  where Ω, τ are the bandwidth and pulse width, respectively. Thus, both the transmitting and receiving antennas should be designed to operate over a wide bandwidth.

- Radiation Pattern. The transmitting antenna needs to have a beam narrow enough to illuminate the region of interest efficiently with a large gain. However, the beam cannot be too focused, since TR theory is based on waves diverging outwards from a point source. In contrast, TR theory assumes the receiver array to be point receivers [20]. Thus the receiving antennas should behave in radiation mode as point sources having omnidirectional radiation patterns. Since the radiation pattern for the transmitting antenna needs to be different from that of the receiving antenna, the same antenna cannot be used both as transmitter and receiver.

- Polarization. The confinement of the electric or magnetic field along the plane of propagation leads to linear polarization. However, antennas may have field components orthogonal to the direction of propagation, leading to cross-polarization. Cross-polarized electric field components from the transmitting antenna are lost when using a 2D image reconstruction algorithm, thus degrading the overall imaging quality of the 2-D algorithm [53]. In order to reduce the undesired field components, the cross polarization of the antenna should be maintained as low as possible.

Simulation studies for antenna design were performed using the commercial high frequency electromagnetic field simulation software Ansys HFSS. The antennas were fabricated using conventional photolithography. Reflection coefficients were measured using an Agilent N5227A network analyser and radiation patterns were measured using a SATIMO Starlab near-field measurement system.

4.3 Transmitting antenna

Based on the crucial factors of the TRA discussed above, a modified slot-edged antipodal Vivaldi (SE APV) antenna is chosen as the transmitting antenna. Introduced by Gibson in 1979 [54], the Vivaldi antenna serves as a potential candidate for wide band applications due to its broad impedance bandwidth and ease of planar structure integration. In conventional vivaldis, the transition from microstrip to slotline restricts extension of impedance bandwidth and generates high cross-polarization due to assymetric feeding. With the Vivaldi antenna, the bandwidth limitation due to the microstrip to slot-line transition can be removed by choosing a proper feed. One solution used in this manuscript is to use a microstrip to stripline or a two-sided slotline transition [55], as recently used by many researchers [56, 57]. Thus, no external balun is required to operate with unbalanced transmission lines that are typically used as microwave feed networks [58].

4.3.1 Design parameters

An exploded top-view design of the proposed antenna, along with its dimensions is shown in Fig. 4.1(a). The fabricated antenna is shown in Fig. 4.1(b). In this design, the tapered slots are modeled as elliptical transitions, with the curve defined as

$$y = b\sqrt{1 - \frac{x^2}{a^2}} \tag{4.2}$$

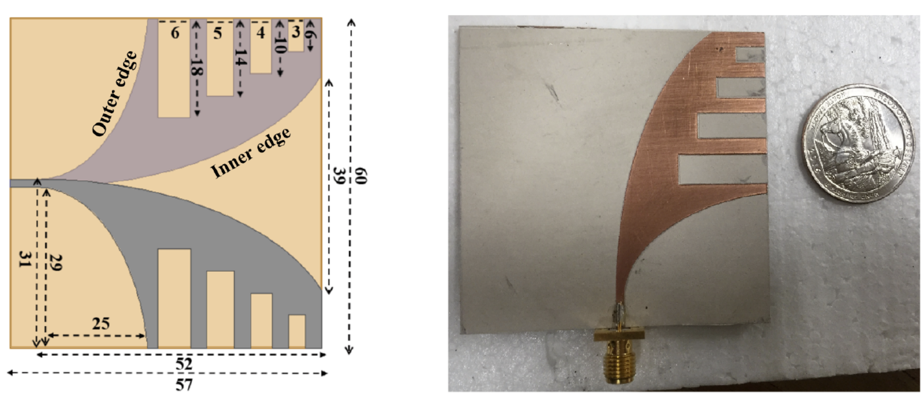

(a) (b)

Figure 4.1: Design of the proposed transmitting antenna. (a) Vivaldi design (mm). (b) Fabricated antenna (US quarter dollar shown for comparison).

By choosing a substrate (Rogers RT Duroid 6010) with a high dielectric constant of $\varepsilon_r =$ 10:2, the antenna size is miniaturized to 6 cm $\times$ 5.7 cm. Although an increased antenna size reduces the lower end frequency of operation, the antenna needs to be small enough to be integrated into imaging applications such as breast tumor detection.

The key parameters that determine the performance of the antenna include: a) elliptical axes of the inner and outer edges, b) microstrip line dimensions, and c) slot dimensions. The inner edge is primarily responsible for the current flow, since most of the current is confined along the inner edge during the operation of the antenna. Since the opening rate of the edge decides the current concentration, it is a critical parameter for antenna design. The key factor in determining the lower end frequency is the opening width. Since the vivaldi antenna operates as a resonant antenna at the lower frequency end (f_m), the initial antenna opening width (W_{in}) can be estimated by the following expression [54, 59]:

$$W_{in} = \frac{c}{2 f_m \sqrt{\varepsilon_e}}, \tag{4.3}$$

where fm is the minimum frequency and ε_e is the effective dielectric constant of the antenna. The relationship between radiation properties and the outer edge has been extensively studied in [60]. Although the dominant current flows along the inner edge, a sharp increase in the outer edge sets up current along the outer edge. This effect produces a narrower mainbeam and higher sidelobes. The major axis of the inner and outer edges and the microstrip line dimensions were optimized using HFSS with respect to its UWB performance, with the constraint of keeping the antenna size as small as possible. From (4.3) and optimization based on HFSS simulations, W_{in} is finally calculated to be around 39 mm.

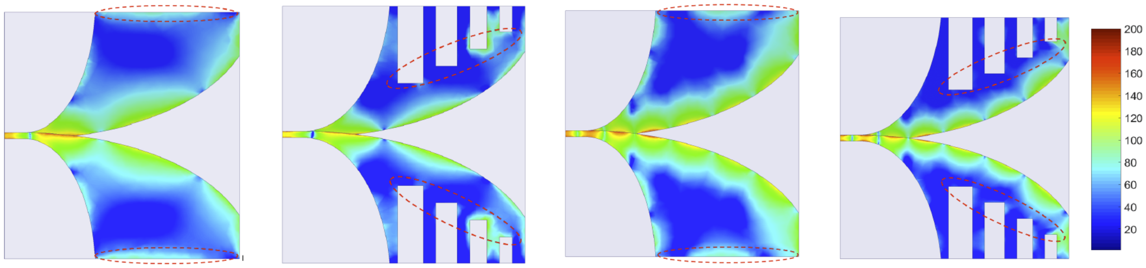

(a) (b) (c) (d)

Figure 4.2: Current density for APV vivaldi (Units in A/m): (a) 4 GHz, (c) 8 GHz, SE APV antenna: (b) 4 GHz, (d) 8 GHz.

4.3.1.1 SE APV antenna

The surface current distribution for a conventional APV antenna shows strong edge currents, marked in the dashed-line region of Figs. 4.2(a), (c). The currents radiate vertically, leading to undesired side and back lobes. In order to reduce these surface currents, four slots are etched at the ends of the twin lines of the antenna to form the SE APV antenna. As seen from Figs. 4.2(b), (d), the modification is capable of eliminating the unwanted currents at the edges. This leads to an enhanced end fire direction radiation and thus weakens the back-direction radiation.

4.3.2 Antenna characteristics in the UWB range

The comparison of simulated and measured reflection coefficients, given in Fig. 4.3(a), shows good correlation. The slight difference in the measured and simulation results possibly arises due to soldering inaccuracies, introduction of the 50 SMA connector for feeding the antenna or fabrication errors. It is noted that $|S_{11}| \leq 10$dB over the entire band. Additionally the impact of a small metallic cylindrical target (radius and height 5mm) in the near-field (1 cm away) of the antenna is observed from Fig. 4.3(a). The $|S_{11}|$ results show sensitivity due to the presence of the target throughout the frequency band of 3 to 10 GHz.

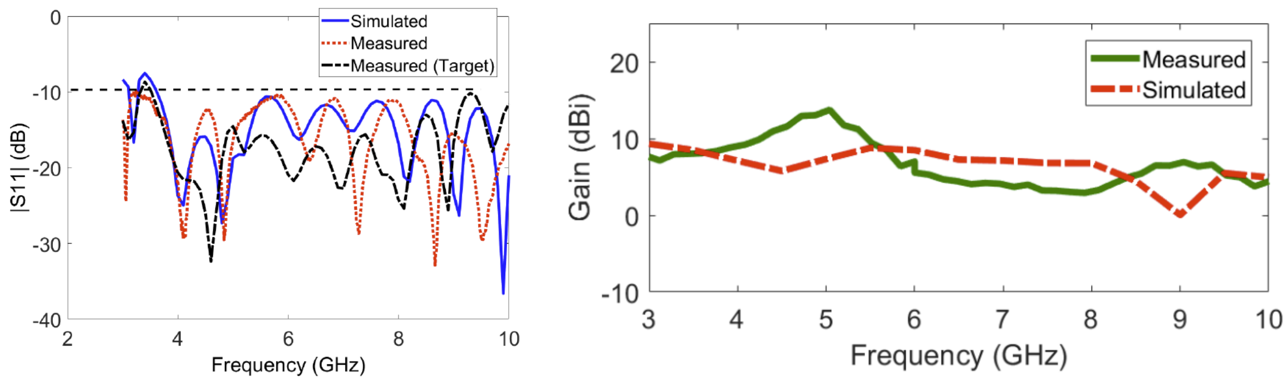

(a) (b)

Figure 4.3: Transmitting antenna performance. (a) Reflection coefficients comparison. (b) Maximum realized gain comparison.

The radiation properties of an antenna vary, depending on the near field and far field ranges of the antenna. The far field region is commonly expressed to exist at distances greater than $2D^2/\lambda$ [59], where D is the maximum dimension of the antenna and λ is the wavelength. For an UWB antenna, the far field distance varies depending on the frequency. For the proposed antenna, the far field ranges vary approximately between 0.1m to 0.5 m. For efficient imaging applications, the sample to be imaged needs to be in close proximity of the antenna. The antenna may operate in far field or near field ranges depending on the distance between the antenna and the imaging region. Hence the radiation properties of the antenna need to be studied for both ranges.

4.3.2.1 Far field radiation patterns

Some of the crucial elements such as gain, radiation pattern and polarization of the antenna can be determined from the far field radiation characteristics of the antenna. As shown in Fig. 4.3(b), the comparison between the simulated and measured boresight gain of the antenna shows slight discrepancies, however the measured realized gain is greater than 5

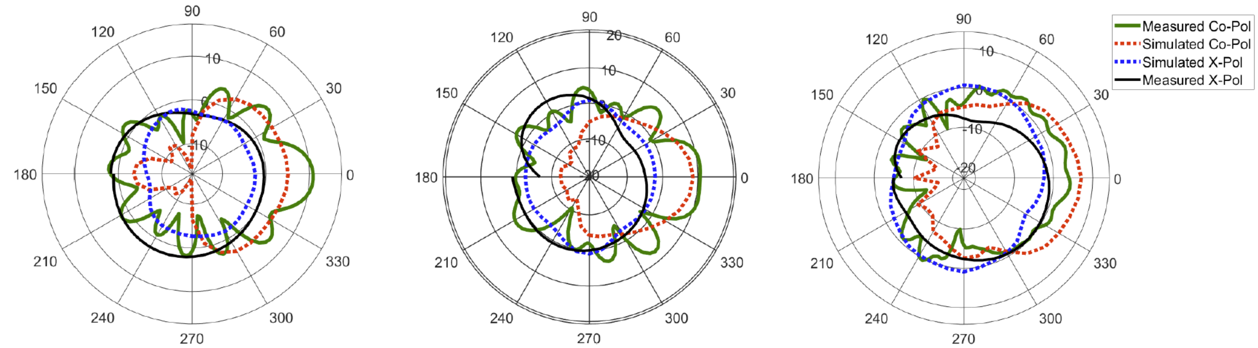

(a) (b) (c)

Figure 4.4: Transmitting antenna far field realized gain radiation pattern. (a) E Plane: 4 GHz. (b) E Plane: 6 GHz. (c) E Plane: 8 GHz

dBi in most of the frequency band. A maximum measured gain of 14 dBi is achieved at 5 GHz. The simulated and measured radiation patterns at 4, 6 and 8 GHz (Figs. 4.4(a), (b), (c)) show good correlation. The antenna shows nice end-fire performance with the main lobe aligned along the direction of the tapered slots. All the operating frequencies maintain the same polarization plane and similar radiation patterns. The transmitting antenna has an uniformly narrow beam with a moderately large gain throughout the frequency range. However, the beam is not too focused, which is ideal from the time reversal point of view. As discussed before, the cross polarization of the transmitting antenna should be maintained as low as possible. It is noticed that the cross-polarized gain is much lower than the co-polarized gain throughout the frequency range, with a minimum difference at boresight of 8 dBi. The presence of strong horizontal components of the surface current radiating electric fields along the sides lead to relatively high cross-polarization in the E Plane.

Several variations of the vivaldi antenna were tried while finalizing the design of the antenna. Those designs are shown in Fig. 4.5. A comparison of the reflection coefficients and E plane radiation pattern for the different designs of the vivaldi antenna are shown in Figs. 4.6 (a, b). The reflection coefficients of both designs 3 and 4 are less with respect to

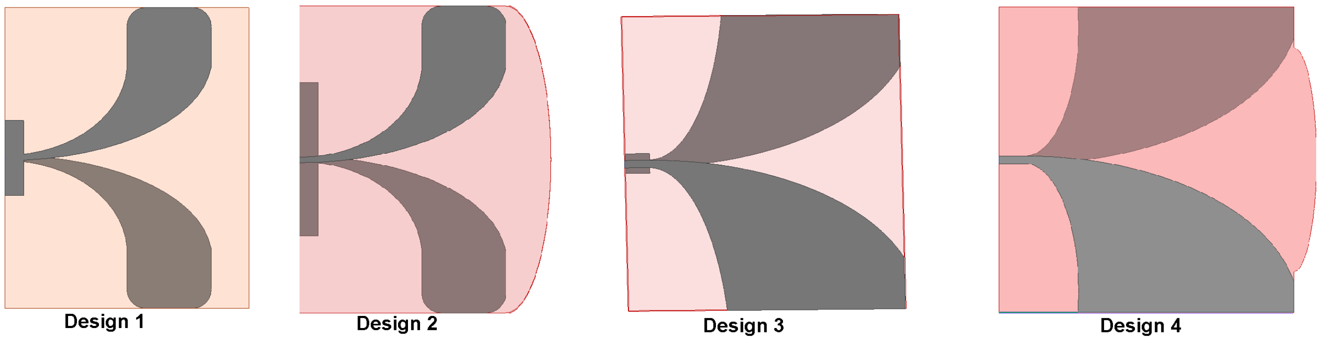

Figure 4.5: Other tried vivaldi antenna designs

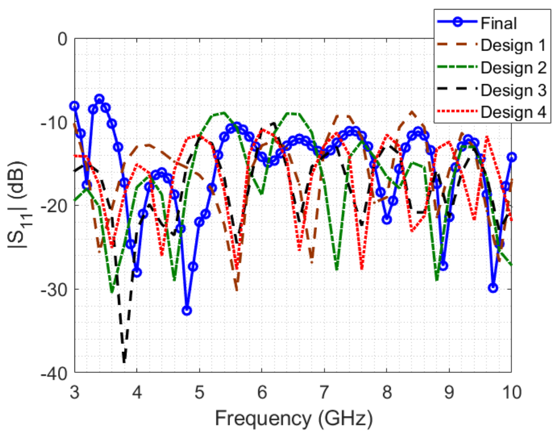

(a)

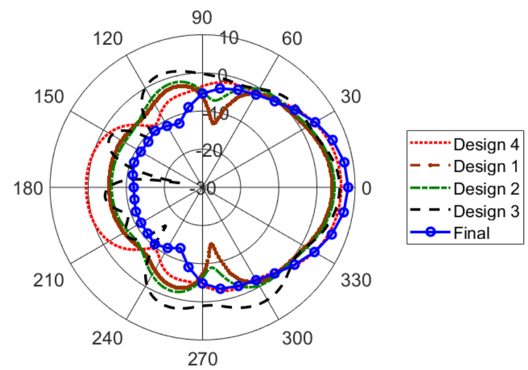

(b)

Figure 4.6: Performance of various designs: (a) Simulated reflection coefficients (b) Simulated E Plane radiation pattern at 6 GHz

the final design. However, the final design has less peaks and is relatively flat with respect to all the other designs, which is desirable from a flat ultra-wide band perspective. The final design has much higher gain, a stable beam width and much less side and back lobes than all the other designs. This is also true for other frequencies in the spectrum.

4.3.2.2 Near field radiation patterns

The near field radiation pattern for the transmitting antenna was computed using HFSS at 2 cm radial distance from the apex of the antenna. Fig. 4.7(a) present the magnitude of the simulated radiated electric fields in the E-plane at 4 GHz, 6 GHz and 8 GHz. As seen from

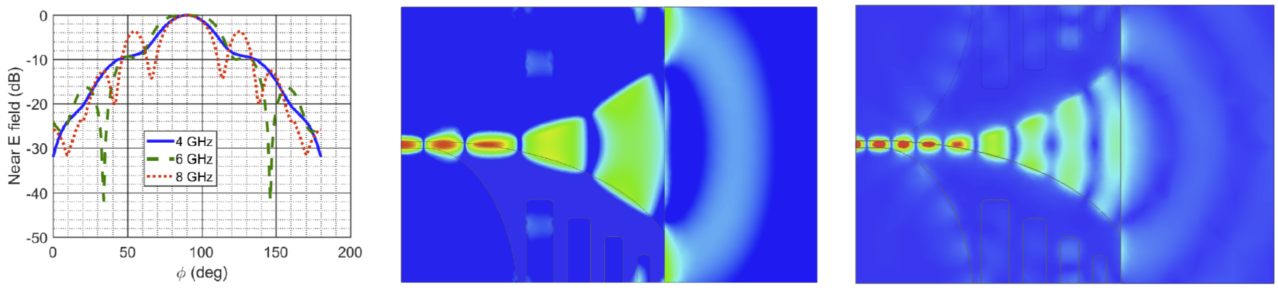

(a) (b) (c)

Figure 4.7: Transmitting antenna near E-field pattern. (a) E plane near field radiation pattern. (b) Electric field: 6 GHz. (c) Electric field: 10 GHz.

Fig. 4.7(a), the E-plane radiation pattern is uniform with the intensities almost equal at all frequencies. The beam is relatively uniform with a half-power beamwidth (HPBW) of 41.2°, 32.7°and 30°at 4 GHz, 6 GHz, and 8 GHz respectively. However, the presence of relatively high intensity side lobes (-4.8 dB for 4 GHz) might degrade the imaging quality. Hence, special attention needs to be taken so that the size of the sample to be imaged is less than or equal to the HPBW of the antenna. Similar radiation intensities noted at all frequencies at $\theta = 90°$, $\phi = 90°$ensures that the peak realized gain is uniform at all frequencies in the near field range. The simulated E-field distributions, depicted in Figs. 4.7(b), (c) for 6 GHz and 10 GHz on xy-plane, show the fields spreading along the tapered slot region and radiating from the top edge of the antenna, thus displaying strong end fire radiation characteristics.

4.4 Receiving antenna

As mentioned before, TR theory assumes the receiver array to be point receivers, along with UWB performance. Thus, ideally the receiving antennas should have omnidirectional radiation patterns. Conventional monopole antennas have several advantages such as low cost, ease of fabrication and omnidirectional radiation pattern in the transverse plane, but does not

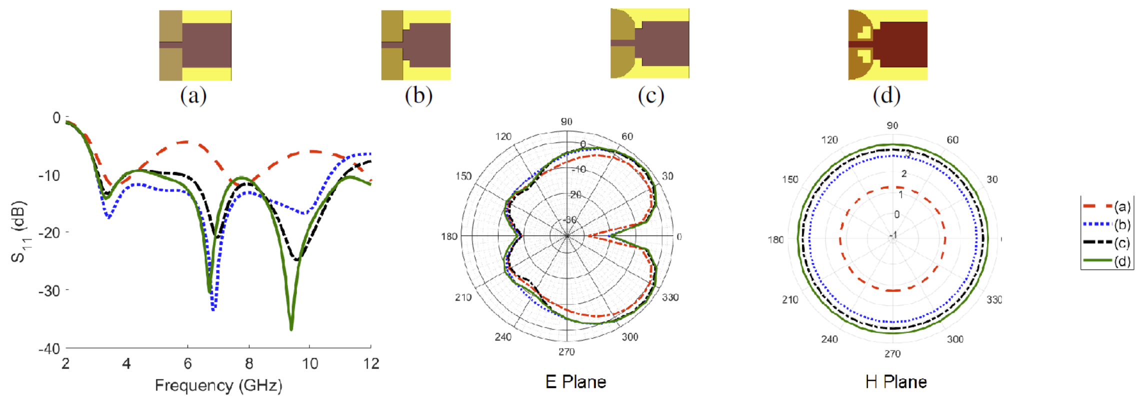

Figure 4.8: Monopole antenna design and its evolution.

yield large bandwidths [59]. Recently several approaches and techniques have been proposed to tailor the antenna towards wideband applications. In the regime of wideband antennas, planar monopole antennas [50] have garnered huge recognition due to their flat structure, small size and ease of integration. A planar monopole replaces the conventional wire-element based monopole design with a planar element. In this research, a reduced-ground slotted rectangular (RGSR) monopole is selected as the receiving antenna. The theoretical resonance frequency (f_t) for the fundamental mode of the antenna can be calculated according to (4.3).

The design starts off with an intial monopole antenna with a reduced ground plane and without any feed step. The reduced ground plane is responsible for the wide bandwidth of the antenna, due to absence of fringing fields between the radiating patch and the ground plane. The length of the ground plane is reduced to $\lambda/10$ at the lower frequency end. However, this antenna is matched only at the lower and higher frequency limits. A double feed step between the microstrip line and the radiating patch behaves as quarter wave transformers, thus improving the impedance bandwidth. The blending ground plane edges help in matching at the higher frequencies. The two L shaped slots (smoothed) in the ground plane further help in impedance matching and thus enhance the bandwidth of the antenna and help miniaturize it to an area of 3.5 cm by 3.2 cm. Fig. 4.8 shows the effects of the step by step evolution of the antenna, as mentioned above. A monopole-like radiation pattern with nulls appearing at the center for the E plane omnidirectional radiation in the H plane is observed, with the final evolved design (d), providing the maximum gain.

An exploded top-view design of the RGSR monopole antenna and its dimensions are shown in Fig. 4.9(a). FR4, with a dielectric constant of $\varepsilon_r = 4{:}4$, is selected as the substrate since it is inexpensive, thus reducing the cost of fabrication. The fabricated antenna is shown in Fig. 4.9(b). The comparison of the simulated and measured reflection coefficients given in Fig. 4.10(a) show that $|S_{11}| <$ -10 dB over the entire bandwidth. The simulated and measured E-plane radiation patterns at 4, 6 and 8 GHz exhibit a monopole-like radiation, as shown in Fig. 4.10(b, c, d). A maximum gain of 4.2 dB is achieved at 6 GHz.

An examination of the radiation efficiency of the two antennas shows near constant values across the specified band of approximately 80-85%, as seen in Fig. 4.11. A comparison of the performance (fractional bandwidth (BW), maximum size (ρ) and maximum gain (G)) of

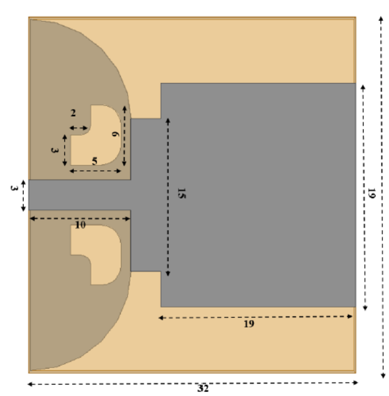

(a)

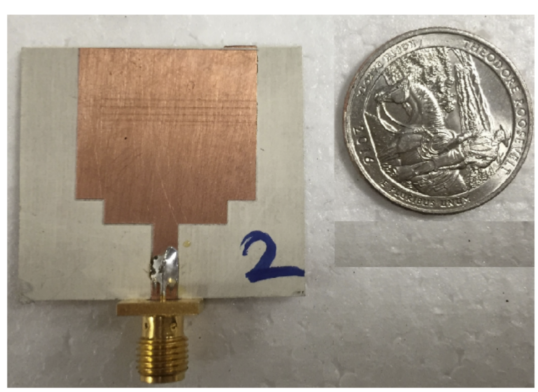

(b)

Figure 4.9: Receiving antenna. (a) Monopole design (mm). (b) Fabricated monopole antenna.

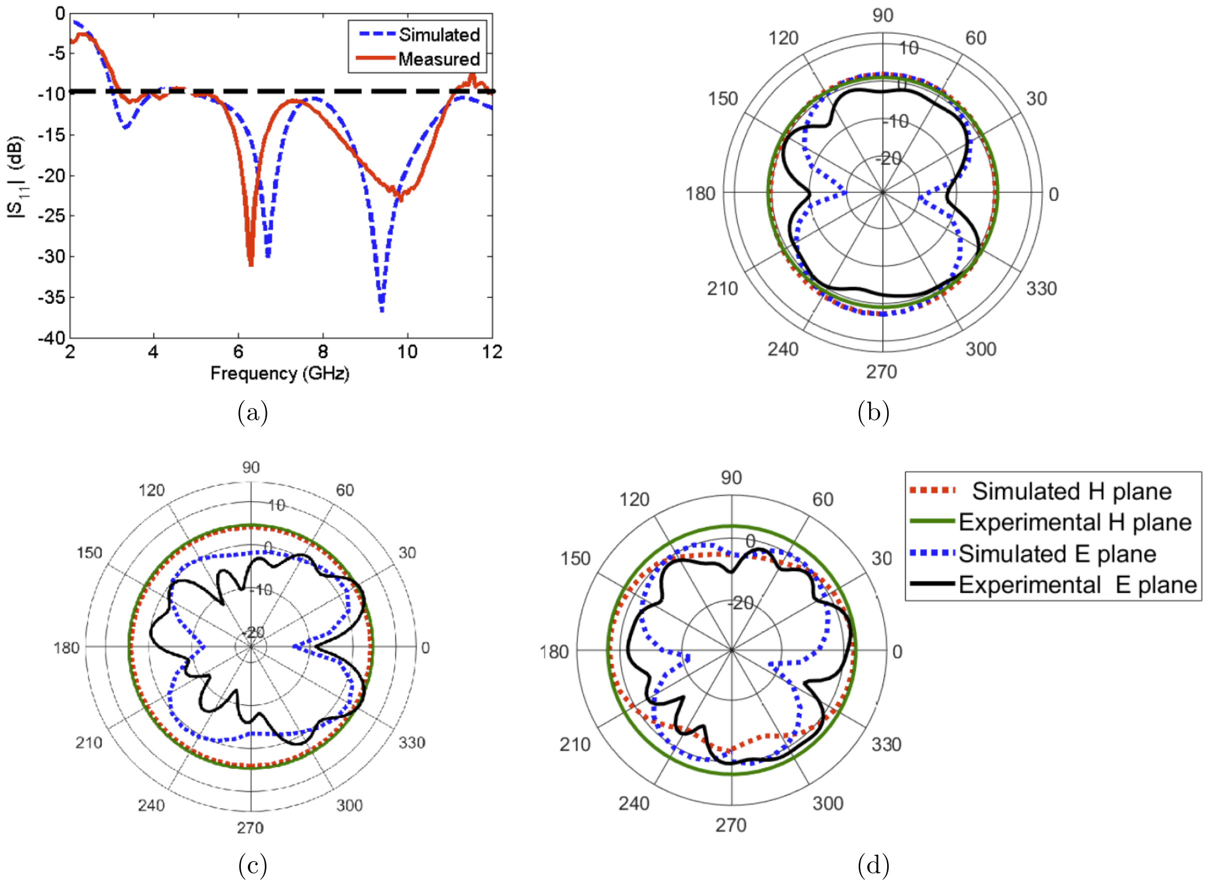

Figure 4.10: Proposed receiving antenna and its performance. (a) Reflection coefficients comparison. (b) Radiation pattern: 4 GHz. (c) Radiation pattern: 6 GHz. (d) Radiation pattern: 10 GHz.

the designed antennas with Vivaldi antennas and planar monopole antennas described in the literature is presented in the table of Fig. 4.11 (b). It is observed that the achieved gain of the SE-APV antenna is much more than the antennas presented in [56, 57], while maintaining a small size and a comparable BW. Similarly, the RGSR antenna achieves higher gain and BW than the UWB antennas proposed in [50, 61], while maintaining a comparable size. Besides the improved antenna performance, the concept of using different transmitter and receiver antennas, as well as choosing the specific antenna types in order to implement TR for imaging applications, is introduced in this research. Using different antennas is greatly desirable due to several factors as mentioned in Section 4.2.

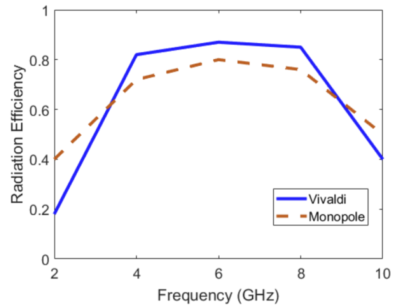

(a)

Antenna	BW	ρ (cm)	G (dB)
SE APV	3.5	6	14
[14]	5.6	6	10
[15]	3	8	11.5
RGSR	3.5	3.5	4.2
[7]	2.1	3.5	3.6
[19]	3.5	4.1	4

(b)

Figure 4.11: Antenna performance : (a) Radiation efficiency of the antennas, (b) Table 1. Comparison of different antennas

4.5 Breast tumor simulation

An imaging system was mimicked by conducting an HFSS simulation with the transmitting and receiving antenna and a breast phantom model with and without a tumor at the center. The breast tissues were considered to be a cylinder of radius 9 cm and r=7. The tumor was considered to be a sphere of radius 8 mm and ε_r=50. The S_{12} result shows attenuation due to the scattering and reflection in the presence of the tumor almost throughout the frequency band of 3-10 GHz (Fig. 4.12). The UWB frequency domain data can be converted into time domain pulses, which can be used for time reversal imaging of tumors. Thus, simulations indicate that the system is potentially capable of detecting tumors.

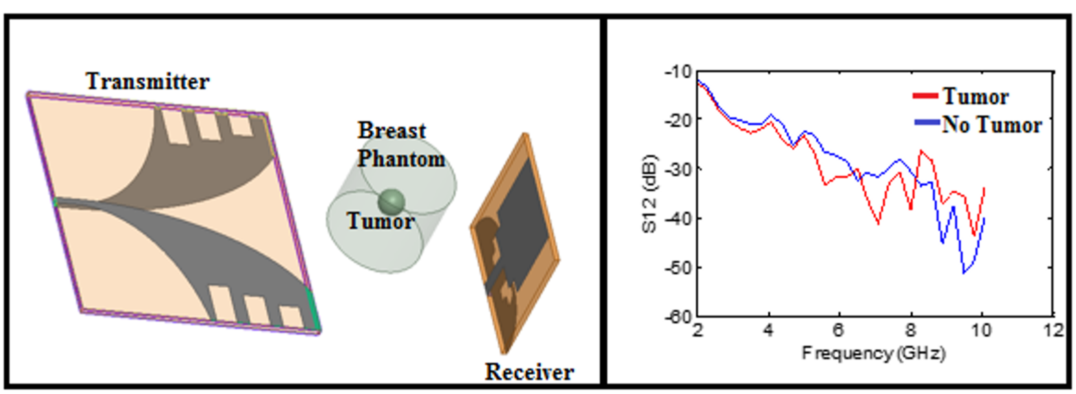

Figure 4.12: HFSS Simulation : S21 changes due to presence of tumor

4.6 Time domain characterization

The antenna system is to be integrated into a time-domain setup and used in a TR algorithm. The quality of the received pulse is directly related to the quality of the temporal focusing of TR. Hence, the antenna system needs to be characterized in the time domain. An HFSS simulation is performed with the transmitting and receiving antennas separated by a distance 150 mm, as shown in Fig. 4.13(a).

4.6.1 Group delay

A critical parameter for an UWB antenna is the group delay, which measures the time signal distortion introduced by the antenna. In an ideal, distortionless signal transmission, the antenna system has a constant group delay (linear phase response) over the whole bandwidth. Equal group delay for all frequencies in a signal ensures that the signal received by the antenna system has the same shape as the transmitted signal. Fig. 4.13(b) illustrates the group delay vs frequency for the configuration. Although the group delay is not constant throughout the frequency range, the plot shows an average group delay value of approximately 1.2 ns, with a few deviations between 8.5 to 9 GHz. Thus the antenna system can be reliably used for transmitting a short pulsed signal and receiving the scattered signal without serious distortion.

4.6.2 Time domain response

The transient response for the specific configuration shown in Fig. 4.13(a) is also studied. The received signal s(t) can be represented by a convolution of the impulse response, as

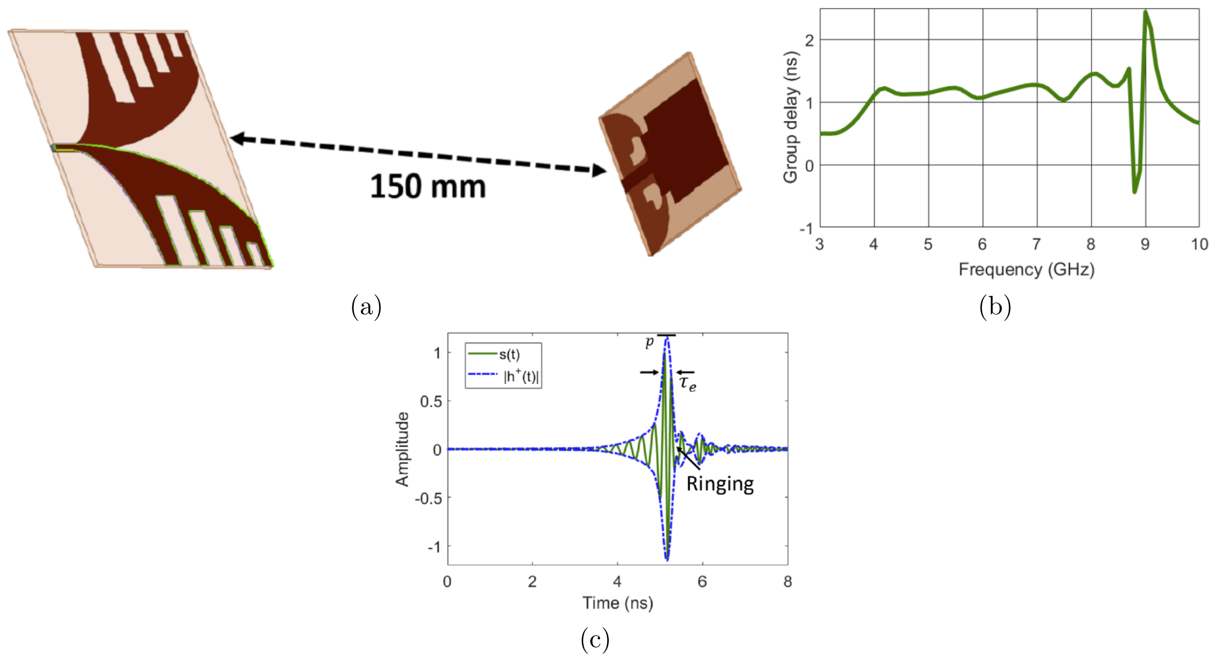

(a) (b) (c)

Figure 4.13: Time-domain analysis for the TRA. (a) TRA configuration. (b) Group delay of the TRA. (c) TRA time-domain transient response

given by the following expression [62]:

$$s(t) = u_{Tx}(t) * h_{Tx}(t;\theta;\phi) * h_{ch}(t) * h_{Rx}(t;\theta;\phi). \tag{4.4}$$

Here u_{Tx} is the transmitted signal and h_{Tx}, h_{ch} and h_{Rx} are the transmitting antenna, medium channel and receiving antenna impulse response functions. For the schematic shown in Fig. 4.13(a), the complex S_{21} measurements are transformed into the time domain to obtain the received time pulse. The received time signal is shown in Fig. 4.13(c). The antenna dispersion can be analyzed from its analytic impulse response, which is calculated by the Hilbert transform $\mathcal{H}$ of $s(t)$, given by $h^+(t)$ [62]. The envelope $|h^+(t)|$ localizes the energy distribution versus time and thus measures the dispersion of an antenna. The specific quantities investigated in this case are:

- Peak Value of envelope $p(\theta;\phi)$. This quantity is a measure of the maximum value of the strongest peak of the time domain response. A high peak value is desirable, since it ensures a stronger peak. As seen from Fig. 4.13(c), a value of $p(\theta;\phi)$ of 1.16 is achieved.

- Envelope width τ_e. The envelope width is a measure of the temporal broadening of the radiated impulse. Practically, τ_e should be small in order to obtain high resolution and data rate. The range resolution is governed by τ_e, with smaller pulse width leading to better resolution. The envelope width can be obtained from the full width at half maxima of the envelope. As seen from Fig. 4.13(c), a τ_e value of 160 ps is achieved.

- Ringing. Several factors such as multiple reflections in the antenna are responsible for oscillations of the received pulse after the main peak, as observed from Fig. 4.13(c). This phenomenon is known as ringing. Ideally, the duration of ringing (τ_r) should be less than a few τ_e. Specifically, a high value of τ_r is undesirable for temporal focusing of the time reversed electromagnetic fields. The time duration within which the envelope has fallen from $p(\theta;\phi)$ to a lower bound $\alpha.p(\theta;\phi)$ is measured as τ_r. As seen from Fig. 4.13(c), a value of τ_r for $\alpha = 0{:}1$ of 200 ps is achieved.

4.7 Experimental results

A passive TR experiment for imaging a metallic cylinder (radius 1.6 cm) was conducted using a pulsed time domain laboratory setup and a FDTD 2D code for back-propagation of the TR fields [63]. The experimental configuration and setup are shown in Figs. 4.14 and explained in details in [63]. A small arch range of radius 10 cm with a circular platform was used to position the antennas. The receiving monopole antenna was moved, while keeping

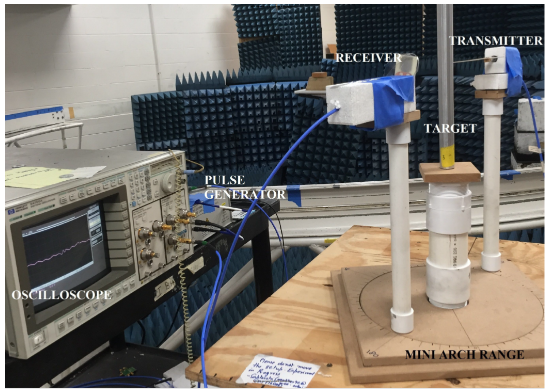

Figure 4.14: Time domain compact imaging setup

the transmitting Vivaldi antenna stationary, in order to emulate the receiver array system. The time domain system generates a pseudo-Gaussian pulse signal of bandwidth 10 GHz, which is fed as input to the vivaldi antenna.

The setup is a miniaturized version of [63], tailored for precise near field imaging applications, such as micro-cracking detection in composite NDE and breast tumor diagnosis in medical imaging. While the experiments in [63] are meant for far-field detection purposes only, the present setup can work both in transmission and reflection modes (with 350 degrees coverage) as a near-field and far-field system, in order to gain better imaging quality. Since all parts of the setup, including the sample stand and antenna stands, can be adjusted, it is possible to measure cross-polarized field components and thus the potential for performing 3D imaging. Moreover, while horn antennas were used in [63] for target localization experiments in the reflectivity arch-range, they could not be utilized for near field imaging in the mini-arch range setup, since they produce a plane wave at far-field distances ($\sim$ 3:5 m), and are intended for diffraction limited imaging. Additionally, the relatively large size and 3D structure of the horn antennas make them undesirable for compact imaging applications due to inefficient illumination of the imaging domain, size and weight constraints and their inability to be integrated into planar circuits. Hence the designed planar microstrip antennas are preferred candidates for the mini arch-range setup shown in Fig. ??(a).

The scattered fields from the target are recorded by the monopole antenna. These fields are time reversed and back-propagated using the numerical model. At the localized time instant, the electric fields are efficiently focused at the metal target location, as displayed in Fig. 4.15(a). The time integrated electric energy shows the energy localized around the target region, as displayed in Fig. 4.15(b). The full width at half maximum (1.8 cm) of the cross range energy signal, indicated by the solid black line of Fig. 4.15(d) can be utilized to estimate the actual size of the target. A simulation is performed for the similar configuration using 2D FDTD codes Fig. 4.15(c), demonstrating excellent comparison between experimental and

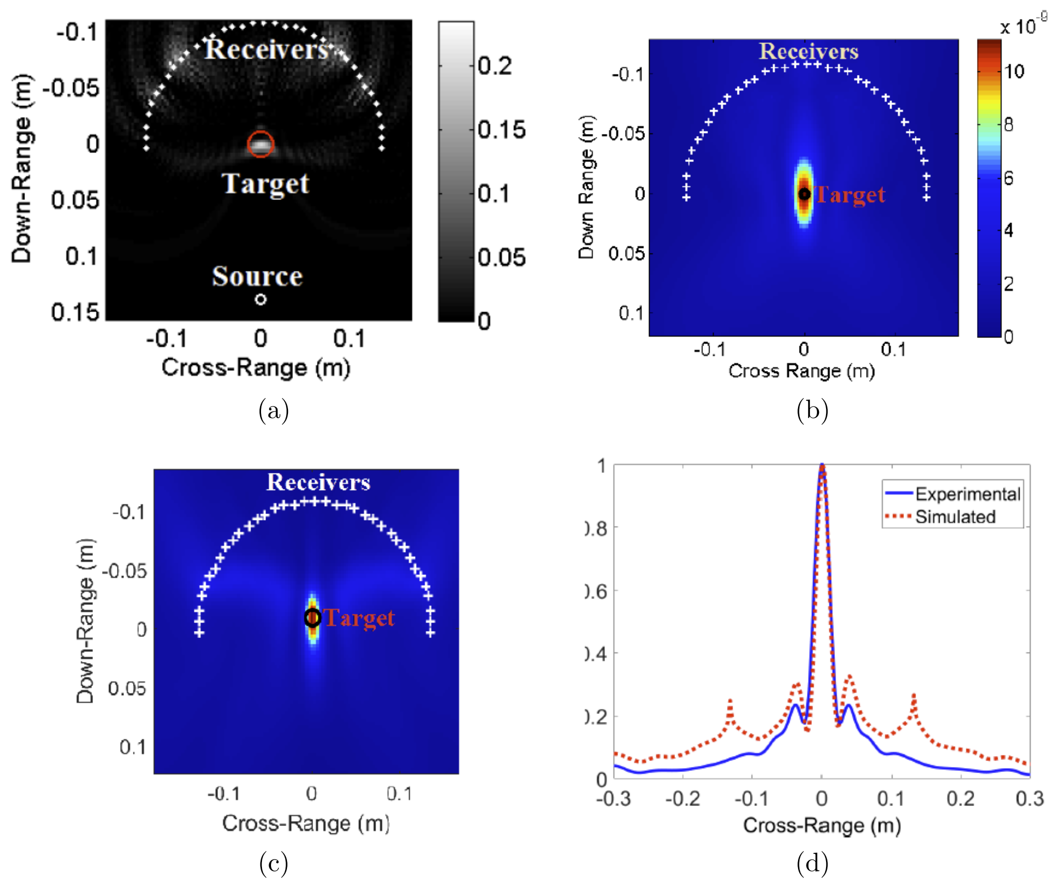

Figure 4.15: Time reversal imaging results (a) Focused field, (b) Measured TR energy, (c) Simulated TR energy, (d) Comparison between simulated and measured TR signals

simulation results, as shown in Figs. 4.15(b), (c) and (d)).

4.8 Conclusion

Microstrip transmitting and receiving antennas, operating between 3 GHz and 10 GHz are designed to be used in a TRM for imaging applications. A TSE APV antenna and an RGSR monopole antenna are proposed and developed as the transmitting and receiving antennas of the system. The efficacy of the transmitting antenna was evaluated at both far and near field ranges. The antennas are optimized according to the requirements of the system, characterized in both frequency and time domain, and fabricated. There is good match between simulation and measurement results. Measurement results show that both antennas meet the requirements for a TR system. Accurate measurement results demonstrate the feasibility of the TRA for imaging applications. The imaging system can be used in several applications such as complicated long range radar imaging, rapid inspection of composites and breast tissue imaging. Future work involves evaluating the super-resolution capabilities of TR and testing the robustness of the system for detection of tumors in realistic multi-layered breast phantoms as well as nondestructive evaluation of composite structures.

Chapter 5

Breast tumor imaging and hyperthermia by time reversal

5.1 Introduction

X-ray mammography is the most common breast cancer screening technique [64]. However it is often uncomfortable due to breast compression. Moreover, it can add risk due to exposure to low levels of ionizing radiation [65]. The limitations of existing techniques and practices motivate the development of new imaging modalities for breast cancer treatment applications. With the advent of several imaging modalities for biomedical applications, there has been a huge thrust in using microwaves as a complimentary system for breast tumor screening and hyperthermia based treatment applications. The increasing number of publications attests the rising interest in this topic. Experimental data have revealed contrasts in dielectric properties of malignant tumor tissue relative to non-malignant, normal breast tissue ranging from 2:1 to 10:1 [66]. Preliminary clinical examinations have been reported for a cylindrical confocal microwave imaging system using spacetime beamforming [67]. Additionally, microwave induced local hyperthermia has been shown to be effective in several clinical studies, including breast cancer as an adjuvant method to radiation and chemotherapy [68]. While some narrow band signal schemes have been used for hyperthermia treatment applications [69], ultra-wideband (UWB) systems offer several advantages such as tighter focal spots and reduced hot spot anomalies due to its lower sidelobe peaks [70]. A comparison of performance between UWB and narrow band systems of hyperthermia for breast cancer treatment has been reported in [71].

TR can be potentially used for imaging tumors since they behave as secondary sources. TR was used for ultrasonic biomedical imaging applications such as for lithotripsy and transcranial therapy applications [20]. Promising simulation results using TR for detection of breast tumors has been obtained by Kosmas et. al [53]. The biggest advantage of time reversal imaging (TRI) is the fact that a physical TRI system has the potential to focus the non-ionizing microwaves inside the tumor region. The focused fields might preferentially heat the tumor, thus opening up the scope towards microwave-induced thermal therapy applications [72, 73]. While existing microwave imaging techniques would need separate hardware systems for imaging and thermal therapy applications, the theory behind TR makes the possibility of using the same TRI hardware system for imaging and thermal therapy applications, as has been done for transcranial therapy by Fink et al. using ultrasonic waves [74].

This chapter deals with a novel experimental TRI system based on a passive TRM for imaging and thermal therapy of breast tumors. The overall idea is shown in Fig. 5.1. The application of TR for detection of breast tumors is challenging because of several factors. Prior TR simulations for breast imaging assumed perfect knowledge of breast properties, which is unrealistic in practical biomedical applications [53]. Work on extracting tumor contribution from total fields for monostatic radar setup is reported in [1]. However, TR based imaging systems require a bistatic radar setup in order to obtain the scattered fields. It is non trivial to extract tumor contribution from total fields for the bistatic setup due to the different ray paths associated with each transmitter-receiver pair. A novel contribution in this research is the development of an algorithm that is capable of extracting tumor contribution from total fields in a bistatic radar setup. The first part of the chapter describes a signal processing algorithm based TRI system for detecting tumors from total fields. Typically, papers published in this field assume complete knowledge of the medium heterogeneity in the back-propagation model [75]. However in this chapter, the robustness of the algorithm is demonstrated without considering the medium heterogeneity, and knowing only the nominal breast properties. Simulation studies and parametric analysis are conducted to determine the robustness of the algorithm with respect to tissue variability, skin reflection and noise. From a simulation standpoint, the studies in this research provide a much more realistic scenario as encountered in practical biomedical applications. Deng et al [76] have worked on a hybrid TR microwave imaging experiments for breast tumor such as microwave induced thermal or acoustic techniques. However not much work is reported on active TR microwave imaging with experimental results. The second part of the chapter presents a novel experimental

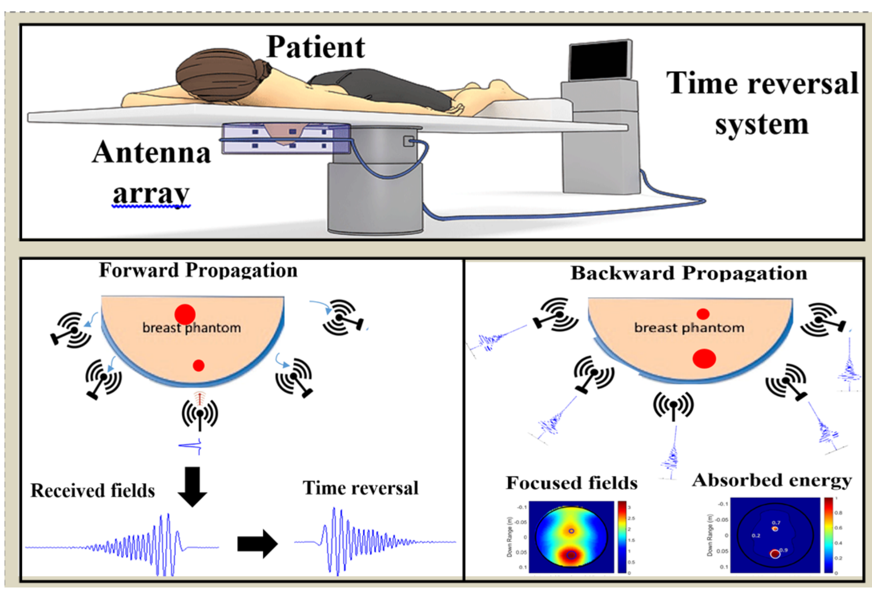

Figure 5.1: Schematic of the TRI system

system for breast tissue imaging and determining heat absorption rates for a simple 2D breast phantom. The design of the time reversal mirror for imaging applications is discussed in the previous chapter and is integrated in the pulsed time domain system for breast tissue imaging. Initial results from simulations and experiments demonstrate the robustness of the approach and lay the foundation for a microwave imaging system for detection of tumors in multi-layered breast tissues. The efficiency of the overall algorithm and experimental system is demonstrated, laying the foundation for potential therapeutic applications for breast cancer.

5.2 Theory and principles

The theory and algorithm of TR for imaging has been discussed previous chapters and are not repeated here. However there are some new concepts added to the algorithm such as TR modeling in presence of losses and calculating the absorbed heat that is discussed below.

5.2.1 FDTD modeling

Breast tissues are lossy and inhomogeneous. The reversed electric field FDTD equation for a lossy medium [53] is given by

$$\begin{aligned} E_z^{n+1}(i,j) = \frac{1+\frac{\sigma\Delta t}{2\varepsilon}}{1-\frac{\sigma\Delta t}{2\varepsilon}} E_z^n(i,j) - \frac{1}{1+\frac{\sigma\Delta t}{2\varepsilon}} \frac{\Delta t}{\varepsilon\Delta x} \Bigg(H_y^{n+\frac{1}{2}}(i+\frac{1}{2},j) \\ -H_y^{n-\frac{1}{2}}(i-\frac{1}{2},j) - H_x^{n+\frac{1}{2}}(i,j+\frac{1}{2}) + H_x^{n-\frac{1}{2}}(i,j-\frac{1}{2}) \Bigg), \end{aligned} \tag{5.1}$$

where ε and σ are the material permittivity and conductivity, and Δt and Δx are the FDTD time steps and cell size, respectively. The change of sign in the conductivity in (5.1) is crucial since the propagating medium is also reversed in order to compensate for the losses. The standard leap frog scheme is adopted to solve the FDTD equations [34]. The inhomogeneity associated with breast tissues will be introduced later in the paper and does not affect (5.1). The sensors are modeled as point sources and are used to record the scattered fields. The input source for simulations is chosen as a short modulated Gaussian pulse with a modulating frequency $f_m = 2$ GHz, pulse width of 120 picoseconds, which corresponds to a bandwidth of 5.5 GHz [63].

5.2.2 Hyperthermia study via TR

Hyperthermia is an effective, thermal therapy technique used to elevate cell temperatures and thus induce cytotoxic effects in tissues, leading to cell damage and increased vulnerability to radiation and toxins [77]. The objective of this treatment is to elevate the temperature of tumor cells to $\sim 42°C - 43°C$, while maintaining the temperature of the rest of the tissues below $42°C$ [71]. Recent research on the development of cheap and compact RF circuits for TR of UWB pulses with nanosecond temporal durations has demonstrated the possibility of a physical TRI system [78]. One of the biggest advantage is TR lies in the fact that a physical TR system can focus the non-ionizing microwaves inside the tumor, leading to preferential heating of the tumor. This opens up the scope towards hyperthermia treatment applications. The specific absorption rate (SAR) evaluates the heat generated in the tissue by the electrical field [79], as given by

$$\mathrm{SAR} = \frac{1}{2} \int \frac{\sigma(r)|E(r)^2|}{\rho(r)} dr, \tag{5.2}$$

where σ and ρ are the tissue electrical conductivity and density respectively, and $|E(r)|$ is the magnitude of electric field in the breast tissues. The feasibility of utilizing this approach for measuring heat absorbed by the tumor for potential therapy, in complement with imaging applications is investigated.

5.2.3 Quantitative metrics

Several quantitative metrics can be utilized as performance indicators of the method. The mean electric energy (mE) and mean SAR ratio (mSAR) are introduced to quantify the relative absorbed energy in the tumor. They serve as quantitative comparisons for detection capability of the focused field images and are given by

$$\mathrm{mE} = \frac{\frac{1}{X_t}\sum^{A_t} E(x,y)}{\frac{1}{X_{nt}}\sum^{A_{nt}} E(x,y)},; \qquad \mathrm{mSAR} = \frac{\frac{1}{X_t}\sum^{A_t} \mathrm{SAR}(x,y)}{\frac{1}{X_{nt}}\sum^{A_{nt}} \mathrm{SAR}(x,y)}, \tag{5.3}$$

where X_t is the total number of pixels, A_t is the area of the tumor region, X_{nt} is the number of pixels and A_{nt} is the area of the rest of the breast region.

5.3 Simulation studies

5.3.1 Breast phantom model

The breast phantom model chosen for simulation is a two-dimensional coronal section of radius 8 cm, with the dimensions matching a realistic breast slice obtained from the University of Wisconsin Numerical Breast Phantom Repository coronal section for fatty tissue [66]. The tumor, of radius varying from 8 mm, is placed at different locations inside the breast phantom. The breast is assumed to comprise mostly fatty tissues with ε_r=7 and σ=0.012

S/m at 6 GHz with 20 % tissue variance, while the tumor is assumed to comprise mostly fibroglandular tissues with ε_r=50 and σ=0.086 S/m at 6 GHz. The frequency dispersive nature of the breast tissues is not studied as part of this research as it does not significantly affect the focusing capability. Additional phase shifts due to dispersion are compensated automatically through phase conjugation, thus causing only dispersive attenuation. Previous researchers have introduced filtering compensation techniques to deal with frequency dispersion and have demonstrated the robustness of TR with respect to the frequency dispersive nature of breast tissues [29]. Additionally, as pointed out in [53] by Kosmas et. al., the scattered signal from the tumor in the presence of skin is an amplitude scaled and time delayed version of the corresponding scattered signal without the skin. The background subtraction and the early time content removal and the time gating modules of the signal processing algorithm would also lead to considerable reduction of the effect of skin. However, the authors acknowledge that there might be added complexities to the algorithm performance as well as the TRI results, since the scattering from the tumor might be significantly weaker than the reflection from the breast-skin interface. The effect of the skin layer is not studied as part of this research and will be investigated as part of future research. The position

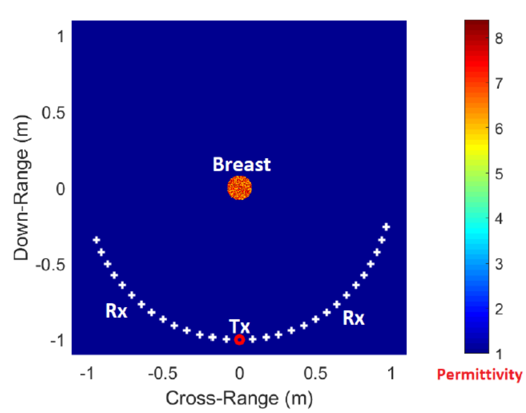

Figure 5.2: Simulation schematic with breast and antenna positions

Figure 5.3: Typical microwave imaging setup (Patient interface table, patient getting her breast scanned) [1]

of the tumors is varied in different simulations. The simulation schematic along with the antenna array system is shown in Fig. 5.2. From a clinical implementation point of view, the patient is expected to lie in prone position on an examination table with her breast extending through a hole, similar to the TSAR prototype system shown in Fig. 5.3 [1]. In such a case, only the breast is subjected to electromagnetic fields radiated from the array (with microwave absorbers placed surrounding the area), so that reflections from the rest of the body contributing to the recorded signals is reduced.

5.3.2 Feasibility study

First, a feasibility study is performed with exact knowledge of the tumor contribution. This study provides the exact and ideal solution. The total fields with and without the presence of the tumor, shown in Fig. 5.4(a) are subtracted in order to obtain the tumor contribution for each receiver element. The time-reversed tumor contribution is back-propagated in the breast model, taking into consideration nominal values of tissue properties (heterogeneity unknown). As shown in Fig. 5.4(b), the entropy plot during back propagation has a minimum at time instant A, which shows the wave localized at the tumor location (Fig. 5.4(c)). The integrated energy method shows focusing of the energy around the tumor region, as shown

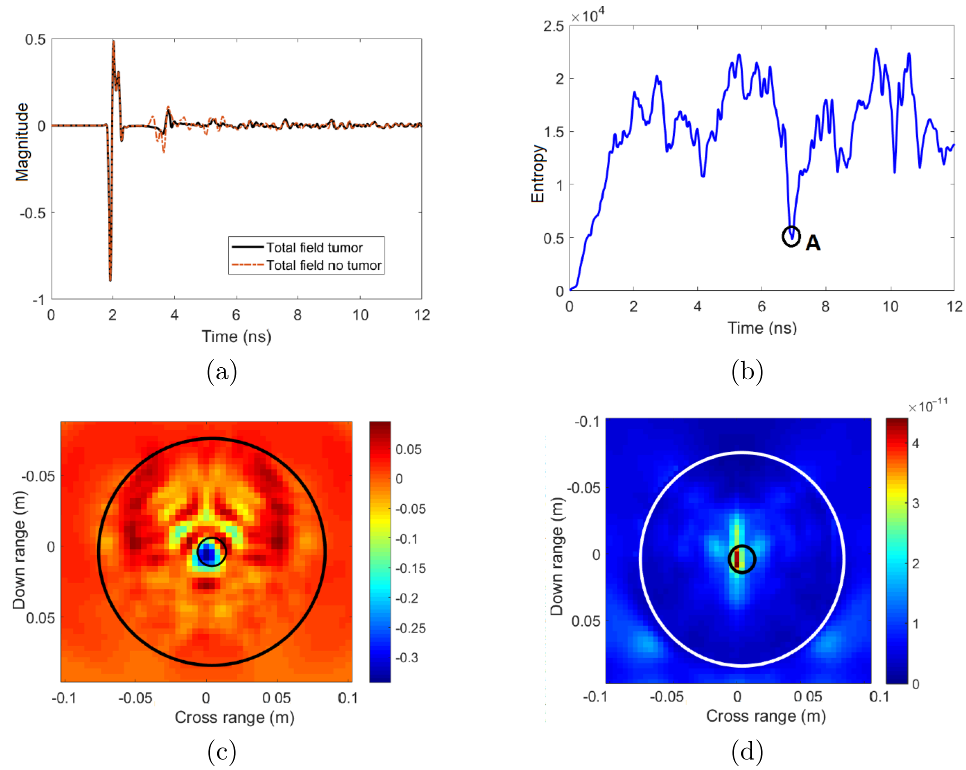

Figure 5.4: TR for breast tumor detection feasibility study: (a) fields scattered from breast, (b) entropy plot, (c) electric fields at A, (d) integrated energy

in Fig. 5.4(d). Additional artifacts are observed in Fig. 5.4(c, d) due to the lack of knowledge of the medium heterogeneity.

5.3.3 Signal processing algorithm

In conventional TR as mentioned above, the forward scattered signals with and without the target (total fields) are subtracted to obtain the target signal (scattered fields), and the result is time-reversed and back-propagated to focus at the target locations. Thus the main requirement for target detection is accurate knowledge of the scattered fields based on properties of the background medium. This requirement is unrealistic in biomedical applications.

Exact knowledge of the electrical properties of fibroglandular tissues is difficult. Exact knowledge of the background fields is also difficult under clinical imaging conditions. Hence, a signal processing algorithm is needed to extract the tumor response from the total fields. There has been some research that discuss clutter removal techniques for a monostatic radar setup. However, the main goal of the algorithm is to calculate tumor response from total fields, where clutter removal is one sub-step. This is non-trivial because the response is dominated by reflections from the breast interface and also includes clutter due to reflections from inhomogeneities. This paper presents a novel signal processing algorithm that minimizes clutter due to reflections from breast-skin interface and extracts tumor contribution from total scattered fields. As shown in Fig. 5.5, the algorithm consists of four major modules [80]:

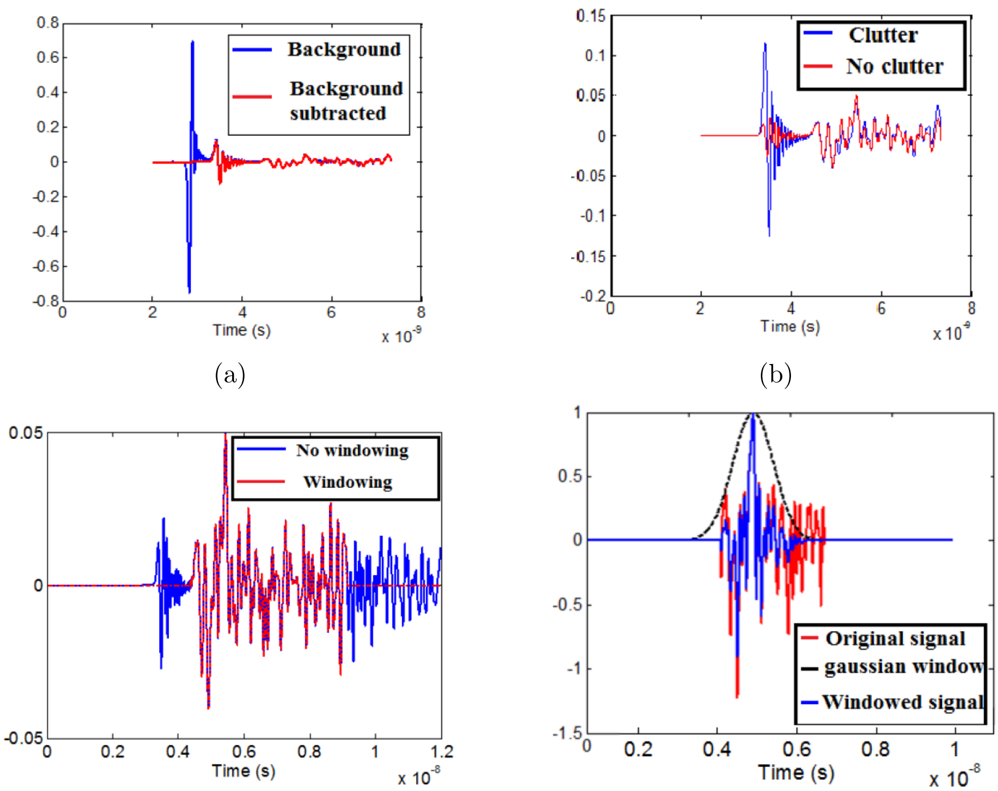

(a) (b) (c) (d)

Figure 5.5: Major modules of the signal processing algorithm: (a) Background subtraction, (b) Early time content removal, (c) TOA based time gating, (d) Gaussian windowing

- Background Subtraction: The background signal comprises clutter from surrounding targets as well as antenna cross coupling due to strong side and end lobes. The background signal E_{bg} is obtained with no breast phantom present and subsequently subtracted from the scattered fields signal E_s to give the background subtracted signal E_1, given by

$$E_1(n;t) = E_s(n;t) - E_{bg}(n;t); \quad n = 1 \text{ to } N, \tag{5.4}$$

where N is the total number of channels. The output of this module is $E_1(n;t)$.

- Early time content removal. The early time content, dictated by reflections from the breast interface, is removed from the late-time content that contains tumor backscattered signals by subtracting the average of all the channels ($\overline{E_1}$) from each channel (E_1), given by

$$E_2(n;t) = E_1(n;t) - \overline{E_1}(n;t). \tag{5.5}$$

The output of this module is $E_2(n;t)$.

- Time of arrival (TOA) approach for time gating. The TOA approach can be used to detect the tumor response, which is present between the early time when the wave hits the breast front wall to the late time when the wave hits the breast back wall. Hence, windowing the signals based on the TOA approach significantly reduces secondary clutter signals and back wall reflections. The output of this module is $E_3(n;t)$.

- Temporal Gaussian windowing. The last step consists of windowing the processed signal (E_3) by multiplying with a short Gaussian pulse so as to resolve tumors smaller than the central wavelength of the excitation pulse. Thus, the windowing approach maintains the necessary amplitude and phase information, given by

$$E_f(n;t) = E_3(n;t) \cdot e^{-\left((t-t_p)/\tau\right)^2} \tag{5.6}$$

where t_p, τ are the peak instant and the taper parameter of the Gaussian window respectively and E_f is the output of the module, which is the final processed electric field, serving as the input to the time reversal simulation.

The scattered fields (E_s) are fed into this signal processing algorithm to yield the processed fields (E_f) given in (5.6), which are reversed in time and back-propagated in a medium with nominal values of the breast electrical properties known. The variance of tissue dielectric property is assumed to be unknown, as is the case in a realistic scenario.

5.3.4 Imaging results

Three important cases were considered based on the breast phantom model to test the robustness of the algorithm.

- Case I: The tumor was chosen to be at the center of the breast. The spatio-temporal focusing instants are calculated from the minimum entropy criterion, discussed in Chapter 2 and are shown in Fig. 5.6(a). Five minima are observed in the entropy curve denoted by time instants A,B,C,D and E. The minimum corresponding to time instant A shows the TR wave initiating to back-propagate from the receiver array, as seen in Fig. 5.6(b). Time instants B and D show the wave entering and exiting from the breast interface (Figs. 5.6(c), (e)). Time instant C shows the wave localized at the tumor location (Fig. 5.6(d)). The minimum corresponding to the time instant E shows the wave localized at the tumor location again, due to the secondary scattering contribution from the tumor (Fig. 5.6(f)). Although breast scattering contributions are not fully eliminated, as evident from Figs. 5.6(c) and (e), the entropy technique is capable of attaining efficient spatio-temporal localization. The localized image obtained from the integrated energy image is spatially focused at the tumor location in Fig. 5.7(a). The column and row pertaining to the peak value of Fig. 5.7(a) is plotted in Fig. 5.7(b). The full widths at half maximum of the cross (row) and down (column) signals (0.022 m, 0.025 m) are almost equal to the size of the tumor (0.02 m).

- Case II: Next, the tumor was placed off-center, close to the breast interface. Fig. 5.7(c) shows that the integrated energy image is able to detect the tumor. This proves that the algorithm is successfully able to remove the dominant reflections from the breast interface and is able to discriminate the tumor. However some artifacts are observed due to reflection and scattering from other objects. Additionally, it was hard to detect

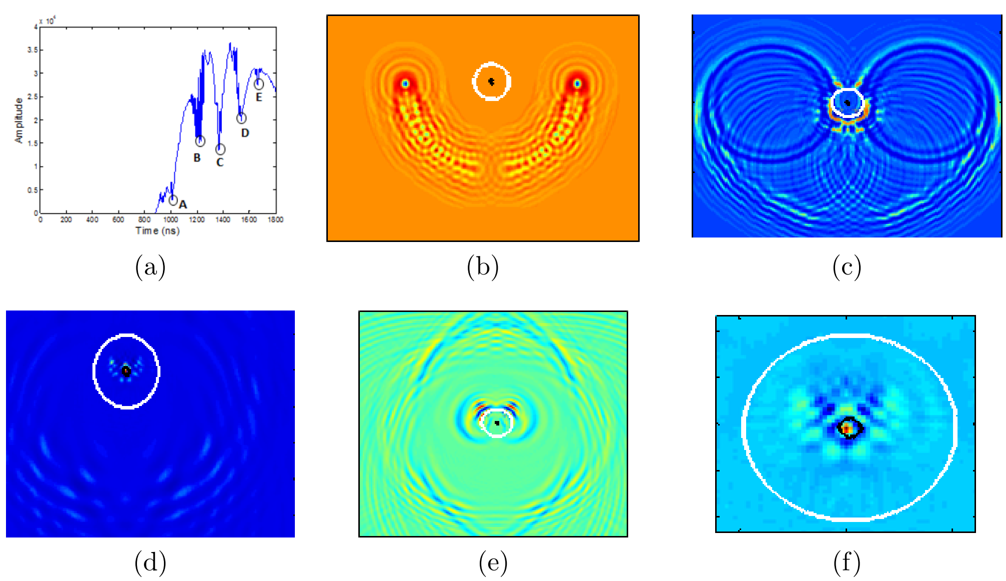

Figure 5.6: Entropy method used for temporal localization: (a) Entropy plot, (b) Electric fields at time instant A, (c) Electric fields at time instant B, (d) Electric fields at time instant C, (e) Electric fields at time instant D, (f) Electric fields at time instant E

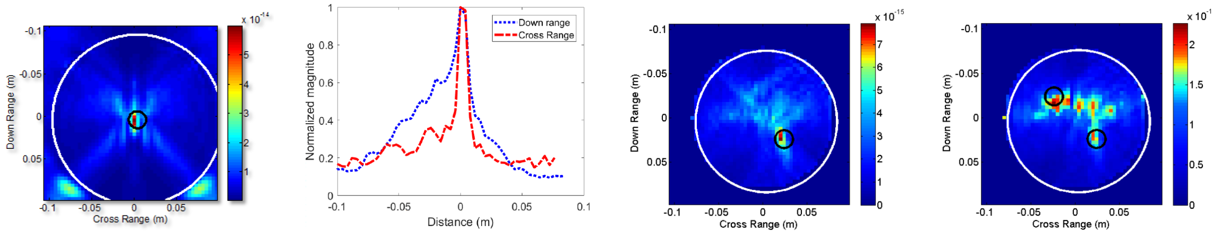

(a) (b) (c) (d)

Figure 5.7: Modified TR for tumor detection simulation study: (a) Case I: Integrated energy, (b) Case I: Cross, down range signals, (c) Case II: Integrated energy, (d) Case III: Integrated energy

tumors too closely spaced to the breast interface due to the breast wall reflection signal dominating the tumor interaction. Simulations studies estimate the minimum gap between the tumor and the breast interface to be 1.2 cm.

- Case III: Finally a more complicated case is considered that includes two closely spaced tumors slightly offset from the center of the breast with identical shape, size and material properties. Fig. 5.7(d) shows that the integrated energy image is able to detect both tumor locations. However, we also observe some artifacts in between the tumor locations, due to cross-coupling between the two tumors. These artifacts can be reduced by more advanced time-reversal methods that focus the wave selectively on individual targets [81]. Additional simulation studies have been conducted to study the effect of spacing between two closely spaced tumors. The minimum gap between the tumors is estimated to be 1.5 cm.

5.3.5 Parametric studies

Simulation studies replicating the desired experiments are conducted to determine the feasibility of the algorithm. Parametric studies as well as specific simulation cases are considered to determine the robustness and limits of the TRI algorithm with respect to medium inho-

Table 5.1: Simulation cases

Parameters	Details	Cases	Threshold
Heterogeneity	ε_r, σ variance	20%, 40%, 80%	75%
	Scatterer	1,2, unknown	-
Tumor spacing	2 tumors	1 cm,4 cm, 2.8 cm	1.5 cm
	3 tumors	2.5 cm, 5 cm	-
Material contrast	1-10	-	2.25
Bandwidth	2-48 GHz	-	3 GHz
Noise	SNR	-	2 dB

mogeneities, electrical property contrast between breast and tumor tissues, multiple tumors and the bandwidth of the input pulse. A default tumor radius of 4 mm is chosen for the parametric studies. The quantitative metrics used in the studies are given by mE and mSAR. Five different sets of parameters considered are outlined in Table 5.1, and corresponding results are presented in the following section.

5.3.5.1 Tissue heterogeneity

It is difficult to estimate the heterogeneity of dielectric properties of breast tissues due to multiple reasons, such as water and fat concentrations that vary with each individual. Tissue heterogeneity can be attributed due to variations of nominal dielectric properties of tissues as well as presence of non-tumorous scatterers. Although the expected variations have been reported in literature to be $\sim$ 10-20% variations of up to 80% of the nominal values (ε_r=7, σ=7 S/m) are considered here. The dielectric properties ($\varepsilon_r^v, \sigma^v$) is modeled as a uniformly distributed random variable in the range, given by $\varepsilon_r^v \sim U\Big(\varepsilon_r(1+\psi), \varepsilon_r(1-\psi)\Big); 0 \leq \psi \leq 1$, where ε_r is the nominal value. Here U denotes uniform distribution and ψ is the variance. TR back-propagation simulations are performed, with only the nominal values of the electrical properties of breast tissues known. The behavior of TRI is similar to that of a matched filter, producing a sharp peak where the fields focus. In the absence of medium heterogeneity, the TR signal (s_{TR}) for N receivers with an impulse input is given by

$$s_{TR}(t) = \sum_{n=1}^{N} h_n(t) * h_n(-t), \tag{5.7}$$

where $h_n(t)$ and $h_n(-t)$ are the forward and backward impulse response functions. When a medium heterogeneity $\delta_n(t)$ is considered, s_{TR} is given by

$$s_{TR}(t) = \sum_{n=1}^{N} h_n(t) * \Big(h_n(-t) + \delta_n(-t)\Big). \tag{5.8}$$

Fig. 5.8 (a) shows the parametric variation of mE and ξ with variation of tissue. Three specific cases for an off-centered tumor of radius 4 mm are simulated and shown for tissue variance of 20, 40 and 80%. As shown in Figs. 5.9 (a),(b) and (c), the results show that increased dielectric variance leads to an increase in forward and backward impulse response function mismatch, thus leading to lower mE. Although the imaging quality is not severely hampered by marginal dielectric variance, the tumor is barely detected for 80% variation.The threshold of tissue variation is estimated as 72%. The SAR images, shown in Figs. 5.9 (d),

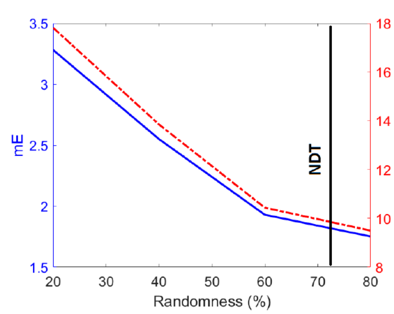

(a)

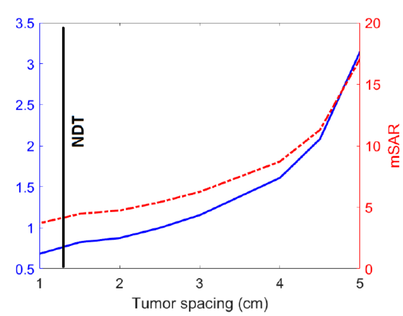

(b)

Figure 5.8: Results of parametric studies: mE and mSAR with (a) tissue dielectric variance, (b) tumor spacing (NDT: non detectable tumor)

(e) and (f) show a similar trend in absorption with the tumors absorbing higher energy than the surrounding tissues, with approximately 30% higher absorption for 80% tissue variation. It is worth mentioning that there is no SAR increase indicated at the surface, close to the antennas since (5.3) is calculated only inside the breast region, which is the region of interest. Inhomogeneities occurring from presence of non-tumorous scatterers is not studied as part of this research and will be investigated in the future.

The presence of non-tumorous scatterers in breast tissues may also lead to medium heterogeneity. The robustness of the TRI algorithm to detect a tumor in the presence of elliptical single and multiple scatterers with ε_r=4 and σ=0.012 S/m with a 20% tissue variance is investigated. Although the scattered fields consist of scatterer and tumor contributions, a

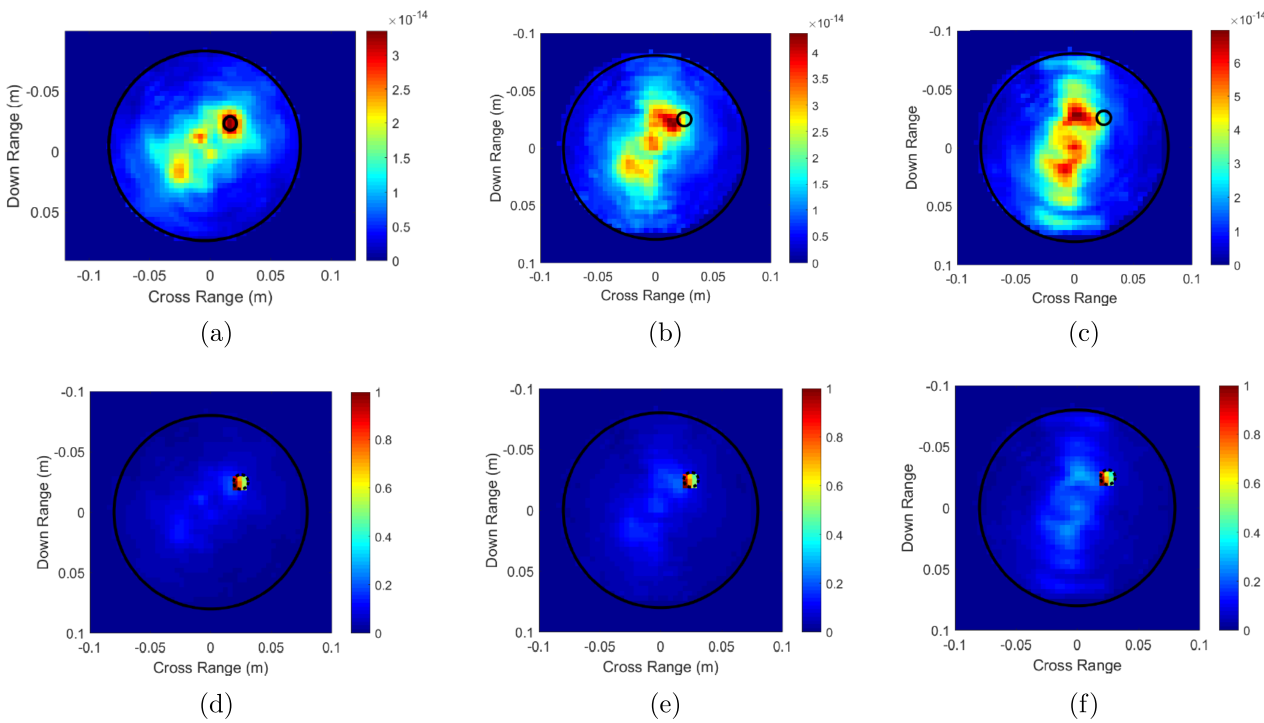

Figure 5.9: Case I- TR imaging results for variation of tissue. (a, d): 20 % heterogeneity (a) Energy (mE=5.2) (d) Absorption (mSAR=18); (b, e): 40 % heterogeneity (b) Energy (mE=4.6) (e) Absorption (mSAR=13); (c, f): 80 % heterogeneity (c) Energy (mE=2.5) (f) Absorption (mSAR=9.5)

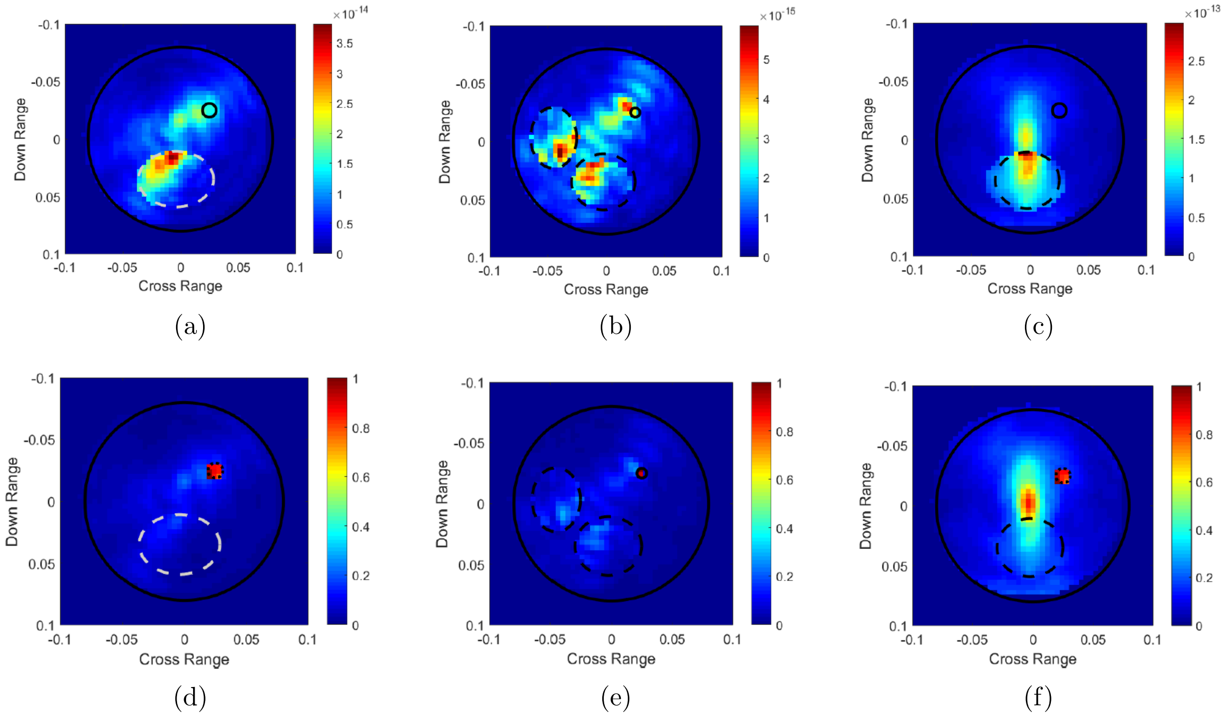

Figure 5.10: Case I- TR imaging results in presence of inhomogeneity. (a, d): 1 ellipse major axis 6 cm (a) Energy (mE=3.2) (d) Absorption (mSAR=12); (b, e): 2 ellipsis major axis 5 cm (b) Energy (mE=3.4) (e) Absorption (mSAR=15); (c, f): unknown scatterer (ellipse major axis 6 cm) (c) Energy (mE=0.5) (f) Absorption (mSAR=8)

significant portion of the TR field still focuses on the tumor, and thus detection is possible for single and multiple scatterers, as shown in Figs. 5.10(a) and 5.10(b), when the scatterer property is known in the TRI model. If the scatterer size is much larger than the tumor, higher TR energy is focused around it, rather than around the tumor, as observed in Figs. 5.10(a,c). Some additional artifacts are observed between the tumor and the scatterers due to the cross coupling between them. For two well resolved scatterers, the TR signals correspond to a linear combination of non-null orthogonal eigenvectors. However, since the inhomogeneities and tumor are not point scatterers and are not well separated, the corresponding eigenvectors are non-orthogonal, resulting in poor image quality. However, when the scatterer property is unknown, the tumor cannot be detected, as seen in Fig. 5.10(c).

The focusing ability of the TR method, which is due to its matched filter property is lost since the forward and backward impulse response functions, as defined in (5.8), are different. Sophisticated signal processing algorithms are required in this case to extract the tumor contribution from the scattered fields. These algorithms employ selective focusing methods such as decomposition of the time reversal operator method [82] to extract the eigen value corresponding to the tumor and steer its eigen vector towards the tumors. Additional clutter, breast inhomogeneities and skin-wall interaction can be eliminated by employing a time of arrival approach to determine the time duration when the wave is localized inside the breast region. These are currently being investigated and not addressed in this research. The TR SAR images (Figs. 5.10(d,e,f)) are much more focused at the tumor, since the conductivity of the tumor is larger than the surrounding fatty tissues and other scatterers.

5.3.5.2 Tumor spacing

Incidence of multiple tumors in the breast in form of multi-focal or multi-centric disease have been reported in the literature to range between 6 to 60 % [83]. Multi-centric disease has been reported to occur in breast cancer cases, where multiple lobules or ducts of size around 2 cm with minimum spacing around 0.5 cm may develop in different breast segments [84]. TR has the capability of imaging multiple targets, as long as the separation between them is of the order of a wavelength. This is challenging for imaging breast tissues, as tumors might be near each other or to the skin interface. The feasibility of the TRI algorithm for detection of multiple closely spaced tumors is studied in this section. Fig. 5.8(b) shows the parametric variation of mE and mSAR with the spacing between two tumors, with the minimum spacing, below which the tumor is not detected in the energy image estimated as 1.5 cm, which is approximately half of the down range resolution. This is due to the

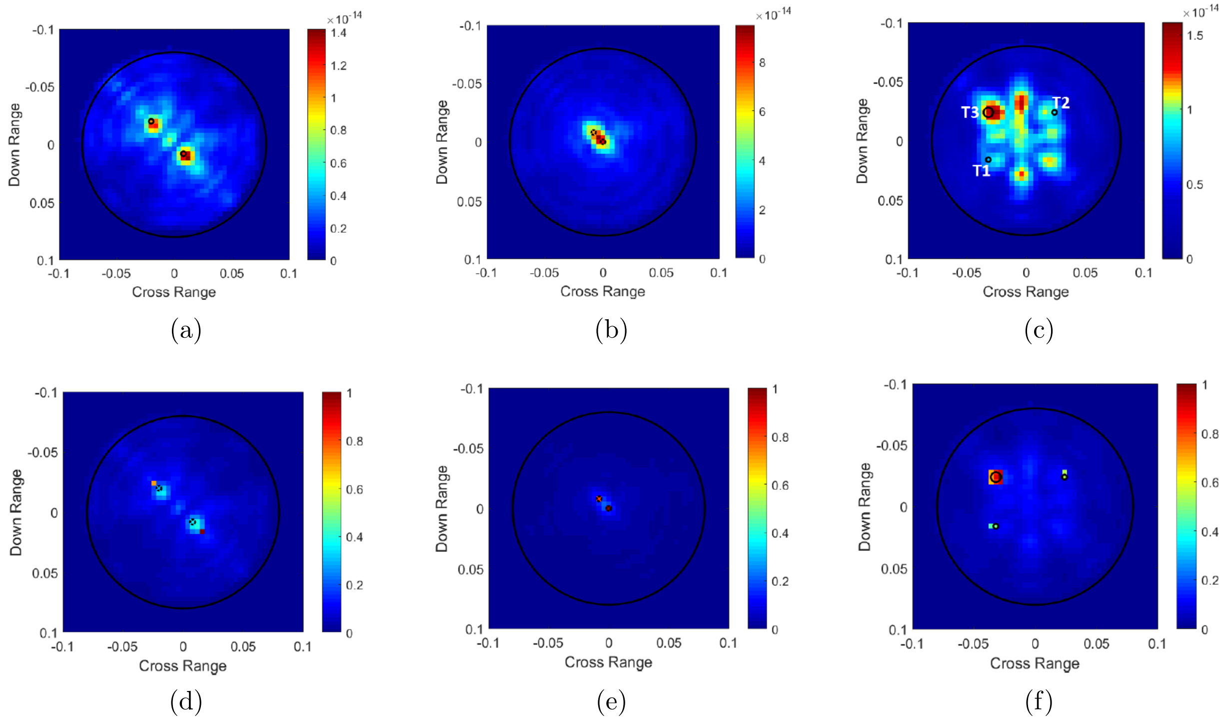

Figure 5.11: Case II- TR imaging results for varying gap between tumors. (a, d): 2 tumors gap=2.8 cm (a) Energy (mE=1) (d) Absorption (mSAR=7); (b, e): 2 tumors gap=1.4 cm (b) Energy (mE=0.6) (e) Absorption (mSAR=5.5); (c, f): 3 tumors gap=5 cm and 8 cm (c) Energy (mE=1) (f) Absorption (mSAR=9)

multi-path scattering from the tumors that increase the TRM aperture and hence leads to super resolution. An increase in spacing between two tumors leads to reduced cross-coupling and hence better imaging quality and higher mE and mSAR. Three specific cases are studied for imaging two and three tumors. For two tumors closely spaced with a gap of 2.8 cm, as shown in Fig. 5.11(a), the back-propagated wave focuses equally at the two tumor locations, showing two sharp peaks at the respective tumor locations. However, when the gap is 1.4 cm (lower than the threshold value obtained from Fig. 5.8(b)), the strong cross coupling between them and the limits of diffraction resolution are responsible for producing an extended focal spot, as shown in Fig. 5.11(b). A third case is considered with 2 tumors of radius 0.6 cm named as T1 and T2 and a bigger tumor of radius 1.2 cm named T3, placed

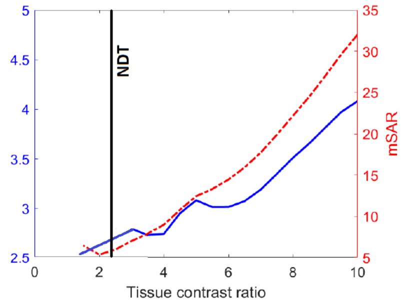

(a)

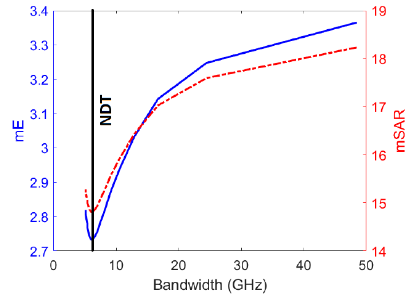

(b)

Figure 5.12: Results of parametric studies: mE and mSAR with (a) tissue contrast, (b) input pulse bandwidth

inside the breast. The gap between T1 and T3 is 5 cm, while the gap between T2 and T3 is 8 cm, with their exact locations shown in Fig. 5.11(c) It is seen that the detection capability of cross-range separated tumors is better than for down-range separated tumors, since TR cross-range resolution is better than down-range resolution. The TR wave focuses more on T3 since it is larger than the other tumors. Additionally, cross-coupling between the tumors leads to artifacts as shown in Fig. 5.11(c). The SAR image, seen in Fig. 5.11(d), shows a similar trend in absorption with the tumors absorbing higher energy than the surrounding tissues. Figs. 5.11(e) and 5.11(f) show that for two closely spaced tumors as well as a tumor, breast fatty tissues surrounding the tumors absorb a considerable amount of energy, which is undesirable for thermal therapy.

5.3.5.3 Material contrast ratio

The dielectric properties of the non-malignant breast tissues vary significantly with varying fat and water concentrations. In general, fibroglandular tissues have much higher ε_r, σ than fatty tissues and their dielectric properties may be closer to that of malignant tissues. Tumor detection might be difficult in such cases due to less dielectric contrast. The capability of TR to detect tumors for different dielectric properties of breast tissues is investigated. The dielectric constant and conductivity ratio between the tumor and surrounding breast tissues is defined as contrast ratio. Simulations are conducted by varying the contrast ratio from 1 to 10 in order to determine the robustness of TRI. Fig. 5.12(a) shows the parametric variation of mE and mSAR with the contrast ratio between breast and tumor tissues. The threshold of the contrast ratio, below which the tumor is not detected in the energy image is estimated to be 2.25.

5.3.5.4 Bandwidth

The imaging quality of TRI also depends heavily on the input pulse width, since TR involves focusing both in space and time. Fig. 5.12(b) shows the parametric variation of mE and mSAR with respect to the pulse bandwidth. A pulse with a shorter width and hence a bigger bandwidth leads to better range resolution and thus leads to enhanced imaging quality. The relationship between the range resolution (S_r) and pulse width (τ) is given by $S_r \geq \frac{c}{2\tau}$. Thus, an increase in bandwidth leads to increased mE and mSAR respectively, as seen in Fig. 5.12(b). The bandwidth threshold, below which the tumor is not detected in the energy image is estimated to be 3 GHz.

5.3.5.5 Effect of noise

Measurement noise $n_r(t)$ is uncorrelated with the impulse response of the medium. The back-propagated signal in presence of noise is given by $h_r(-t) + n_r(t)$. Thus, the time reversed signal can be represented as

$$\mathrm{S_{TR}}(t) = \sum_{r=1}^{N} h_r(t) * h_r(-t) + \sum_{r=1}^{N} h_r(t) * n_r(t) \tag{5.9}$$

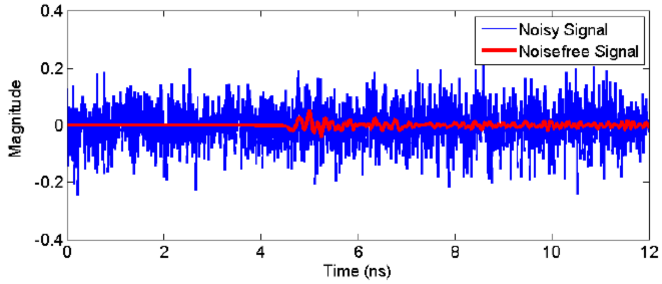

(a)

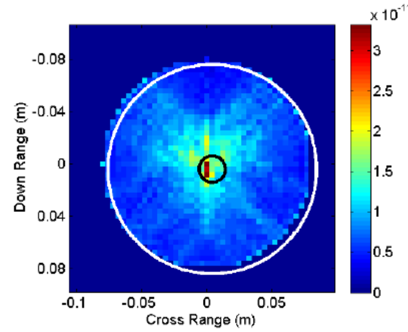

(b)

Figure 5.13: (a) Addition of 5 dB noise to the simulated signals, (b) Integrated energy image still detects tumor

Additive white Gaussian noise with an SNR of 5 dB is added individually to all receiver signals after measuring the power of the signals. A typical noise-added receiver signal is shown in Fig. 5.13(a). As long as the phase difference between successive receiver array elements is unhampered, TR focusing can be achieved effectively, as seen in Fig. 5.13(b). The SNR threshold below which the tumor cannot be imaged is determined to be as low as 2 dB.

These results demonstrate the feasibility and parametric limits for robustness of the proposed approach with respect to breast tissue variation, tumor separation, material contrast, bandwidth and noise. Other parameters such as target size, receiver array size and number of elements have been studied as part of previous research on TR for radar imaging [27, 63], which is valid from a breast tumor application point of view.

5.4 Experimental studies

Passive TR experiments are conducted using the pulsed time domain system described in Appendix B, coupled to a back-propagation FDTD 2D code [63]. Microstrip transmitting and receiving antennas to be used for TRI applications were designed as part of a prior research [85]. Based on the properties of TR and its imaging applications, an antipodal Vivaldi antenna and a monopole antenna were proposed for the transmitter and receiver designs, respectively. The overall process was initially validated by conducting an experiment for detecting a single metallic target [85]. Next, the system was utilized for detection of tumors in a multi-layered breast phantom. The experimental setup, breast phantom design and the corresponding TR results are presented in the next sections.

5.4.1 Experiment details

The measurement system is shown in Fig. 5.14 (a). The mini-arch arch range of radius 10 cm described in the previous chapter is used for the experiments [86]. The back-scattered fields are recorded and measured using the similar time domain setup as mentioned in the previous chapter. The breast phantom is placed in the sample stand in between the transmitting and receiving microstrip antennas. The target data are collected for 26 evenly spaced receiving antenna points, the limit obtained from parametric studies previously, with increments of 10°spread over a 260°angular coverage. In order to be utilized as a physical, active TR system for rapid clinical investigations, the passive TR experimental system needs to be modified into two modules. The first module would comprise the transmitter and multiple receiver channels with RF switching circuits for automated scanning. The second module would comprise TR based RF circuits as mentioned before [78], which can calculate the pulse delay and amplitude scaling for each channel, modify and time reverse the received waveforms and feed them as input to individual receiver channels, in order to perform physical time reversal.

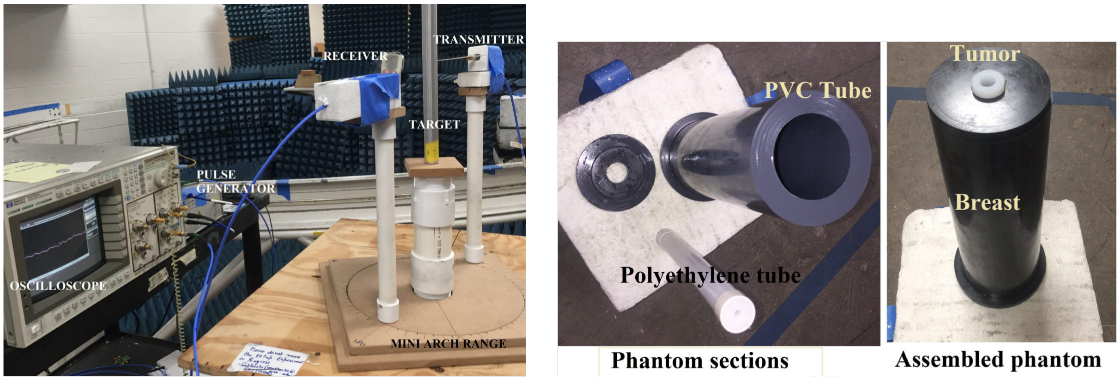

(a) (b)

Figure 5.14: Experimental setup for imaging : (a) Time domain experimental system, (b) Breast phantom

5.4.2 Breast phantom experiment

Traditionally, a phantom that closely mimics human tissue properties is invaluable in studies using modalities such as ultrasonic, magnetic resonance and computerized tomography. With the ever-increasing demand of cellular and other devices that radiate electromagnetic energy, there has been an increase in the study of effect of electromagnetic interaction with biological tissues, particularly in the microwave regime [87]. This has led to an increase in the need for phantoms that can mimic electromagnetic properties of biological tissues. Several breast phantom models are being developed, based on low and high water content. Dielectric spectroscopic measurements involving electrical properties of normal and malignant breast muscles have been using Cole-Cole parametric dispersion models [88]. The properties of biological tissues vary to a large extent depending on the level of water content of these tissues. Since water has a very high dielectric constant, the proportion of water present in the tissues changes the tissue properties to a large extent.

Many sample phantom models have been developed by researchers to mimic human tissues throughout the electromagnetic frequency spectrum [88]. A brief review of some of these efforts are discussed below:

- Guy developed high-water content tissues using a recipe of TX-150, ethylene powder, water and Sodium Chloride (NaCl) [89]. By varying the relative proportions of the contents, the materials could be used from 13.56 to 2450 MHz. Unfortunately, low-water content materials could not be simulated by this technique.

- Bini et. al developed a gel based phantom, comprising polyachrylamide gel as the chief ingredient [90]. Although these materials are optically transparent, having good mechanical properties, they have limited life, and the chemicals are expensive. Also the fabrication procedure is complicated.

- Lagendijk et.al. produced a dough to model low-water content tissues at 451 MHz, consisting of simple products like our, oil and saline [91]. Similar work was done by Robinson et. al. to simulate muscle and fat at 1000 Mhz [92].

- Suroweic et. al. designed a polyachrymide based gel recipe which emulated tissue properties from a wideband of 500 MHz to 3 GHz [93].

- Lazebbnik and Hagness described a new class of oil in gelatin dispersion based material which simulates human tissues over a wide range of microwave frequencies, for both low and high water content materials [94]. The materials required for this solid, heterogeneous phantom are inexpensive and easily obtainable.

Based on the above study, three primary phantom candidates are chosen for this research, each having unique properties. The details of these phantoms are mentioned in Appendix B. Out of many potential phantom recipes, the liquid breast phantom is used in this research [94], as shown in Fig. 5.14(b).

The prime reason for choosing the simple cylindrical phantom is the fact that a 2D slice of a cylinder represents a circle, which in turn represents a breast coronal section, keeping in mind that the algorithm is meant for 2D imaging. Since the 2D TR model is invariant along the z direction, the phantom is chosen to be cylindrical, filled with a breast fatty tissue simulant. A 2D slice of the phantom corresponds to a circular shaped breast coronal section. A PVC tube of outer diameter 10 cm and wall thickness 1.25 cm, height 30 cm and dielectric constant of 3 represents the breast interface. The breast fatty tissue is created by filling the tube with Soybean oil, which is cheap, non-toxic and has electrical properties very close to those of fatty breast tissues (ε_r=2.6, σ=0.05 S/m at 6 GHz) is poured in a PVC cylindrical tube (ε_r=3). It is important to note that although the dielectric properties of the products fall slightly below the expected range for fatty breast tissues, the dielectric contrast between the tissue and tumor simulant is maintained similar to that of an actual tissue. The tumor is constructed using a 35 % dilute diacetin solution (ε_r=8.7, σ=1.9 S/m at 6 GHz). Thus, the dielectric contrast between the tumor and normal tissue is maintained at 3.3:l at 6 GHz. Polyethylene (PE) cylindrical containers of inner diameter 1.2 cm and 0.6 cm and height 30 cm and (ε_r=2.3), is filled with the diacetin solution. It is important to mention again that the height of the breast tissue and tumor is set to 30 cm, in order to make the problem essentially z invariant and hence a 2D problem. The phantom is positioned in place of the target in the previous experiment. The distances between the phantom and the transmitter and receiver antennas are maintained at 1.2 cm and 1 cm respectively, in order to ensure ease of movement. Although a matching medium between the antenna array and breast would couple energy into the breast more efficiently by reducing interface reflections, it is not used in this experiment in order to reduce design complexities. Some benefits of the phantom include stability, low cost, ease of disposal and dielectric contrast. The axially-invariant geometry allows a 2D imaging method.

5.4.3 Experimental results

Initially, the unprocessed time reversed scattered field data are back-propagated in the medium. It is worth mentioning that only the nominal values of the electrical properties of soybean oil are used in the model, with no information on the heterogeneity or frequency dispersion. Several experiments are described next along with TRI results.

5.4.3.1 Single tumor

In the first case, the tumor simulant of radius 1 cm was placed at the center of the tube. The TR energy image in Fig. 5.15(a) shows the energy localized throughout the breast region. The early-time content of the total scattered signals is dominated by reflections from skin, whereas the late-time signal contains tumor backscattered fields and other secondary backscattering. The energy image highlights the entire breast region as an extended scatterer. Since the transmitting antenna is polarized along the vertical axis, the TR image shows the energy focused along the vertical axis direction. Next, the scattered fields from the breast phantom were processed using the signal processing algorithm in order to determine the tumor contributions from the total fields. The time reversed tumor contribution in the receiving antenna array (see Fig. 5.15(b)) is back-propagated numerically. The minimum entropy technique determines the wave focusing instants, as shown in Fig. 5.15(c). Three minimum instants are observed. Time instant A shows the TR wave entering the breast region (Fig. 5.15(d)), while time instant C shows the TR wave exiting from the breast interface (Fig. 5.15(e)). Time instant B shows the TR wave focused near the tumor region, as shown in Fig. 5.15(f). The integrated TR energy shows the wave localized around the tumor

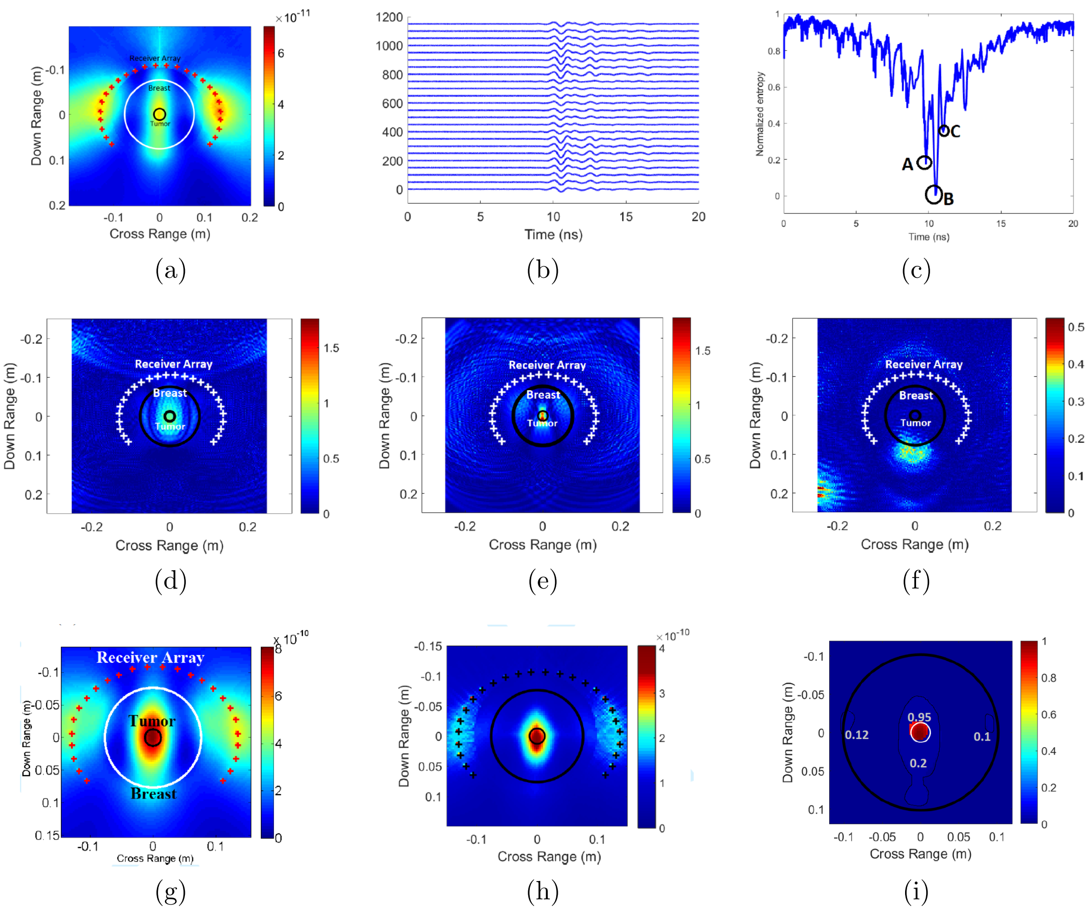

Figure 5.15: Experimental results for breast phantom with a 1 cm radius tumor (a) Energy: raw fields (mE=1.5), (b) Tumor contribution, (c) TR entropy plot, (d) Electric fields at A, (e) Electric fields at B, (f) Electric fields at C, (g) Energy: processed fields, (h) Energy: scattered fields, (i) SAR of processed fields

region, as displayed in Fig. 5.15(g). These results are compared with an idealistic scenario where the exact tumor contribution is known. Total fields scattered by the phantom are measured with the tumor removed from it. The exact tumor contribution was determined by subtracting the total fields with and without tumor. The exact time reversed tumor contribution is back-propagated in the model. The integrated TR energy shows the wave precisely localized inside the tumor (Fig. 5.15(h)). The effectiveness of the signal processing algorithm is clearly demonstrated by the similarity between Fig. 5.15(g) and Fig. 5.15(h). The contour boundaries along with scale values of the TR SAR image (Fig. 5.15(i)) shows

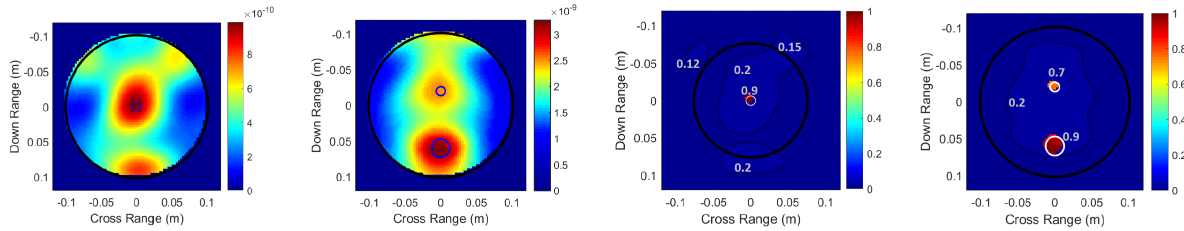

(a) (b) (c) (d)

Figure 5.16: Experimental results for breast phantom with (a,c) a 0.5 cm radius tumor (a) Energy: processed fields, (c) SAR (mSAR=23), (b,d) two tumors (b) Energy: processed fields,(d) SAR (mSAR=20)

that most of the heat is absorbed by the tumor region, with approximately 60% more absorption than surrounding tissues. This demonstrates the possibility of using microwave TR for thermal therapy applications.

A similar procedure was followed for a much smaller tumor of radius 6 mm. The TR energy for this case is focused around the tumor, but has a wider spreading effect. Moreover, a significant fraction of the energy is localized at the breast-skin interface as seen in Fig. 5.16(a). This is a limiting situation for the experiments, and tumors smaller than 5 mm are barely detected by TR. Although the TR SAR image (Fig. 5.16(c)) again shows considerable heat absorbed by the tumor region with approximately 40% more absorption than the surrounding tissues, a portion of the heat is also absorbed by the skin-breast interface as well as surrounding tissues. Thus higher energy might be required to elevate the temperature of the tumor, which might lead to excessive heating of the surrounding tissues. Careful studies need to be conducted to ensure that the surrounding tissues are not affected.

5.4.3.2 Multiple tumors

The capability of the experimental imaging system was also investigated for detection of multiple tumors in the breast region. The two tumor simulants used in the prior cases are placed together in the breast region, with the small tumor placed at the center and the big tumor located closer to the breast wall. The gap between the two tumors is 7 cm, which is approximately 3 times the down-range resolution. The back-propagated integrated energy shows most of the energy focused around the tumor locations, as shown in Fig. 5.16(b). The spreading effect is still observed due to prior mentioned reasons as well as cross coupling between the tumors. More energy is focused at the larger tumor, because of its larger scattering cross-sectional area. The TR SAR image given by Fig. 5.16(d) reveals that most of the heat is absorbed by the tumor region with approximately 50 % more absorption than the surrounding tissues. However, regions close to the tumor are also heated by significant energy absorption.

5.5 Conclusion

A microwave TRI system is proposed for detection of breast tumors. The SAR of the time reversed fields describes the absorption rates of the breast tissues for potential thermal therapy applications. A signal processing algorithm is developed that is capable of extracting the tumor contribution from the total fields, without complete knowledge about the variation of the breast dielectric properties. The capability to detect and localize single and multiple tumor locations without prior knowledge of material randomness demonstrates the robustness of the simulation framework. Precise results and high imaging quality achieved from the simulation studies validate the efficacy of this research. The novel algorithm is combined along with a specifically designed pulsed time domain experimental system for localizing tumors in a liquid breast phantom. Initial results demonstrate the feasibility of the system for imaging breast tissues. The main contributions of this study are the robust signal processing algorithm in the absence of accurate knowledge of tissue variance, a microstrip UWB antenna system for TR, experimental setup, experimental results on a simple breast phantom and data interpretation using the algorithm. The SAR studies reveal much higher absorption rates for tumor tissues than surrounding breast tissues. However, studies need to be performed to evaluate the temperature inside the breast. The authors acknowledge that although the demonstrated experimental results look promising, they represent preliminary, near ideal cases with a lot of scope for future research. As part of future work, experiments with this setup on more realistic breast phantoms with multiple, sub-wavelength sized tumors need to be performed. Also a multiple signal classification system needs to be developed in order to reduce cross-coupling between multiple tumors and account for frequency dispersion of breast tissues to investigate the robustness and super resolution capabilities of the proposed microwave TRM. Finally the increase in breast tissue temperature needs to be calculated from the bio heat transfer equation, as well as measured for gelatin based phantoms, in order to determine the potential of the TRI method for thermal therapy applications.

Chapter 6

Microwave imaging of composites

6.1 Introduction

Composites are being increasingly used to replace metals, partially or completely, in various industries including aerospace, shipping and automotive industries because of their light weight, corrosion resistance and mechanical strength. However, the structural integrity of such composite structures can be severely compromised if there are manufacturing or in sevice defects such as disbonds or impact damage. These factors can significantly affect the strength of the materials and degrade their performance. Hence there is need for detecting these anomalies during manufacturing and maintenance.

Electromagnetic NDE techniques are well suited for dielectric materials such as composites because of the ability of electromagnetic waves to interact with these materials. The scattered field depends on dielectric properties of the medium, and hence provides information about the structural integrity of these materials. While far field electromagnetic inspection systems have the capability of rapid, large area inspection because of large standoff measurement capability, near field techniques enable higher resolution and exact sizing of flaws. Moreover, the wide range of the electromagnetic spectrum provides greater penetration and thus sub-surface flaw detection capabilities using lower frequencies as well as better resolution and thus sub-wavelength flaw detection using higher frequencies. A synergistic integration of far field and near field techniques into a hybrid monitoring system is therefore promising.

This chapter investigates the feasibility using a far field microwave TRM in reflection mode for NDE of composite materials. Reflection mode measurements are crucial in experiments having only single side access to test samples, such as NDE of metal-composite joints, through-the-wall target detection applications, ground penetrating radar and biomedical applications such as breast tumor detection. The modified TR algorithm provides the necessary framework for the 2-D numerical model used for simulations. Scattered electromagnetic fields from composite samples at long distances are received by an antenna array system. Back-propagation of the time reversed fields focuses back at the defect locations. Simulation studies demonstrate the feasibility and robustness of this approach to detect disbonds in metal-composite joints. A pulsed time domain laboratory system coupled with the TR back-propagation simulation model is setup for performing NDE experiments. The system is initially validated using well-defined, prototype defects. Finally experiments are conducted to detect practical defects in real GFRP composite structures such as impact damages. Subsequently, a near field microwave imaging system is set up using near field probes such as open ended waveguides, coaxial tip probe and a VNA. The near field results are utilized as a frame of reference to compare the quality of the far field results. Accurate results achieved with experimental measurements demonstrate the efficacy of the methodology and lay the foundation for a robust microwave imaging system for NDE of composites.

6.2 Composite materials

Composite Materials are manufactured by combining two or more materials with different properties. The two materials work together to give unique properties. Some of them are light, strong and flexible nature, non corrosive and long life. Some of the different type of composites are:

- Natural Composites : Wood, Bone
- Engineered Composites : GFRP, CFRP

Over the past few decades, there has been a significant increase in the use of composite materials to increase the strength of infrastructures in general. Fiber reinforced polymer (FRP) composites are being increasingly used due to their application in the structural rehabilitation of buildings, bridges, etc. and in the defense industry. Research work on using FRP Composites to strengthen structures has been initiated from the late 1980s [95]. Fiber reinforced polymer (FRP) composites are a superior design choice for many applications due to a multitude of benefits they offer over traditional engineering materials. Their light weight, high specific stiffness and strength can significantly increase their performance [96]. Glass fiber Reinforced Polymers (GFRP) have been increasingly used in the aerospace, automobile and civil industries to replace metals, fully or partially (see Fig. 6.1) [97, 98]. Combined with design flexibility and strategic tailoring of mechanical properties, these key advantages propel the wide acceptance of composites in aviation, space, marine, automotive, sporting and construction industries. The use of composites have been rapidly increasing since the last decade. This is particularly true in aerospace applications. For instance, nearly half of the airframe of the Boeing-787 Dreamliner is now created using carbon and glass FRP composites (Fig. 6.1). In structures involving metals and composites, adhesively bonded

(a) Assembly of Boeing-787 [98] (b) Wind turbine blade [97] (c) Assembly of blade

Figure 6.1: Applications of composite materials

joints are now preferred in contrast to conventional fasteners as they provide light weight designs thereby reducing potential stress concentrations. For a good insight into the usage and functioning of these materials, significant research has been done on their quality and long term durability [99].

6.3 NDE of composites

The increasing need and usage of such advanced materials have led to several major challenges regarding their durability and robustness. Composites are prone to several types of flaws both during manufacture and in service use. These include delamination, disbonds, voids, cracks and fiber breakage and foreign objects. An example is the 2001 American Airlines 587 disaster which was caused by a failure in the carbon fiber vertical stabilizer [100]. Although the applications of these materials have been receiving significant attention, methods to monitor their structural health are still a focus of considerable interest. Accurate numerical modeling of different damage modes as well as the theoretical prediction of post-damage residual life is yet to be developed and validated [101]. The elastic nature of FRP composites depends a lot on the mechanical properties of fibers and matrix, the

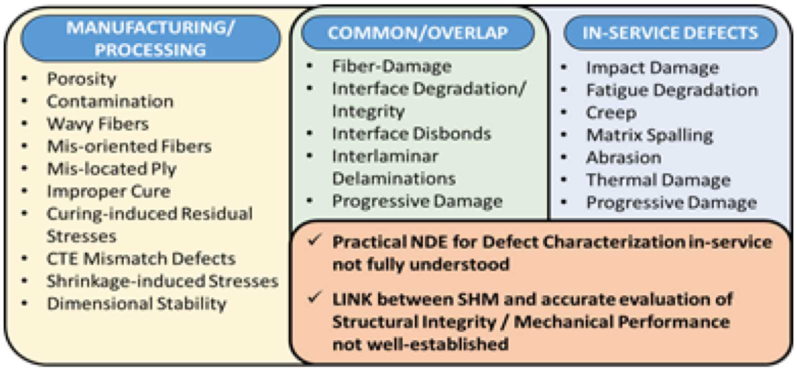

Figure 6.2: Summary of common defects in composites

strategic stacking sequence of layers and selection of weave patterns. Several factors such as anisotropy and differences in material properties at the interlaminar interfaces are a prime reason for many flaws (see Fig. 6.2). Further, FRP composite laminates may be disbonded from the substrate metals due to various issues such as temperature gradients, high stress and use of improper adhesives. Hence, non-destructive evaluation (NDE) is of critical importance to detect defects and evaluate the integrity of structural composites during their service life to ensure their safety of a vehicle and mainly its occupants [99].

Research work on using FRP Composites to strengthen structures has been initiated from the late 1980s. In structures involving metals and composites, adhesively bonded joints are preferred in contrast to conventional fasteners as they provide light weight designs thereby reducing potential stress concentrations. Various types of defects may be formed in the composites such as delamination, voids, cracks and fiber breakage and disbonds [102]. Disbond is defined as a separation between the composite material and the metal structure to which it is adhesively bonded [103]. Disbonds differ from delamination, which refer to similar separation between adjacent layers of the composites. The FRP composite laminates may be disbonded from the substrate metals due to various issues such as exposure to extreme temperature gradients, high stress, improper installation and improper adhesives bonding. Since, often the disbonded region is at the junction between the two materials, a robust and effective nondestructive technique is required to detect potential disbonds.

The most widely used inspection technique is visual testing, which is ineffective in case of buried anomalies that are not visible. Current industrial practice involves well established non-destructive evaluation (NDE) techniques such as ultrasonic inspection with water-coupled and air-coupled transducers, UT phased arrays [104, 105], pulsed flash thermography, X-ray and optical inspection, which furnish precise information about the severity of damage and its location. With the recent advances in sensors, numerical modeling, image processing and material science, a range of NDE techniques spanning the electromagnetic spectrum is growing rapidly. Eddy Current testing, Microwave and X-rays are some of the electromagnetic NDE systems used in industry. Among these methods, Microwave NDE is particularly suited in this application, to detect defects in lossless and low-loss dielectric materials because microwaves have the ability to propagate and penetrate deep into these materials, without suffering much attenuation [106]. The microwave spectrum ranges from 300 MHz to 30 GHz, with wavelengths ranging from 1000 to 10 mm. The scattered field depends on the dielectric properties of the medium, and hence provides information about the structural integrity of these materials [107]. Unlike ultrasound techniques microwave techniques provide a non-contact method and do not require a couplant. Availability of several types of probes and sensors allow large area inspection in an optimal manner.

6.4 Prior work in microwave NDE

Microwave NDE techniques are sensitive to geometrical as well as material properties of the medium. The polarization effects can be utilized to detect defects at certain angles and layers in the material. Some of the applications of microwave NDT techniques are:

- measurement of thickness of coating in layered dielectric composites such as plastic and ceramics [108],
- measure variation of thickness of each layer in dielectric media [107],
- defects such as disbond and void detection in stratified media [109],
- detection of interior flaws, impact damage, fiber misorientation and breakage [110],
- disbond detection in CFRP strengthened cement based structures [106],
- flaw detection in Sprayed on Foam Insulation (SOFI) in space shuttles [111],
- evaluation of moisture content [112], curing in chemically reactive media,
- relating electrical properties to mechanical properties of materials [113],
- surface crack detection or fatigue detection in steel substrates [106].

Also, TR has shown its sensitivity as a potential NDE technique. The ultrasonic TRM is used for focusing on millimeter sized defects beneath plane or curved surfaces of titanium sheets, as well as enhanced inspection of samples with high ultrasonic speckle noise level [114]. The time reversed defect signal was processed using normalized correlation co-efficient and deviation histogram techniques, which distinguishes the defect from speckle noise. Since

TRM contains information on both the defect shape and the medium, it can detect hard-α defects of titanium metal, which are generally difficult to detect because of their low reflectivity and irregular shapes [115]. Although lamb waves are dispersive, time reversal can detect defects in thin plates utilizing lamb waves since it can compensate for dispersion losses. The effect of time reversal using lamb waves to detect flaws is validated with experiments conducted in [116]. Elastic waves have also been back propagated to interact with a circular cylindrical tube using FDTD model to find defects inside a cylinder [117]. Recently, time reversal of microwave fields has been examined for applications such as defect detection and imaging.

6.5 Time reversal algorithm for far field NDE

6.5.1 Theory of TR for NDE

The time reversal algorithm involves back-propagation of the perturbed field in the healthy sample. The perturbed field is the difference between the field scattered by a defective sample and the field scattered by a healthy sample. The back-propagated signal focuses on the defect location since the perturbation field can be thought as the field produced by an equivalent source at the defect location. This is a well known result that can be easily understood by considering two scenarios (Fig. 6.3).

The first scenario involves an incident field impinging on the healthy sample. The second scenario refers to the same incident field impinging on the defective sample. With reference to the first scenario (healthy sample), the total field (φ_0) satisfies:

$$\nabla^2\varphi_0 - \frac{n_0^2(r)}{c^2}\frac{\partial^2\varphi_0}{\partial t^2} = 0 \tag{6.1}$$

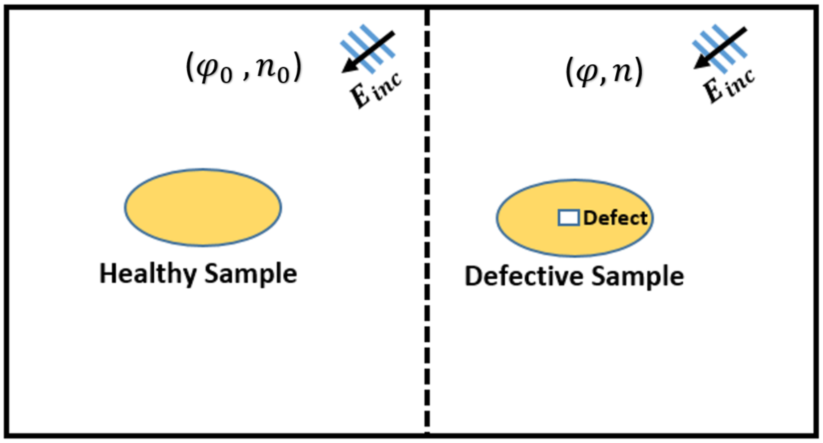

Figure 6.3: Wave incident on healthy and defective samples

where n_0 is the refractive index for the healthy sample. Similarly, the total field φ in the presence of the defective sample satisfies:

$$\nabla^2 \varphi - \frac{n^2(r)}{c^2} \frac{\partial^2 \varphi}{\partial t^2} = 0 \tag{6.2}$$

and, therefore, the perturbed field $\delta\varphi = \varphi - \varphi_0$ satisfies

$$\nabla^2 \delta\varphi - \frac{n_0^2(r)}{c^2} \frac{\partial^2 \delta\varphi}{\partial t^2} = f(r) \frac{n_0^2(r)}{c^2} \frac{\partial^2 \varphi}{\partial t^2} \tag{6.3}$$

where $f = n^2/n_0^2 - 1$. It is worth noting that f is non-vanishing in the region occupied by the defect only. Thus, the perturbation field $\delta\varphi$ can be thought as the field produced by an equivalent source occupying the region of the defect and radiating into the healthy sample. Thus, back-propagating the perturbed field in a defect free sample focuses the waves back to the defect location. This theory forms the basis of the time reversal algorithm depicted in the following sub-section. We stress that the r.h.s. of (6.3) contains the total field at the defect region which is unknown and cannot be measured in a nondestructive manner. Thus (6.3) allows only to understand that the region occupied by the defect is the source for the

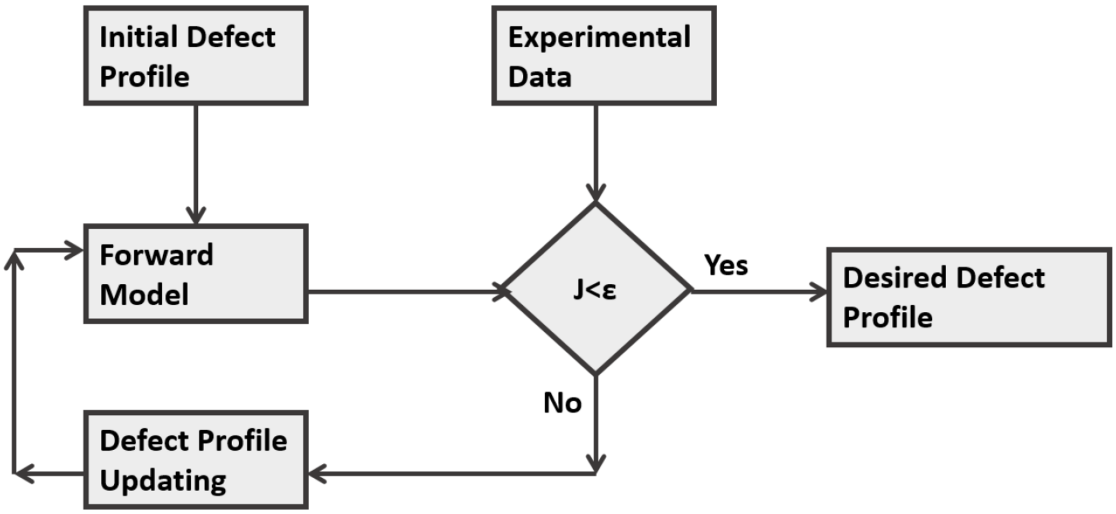

Figure 6.4: Model-based defect imaging : Iterative approach

perturbed field.

6.5.2 NDE algorithm

In NDE problems, generally the inverse problem is an iterative model based approach, where an initial defect profile is assumed, compared with experimental data and iteratively updated, with the objective of minimizing the cost function, as shown in Fig. 6.4. When the achieved cost function is less than a desired threshold value, the desired defect profile is achieved. Such conventional inverse imaging problems based on error minimization to determine location of a target are generally iterative. Such an iterative procedure may have a slow convergence rate and thus can be computationally intensive [16, 17, 5]. As mentioned in Chapter 2, the proposed time reversal algorithm uses a non-iterative approach as shown in Fig. 6.5 leading to reduced computational time.

The basic time reversal process is given by the following steps:

- a short pulse is transmitted from an antenna to the region of interest where the sample

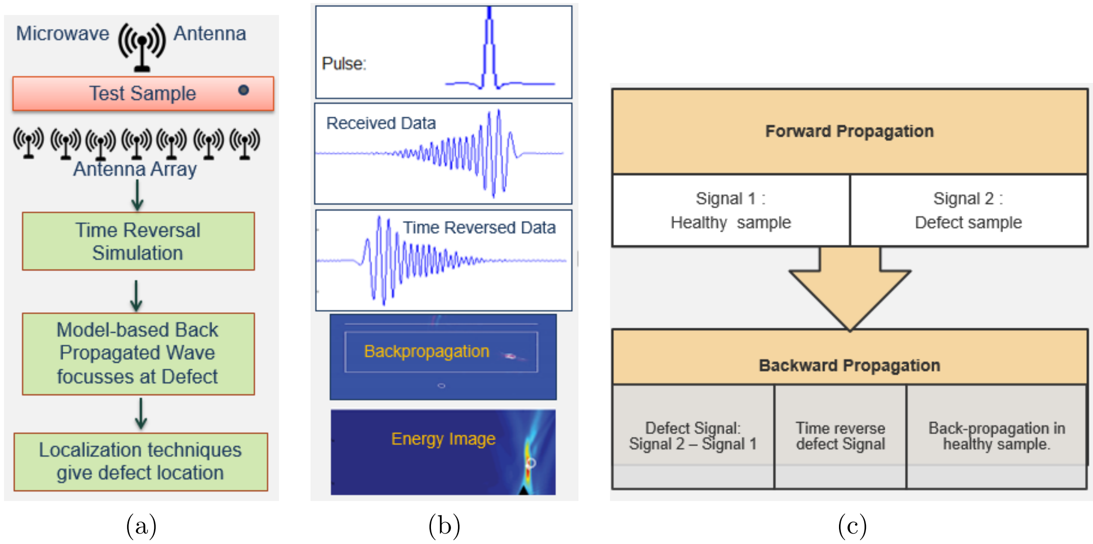

Figure 6.5: Time Reversal for NDE (a) Algorithm, (b) Example (c) TR processing

is positioned;

- scattered signals due to the defective sample and healthy sample are measured by the receivers;
- the two signals are subtracted from each other in order to obtain the perturbation signal;
- a numerical simulations where the perturbation signal waveform is reversed in time and backpropagated to the healthy sample is carried out;
- localization techniques are applied to obtain spatio-temporal focusing.

Since defects behave as secondary sources, TRM can be utilized to detect defects and provide defect locations. For a defect geometry model, exploiting a single excitation source, the scattered electric fields are measured by a receiver array. The defect signal is deducted from the background signal, time reversed and forward propagated again. The model back-propagates the time reversed signal, primarily to the defect location. The peak of the

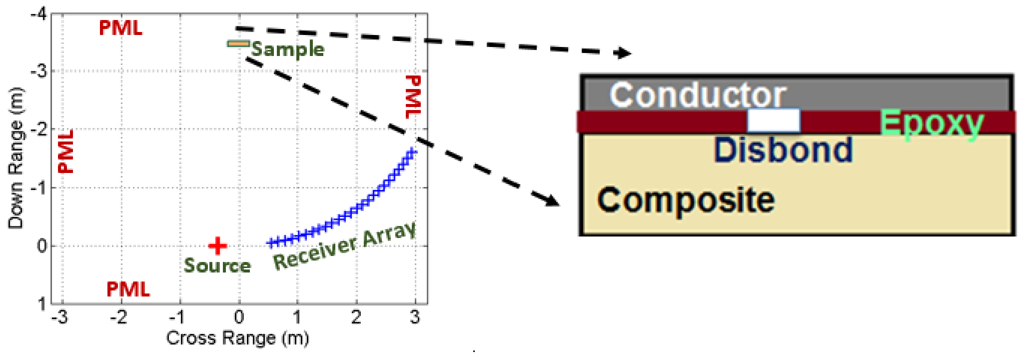

Figure 6.6: Time Reversal Simulation Schematic

integrated energy of the back propagated fields is calculated to obtain the exact defect location. A schematic of the simulation setup for disbond detection in metal composite joints is shown in Fig. 6.6.

6.5.3 Quantitative metrics

In order to evaluate the accuracy and quality of the imaging algorithm, two quantitative metrics are utilized.

- Detection Error: The detection error is defined as the relative difference between the actual and predicted position of the defect ξ_d :

$$\xi_d = \frac{|\rho_m - \rho_a|}{L_a} \tag{6.4}$$

  where ρ_m, ρ_a are the measured and actual positions of the defect, while L_a is the actual size of the defect, selected as the region of interest (ROI).

- Sizing Error: The sizing error is defined as the relative difference between the actual

Table 6.1: Materal Properties

Material	**Relative Permittivity**	**Loss Tangent**	**Spatial dimensions** (m×m)
GFRP	4.6	0.017	3×3
Epoxy	2.8	0.012	3×0.06
Disbond	1	0	0.06×0.06

and predicted size of the defect ξ_s :

$$\xi_s = \frac{|L_m - L_a|}{L_a} \tag{6.5}$$

where L_m and L_a are the measured and actual sizes of the defect.

6.6 Far field simulation studies

The theoretical concepts and numerical model lay the foundation for simulation studies in order to detect disbonds in metal-composite joints. Simulation studies replicating the desired experiments were conducted to understand the feasibility of TR for defect detection. The geometry of the problem consists of a Glass Fiber Reinforced Polymer (GFRP) composite material adhesively bonded to the metal (conductor) by an epoxy layer. Disbonds are modeled as air gaps in the epoxy layer, whose spatial dimensions are of the order of λ. The basic schematic for the simulation is shown in Fig. 6.6. The transmitter is modeled as a point source, and a circular array of sensors is used to collect the back-scattered fields. The material properties and spatial extents of the sample are chosen from [118] and represented in Table 6.1. As mentioned in the time reversal algorithm before, two forward propagation signals (scattered fields) through the healthy and defective samples are obtained, shown in

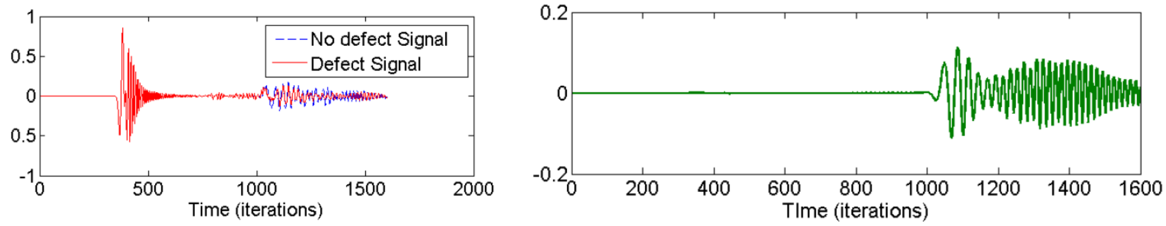

(a) (b)

Figure 6.7: Simulation signals (a) Healthy and unhealthy signals, (b) Defect contribution

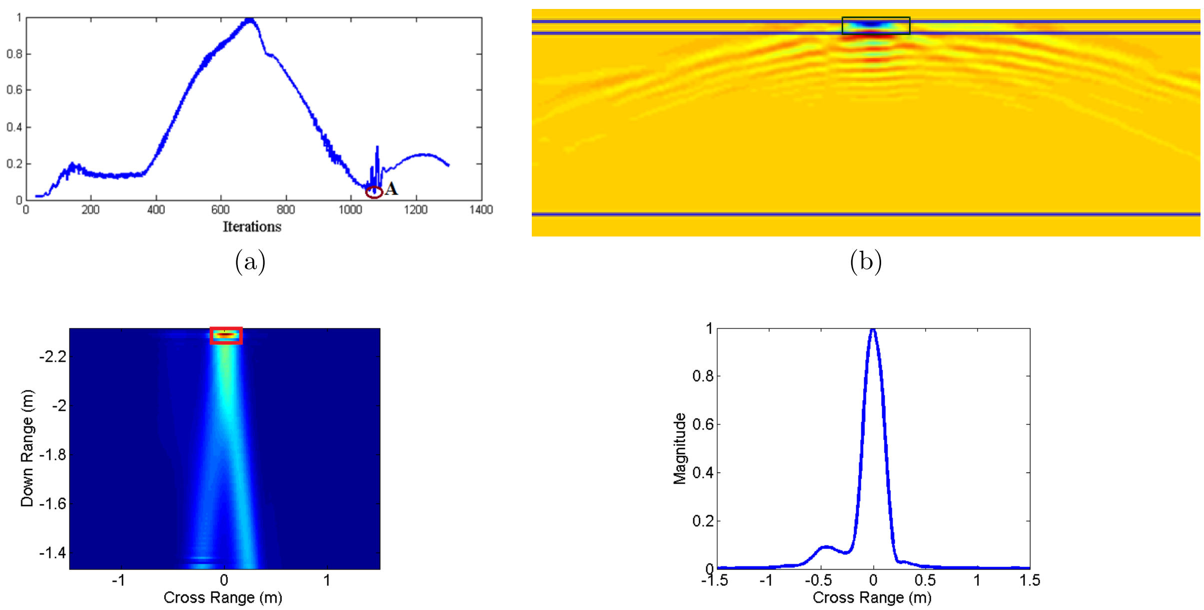

(a) (b)

(c) (d)

Figure 6.8: TR Simulation Results for NDE of composites (a) Entropy plot, (b)Electric fields at minimum entropy instant, (c) Integrated energy image, (d) Cross range signal

Fig. 6.7(a). The two signals are subtracted for each receiver antenna of the array to get the defect contribution only, as shown in Fig. 6.7(b). The time reversed defect signal is back-propagated in a healthy sample using the numerical model.

The spatio-temporal focusing instant A obtained from the entropy localization is shown in Fig.6.8(a). The electric field image corresponding to time instant A shows the localized fields very close to the actual disbond location, as seen in Fig.6.8(b), while the integrated energy image shows the energy localized around the defect location, given by Fig.6.8(c). The row of the energy image corresponding to the peak value is named as the cross range energy signal. Fig.6.8(d) shows that the FWHM of the cross-range signal (6.2 cm) is almost equal to the length of the disbond (6 cm) and hence can be used to determine the spatial dimensions of the defect. Thus, while the minimum entropy criterion is capable of determining the exact focusing instant at which the waves are localized around the target, the integrated energy is capable of providing a focal spot around the target.

6.6.1 Multiple defects

The time reversal algorithm demonstrates its ability to focus on multiple disbonds present in the epoxy layer. Fig. 6.9 (a) shows the time reversed energy image for a sample with two disbonds of equal size (size=$\lambda/2$). The back-propagated wave focuses equally at the two disbond locations, since equal fields are scattered by both disbonds. Thus, the energy image shows two sharp peaks at the disbond locations. The error between the actual and measured disbond locations is about 2%. However, when one disbond is significantly bigger than the other, the time reversed wave is more focused on the bigger disbond. 6.9 (b) shows the time reversed energy image for two defects, one three times bigger (size=$3\lambda/2$) than the other defect (size=$\lambda/2$). Most of the TR energy is focused around the bigger disbond,

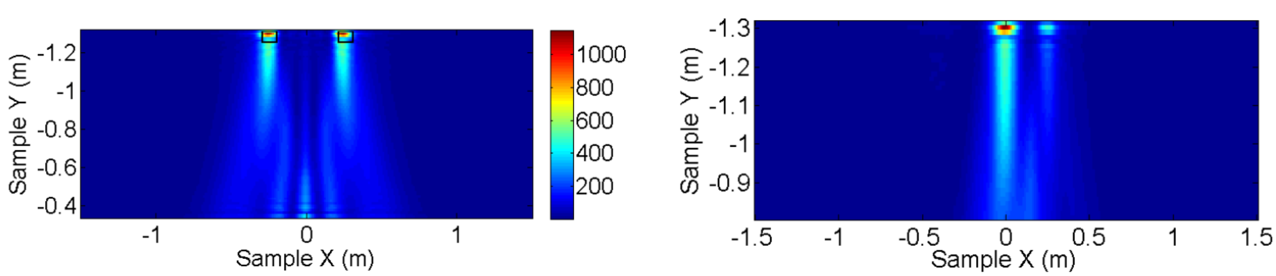

(a) (b)

Figure 6.9: TR images for multiple defects (a) Equal disbonds, (b) Unequal disbonds

while relatively less energy is focused around the smaller defect. Advanced signal processing techniques based on time reversal can be utilized to selectively focus closely spaced defects, and will be investigated in the future.

6.6.2 Extended defects

One of the unique properties of this algorithm is its ability to estimate the length of extended disbonds in the metal-composite joint. From the one dimensional scan of the integrated energy image, the peak value gives the location of the defect (Fig. 6.10). Moreover, we can also predict the length of the disbond as the FWHM distance of the cross range signal (Fig.

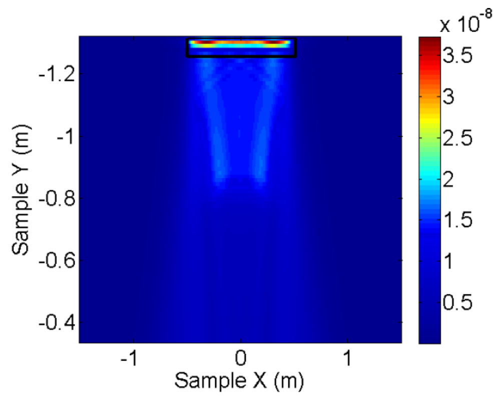

Figure 6.10: Energy image for extended disbond

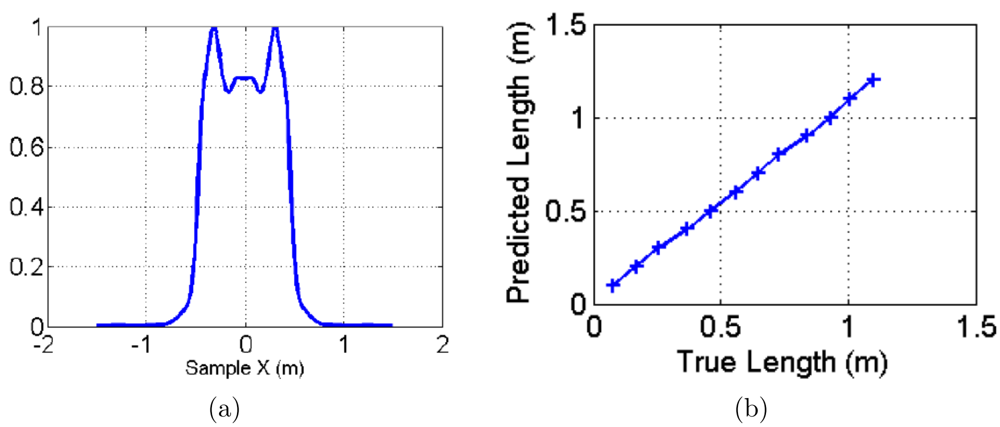

Figure 6.11: Extended disbonds: (a) Disbond signal, (b)Estimation accuracy

6.11(a)). The predicted length has been plotted with respect to the actual defect lengths, varying from 0.15m to 1.2m in Fig. 6.11(b). The disbond length has been predicted with an accuracy of around 92%.

6.6.3 Noise injection

The robustness of the time reversal algorithm has been demonstrated by adding noise to the received signals. AWGN with SNR of 5 dB, shown in Fig. 6.12(a) is added to the individual receiver antenna signals. The back propagated noisy time-reversed fields show good defect focusing ability. Since, the phase difference between the relative array elements are not hampered by addition of uncorrelated noise, time reversal focusing is achieved efficiently, even for very low signal to noise ratios. Fig. 6.12 (b) shows that the integrated energy image of the composite sample still highlights the disbond location.

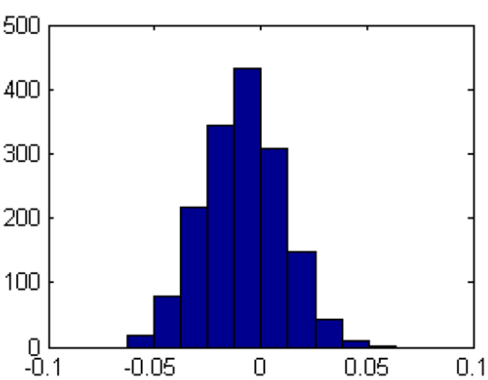

(a)

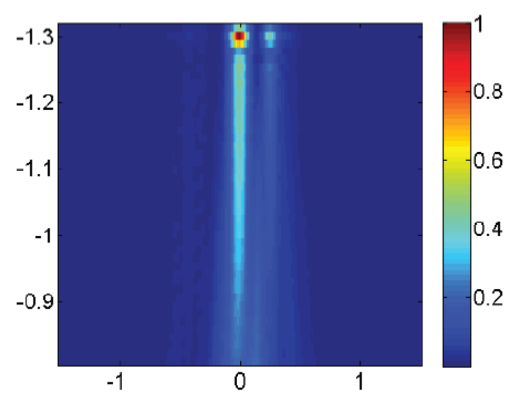

(b)

Figure 6.12: TR imaging in presence of noise (a) AWGN distribution used as noise for time reversal with SNR 5 dB, (b) Noisy TR image

6.7 Parametric analysis

A parametric analysis of the TR method is performed in order to properly estimate the limits of the model based method. The minimum value of the parameters obtained from these studies is then utilized in the experimental setup.

6.7.1 Defect size

A parametric study and analysis of the length of the disbond is described in this section with respect to the resolution of time reversed signal. Since the electrical properties of a disbond (air) are much different from that of the surrounding materials, it scatters the electromagnetic fields, behaving as a secondary source. Thus, subtracting the effect of the primary source, the defects behave as the primary contributing energy source. Bigger disbonds scatter more fields and thus behave as a stronger source of energy. Hence the maximum TR energy at the defect increases as its length increases. This observation is plotted in Fig 6.13 (a). The focal spot determines the minimum size of the defect ($\lambda/2$), that can be detected. The minimum disbond length that can be detected is 2 cm (0.13λ).

6.7.2 Receiver array aperture

A parametric analysis of the total number of sensor elements and the effective length (aperture) of the receiving antenna array is examined. Theoretically, as the length of the receiving antenna array, as well as the number of individual elements are increased, more detailed information on the reflected and scattered fields is known,leading to higher lateral resolution of the resultant image. This results in better focusing and higher energy at the defect location. Thus the TR energy peak at the defect location increases as the length and the number of

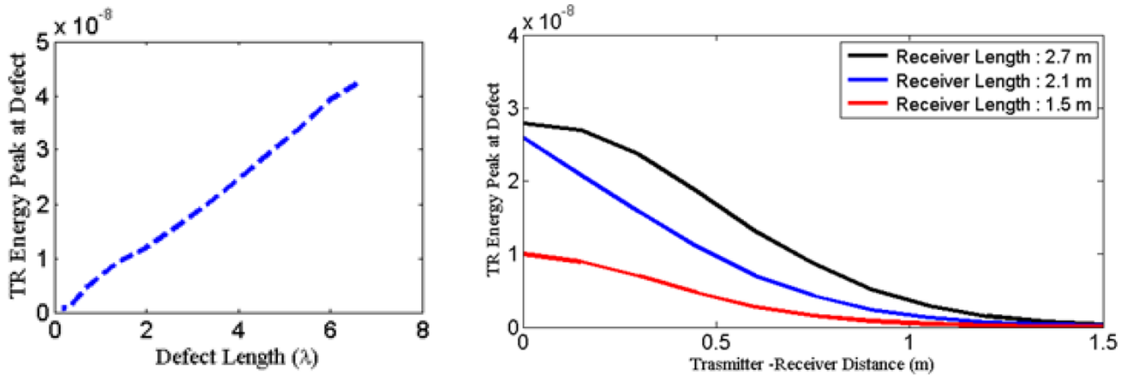

(a) (b)

Figure 6.13: Parametric analysis (a) TR peak with defect size, (b) TR peak with receiver aperture

array elements of the receiver is increased.

Simulation results in Fig 6.13 (b) depict that the lateral resolution is increased, when the effective aperture of the antenna and the number of array elements of the receiver are increased. However, with limited aperture and less sensors, the TR method is still able to image the defect location. From the simulation studies, we can conclude that a minimum of 10 sensors are required to find the true location of the defect.

6.7.3 Transmit-receive distance

An important contributing factor determining the feasibility of the method is the distance between the transmitter and the receiver array. A parametric study of the separation distance was conducted, for different aperture lengths of the receiver array. We vary the transmit-receive distance of 0 to 10 λ. We observe that as we increase the distance, the intensity of the TR energy peak decreases. However, even at a separation of 10 λ, the method is able to detect the disbonds. Thus, this method can be potentially used as a far-field imaging technique for defect detection. Fig 6.13 (b) shows the variation of energy with the separation distance, for different antenna apertures.

6.8 Experimental analysis

A far-field passive time reversal system is set up for conducting NDE experiments in reflection mode. The system comprises the previously described time domain laboratory setup, coupled with the TR back-propagation code. The experimental system is initially validated by imaging well defined defects in calibration standard samples. Finally, the system is utilized for imaging practical defects in GFRP composite samples. Scattered fields from the test samples are recorded by the receiver horn antenna array and back-propagated in the time-reversal simulation model. Background clutter is reduced by measuring the background signal without the presence of a sample and, subsequently, subtracting it from the perturbed field signal. Localization techniques have been utilized to obtain precise spatio-temporal focusing. Four different experimental scenarios are outlined in Table 6.2, and corresponding results are presented in the following sections.

6.8.1 Far field experimental setup

The experimental configuration is shown schematically in Fig. 6.14 and explained in detail in Chapter 3. The samples are positioned at the center of the arch range, where the beam of the transmitting antenna is focused. The center of the frequency spectrum is 10 GHz with corresponding wavelength (λ) of 0.03 m. A photograph of the experimental setup with the sample placed at the center of the arch-range has been shown in Fig. 6.15.

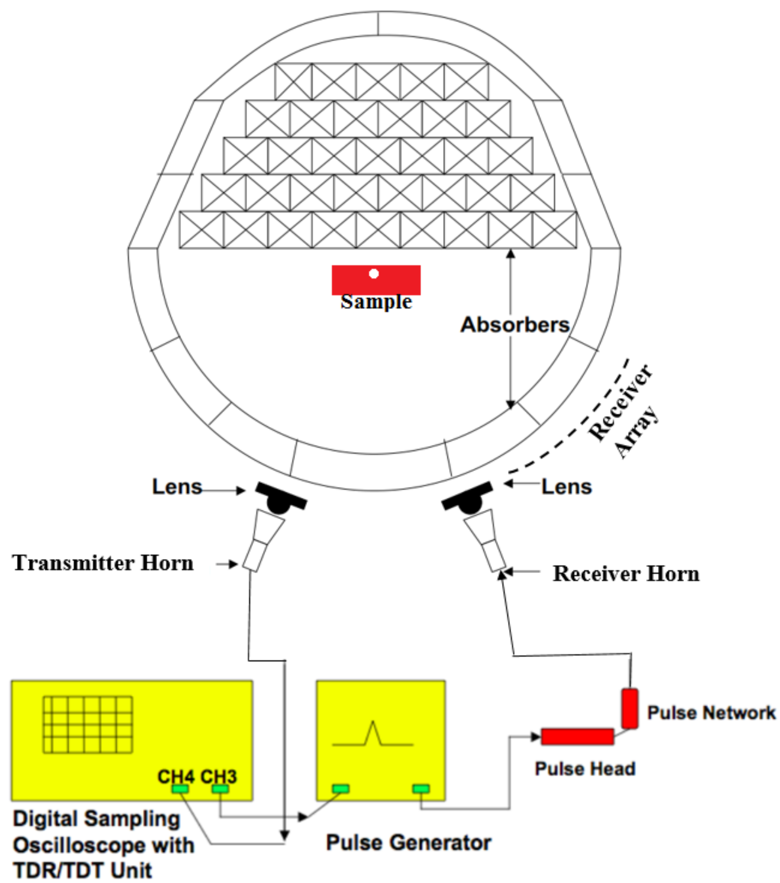

Figure 6.14: Experimental schematic

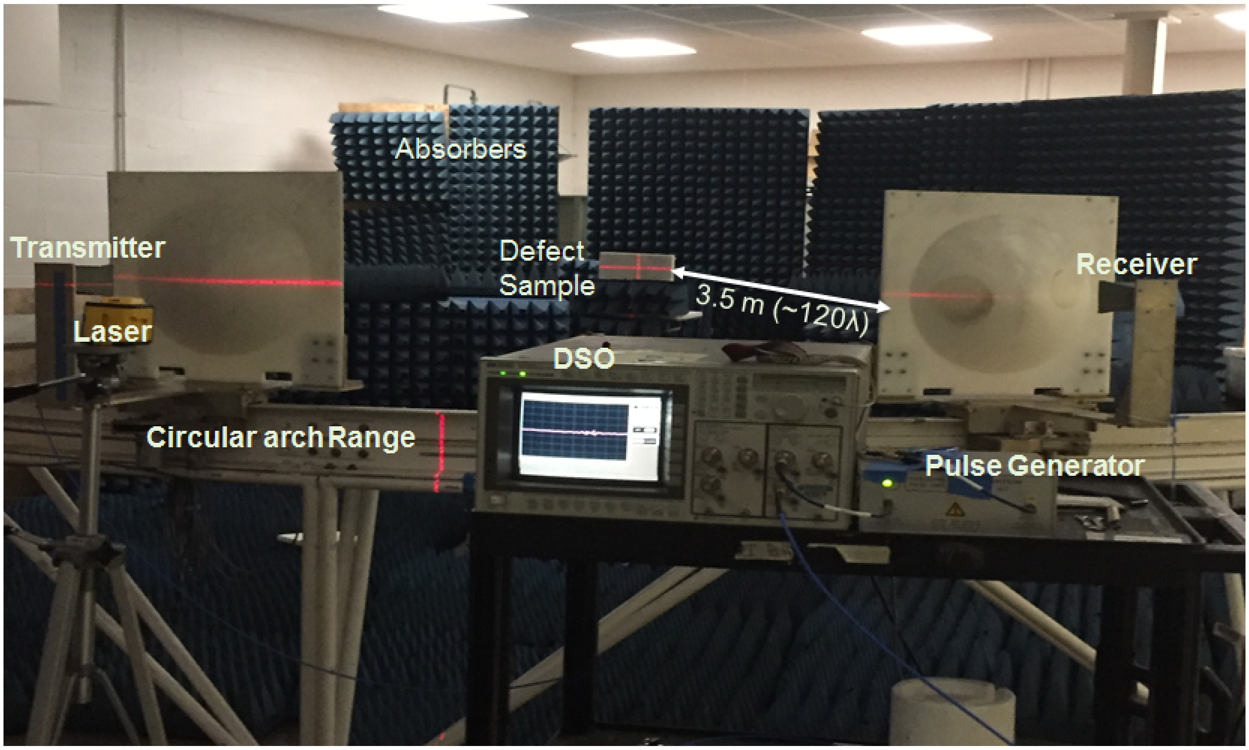

Figure 6.15: Far field experimental setup

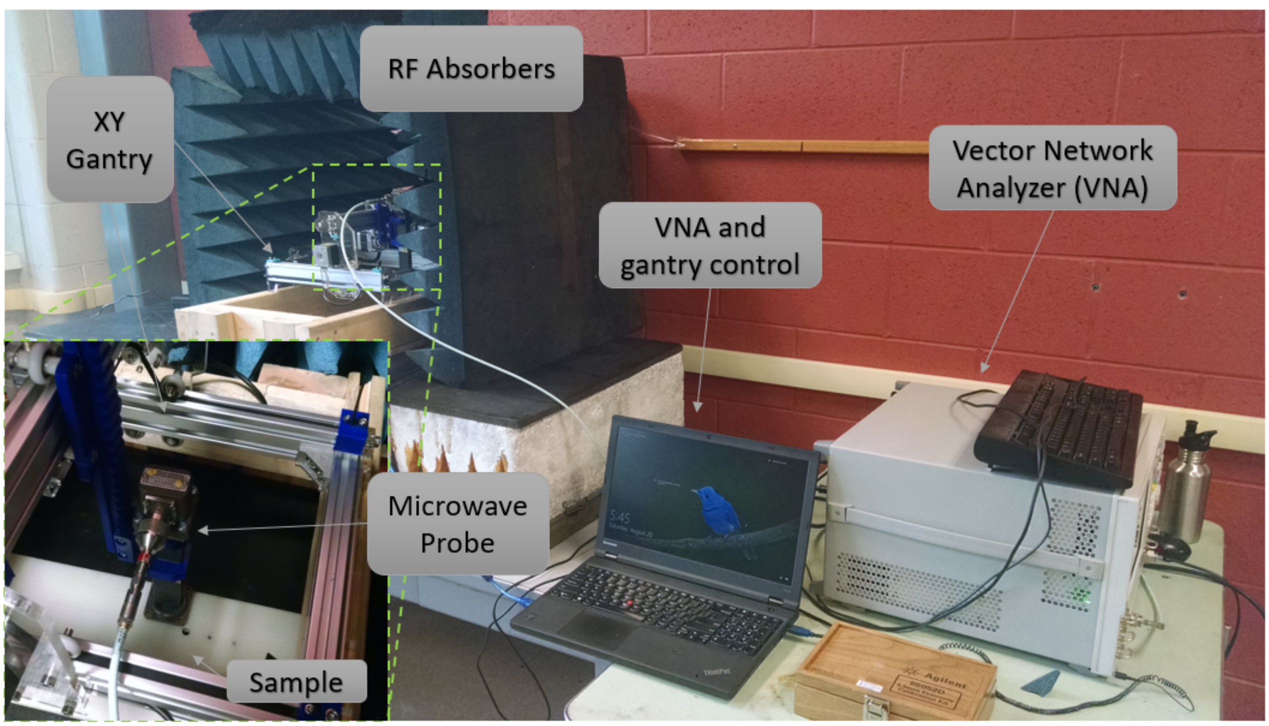

Figure 6.16: Near field experimental setup

6.8.2 Near field experimental setup

The near field experimental system is set up using a a E5070B Vector Network Analyzer (VNA), coupled to a X-Y scanning platform. An in house C sharp code is used to control the VNA, X-Y gantry and collect the data [119]. The experimental setup is shown in Fig. 6.16. Some of the conventional probes used in near field microwave imaging are aperture in waveguide, scanning tunneling microscopy (STM), atomic force microscopy (AFM), and open ended transmission line [16][20]. These probes have been extensively studied by researchers and used in several industrial applications.Two different probes are used as the microwave probe, an X-band (8-12 GHz) waveguide feed and a standard RG58 coaxial cable with an extended metallic tip. The VNA is calibrated at the end of the cable where it connects to the probe. The results obtained from the near field imaging system are used as a frame of reference for correlating the imaging quality of the far field experiments.

6.8.2.1 Open ended waveguide probe

An X-band open ended waveguide feed is chosen as a near field probe. The open ended waveguide has been previously used for inspecting composite structures. A lot of research has focused on determining the near field radiation pattern and gain of the open ended waveguide. The far-field E-plane pattern ($E_E(\theta)$) can be accurately predicted using the Stratton-Chu formula and integrating over the aperture of the waveguide.

$$E_E(\theta) = A_E \frac{1 + (\beta/k)cos\theta + \tau(1-\beta/k)cos\theta}{1 + (\beta/k)cos\theta + \tau(1-\beta/k)} \times \frac{sin[kb/2sin\theta]}{kb/2sin\theta} \tag{6.6}$$

where a, b are the waveguide aperture dimensions, τ is the reflection coefficient, A_E is the constant which is related to the field amplitude and the normalized propagation constant β/k

is given by $\sqrt{1-(\frac{\pi}{ka})^2}$. The open ended waveguide is simulated using HFSS to understand its sensitivity and performance as shown in Figs. 6.17. Fig. 6.17 (a) presents the magnitude of the simulated radiated electric fields in the E-plane at f_r. The simulated E, H plane far field radiation patterns of the open ended waveguide probe are shown in Fig. 6.17 (b). They show nice end-fire radiation property with a peak gain of 6.5 dB and low back-lobes at 8, 10 and 12 GHz. The efficient radiation property of the antenna can be used for detection of targets placed far away from the probe. The near field radiation pattern of the probe is plotted as a function of the distance from the apex of the probe. As seen from Figs. 6.17(c), the fields are maximum close to the aperture, but decays for increased lift-off distances (~5 dB for 15 mm). The reflection coefficients of the waveguide probe varies due to perturbation in electromagnetic fields due to the presence of a metallic target of varying sizes placed 5 mm away from the aperture, as shown in Fig. 6.17 (d). Another simulation is conducted with the probe placed 2 mm away from a GFRP composite sample with a 1 mm circular hole defect. The effect of the defect on the reflection coefficients is shown in Fig. 6.17(e).

6.8.2.2 Extended coaxial probe

An open ended coaxial probe with an extended copper tip, operating at a narrow band frequency of around 7 GHz (l= 42.8 mm). A standard RG58 coaxial cable is used to fabricate the probe. The outer copper section along with the dielectric enclosure is removed to create an extended copper tip, as shown in Fig. 6.18(a). Since the impedance of the coaxial probe is matched to 50W, no additional matching circuits are required. Electromagnetic fields radiate out from the extended tip of the coaxial probe, with monopole antenna like radiation pattern. The resonant frequency of the probe is determined by the length of the extension, similar to a quarter wave monopole. Increasing the length of extension decreases the resonant

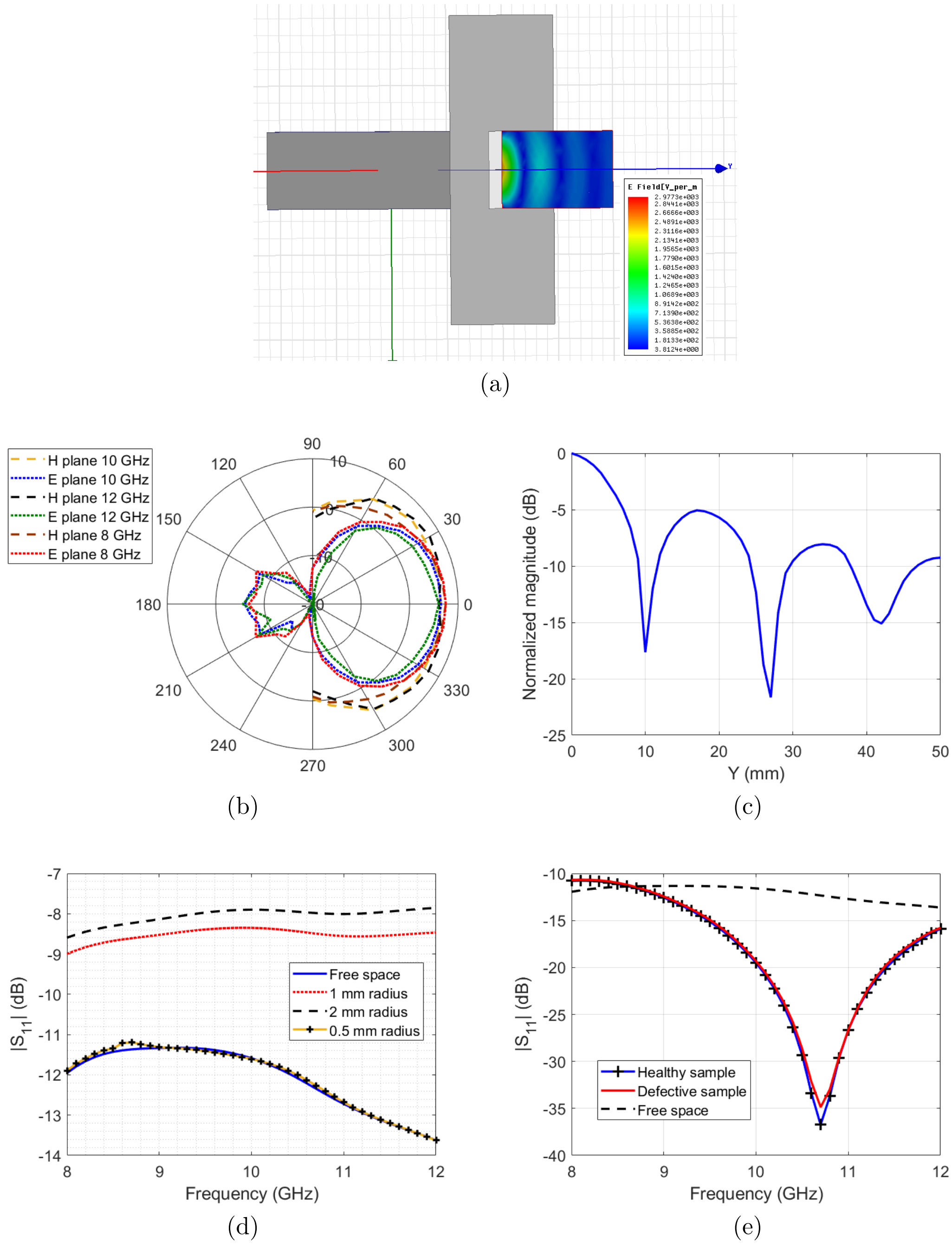

Figure 6.17: Open ended waveguide simulation results (a) Cross section of radiated near E field at 10 GHz, (b) Radiation pattern of the probe, (c) Near E field radiation pattern of the probe, (d) Reflection coefficients for the probe in presence of circular metal targets of different radius, (e) Reflection coefficients for the probe in presence of healthy and defective samples

frequency of the probe, as shown in Fig. 6.18(b). The coaxial probe provides a wider band of operating frequencies and also eliminates the requirement of matching circuit. The reflection coefficients of the coaxial probe is affected by the perturbation in electromagnetic fields due to the presence of a target or a defect inside a sample. A simulation is conducted with the coaxial probe placed 0.5 mm away from a GFRP composite sample with a 2 mm circular hole defect. The effect of the defect on reflection coefficients is shown in Fig. 6.18(c). The measured reflection coefficient shows the resonant frequency at 7.8 GHz, as seen in Fig. 6.18(d). The radial component near E-field of the monopole antenna can be expressed as [120]:

$$E_r = -j\eta \frac{(I_0 l e^{-jkr})}{(2\pi k r^3)} cos\theta, \tag{6.7}$$

where I_0 is the current, l is length of the antenna, η is intrinsic impedance of the medium and k is the wave number. The simulated far field radiation pattern shows monopole like radiation with nulls at the center for E plane and omni directional radiation in H plane at f_r. The field decays very fast ($O(1/r^3)$ and is a function of the wavelength ($\lambda = 2\pi/k$), antenna length (l) and η. Higher frequency provides finer resolution, at the expense of reducing the near field range ($R = 0.62\sqrt{D^3/\lambda}$, D is the maximum overall antenna dimension) and thus requiring smaller lift-off distances. Fig. 6.18(e) presents the magnitude of the simulated radiated electric fields in the E-plane at f_r. As seen from Figs. 6.18(e, f), the fields are maximum at the center, but decays rapidly for increased lift-off distances ($\sim$15 dB for 4 mm). This is because the lift-off distance has a significant impact on capacitive coupling between the probe and the sample. Thus, the choice of frequency is based on a trade-off between resolution and lift-off distance. The near field radiation pattern for the probe was computed using HFSS at different distances from the apex of the antenna and these results

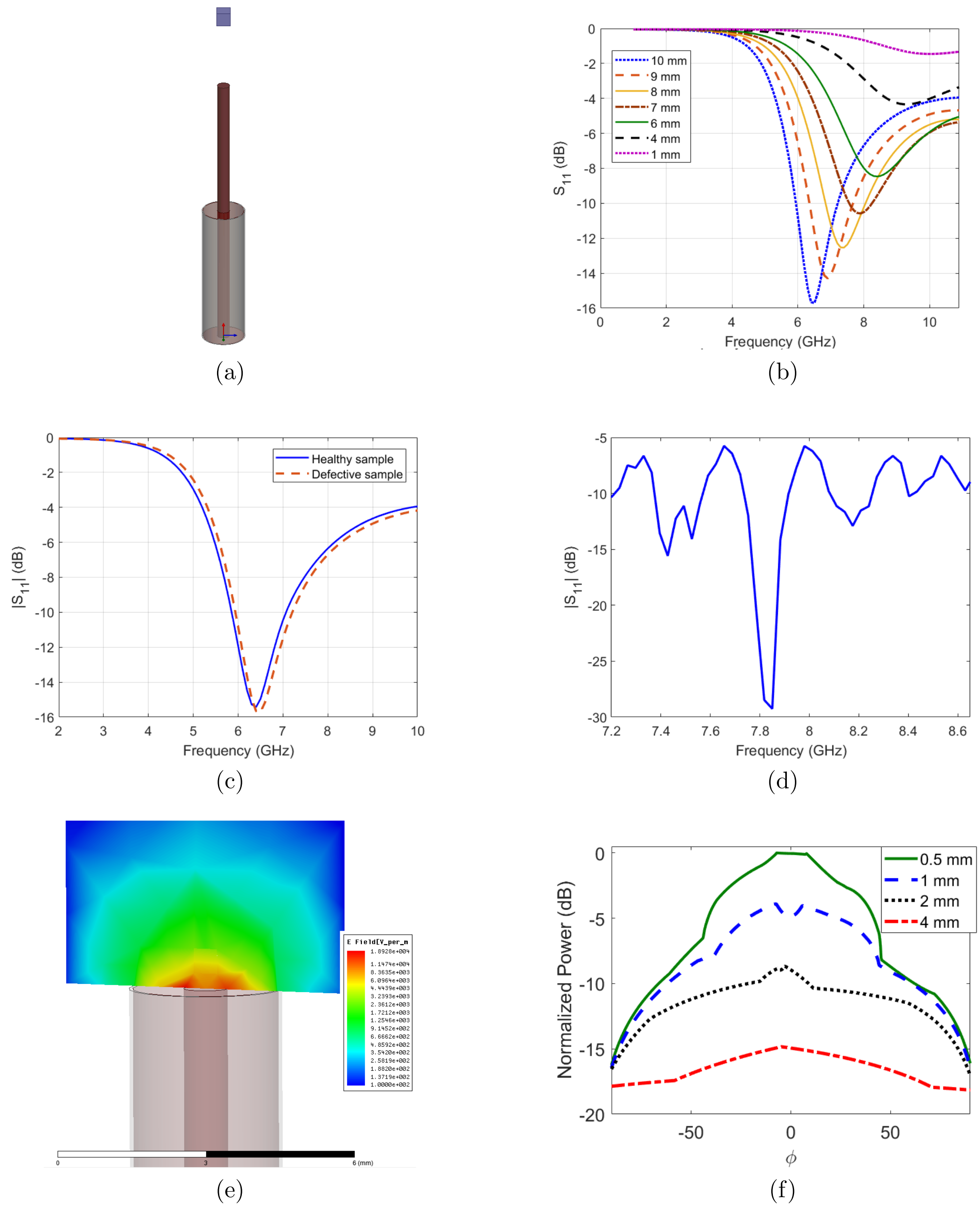

Figure 6.18: Coaxial probe results (a) Probe, (b) Simulated reflection coefficients for the coaxial probe with varying tip extensions, (c) Simulated reflection coefficients for the coaxial probe with varying tip extensions, (d) Measured reflection coefficients for the coaxial probe, (e) Cross section of radiated near E field, (f) Near E field radiation pattern of the probe

are shown in Fig. 6.18 (f). In accordance with (6.7) it is observed from Fig. 6.18(f) that the field decays as a rate of $(O(1/r^3)$ where r is the distance from the probe.

Table 6.2: Experiments

Case	Sample	Sample size (mm)	Defect	Defect size (mm)
I	Metal-composite	150×150	Disbond	30×10
II	Metal-composite	150×150	Disbond	30×10
III	GFRP	150×150	3 Drilled Holes	4,2,1
IV	GFRP	150×150	Impact Damage	20

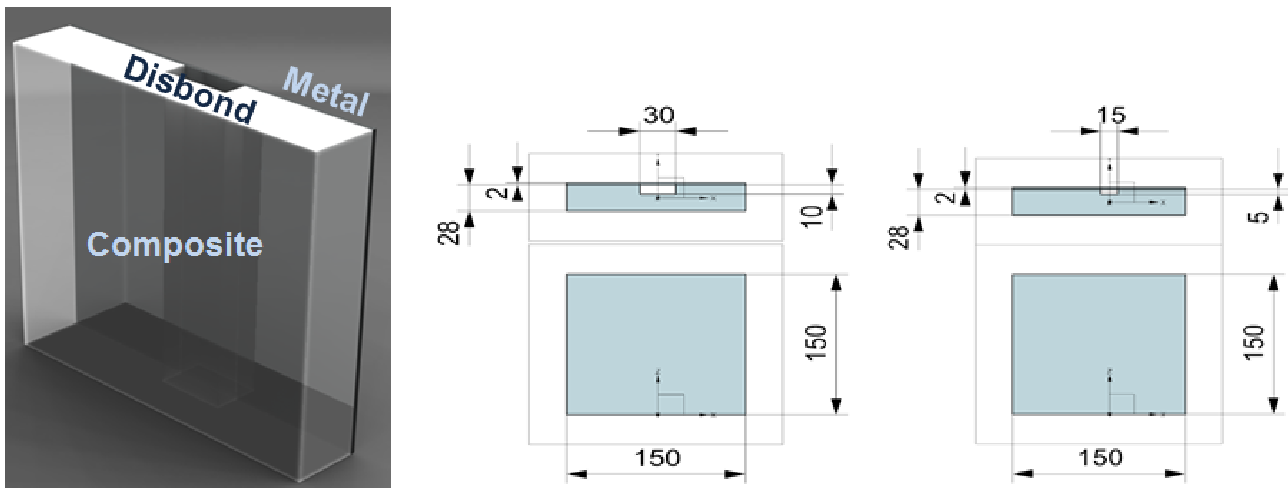

(a) (b) (c)

Figure 6.19: Prototype samples: (a) Prototype sample schematic, (b) Sample I dimensions, (c) Sample II dimensions

6.8.3 Experimental results

6.8.3.1 Prototype samples: I, II

The passive TR imaging system was validated using two simulated metal-composite joint samples [121]. The samples were composed of Teflon square block of dimensions 150×150 mm^2 and thickness 28 mm, bonded to a aluminum sheet of thickness 2 mm by Teflon bolts at the edges. Teflon has a dielectric constant ($\epsilon_r = 2.1$) and is almost lossless ($\tan\delta = 0.00028$). The sample geometry along with its dimensions are shown in Fig. 6.19. For ease of fabrication of the disbond, instead of creating air voids in an epoxy layer bonding the metal and composite, a groove was machined int eh teflon layer at the metal-composite interface.

The groove is designed to be running down the entire length so that:

- The defect is invariant along the out of plane direction. Since the back-propagation model uses a 2-D model, the sample closely resembles a 2-D metal-composite plane with a disbond, as shown in the top view of Fig. 6.19.

- The incident field from the TEM horn antenna is vertically polarized. This corresponds to a TMz mode for a 2-D case ($E_x, E_y = 0$), similar to the incident field used for simulations.

- The setup mimics the simulation schematic and thus serves as a good validation case.

In order to test the detection capability of the system, two samples of varying defect dimensions are used in this study (listed in Table 6.2). The first defect dimensions (Sample I) are $\lambda \times (\lambda/3)$, thus corresponding to a well resolved defect in both axes. However, the second defect dimensions (Sample II) are $(\lambda/2) \times (\lambda/6)$, corresponding to a defect with dimensions below the resolution limit in one axes. An identical healthy sample without the presence of the disbond was also used for obtaining the healthy signal.

The scattered fields due to the defective and healthy samples are recorded by the receiver horn antenna array, and used in the time reversal algorithm. Visualization of the TR fields show the wave focused at the defect in both cases. The focusing instants can be obtained from the entropy method, as shown in Fig.s 6.20(a) and 6.20(b). The integrated energy image shows the energy focused around the disbond in both cases, as shown in Fig.s 6.20(c) and 6.20(d). The full width at half maximum (FWHM) of the cross range signals (29.2 mm, 14.5 mm) is almost equal to the width of the defects (30 mm, 15 mm), as shown in Fig.s 6.20(e) and 6.20(f). Thus the defect dimensions and the focusing instants can be accurately estimated using the TR system. The near field imaging results presented in

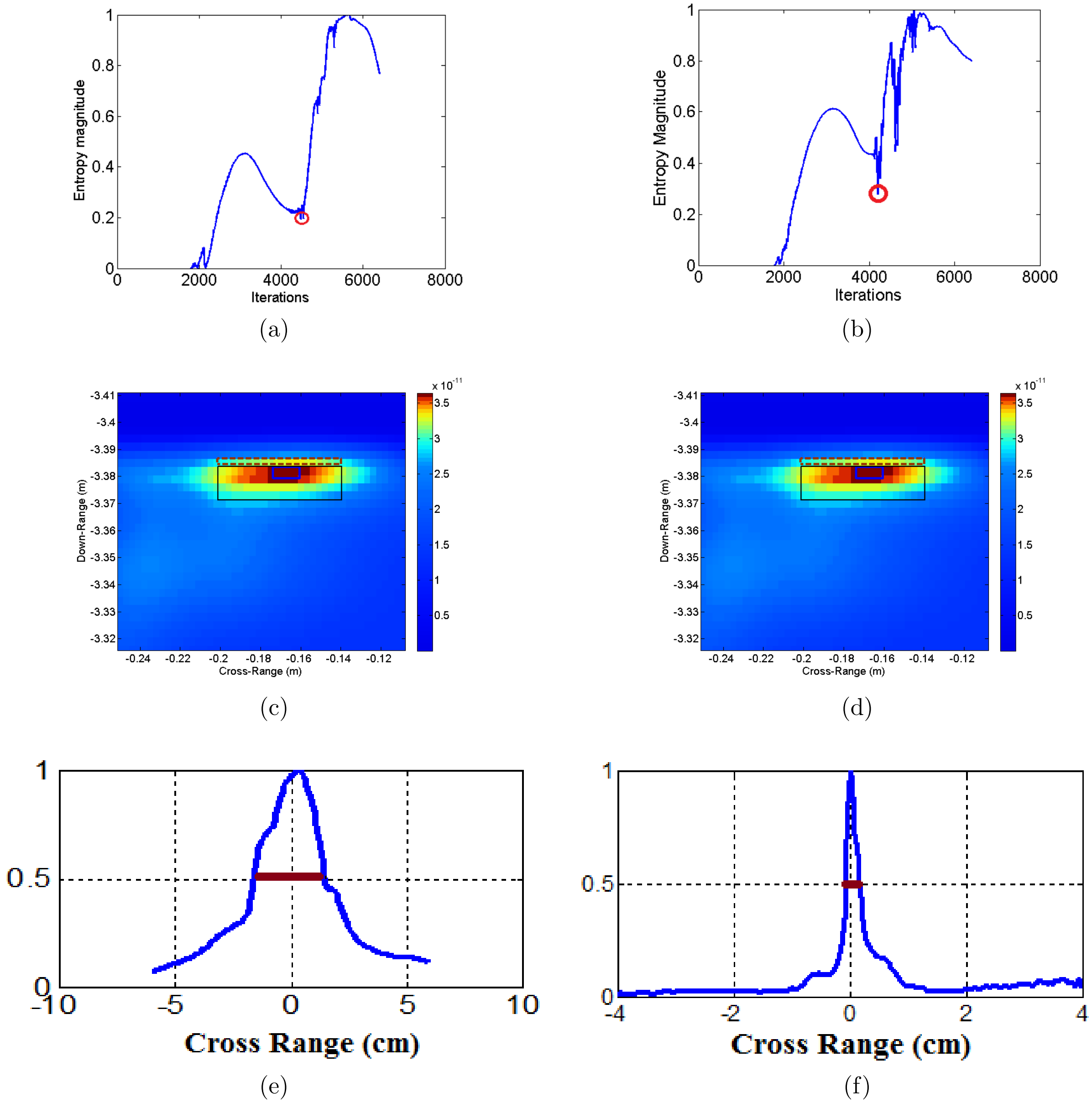

Figure 6.20: TR experimental results: prototype sample (a) Entropy: Sample I, (b) Entropy: Sample II, (c) Energy: Sample I, (d) Energy: Sample II, (e) Cross Range Signal : Sample I, (f) Cross Range Signal : Sample II

Figs. 6.21 (a) and 6.21 (c) clearly show good correlation between the magnitude of reflection coefficient and the defect extents. Fig. 6.21 (b) and 6.21 (d) also show the distinct change in phase of the complex reflection coefficient at the defect edges demonstrating the feasibility of near field microwave measurements for defect detection.

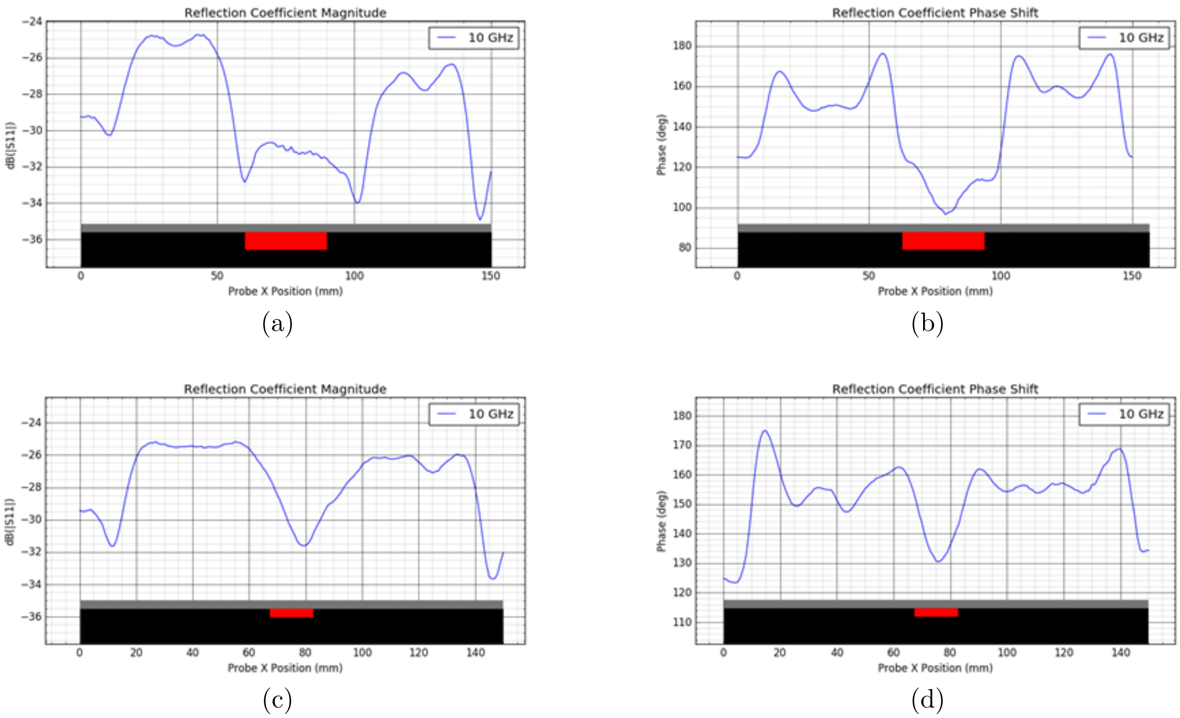

Figure 6.21: Near field experimental results: prototype sample (a) Magnitude 10 GHz: Sample I, (b) Phase 10 GHz: Sample I, (c) Magnitude 10 GHz: Sample II, (d) Phase 10 GHz: Sample II

6.8.3.2 Real composite samples: III, IV

Once the system is validated, it is utilized for imaging damage modes in real composite samples. The composite samples were fabricated at the MSU Composite Vehicle Research Center (CVRC). In this study, the vacuum assisted resin infusion technique was used to manufacture a glass fiber reinforced polymer (GFRP) laminate (fibers woven at 0°and 90°). The reinforcement was S2-glass plain weave fabric (Owens Corning ShieldStrand S) with areal weight of 818 g/m^2. The resin used was a two part toughened epoxy, namely SC-15 (Applied Poleramics Inc., CA). The laminates were cured in a convection oven at 60°C for 2 hours followed by a post cure of 4 hours at 94°C. The laminate coupons were cut by water cooled, diamond coated-disc cutting machine to achieve a final dimension. Two different

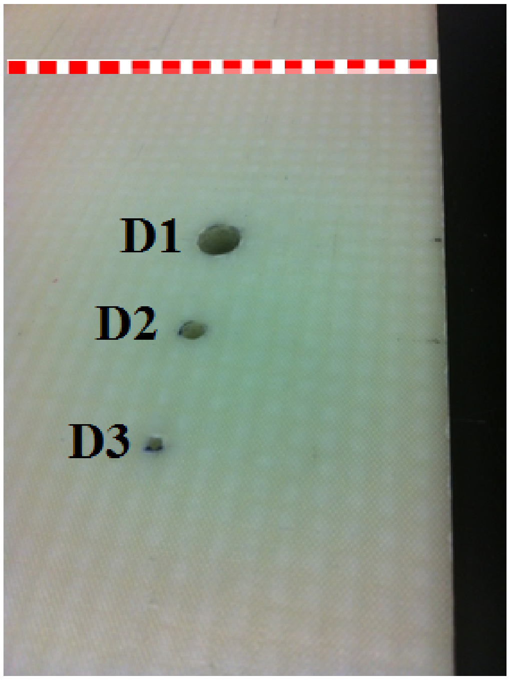

(a)

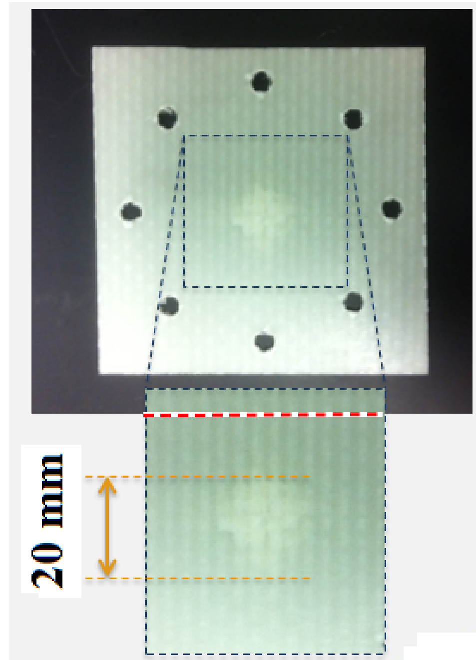

(b)

Figure 6.22: Real GFRP sample damage modes (Red dashed lines indicate the healthy region of the samples) (a) Drilled holes, (b) Impact damage

damage modes were investigated in this research. The first sample was a sixteen layer cured and laminated with a thickness of 9 mm. The defect consisted of 3 through wall drilled holes of radius 4 mm (D1), 2 mm (D2), and 1 mm (D3), separated from each other by an inch. Carbide-tip drills were used to create the holes. Theoretically, the 4 mm radius hole is within the diffraction limit for detection in the far field, but the other two holes are beyond diffraction limits. The second sample was a four layer cured laminated with a thickness of 2.8 mm with an impact damage, having a length of approximately 20 mm. A drop-weight impact test was performed using a 12.5 mm (1/2 inch) tip (impactor), with 20 J energy to create the impact damage. The two samples are shown in Fig. 6.22.

The healthy region of the samples (shown in Fig. 6.22) were used to obtain the signal corresponding to the healthy sample.

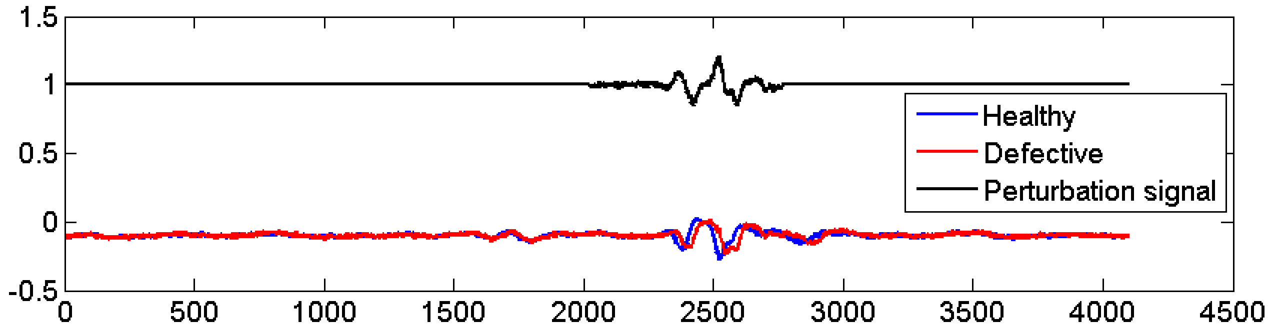

Figure 6.23: Experimental signals of one receiver element for Sample III

- Drilled holes : The two signals corresponding to the healthy and defective samples and the perturbation signal for a single receiver element are shown in Fig. 6.23. The perturbation fields for the receiver array were back-propagated in the TR simulation mode to image the sample, with the results shown in Fig. 6.24. The integrated energy

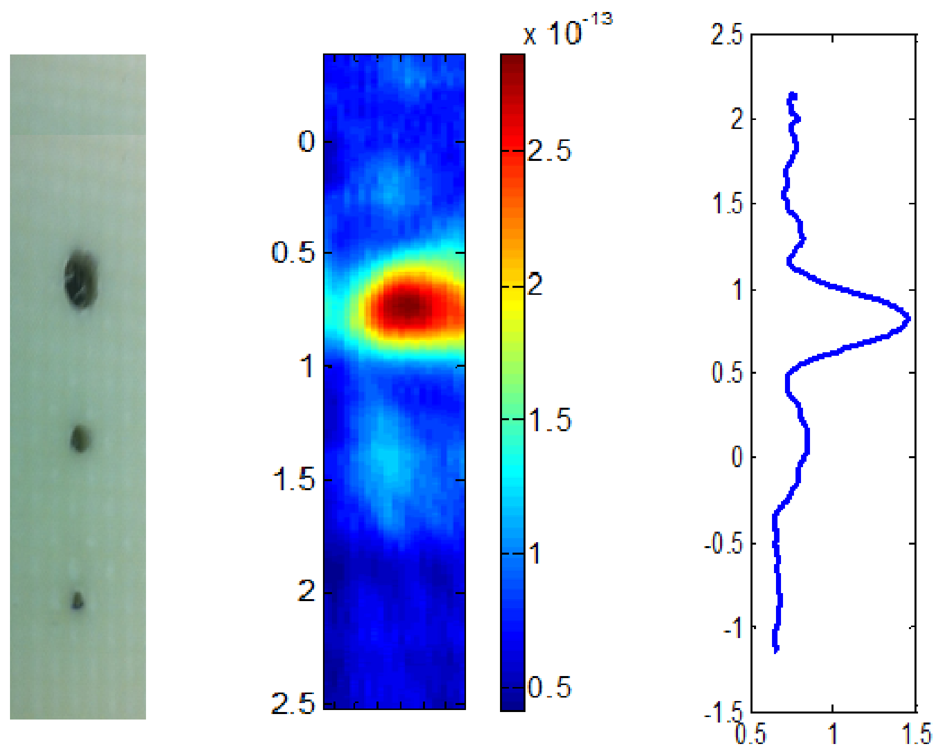

(a) (b) (c)

Figure 6.24: Experimental results: Sample III (a) Sample, (b) TR Energy, (b) CR Signal

image shows the energy localized around the sample region corresponding to D1 and D2. However D3 is not detected, since the dimensions are much smaller than the corresponding wavelength, with the hole diameter almost equal to $\lambda/15$. The cross range signal shows the 8 mm ($\sim \lambda/4$) hole detected clearly and a somewhat small peak at the 4 mm ($\sim \lambda/8$) hole. Although previous studies have shown the capability of TR algorithm to detect multiple defects, focal resolution limits the ability of this technique to image two closely spaced defects, due to cross coupling between the two defects. Also the amplitude of the back-propagated fields is proportional to defect size. Hence the electric field reaches a higher value at D1 whose scattering cross section is larger than D2. Thus, D1 produces much stronger energy peaks in comparison to D2, as shown in the energy images with the FWHM almost equal to the size of the defects, as shown in Fig. 6.24.

The near field imaging results of the open ended waveguide for three frequencies (8 GHz, 10 GHz and 12 GHz) are presented in Fig.s 6.25. The near field imaging result of the coaxial probe at 8 GHz is presented in Fig. 6.29 (b). These results show good correlation between far field imaging results. While D1 and D2 are identified clearly at 8 GHz and 10 GHz, the third hole is barely detected at 12 GHz using the open endede waveguide. Although there are some lift-off errors along the edge of the sample, all three holes are clearly detected at 8 GHz using the coaxial probe. This clearly demonstrates the effectiveness of both near field probes. While the open ended waveguide typically functions as an antenna and can provide sub-surface information at high lift-off distances, the coaxial probe works as a fringing field probe, with limited sub-surface information. On the other hand, the coaxial probe provides finer resolution than the waveguide, since the tip size of the probe is much smaller than the aperture of

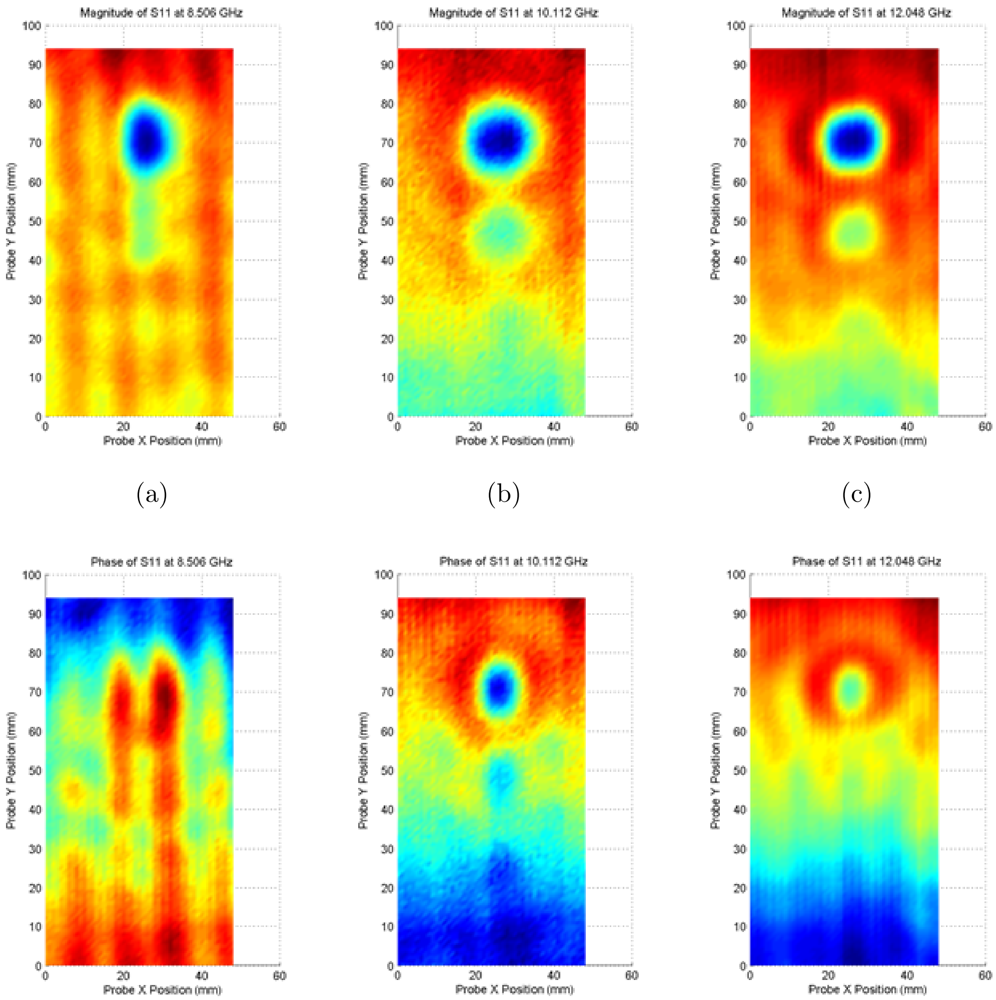

(a) (b) (c)

(d) (e) (f)

Figure 6.25: Near field experimental results: Sample III (a) Magnitude: 8 GHz, (b) Magnitude: 10 GHz, (c) Magnitude: 12 GHz, (d) Phase: 8 GHz, (e) Phase: 10 GHz, (f) Phase: 12 GHz

the waveguide. While far field measurements could not detect D3 due to its resolution limit, near field measurements can weakly detect D3 since its resolution is typically dictated by aperture size and choice of frequency. Thus near field can exceed diffraction limit and provide finer resolution than the far field system at a similar frequency resulting in increased resolution at the expense of longer measurement time and smaller liftoff distance requiring the sensor to be physically close to the sample.

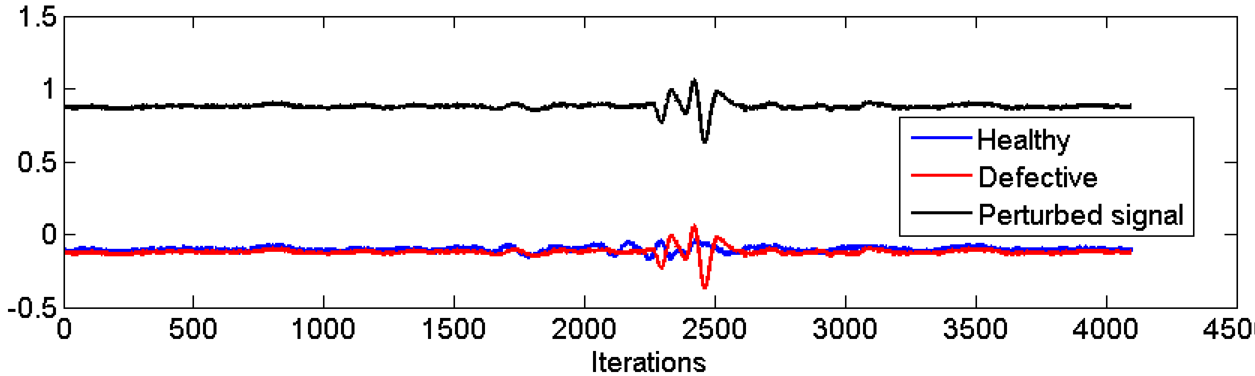

Figure 6.26: Experimental signals of one receiver element for Sample IV

- Impact damage: The two signals corresponding to the healthy and defective samples and the perturbed signal for a single receiver element are shown in Fig. 6.26. The time reversed perturbation signals from the receiver array were back-propagated numerically to image the sample. The integrated energy image shows the energy localized around the impact damage. The cross range signal shows the extended defect clearly detected, with the FWHM (2.1 cm) approximately equal to the defect's physical size (2 cm), as shown in Fig. 6.27. The near field imaging results obtained using the open ended waveguide probe at 10 GHz are presented in Fig. 6.28. The near field imaging result obtained using a coaxial probe at 8 GHz is presented in Fig. 6.29 (b). The far field images show good correlation with near field images. The advantage of the far field technique is clearly demonstrated from the fact that the system provides images with comparable resolution with much less scanning time and larger separation distance.

In accordance with the experimental results obtained in this paper, we observe that precise imaging of defects depends on several factors. It is important to note that it is impossible to focus back ideally at the defect, since the finite TR array has access to limited scattered field data (40°). Moreover it is assumed that the receiver antenna, which is actually a horn antenna of finite aperture size, is treated as point sources in the back-propagation

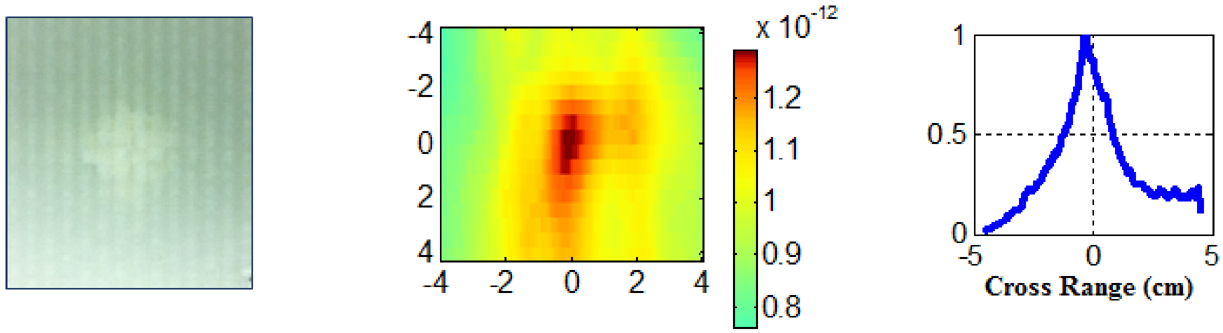

(a) (b) (c)

Figure 6.27: Experimental results: Sample IV (a) Sample, (b) TR Energy, (b) CR Signal

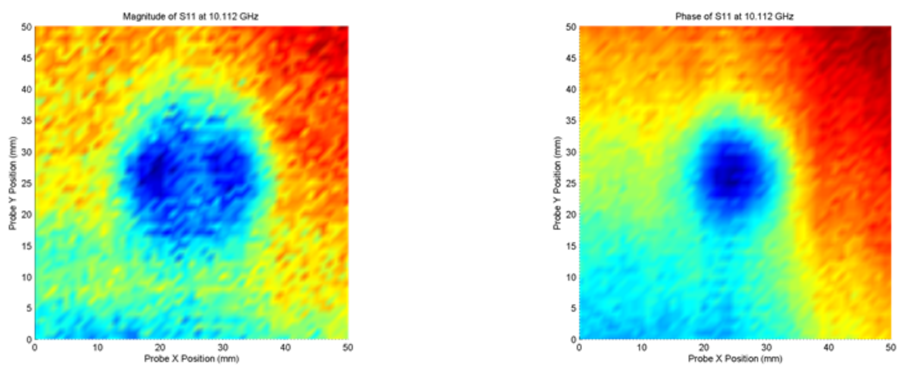

(a) (b)

Figure 6.28: Near field experimental results: Sample IV (a) Magnitude: 10 GHz, (b) Phase: 10 GHz

model. This results in a stretched out integrated energy image as shown in Fig. 6.24, since the forward and backward media are not exactly reversible. The entropy-based localization technique is able to determine focusing time instants quite accurately. Effective detection depends on the size of the defect, while the TR resolution follows diffraction limits along both cross range and down range directions. Thus, although a defect having smaller dimensions ($\sim \lambda/2$) can be detected as shown in Figs. 6.20(d) and 6.24, the focal spot will be limited to the resolution limit($\sim \lambda/2$). It is also seen that while the TR algorithm has the ability to detect multiple defects, focal resolutions limit the ability of this technique to accurately

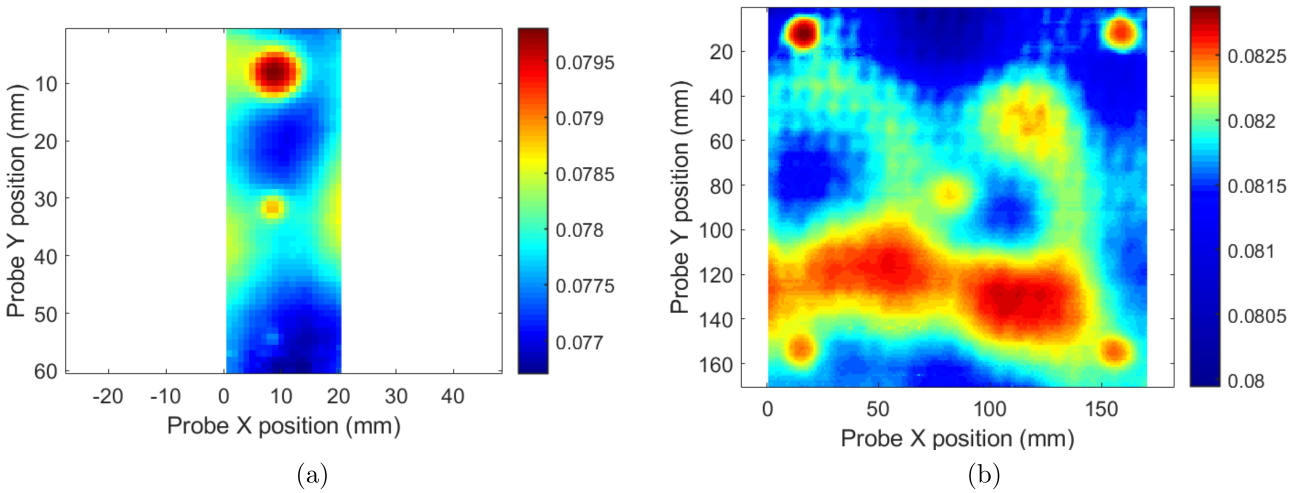

Figure 6.29: Coax probe results (a) Sample III Phase: 8 GHz, (b) Sample IV Phase: 8 GHz

image two closely spaced defects, as is shown in Fig. 6.24. The TR image fields corresponding to two closely spaced defects interfere with each other, resulting in poor image quality due to cross coupling between the defects. In addition, since the amplitude of the back-propagated fields is proportional to the scattering cross section of the defects, it is difficult to detect small defects adjacent to a big defect [5], [23], as seen in Fig. 6.24. The ability of the imaging system to image and size precisely an extended defect such as an impact damage is also demonstrated. The computational error along with the above-mentioned factors involved in modeling the problem is responsible for the error associated with detection and sizing.

The detection error (ξ_d) and sizing error (ξ_s), as defined in (4) and (5), are calculated for all the different cases studied and summarized in Table 6.3. As interpreted from the table, the highest ξ_d of 14.5%, and ξ_s of 100%, is achieved in Case III, since the the dimensions of the 4 mm ($\sim \lambda/8$) hole is much smaller than the corresponding wavelength. Hence it is much harder to accurately detect and size the defect. The lowest ξ_d of 2%, and ξ_s of 2.33%, is achieved in Case I. As mentioned before, this is the best case scenario, since the defect can be approximated as a 2-D disbond (similar to simulations), with dimensions of the order of

Table 6.3: Detection error and imaging quality

Case	L_a(cm)	L_m(cm)	ξ_d (%)	ξ_s (%)
I	3	2.92	2	2.33
II	1.5	1.45	4	3.33
III				
Defect 1	0.8	1	6.67	20
Defect 2	0.4	0.8	14.5	100
Defect 3	0.2	NDT	-	-
IV	2	2.1	10	5

the wavelength.

6.9 Conclusion

This chapter deals with the application of reflection mode microwave TR processing to NDE of composite materials, particularly for imaging disbonds in adhesively bonded metal-composite joints. Disbonds as small as 2 cm (0.13λ) are effectively detected by this technique. Multiple disbonds at the joint are effectively detected by this algorithm. Additionally, we observe that the time reversed energy is back propagated and focused in proportion to the defect size. Extended disbonds, as big as 1.2 m (8λ) are detected by this algorithm. The full width at half maxima (FWHM) of the one dimensional energy signal at the disbond center location, also predicts the length of the disbond with 92% accuracy. The robustness of the time reversal algorithm is tested by injection of AWGN noise to the received array signals. The time reversal algorithm is seen to focus at the disbond even in the presence of high noise, since the time delay between successive receiver array elements is not distorted. Initial results of the time reversal algorithm are promising. Next, a model-based parametric study was performed to understand the influence of defect length, distance between the transmitter and receiver, aperture size on the measured signal. The results of the parametric study are used to optimize and determine the limits of capability of the experimental set up.

A pulsed time domain laboratory system coupled with the TR back-propagation simulation model is setup for performing far field NDE experiments. An open ended waveguide and an extended tip coaxial probe are used in a near field imaging system is setup for performing high precision imaging. The far field results show good correlation with the near field imaging results. The near field system requires small stand off distances, small area coverages and a scan time of more than 30 samples per minute (5 hours for Sample IV). In contrast, the far field experimental system is capable of scanning the sample at a large stand off distance with access from single side. The non contact nature of the measurements allow for rapid scanning. Although the experimental measurement and back-propagation took around 5 minutes, it could be conducted in real time with an automated receiver array coupled to a high performance computing simulation server, that imports the data and runs the back-propagation algorithm to localize the defect regions as hot-spots in the energy image.

Future simulation studies involve studying robustness of TR with respect to variations in material properties and selective focusing of defects in composites using the D.O.R.T. and MUSIC algorithms for detection and imaging of sub-wavelength defects This is extremely important since TR wave focuses on the bigger defect, when two defects are situated close to each other. These algorithms are able to utilize the rank deficient nature of the TR matrix in order to selectively focus the TR wave on different defects. More extensive studies must be performed in order to image other damage modes such as sub-surface defects, delamination, fiber breakage and cracks in non-conductive composites such as GFRP as well as conductive composites such as CFRP.

Chapter 7

Enhancement of time reversal imaging using a metamaterial lens

Metamaterials have been increasingly used in the past few decades in the design of novel microwave circuits and sensor systems [122]. They are artifical materials designed with properties derived using periodic structures to create a desired macroscopic behavior such as negative index of refraction, as shown in Fig. 7.1. The unique properties of metamaterials offer several advantages such as sub-wavelength nature, compact design and super-resolution, that is not found in conventional materials [123]. Prior experimental results have demonstrated the ability of a metamaterial lens with a relative refractive index of -1, to form images that overcome diffraction limits [124].

Several physics as well as signal processing based microwave far field imaging techniques

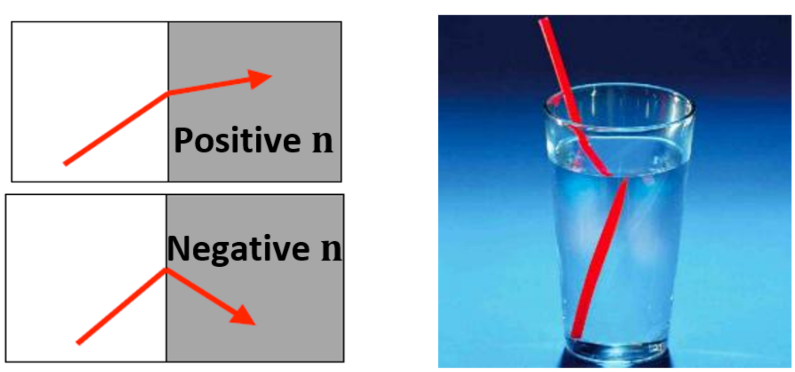

Figure 7.1: A ray passing through a metamaterial region and the image of a straw dipped in a metamaterial region

are being developed to image source, scatterers and anomalies. Previous far field TR simulation and experimental studies have demonstrated diffraction limited imaging resolution [63]. Objects quite smaller than the operating wavelength are not detectable in the far field ranges. While near field imaging techniques provide much higher resolution, the scanning time for large composite areas is relatively large [125]. This issue can be tackled with the use of metamaterials, which can provide high resolution using far field microwave measurements. Recent work has demonstrated the application of utilizing such a lens to increase the sensitivity of microwave NDE techniques for detecting subwavelength size defects, in isotropic dielectric materials [126].

This research proposes the inclusion of a metamaterial lens for improved microwave imaging of composites via TR processing. The unique properties of the lens provide several benefits for high resolution microwave inspection of composites. The limitations of the existing far field NDE system are pointed out, which can be tackled using a metamaterial lens. Simulation studies depict the capability of the lens for focusing fields inside the composite material. Initial simulations using the lens, coupled with the TR imaging algorithm demonstrate the superior focusing, detection and resolution provided by the lens. The chapter is organized as follows. Sections 1 and 2 discusses the physics, numerical modeling and simulation studies of metamaterials. Section 3 couples microwave TR with the metamaterial lens and discusses microwave imaging simulation results. The superior imaging quality and better resolution obtained with the metamaterial lens for detection of source, dielectric targets and closely spaced sub-wavelength defects inside composites demonstrates the benefits of the metamaterial lens as a novel sensor for NDE imaging.

7.1 Wave equation in metamaterials

The simultaneous negative permittivity and permeability of the metamaterial results in a negative refractive index. The refractive index of metamaterials is given by [122]

$$n = -\sqrt{\mu\varepsilon}. \tag{7.1}$$

The most general dispersion equation connecting frequency ω and wave vector of a monochromatic wave k is given by

$$|\frac{\omega^2}{c^2}\varepsilon_{ij}\mu_{ij} - k^2\delta_{ij} + k_i k_j| = 0, \tag{7.2}$$

where $\varepsilon_{ij}, \mu_{ij}$ and δ_{ij} are the permittivity, permeability tensors and the Kronecker delta function. The equation is simplified in the case of an isotropic material to

$$k^2 = \frac{\omega^2}{c^2}n^2, \tag{7.3}$$

where n is the index of refraction of the material, given by $n^2 = \varepsilon\mu$. It might be seen that a simultaneous change of signs of ε, μ has no changes to the above relations. Hence substances with $\varepsilon < 0$ and $\mu < 0$ have properties different from substances having positive ε, μ. Maxwell's curl equations for a monochromatic plane wave in k-space is given by:

$$k \times \mathbf{H} = -\frac{\omega}{c}\varepsilon\mathbf{E} \quad ; \quad k \times \mathbf{E} = \frac{\omega}{c}\mu\mathbf{H}. \tag{7.4}$$

It can be clearly seen that E,H and k form a left handed triplet of vectors for LHMs (in contrary to a right handed triplet for conventional materials), which result in the phase velocity being anti-parallel to the group velocity. The energy flux carried by the wave is determined by the Poynting vector S, given by

$$S = \frac{c}{4\pi}\mathbf{E} \times \mathbf{H}. \tag{7.5}$$

Thus, the vector S always forms a right handed set with the vectors E and H. Accordingly for right handed substances, S and k are in the same direction. For left handed substances, S and k are in the opposite direction. Since k is associated with phase velocities, we can observe that the phase velocity and group velocity are in opposite directions in a LHM structure. The phase velocity is opposite in direction to the energy flux, leading to several phenomenon such as reversed Doppler and reversed Vavilov-Cerenkov effects [127, 128].

The negative refractive index of metamaterials can be utilized in the design of a planar lens that can achieve perfect focusing, thus focusing the radiation from a point source located at a distance d_1 from the plate [124]. The lens can achieve resolution beyond the diffraction limit. Additionally, the evanescent fields that are not transmitted in a conventional lens can be recovered in a metamaterial region due to its negative refractive index [123]. This can be mathematically understood by defining a wave propagating along +z direction with respect to our experimental setup described by a superposition of elementary plane waves of the type:

$$E(x, y, z; t) = \sum_{k_x, k_y} A(k_x, k_y) e^{j(k_x x + k_y y + k_z z - \omega t)}, \tag{7.6}$$

where $k_z = \sqrt{\frac{\omega^2}{c^2} - k_x^2 - k_y^2}$ is real, leading to propagating waves, when $\frac{\omega^2}{c^2} > (k_x^2 + k_y^2)$. However, k_z is imaginary, when $\frac{\omega^2}{c^2} < (k_x^2 + k_y^2)$, leading to the high angular frequency evanescent waves. For a conventional lens, the evanescent wave amplitude decays exponentially along z axis from the source location, giving a highest resolution of $k_{max} = 2\pi/\lambda$. However, in order ot transport the energy along the positive y axis in a metamaterial region, $k_z = -\sqrt{\frac{\omega^2}{c^2} - k_x^2 - k_y^2}$. The evanescent fields (small scale features) are amplified in the metamaterial region. Thus they can be recovered, enhanced and transmitted, leading to super-resolution. Thus, while the resolution of a conventional lens based on materials with positive refractive index and curved surfaces is limited by the operating wavelength, the super resolution property of the metamaterial lens can provide resolution that breaks diffraction limits and is capable of sub-wavelength imaging with increased overall sensitivity and resolution.

7.1.1 Electromagnetic properties of the metamaterial

The metamaterial is characterized by a double negative (DNG) layer can be characterized by electromagnetic plasma equations. Thin wire structures with lattice spacings of the order of a few millimeters behave like an electric plasma with a resonant frequency [11], ω_{pe}, in the GHz region. The ideal dielectric response of a plasma is given by

$$\varepsilon = \varepsilon_0(1 - \frac{\omega_{pe}^2}{\omega^2}), \tag{7.7}$$

which takes negative values for $\omega < \omega_{pe}$, where ω_{pe} is the peak electric plasma frequency. It has also been shown more recently that that a structure containing loops of conducting wire has properties mimicking a magnetic plasma,

$$\mu = \mu_0(1 - \frac{\omega_{pm}^2}{\omega^2}), \tag{7.8}$$

which takes negative values for $\omega < \omega_{pm}$, where ω_{pm} is the peak magnetic plasma frequency. Tuning these parameters, it is possible to attain a value of $\varepsilon = -1$ and $\mu = -1$ atleast at a single frequency. The frequency dispersive electric and magnetic properties of a lossy Drude model characterizing the DNG layer can thus be expressed as [129]

$$\begin{aligned}\varepsilon(\omega) &= \varepsilon_0\left(1 + \frac{\omega_{pe}^2}{\omega_{oe}^2 - \omega^2 + j\tau_e\omega}\right);\\ \mu(\omega) &= \mu_0\left(1 + \frac{\omega_{pm}^2}{\omega_{om}^2 - \omega^2 + j\tau_m\omega}\right),\end{aligned} \tag{7.9}$$

where ε_0 and μ_0 are the free space permittivity and permeability, ω_{oe}, ω_{om} are the frequency edge of electric and magnetic plasma and τ_e, τ_m refer to electric and magnetic losses due to the electric and magnetic collision. It can be easily found out from the above equations that $\varepsilon < 0$ when $\omega_{oe} < \omega < \omega_{pe}$ and $\mu < 0$ when $\omega_{om} < \omega < \omega_{pm}$. The refractive index for the parameter values of $\omega_{pm} = \omega_{pe}$ =20 GHz, $\omega_{om} = \omega_{oe}$ =4 GHz and $\tau_e = \tau_m$=0 to be used in later simulations, are shown in Fig. 7.2.

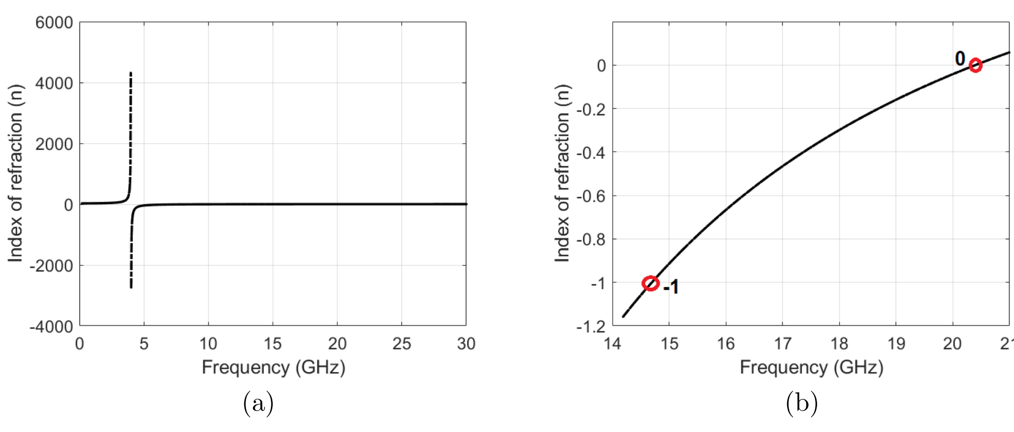

Figure 7.2: Refractive index of metamaterial, (a)Drude model of refractive index for DNG medium, (b) Zoomed in plot shows n=-1 and zero crossover point

7.1.2 Misconceptions surrounding metamaterials

In 1967, Veselago formulated the negative refraction capability of metamaterials mathematically by matching boundary conditions for E and H fields [122]. The solution was purely mathematical, and all such solutions must be checked for physical validity. However, whether such a material can be physically realized by using periodic structures still remains largely unanswered. Munk in his book 'Metamaterials Critique and Alternatives" [130] has discussed the difficulties associated with synthesis of negative index of refraction materials using periodic structures. A brief discussion of arguments including stating the assumptions and limitations of realizing such a physical medium is presented in this section.

7.1.2.1 Assumptions

Some assumptions concerning Veselago's metamaterial medium are as follows:

- The refractive index for a medium with negative ε, μ would become negative. This was derived by matching the boundary conditions at the DPS-DNG interface without considering the physical relevance of such a medium.
- The evanescent waves amplify with distance instead of decaying, when the refractive index becomes imaginary from a mathematical point of view.
- While E,H, k forms a right-handed triplet in an ordinary medium, they form a left-handed triplet in a metamaterial medium.

7.1.3 Misconceptions

While Veselago pointed out the remarkable features of a metamaterial, he added that no such material has ever been produced naturally or artificially. However, almost 30 years later Pendry suggested that such materials can be engineered using a periodic array of split ring resonators and thin wires [131]. Munk in his book [130] has claimed that none of the features pointed out by Veselago is produced by such periodic structures.

- Refraction property of the periodic structure: Munk proves that the direction of backward refraction for an infinite array is not due to the negative refractive index, but due to the grating lobes when $D_z \geq \lambda/2$, where D_z is the distance between individual elements. For a finite array, reradiation due to surface waves (with much lower radiation efficiency around 14 to 20 dB) can be responsible for the backward direction and not refraction. Munk mathematically proves that these fields are inherently right-handed in periodic structures, regardless of the type or shape of the element [130].

- Evanescent wave amplification: The total evanescent field from a periodic array is given by the sum of the fields from individual elements. They can constructively interfere to produce peak or also destructively interfere to produce a null point. Also, if the last array produces a much stronger current than the previous arrays, the total field will be dominated by the field from the last array, and misinterpreted as an amplified evanescent wave. Munk also adds that evanescent wave amplification has only been demonstrated using a capacitively loaded transmission-line model terminated in a resistive load [132].

The above discussion should be kept in mind while physically designing such a metamaterial lens. Although, there have been numerous highly cited claims of designing a metamaterial lens in literature over the past 2 decades [133, 134, 135], Munk's arguments need to be investigated cautiously in order to avoid confusion and misinterpretation among the scientific community. The research conducted in the following sections involve simulations that consider homogenization of metamaterials based on Veselago's ideas. In other words, the simulation studies are conducted considering the metamaterial region as a homogeneous medium with equivalent permeability and permittivity expressions. The possibility of designing such a material will be researched at a later stage. Further simulation studies need to be conducted in the future considering the physical, periodic structures, in order to match simulation studies with experiments and estimate the discrepancies between an ideal homogenized medium and practical periodic structures.

7.1.4 Numerical modeling of the DNG layer

As mentioned in Section II, FDTD is used for numerical modeling of Maxwell's equations. Using the frequency dispersive electromagnetic properties shown in (7.9), the electric constitutive relationship can be modified in the presence of the DNG layer as follows:

$$\begin{aligned} D(\omega) &= \varepsilon_0 E(\omega) + P(\omega), \\ P(\omega) &= \frac{\varepsilon_0\ \omega_{pe}^2}{\omega_{oe}^2 - \omega^2 + j\tau_e\omega} E(\omega), \end{aligned} \tag{7.10}$$

where $E(\omega), D(\omega)$ and $P(\omega)$ are the electric field, displacement current and polarization density of the medium respectively. Since the fields are modeled in time domain, the frequency dependent terms of (7.10) need to be converted to equivalent terms in time domain. The auxiliary differential equation (ADE) method uses inverse Fourier Transform to convert frequency domain equations into corresponding time domain difference equations, given by

$$
\begin{aligned}
j\omega P(\omega) &\leftrightarrow \frac{(P^n - P^{n-2})}{2\Delta t}, \\
(j\omega)^2 P(\omega) &\leftrightarrow \frac{(P^n - 2P^{n-1} + P^{n-2})}{\Delta t^2}, \\
P(\omega) &\leftrightarrow P^{n-1}
\end{aligned}
\tag{7.11}
$$

Using the above relations in (7.10) along with the central difference approximation method, the fields are updated by time marching algorithm as follows:

$$
\omega_{oe}^2 P^{n-1} + \frac{(P^n - 2P^{n-1} + P^{n-2})}{\Delta t^2} - \tau_e \frac{(P^n - P^{n-2})}{2\Delta t} = \varepsilon_0 \omega_{pe}^2 E^{n-1} \tag{7.12}
$$

Arranging like terms the final updating equation for $P(\omega)$, with the fields updated recursively by FDTD is given by

$$
\begin{aligned}
P^n = \left(\frac{\frac{2}{\Delta t^2} - \omega_{oe}^2}{\frac{\tau_e}{2\Delta t} + \frac{1}{\Delta t^2}} \right) P^{n-1} &+ \left(\frac{\frac{\tau_e}{2\Delta t} - \frac{1}{\Delta t^2}}{\frac{\tau_e}{2\Delta t} + \frac{1}{\Delta t^2}} \right) P^{n-2} \\
&+ \left(\frac{\omega_{pe}^2 \varepsilon_0}{\frac{\tau_e}{2\Delta t} + \frac{1}{\Delta t^2}} \right) E^{n-1}.
\end{aligned}
\tag{7.13}
$$

In a similar fashion, the magnetic fields inside a DNG layer can be solved by recursively updating the magnetic polarization density $M(\omega)$, with the fields updated recursively by FDTD is given by

$$
\begin{aligned}
M^n = \left(\frac{\frac{2}{\Delta t^2} - \omega_{om}^2}{\frac{\tau_m}{2\Delta t} + \frac{1}{\Delta t^2}} \right) M^{n-1} &+ \left(\frac{\frac{\tau_m}{2\Delta t} - \frac{1}{\Delta t^2}}{\frac{\tau_m}{2\Delta t} + \frac{1}{\Delta t^2}} \right) M^{n-2} \\
&+ \left(\frac{\omega_{pm}^2 \mu_0}{\frac{\tau_m}{2\Delta t} + \frac{1}{\Delta t^2}} \right) H^{n-1}.
\end{aligned}
\tag{7.14}
$$

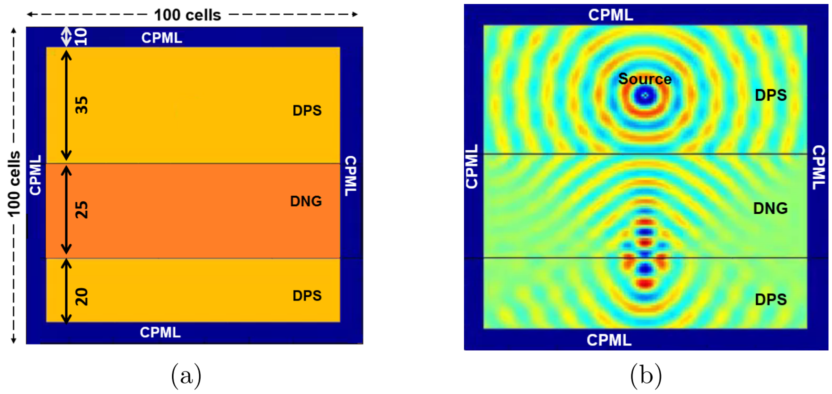

Figure 7.3: Focusing of the metamaterial lens in free space, (a) Simulation schematic, (b) Wave propagation

A simple 2D FDTD scheme as explained in Chapter 2 was used to solve for electromagnetic fields in the Double Positive Region (DPS).

In order to understand and validate the wave propagation nature in the presence of the metamaterial slab, wave propagation simulations are conducted in a DPS-DNG-DPS medium with the schematic and spatial dimensions shown in Fig. 7.3 (a). 10 cells are chosen for the convolution perfectly matched layer (CPML) boundaries, with a 25 cell thick DNG slab (cells 45 to 70) inserted between the DPS regions. An input sinusoidal pulse with central frequency f_0=14.7 GHz was chosen with n=-1. Fig. 7.3 (b) shows the electric field snapshot at T=300 of the electromagnetic wave. The waves undergo a phase reversal of 180°at the first DPS-DNG interface and another phase reversal of 180°at the second DPS-DNG interface. Thus Fig. 7.3 (b) shows negative phase velocity (backward propagation) in the DNG region and positive phase velocity (forward propagation) in the DPS region, as expected in a typical metamaterial behavior.

7.2 Focusing of fields using the lens

The DNG layer can be utilized in the design of a metamaterial lens with perfect refocusing capabilities.

7.2.1 Focusing of the lens in free space

It can be shown in Fig. 7.4 that the the radiation from a point source located at a distance (d_1) from the lens can focus at a point (d_2) in free space. If the thickness (t) of the DNG layer is appropriately chosen, the electromagnetic fields are refracted in the DPS-DNG interfaces such that the field focuses once inside the lens and once outside the lens. The lens thickness t can be chosen according to the following relationship, $d_1 + d_2 = t$ and the corresponding ray diagram shown in Fig. 7.4. This relationship can be derived from the ray diagram as follows:

$$\begin{aligned} h_{m1} &= d_1 \tan\theta_1; \qquad h_{m1} = t_1 \tan\theta_2; \\ h_{m2} &= d_2 \tan\theta_2; \qquad h_{m2} = t_2 \tan\theta_2; \end{aligned} \tag{7.15}$$

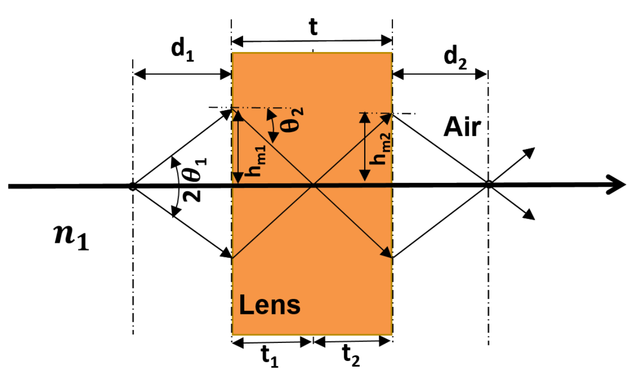

Figure 7.4: Ray diagram of metamaterial lens in free space

where all the parameters h_{m1}, h_{m2}, t_1, t_2 are defined in the ray diagram. Combining the above equations, we obtain

$$\begin{gathered} d_1 = t_1 \tan\theta_2 \cot\theta_1 \qquad d_2 = t_2 \tan\theta_2 \cot\theta_1; \\ d_1 + d_2 = (t_1 + t_2) \tan\theta_2 \cot\theta_1. \end{gathered} \tag{7.16}$$

From Snell's law we obtain a relationship between θ_1 and θ_2.

$$\sin\theta_1 = |n_2| \sin\theta_2, \tag{7.17}$$

where n_2 is the refractive index of the metamaterial lens. Combining (7.16) and (7.17), the relationship between d_1, d_2 and t is obtained.

$$d_1 + d_2 = t \frac{\cos\theta_1}{\sqrt{n_2^2 - \sin^2\theta_1}}. \tag{7.18}$$

It can be observed that for a perfect metamaterial lens (n_2=-1), (7.18) is reduced to $d_1 + d_2 = t$.

FDTD simulations are conducted with the sinusoidal excitation source in order to validate the focusing property of the lens with the chosen parameters d_1= 3.5 λ_0 and t=8λ_0. The electric field snapshot shown in Fig. 7.5 (a), shows the first focal spot inside the lens and the second focal spot outside the lens, with d_2=4.4 λ_0, which satisfies the perfect focusing condition. It can be observed from (7.18), that keeping the thickness of the lens constant, varying d_1 produces the second focal spots at different d_2 position. When d_1 is 2.5 λ_0, d_2 is found out to be 5.4 λ_0, as seen in Fig. 7.5 (b).

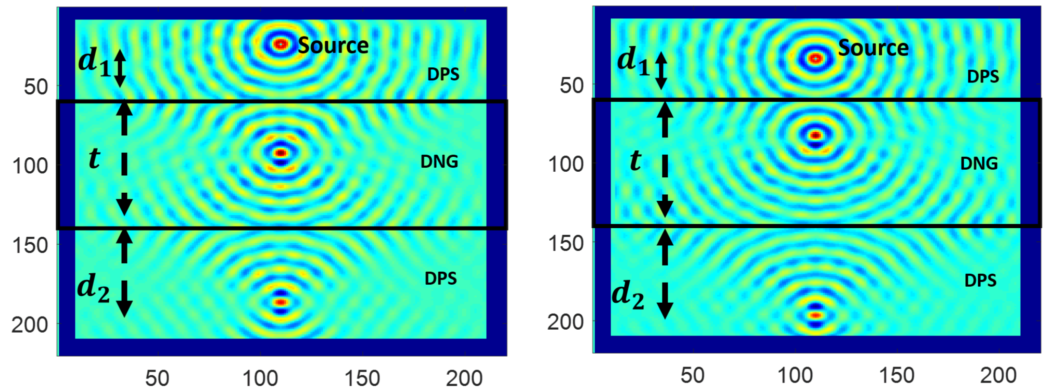

(a) (b)

Figure 7.5: Focusing of the metamaterial lens in free space, (a) Focused fields with lens (d_1= 3.5 λ_0; d_2= 4.4 λ_0; t=8λ_0), (b) Focused fields with lens (d_1= 2.4 λ_0; d_2= 5.5 λ_0; t=8λ_0

7.2.2 Focusing in presence of a composite

The simulations described above show that the lens has perfect focusing capabilities in free space. This section studies its focusing capability in presence of a composite sample. FDTD simulations are conducted with the sinusoidal excitation source at 14.7 GHz in the presence of the lens and composite sample. The simulation parameters are as follows d_1= 3.5 λ_0, d_2^1= 3.5 λ_0 and t=8λ_0. The dimension of the composite is 4λ_0×8λ_0. As observed in the ray diagram of Fig. 7.6 (a), that there is a refraction at the composite boundary, the waves

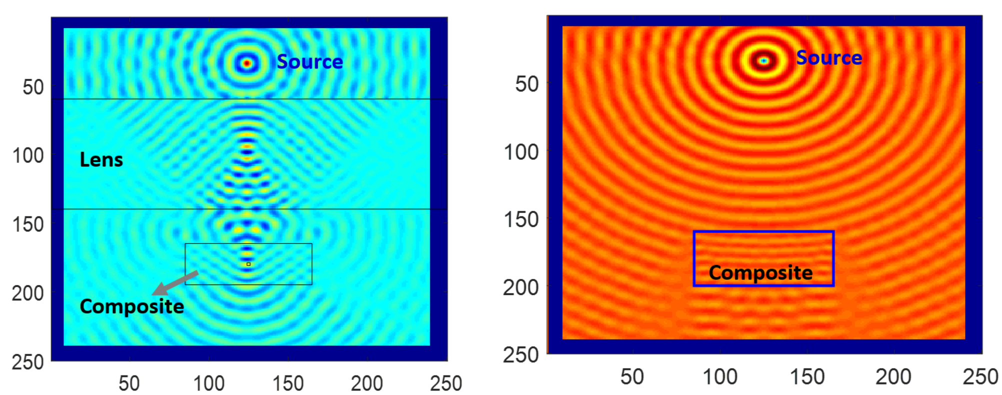

(a) (b)

Figure 7.6: Focusing of the metamaterial lens in composites : (a) Focused wave impinges composite with lens, (b) Near plane wave impinges composite without lens

focus in a region inside the composite. Fig. 7.6(b) shows that in the absence of the lens, near plane waves are incident on the composite, which limits the imaging resolution, while a focused field interacts with the composite in the presence of the lens.

7.2.2.1 Resolution of focal spot

The focal spot of the metamaterial lens in the presence of the composite needs to be studied in order to assess the imaging resolution of the lens. The focusing resolution is determined from the integrated energy of the focused wave on the composite and is plotted in Fig. 7.7. In the absence of the composite sample, there is no additional refraction and all rays combine at the same point, leading to an ideal focal spot with near equal cross and down range resolutions, as shown in Fig. 7.7 (a). In the presence of the composite, the rays constituting the EM wave are refracted at different angles at the air-composite interface. Thus although all the rays focus at the same cross range location, they are focused at different down-range depth regions of the composite sample. From Fig. 7.7 (b), it can be clearly seen that the wave is localized well along the cross range, but poorly localized along the down range. Due to the poor down-range resolution, defects situated along down range will be more difficult to

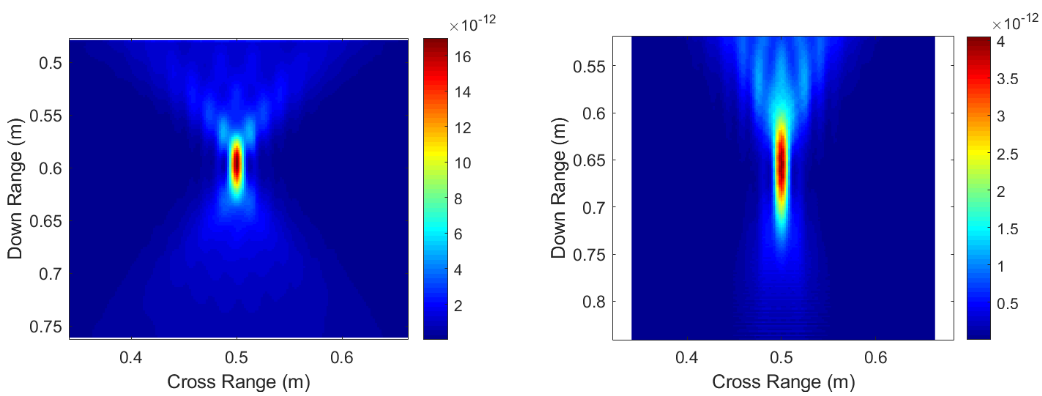

(a) (b)

Figure 7.7: Focusing resolution of the lens, (a) Free Space, (b) Composite

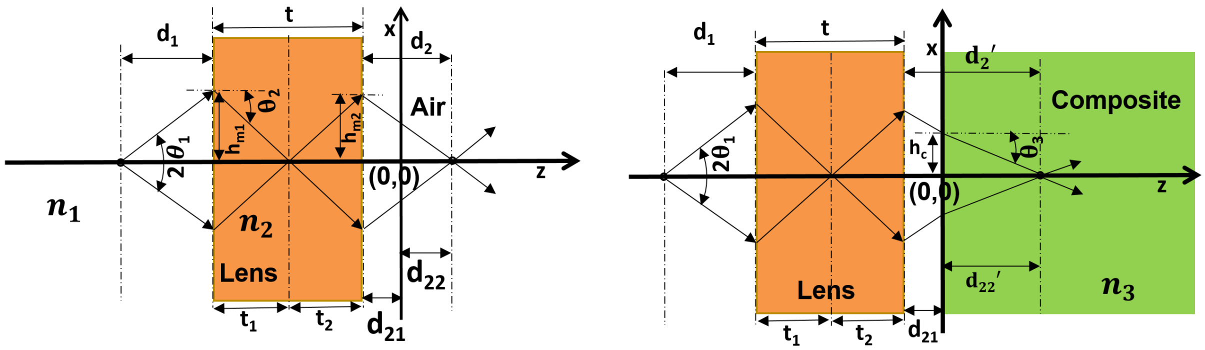

(a) (b)

Figure 7.8: Ray diagram of metamaterial lens in the presence of (a) air, (b) composite half space

detect and resolve than along the cross range. Additional work is needed in order to improve the resolution; such as increasing the operation frequency, varying the refractive index of the lens or using a non-planar lens design. This is not studied as part of this research and will be investigated as part of future research.

7.2.2.2 Location of focal spot inside the sample

The ray diagrams through the lens in the presence of an air half space and a composite half space are shown in Fig. 7.8. The ray undergoes an additional refraction at the composite interface in accordance with Snell's law. Since the wave velocity inside the composite is slower than free space, scaled by the composite's relative dielectric constant, the wave is focused at a distance d_2^1 from the lens instead of d_2 ($d_2^1 > d_2$). The ray diagrams can be utilized to determine the location of the second focus of fields inside the composite sample. From the simple ray diagrams in Fig. 7.8 and application of Snell's law, we have,

$$d_2 = d_{21} + d_{22}; \qquad d_2^1 = d_{21} + d_{22}^1. \tag{7.19}$$

Using Snell's law of refraction at the air-composite interface for Fig. 7.8 (a), we obtain

$$\frac{\sin\,\theta_1}{\sin\,\theta_3} = \frac{n_3}{n_1} = \sqrt{\varepsilon_r}. \tag{7.20}$$

Additionally using simple trigonometric identities from Fig. 7.8, we obtain

$$\frac{h_c/2}{d_{22}^1} = \tan\,\theta_3, \qquad \frac{h_c/2}{d_{22}} = \tan\,\theta_1. \tag{7.21}$$

Combining the above two equations, we obtain

$$\frac{d_{22}^1}{d_{22}} = \frac{\tan\,\theta_1}{\tan\,\theta_3}. \tag{7.22}$$

From (7.22) and (7.19), d_{22}^1 can be calculated as

$$d_{22}^1 = d_{22}\Big(\tan\,\theta_1 \cot\,\theta_3\Big) \tag{7.23}$$

Combining (7.20) and (7.23), we get the analytical expression of d_{22}^1 and determine the exact focusing spot in terms of d_{22}, ε_r and θ_1, as follows:

$$d_{22}^1 = d_{22}\left(\frac{\sqrt{\varepsilon_r - \sin^2\,\theta_1}}{\cos\,\theta_1}\right). \tag{7.24}$$

It is observed from (7.24) that $d_{22}^1 = d_{22}$, when ε_r=1, leading to a focal point at d_2 in free space. However, since the wave consists of a bundle of rays incident at different angles, θ_1 depends on the radiation pattern and beamwidth of the antenna that is used as the source. Thus finding the exact focusing distance is non trivial from (7.24). Using a small angle

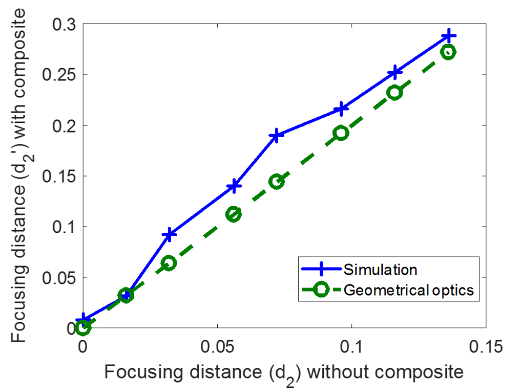

Figure 7.9: Comparison of focal point between simulated and approximated geometrical optics results

approximation and combination of (7.20) and (7.22), the relationship between d_{22} and d^1_{22} can be approximated simply in terms of ε_r as follows,

$$\frac{d^1_{22}}{d_{22}} = \sqrt{\varepsilon_r}. \tag{7.25}$$

The derived expression is compared with numerical FDTD simulations in order to determine the approximation error. For a dielectric sample of $\varepsilon_r = 4$ ($d^1_{22} = 2d_{22}$), Fig. 7.9 shows good comparison between the simulation results and results obtained from (7.25), the error being around ∼5%. (7.25) gives an important yet simple approximate relationship between d_{22} and d^1_{22}. If the bulk dielectric constant of the sample to be inspected can be extracted from a material characterization technique, (7.25) can be utilized to determine an approximate location where the field will be focused in the sample.

7.3 Time reversal with metamaterial lens

The previous section demonstrates the capability of the lens for focusing in free space as well as in composites. Next, the metamaterial lens is coupled with the far field TR imaging algorithm, for achieving high resolution imaging. TR back-propagation simulations based on a transmission mode setup are conducted for detecting the excitation source, sub-wavelength targets and defects embedded inside a composite. The input pulse s(t) is a modulated Gaussian pulse of pulse width 73 ps, corresponding to a 12 GHz bandwidth having a modulating frequency f_0=14.7 GHz,

$$s(t) = e^{-\frac{(t-t_0)^2}{2\sigma^2}} \cos(2\pi f_0 t), \tag{7.26}$$

where the Gaussian pulse is centered at t_0 and σ determines the pulse width.

7.3.1 Source detection in air

Simulations are conducted to image a source in transmission mode with and without the metamaterial lens. The metamaterial lens is placed between the source and the receiver array, as shown in Fig. 7.10 (a). The electric fields are measured by the receiver array, time reversed and back-propagated numerically. The time reversed energy images with and without the lens are shown in Figs. 7.10 (b, c). It is observed that the TR energy is much more focused in cross and down range directions in the presence of the lens. The evanescent field amplification and perfect focusing condition of the lens is responsible for the superior resolution of the image. Although a focal spot is detected in the lens and additional artifacts are observed at the lens interface, they are relatively far away from the source position and to affect the imaging resolution of the lens.

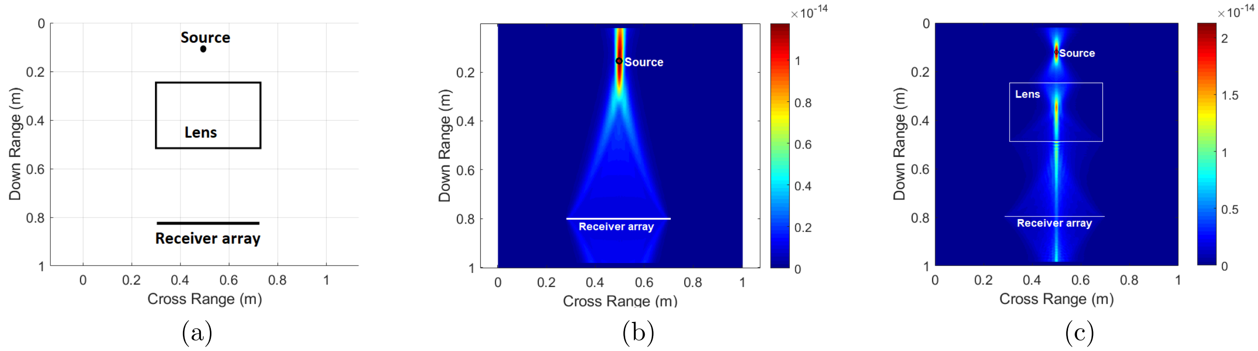

Figure 7.10: TR with metamaterial lens shows enhancement of microwave imaging for source imaging, (a) Schematic of test geometry, (b) TR energy without metamaterial lens, (c) TR energy with lens

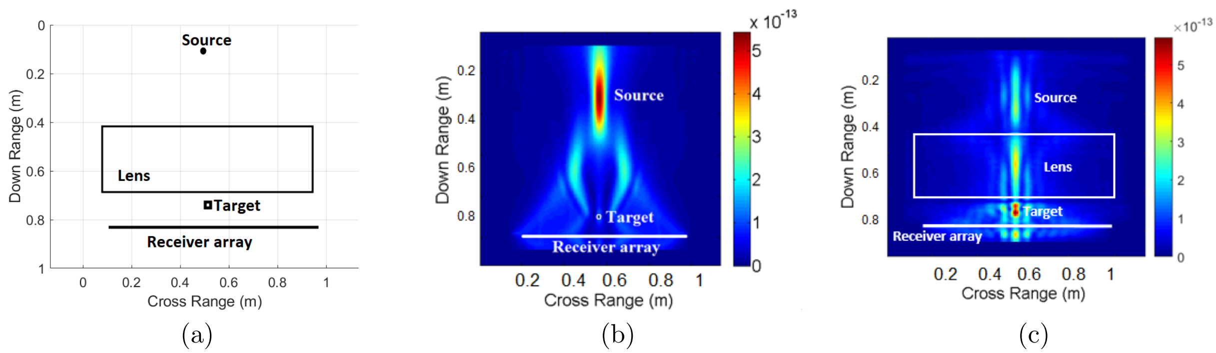

Figure 7.11: TR with metamaterial lens shows enhancement of microwave imaging for sub-wavelength target imaging, (a)Schematic of test geometry, (b) TR energy without metamaterial lens, (c) TR energy with lens

7.3.2 Target detection in air

Next the capability of the metamaterial lens for detecting sub-wavelength targets is demonstrated. A sub-wavelength square target of size 2 mm ($\lambda_0/10$) and relative dielectric constant of 4 is placed with and without the lens as shown in Fig. 7.11 (a). The electric fields are measured by the receiver array in the presence and absence of the target and subtracted in order to calculate the perturbation fields. The perturbation signals are time reversed and back-propagated numerically in the model. The time reversed energy with and without the lens is shown in Figs. 7.11 (b, c). It can be clearly observed that while the TR energy is

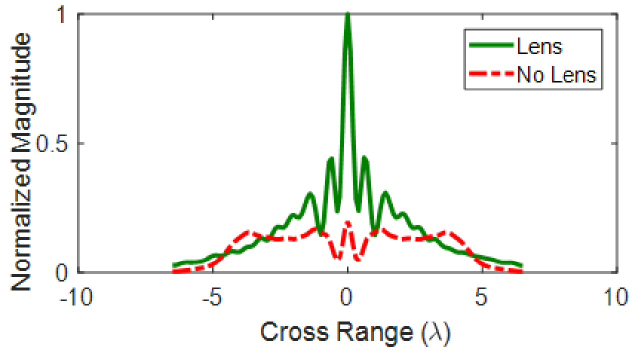

Figure 7.12: Cross range signal of target with and without lens

efficiently localized on the small target with the lens, there is hardly any focusing in its absence. Although additional artifacts are observed at the lens interface with focal spots within the lens and source position, they are relatively far away from the dielectric target region and does not affect the imaging resolution. The TR energy row corresponding to the target plane is termed as the cross range signal. The cross range signal (Fig. 7.12) shows the superior focusing and sub-wavelength target detection capability of the imaging system.

7.3.3 Defect detection in composites

Next, the lens is used for detecting closely spaced sub-surface, sub-wavelength defects inside a composite slab. Several cases involving multiple defects closely separated in the cross range and down range directions are studied. The spatial dimensions of the metamaterial lens used for simulations are 16 cm $\times$ 6 cm ($8\lambda_0 \times 3\lambda_0$).

7.3.3.1 Cross range separated defects

A GFRP slab of dimensions 6 cm $\times$ 5 mm ($3\lambda_0 \times \lambda_0/4$) is placed between the metamaterial lens and the receiver array, as shown in Fig. 7.13(a). Two sub-wavelength square air voids (D1 and D2) of size 2 mm ($\lambda_0/10$) are placed in the middle of the sample, separated in cross range

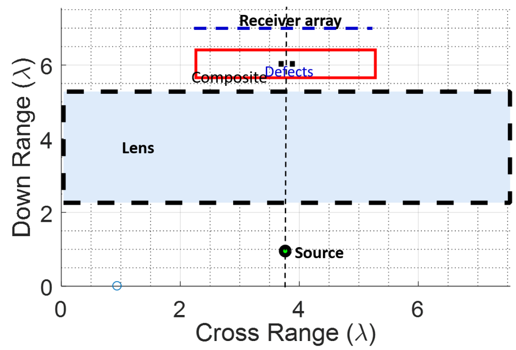

(a)

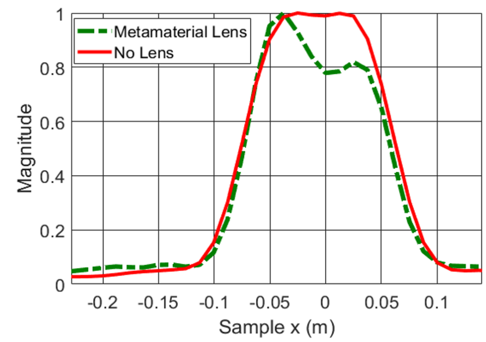

(b)

Figure 7.13: TR with metamaterial lens shows enhancement of microwave imaging for sub-wavelength cross range separated sub-wavelength defects in a composite slab, (a) Schematic of test geometry, (b) TR energy comparison

by a distance of 2 mm ($\lambda_0/10$), as shown in Fig. 7.13(a). TR simulations are conducted for this configuration with and without the lens. Similar to the process mentioned in Section II, the perturbation field is extracted from signals corresponding to reference and test samples, time reversed and back-propagated in the numerical model. Important parameters t, d_1 and d_2 are chosen such that the lens focuses fields on the defect plane. It is also worth mentioning that source location and consequently the focal spot in the composite is closer to defect 1. The time reversed normalized cross range signal comparison with and without the lens is shown in Fig. 7.13 (b). Without the lens, the TR energy image is unable to resolve the closely spaced defects and detects them as an extended defect. However, in the presence of the metamaterial lens, the TR energy is able to resolve both D1 and D2 efficiently. Since the source location is closer to D1 as mentioned before, the focal spot in the composite is closer to D1 and thus more electromagnetic energy interacts with D1 than D2. Thus, although both defects are of same size, higher TR energy is focused on D1.

The focusing spot inside the composite can be shifted in the horizontal plane by translating the source. In order to understand this effect, the source is moved to 6 different

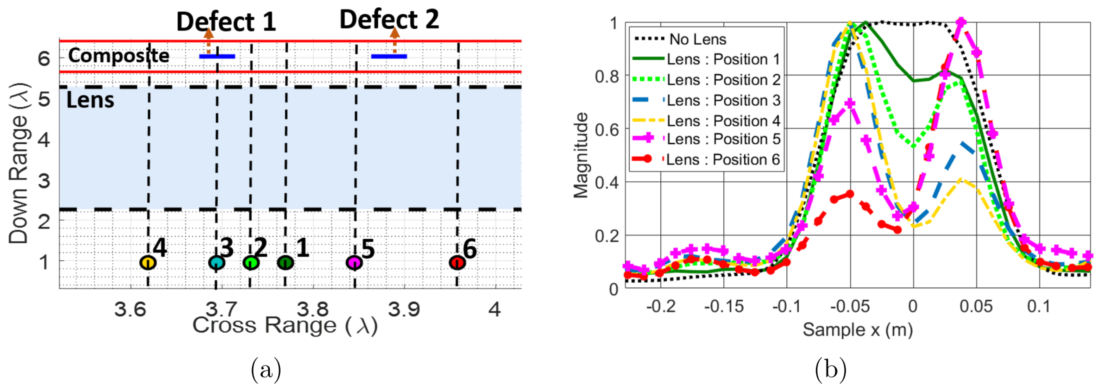

Figure 7.14: TR with metamaterial lens shows enhancement of microwave imaging for sub-wavelength cross range separated sub-wavelength defects in a composite slab, (a) Schematic of test geometry, (b) TR energy comparison

positions as shown in Fig. 7.14(a) and the corresponding normalized TR energy results are displayed in Fig. 7.14(b). From Fig. 7.14 (b), it is clearly observed that the back-propagated TR energy image of a defect reduces as the focal spot shifts further away from the defect. At position 4, minimum energy is focused on defect 2, as it is farthest from the source and is thus exposed to relatively lower electromagnetic fields. Similarly, at position 6, minimum energy is focused at defect 1, as it is farthest from the source. This simulation study shows that the best detection is observed when the horizontal source is closest to the defect. The implication of this results is that one can focus the energy to any desired location in the composite to obtain a high resolution image of the composite sample.

A far field experiment with TR processing was performed previously for detecting 3 drilled holes in a GFRP sample (shown in Fig. 7.15 (a)). Finally, we consider a similar sample discussed in Chapter 6 with three defects (D1, D2 and D3) of dimensions 1 cm × 4 mm ($\lambda_0/2 \times \lambda_0/5$), 4 mm × 4 mm ($\lambda_0/5 \times \lambda_0/5$) and 2 mm × 4 mm ($\lambda_0/10 \times \lambda_0/5$), separated in cross range by a distance of 4 mm ($\lambda_0/5$), as shown in Fig. 7.15(a). TR simulation results with and without the metamaterial lens are shown in Fig. 7.15 (b). Without the metamaterial

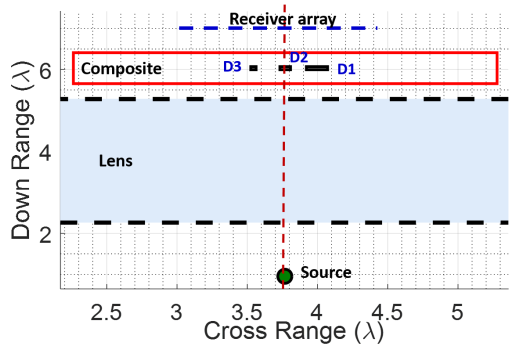

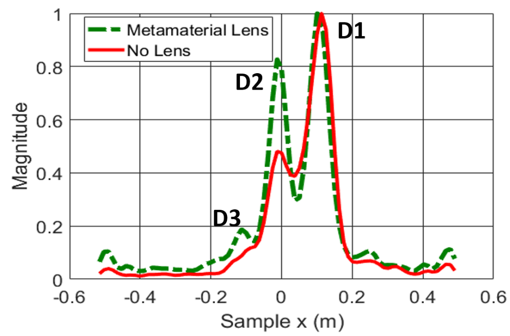

Figure 7.15: TR with metamaterial lens shows enhancement of microwave imaging for a sub-wavelength defects in a composite slab for different source positions, (a) Schematic of test geometry, (b) TR energy comparison

lens, the TR energy is able to clearly detect D1 and weakly detects D2, but D3 is undetected. However in the presence of the metamaterial lens, the TR energy is able to clearly detect all three defects with the strongest indication of D1 followed by D2 and D3 due to its super resolution capabilities. The results indicate that if a physical metamaterial lens is utilized, the resolution of far field microwave imaging can be enhanced.

7.3.3.2 Down range separated defects

As described earlier, the focal spot of the lens is sharp in the cross range, but diffuse in the down range, making it harder to detect and image defects in the down range direction. The previous section demonstrated how the focal spot can be moved horizontally in the sample by moving the source. This section describes how the focal spot can be moved in the vertical direction by moving the source in the vertical direction relative to the sample. In order to understand this effect, the source is moved to 3 different positions, indicated by A,B,C as shown in Fig. 7.16(a). Line scans across the TR energy image obtained for the different positions are presented in Fig. 7.16(b). From Fig. 7.16 (b), it is clearly observed that the

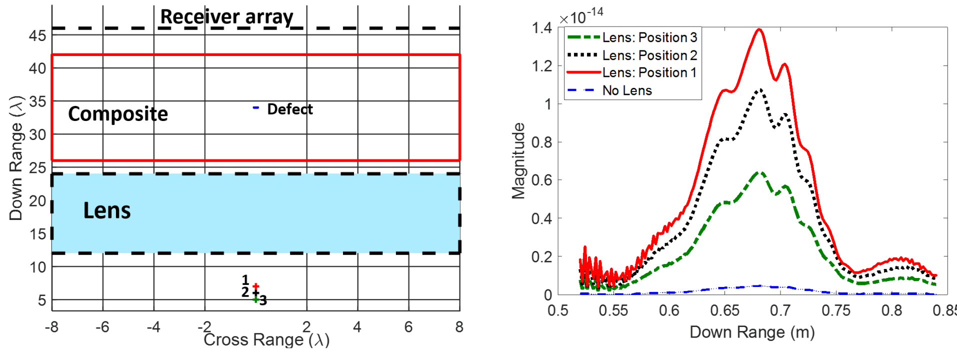

(a) (b)

Figure 7.16: TR with metamaterial lens shows enhancement of microwave imaging for sub-wavelength cross range separated sub-wavelength defects in a composite slab, (a) Schematic of test geometry, (b) TR energy comparison

back-propagated TR energy at the defect reduces as the focal spot shifts down from the defect. Additionally, it is observed that the field amplitude with the lens is 20 times larger than that obtained without the lens. Thus the lens adds sensitivity and focusing property in the down range direction.

In order to determine the minimum separation between 2 defects placed in the down range, TR simulations are conducted for varying separation distances as shown in Fig. 7.17(a) and the corresponding results are displayed in Fig. 7.17(b). While the minimum detectable cross range separation between defects for detection is noted to be $\lambda_0/10$, the minimum detectable down range separation for detection between defects is estimated to be $\lambda_0/3$. The above results demonstrate that a metamaterial lens can be used in conjunction with TR to improve the microwave imaging resolution. Better detection of sub-wavelength targets and higher resolution with superior focusing is achieved using the lens. Simulation results also indicate much more improvement in cross range resolution ($\sim \lambda_0/10$) than the down range resolution.

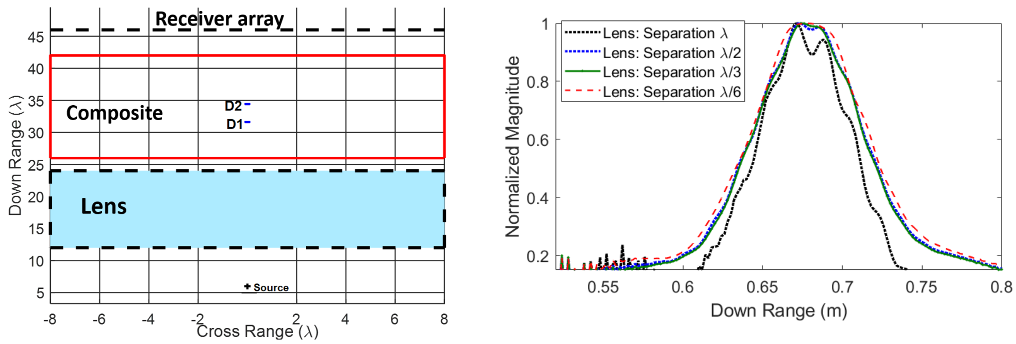

(a) (b)

Figure 7.17: TR with metamaterial lens shows enhancement of microwave imaging for sub-wavelength down range separated sub-wavelength defects in a composite slab, (a) Schematic of test geometry, (b) TR energy comparison

7.4 Geometrical optics formulation for focusing in composites

In the absence of the composite material, rays from a point source comes to a perfect focus at a distance d_2 from the lens. However, the presence of the composite results in a spread and shift of the focal point. The objective of this section is to determine analytically the spread in power density of the focal spot in the composite region, using geometrical optics, as illustrated in Fig. 7.18. The analytical set of formulas and parametric sweeps can be

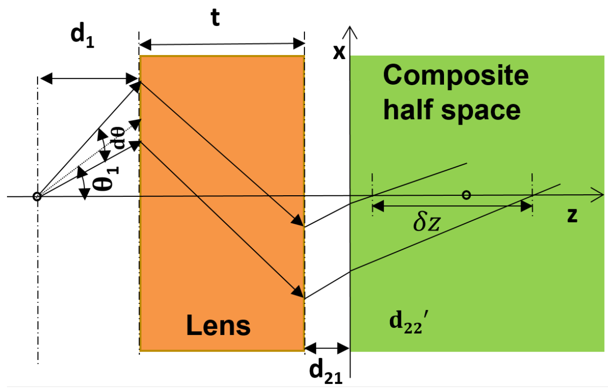

Figure 7.18: Ray diagram of a wave packet of incident angle θ_1 and angular spread dθ in the composite

used in accurately determining the shift and spread of the focused power. The steps for extracting the focal spread (δz) of a ray packet of incident angle θ_1 and angular spread $d\theta$ in the composite are itemized below:

- For incident power P, find power transmitted into composite (P_t).
- Find the focusing point (d_{22}^1) as a function of θ_1.
- Find the power density (p(z)) as a function of z, where z is the distance calculated from composite surface
- Find focal spread (δz) from p(z)

7.4.0.1 Determination of P_t

A point source radiates fields with power P in all directions. Let us consider an arc of angular spread $d\theta$ of this source with incident angle θ_1. The incident power in this region is given by $\delta P_{inc} = \frac{P}{2\pi} d\theta$. The reflectance (R) and transmittance (T) for the 2 media are given by

$$\begin{aligned} R &= \left| \frac{n_1\sqrt{1-(\frac{n_1}{n_2}\text{sin}\theta_1)^2} - n_2\text{cos}\theta_1}{n_1\sqrt{1-(\frac{n_1}{n_2}\text{sin}\theta_1)^2} + n_2\text{cos}\theta_1} \right|^2 \\ T &= \frac{4n_1n_2\text{cos}\theta_1\sqrt{1-(\frac{n_1}{n_2}\text{sin}\theta_1)^2}}{\left| n_1\sqrt{1-(\frac{n_1}{n_2}\text{sin}\theta_1)^2} + n_2\text{cos}\theta_1 \right|^2} \end{aligned} \tag{7.27}$$

It is seen from (7.27) that

$$
\begin{aligned}
T|_{n_1=1} &= \frac{4n_2\cos\theta_1\sqrt{1-(\frac{1}{n_2}\sin\theta_1)^2}}{\left|\sqrt{1-(\frac{1}{n_2}\sin\theta_1)^2}+n_2\cos\theta_1\right|^2}\\
T|_{n_2=1} &= \frac{4n_1\cos\theta_1\sqrt{1-(n_1\sin\theta_1)^2}}{\left|n_1\sqrt{1-(n_1\sin\theta_1)^2}+\cos\theta_1\right|^2}\\
T|_{\theta_1=0} &= \frac{4n_1n_2}{\left|n_1+n_2\right|^2}\\
T|_{n_1,n_2=1} &= 1
\end{aligned}
\tag{7.28}
$$

Based on the above set of equations, the ray undergoes refractions at three interfaces as follows: Interface 1: Air-lens, Interface 2: Lens-air and Interface 3: air-composite. The final transmission coefficient after the ray passes through the three interfaces is given by

$$
\begin{aligned}
T_{tot} &= T_{Int1}\times T_{Int2}\times T_{Int3}\\
T_{tot} &= \frac{4n_2\cos\theta_1\sqrt{1-(\frac{1}{n_2}\sin\theta_1)^2}}{\left|\sqrt{1-(\frac{1}{n_2}\sin\theta_1)^2}+n_2\cos\theta_1\right|^2}\times\frac{4n_2\cos\theta_2\sqrt{1-(n_2\sin\theta_2)^2}}{\left|n_2\sqrt{1-(n_2\sin\theta_2)^2}+\cos\theta_2\right|^2}\\
&\quad\times\frac{4n_3\cos\theta_1\sqrt{1-(\frac{1}{n_3}\sin\theta_1)^2}}{\left|\sqrt{1-(\frac{1}{n_3}\sin\theta_1)^2}+n_3\cos\theta_1\right|^2}
\end{aligned}
\tag{7.29}
$$

For a perfect metamaterial lens, n_2=-1 and $\theta_1 = \theta_2$. Thus (7.29) reduces to

$$
T_{tot} = \frac{4n_3\cos\theta_1\sqrt{1-(\frac{1}{n_3}\sin\theta_1)^2}}{\left|\sqrt{1-(\frac{1}{n_3}\sin\theta_1)^2}+n_3\cos\theta_1\right|^2}
\tag{7.30}
$$

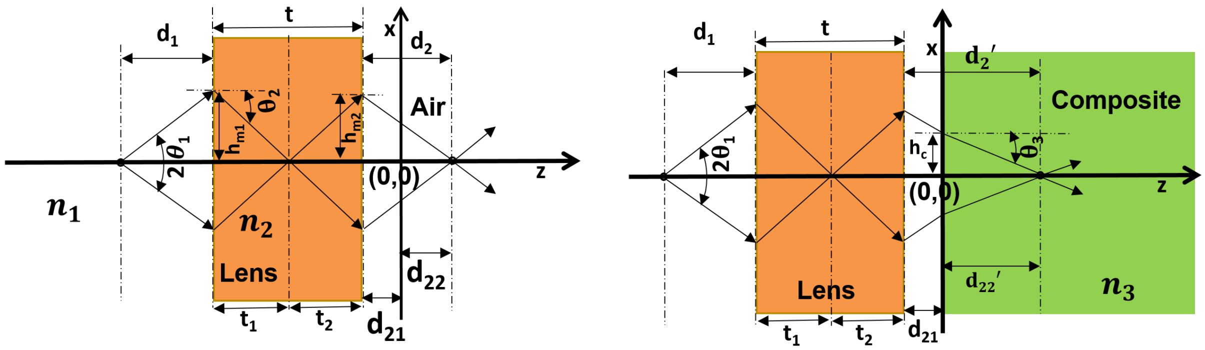

(a) (b)

Figure 7.19: Ray diagram of metamaterial lens in the presence of (a) air, (b) composite half space

Thus the total power transmitted (δP_t) by the ray packet through the metamaterial lens and the composite slab is given by

$$\delta P_t = \frac{PT_{tot}}{2\pi} = P\frac{4n_3\cos\theta_1\sqrt{1-(\frac{1}{n_3}\sin\theta_1)^2}}{2\pi\left|\sqrt{1-(\frac{1}{n_3}\sin\theta_1)^2}+n_3\cos\theta_1\right|^2}d\theta \tag{7.31}$$

7.4.0.2 Determination of d_{22}^1

In the absence of the composite, the focusing point is independent of θ_1. However, in the presence of the composite, the focusing point is dependent on θ_1. The shift in focal spot inside the composite d_{22}^1 can be calculated by ray tracing from Fig. 7.19 as a function of known paramters t, d, $d_{21}, \theta_1, \theta_2$ and θ_3 as follows.

$$\begin{aligned} &\frac{h_{m1}}{2} = d\tan\theta_1 \quad ; \quad t_1 = \frac{h_{m1}}{2\tan\theta_2} \quad ; \quad t_2 = t - t_1 \\ &h_{m2} = t_2\tan\theta_2 \quad ; \quad \frac{h_c}{2} = 2(h_{m2} - d_{21}\tan\theta_1) \quad ; \quad d_{22}^1 = \frac{h_c}{2\tan\theta_3}; \end{aligned} \tag{7.32}$$

The relationship between θ_1 and θ_2 and the relationship between θ_1 and θ_3 are given in (7.20). The final expression for d_{22}^1 is derived as a function of t, d, d_{21}, n_2 and n_3 as

$$d_{22}^1 = \frac{\Big(t\tan\theta_2 - \big(d - d_{21}\big)\tan\theta_1\Big)}{\tan\theta_3} \tag{7.33}$$

For a perfect metamaterial lens, n_2=-1 and $\theta_1 = \theta_2$. Thus (7.33) reduces to

$$d_{22}^1 = \frac{\Big(t - d - d_{21}\Big)\tan\theta_1}{\tan\theta_3} \tag{7.34}$$

7.4.0.3 Determination of the power density function

The power density (p) distribution inside the composite can be obtained as a function of z, where z is the distance calculated from front surface of the composite as

$$p(z) = \frac{\delta P_t}{\delta z} = \frac{\delta P_t}{d\theta_1} \times \frac{d\theta_1}{\delta d_{22}^1} \tag{7.35}$$

7.4.0.4 Determination of δz

Using the above formula, the power density can be directly calculated for specific incident angles. Taking into consideration that a source aperture consists of contains a bundle of rays incident at different angles θ_1, p(x) provides the power density function in the composite region. The spread can be quantified using a threshold where the total power is reduced to 10 % of its maximum magnitude. Alternate values for threshold can be chosen based on the constraints or requirements of the user.

Using the above mentioned method, the power density is calculated for the geometry described by the configuration $d_1 = 3\lambda_0$, t=6λ_0, $d_{21} = \lambda_0$ for varying index of n_3=2,4 and 6. The calculated power density is plotted in Fig.7.20. As seen from Fig.7.20(a), with the increase in n_3, the refracted angle also increases resulting in a larger focal distance. distance. The power spread (δz) is calculated as mentioned in Section 7.2.3.4 for varying n_3 and plotted in Fig.7.20 (b). As seen in Fig. 7.20 (b) with an increase in n_3, the rays are refracted further apart from each other resulting in increased spreading. The power density and spread are calculated for varying d_1 for the configuration, n_3=2, t=6λ_0, $d_{21} = \lambda_0$ and are plotted in Fig.7.21. As seen from Fig.7.21 (a), with the increase in d_1, the focusing distance d_2 decreases in accordance with (7.18). Since the fields focus earlier with increase in d_1, the rays are less separated from each other, leading to lesser spreading, as seen in Fig. 7.21 (b). The power density and spread are calculated for varying lens to composite distance (d_{21}) for the following configuration, n_3=2, $d_1 = 3.6\lambda_0$ and t=6λ_0 and are plotted in Fig.7.22. Since $d_2^1 = d_{21} + d_{22}^1$, an increase in d_{21} leads to a decrease in d_{22}^1 as seen in Fig.7.22 (a). Similar to the previous case, since the fields focus earlier with increase in d_{21}, the rays are less separated from each other, leading to lesser spreading as seen in Fig.7.22 (b). The above curves can be utilized to determine the range of the parameters for achieving a desired resolution. For example in order to achieve a resolution of 2 mm in a composite

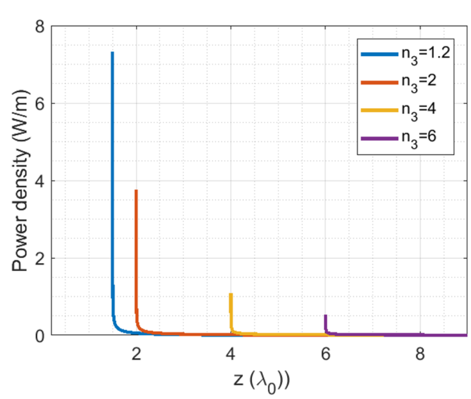

(a)

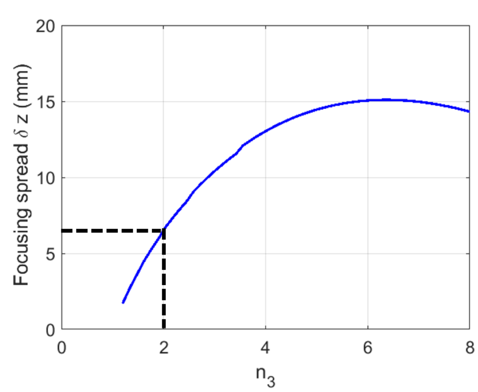

(b)

Figure 7.20: Focusing spread of power for varying d_{21} (a) p(z), (b) δz

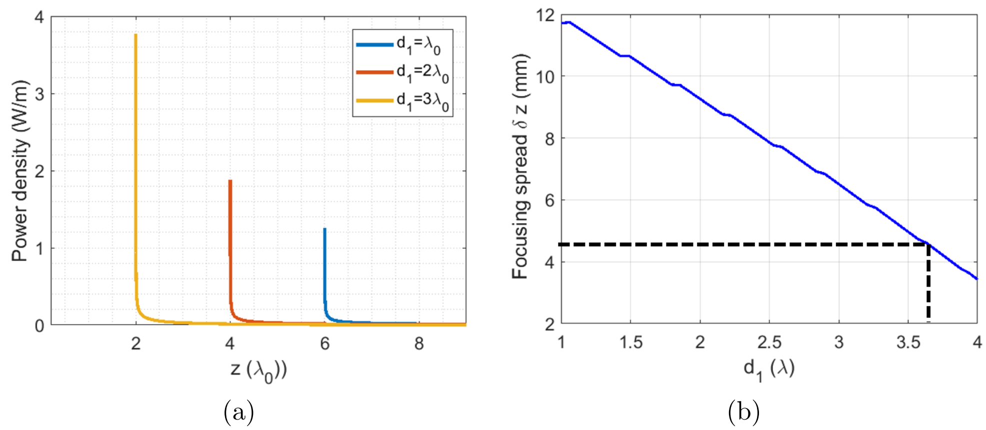

Figure 7.21: Focusing spread of power for varying d_1 (a) p(z), (b) δz

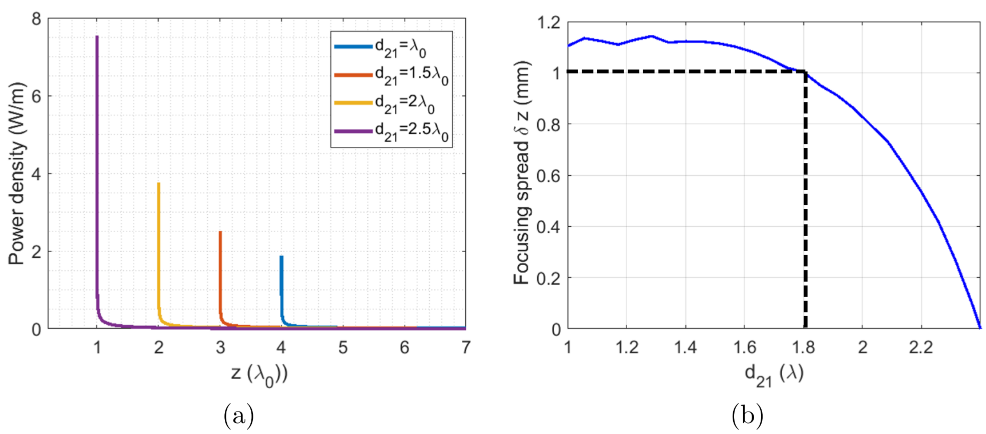

Figure 7.22: Focusing spread of power for varying d_{21} (a) p(z), (b) δz

sample with n_3= 2, the desired parameters are $d_1 = 3.6\lambda_0, 2\lambda_0 \geq d_{21} \geq 1.8\lambda_0$ (indicated by the black dashed lines of Figs. 7.20(b), 7.21(b) and 7.22(b)). It is important to note that the above formulations do not consider the effect of wave diffraction phenomenon and multiple reflections. These issues will be studied as part of future research.

7.5 Conclusion

A metamaterial lens is proposed for enhancement of microwave imaging for NDE of composites. Passive time reversal imaging experiments are performed in order to image practical defects in GFRP samples. The lens is used in conjunction with TR for detecting source, sub-wavelength targets and closely spaced sub-surface, sub-wavelength defects in composite materials. Future work in the field of the metamaterial lens involves several tasks. Analytical expressions derived here need to be extended to model shift in a lossy, imperfect metamaterial lens. Although TR was successfully combined with the lens, all the simulations were performed in transmission mode. In several practical inspections, there is only single side access. Hence the performance of the metamaterial lens for NDE applications needs be reevaluated in reflection mode. Another task involves optimizing the shape and electromagnetic properties of the lens in order to improve its down-range resolution. Finally, in order to evaluate the challenges put forward by Munk[130], the periodic structures involved in the metamaterial lens design needs to be fabricated for experimental validation of the proposed approach.

Chapter 8

Design of a SRR sensor for near field microwave imaging

8.1 Introduction

With the recent advances in sensors [136], numerical modeling [137], image processing [138] and material science, a diverse range of diagnostic [139] and prognostic techniques [140, 141, 142], are being developed for assessing structural integrity and reliability. SRRs have been used in the design of metamaterials, largely due to their frequency selective behavior [122]. Introduced by Pendry in 1999 [131], SRRs behave as sub-wavelength resonators when they are excited by a time-varying magnetic field perpendicular to the plane of the rings. Thus, these structures are able to inhibit signal propagation in a narrow band, close to their resonant frequency [143]. The structures can be modeled as LC resonant tanks, with a resonant frequency dependent on the unit cell parameters such as ring size, width and edge gaps [144]. When excited by a microstrip transmission line, these structures have depicted great potential for bio-sensing applications [145]. The dielectric coupling due to the presence of biomolecules lead to a shift of resonance frequency, which can be utilized for bio-sensing. Using similar concepts, a microwave probe was designed by Wiwatcharagoses et. al. in order to detect buried silicon chip in a plastic card [146].

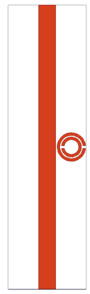

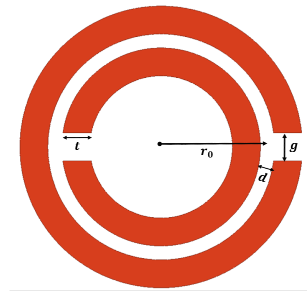

Figure 8.1: Simple microstrip line coupled SRR sensor (a) Sensor design, (b) SRR unit cell

This chapter presents the design of an SRR sensor for microwave NDE applications. Building on the prior research in this field [146], a modified design of the sensor is used for interrogating composites through edge coupling. The use of band stop design allows multiple cells of varying sizes to be integrated in an array format. Each cell resonates at a different frequency, thus providing dynamic tuning capabilities such as high Q factor, greater penetration at low frequencies and high resolution at higher frequencies. Moreover, a built in reference resonator is also integrated on the sensor for calibration of the sensors and providing better signal to noise ratio. The simplistic design of the sensor eliminates the need for complex matching circuits, thus making it compact. Simulation results demonstrate the feasibility of the sensor for detection of small target and defects in composites. Parametric analysis using the simulation model aid in determining the limits of the sensor. The performance of the fabricated sensor demonstrates its efficiency in material sensing applications. Finally, the integration of the sensor in an experimental NDE system for detection of defects in additive manufactured metals and composites validates its use in practical NDE applications.

8.2 Theory and operation

A microstrip line coupled SRR structure is shown in Fig. 8.1. The SRR unit cell behaves as a simple LC resonance circuit, with the resonant frequency f_0 given by

$$f_0 = \frac{1}{2\pi\sqrt{LC}} \tag{8.1}$$

where L and C are the effective inductance and capacitance of the unit cell [147, 148]. The inductance is primarily due to inductance of individual rings and the coupling between the two rings. The capacitance is primarily due to the split gap of each ring and the mutual capacitance between the rings. The split in the ring mainly contributes to the capacitance contribution in (8.1). It is responsible for the negative permeability of the structure and also aids in lowering the resonant frequency, by eliminating the half-wavelength requirement for resonance [149]. The second ring, which is oriented in an opposite direction to the first lowers the resonant frequency further by generating a large capacitance across the gaps between the rings. A time varying magnetic field applied parallel to the axis of the SRR cell induces surface currents on it at its resonant frequency, thus producing a dipolar magnetic field. Thus these structures behave as narrow band suppression, high Q resonators.

A Rogers RT Duroid substrate of ε_r=10.2, thickness of 1.27 mm and a microstrip line of width 1.2 mm is used for simulating the structure. The simulated scattering parameters shown in Fig. 8.2 shows resonance at 9.5 GHz frequency with a Q factor of 35. The resonant frequency shifts when the sensor is brought in close proximity of a sample due to the dielectric loading. Based on the perturbation theory for a cavity resonator [150], the resonant frequency

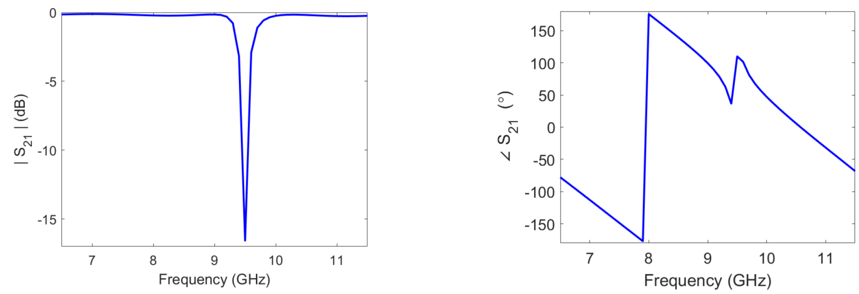

(a) (b)

Figure 8.2: Insertion loss of the SRR sensor (a) Magnitude, (b) Phase

shift (Δf) due to the presence of a material of volume V is expressed as

$$\frac{\Delta f}{f_0} \approx -\frac{\int\int\int_V (\Delta\mu|\mathbf{H}_0|^2 + \Delta\varepsilon|\mathbf{E}_0|^2)dv}{\int\int\int_V (\mu|\mathbf{H}_0|^2 + \varepsilon|\mathbf{E}_0|^2)dv}, \tag{8.2}$$

where $\mathbf{E}_0, \mathbf{H}_0$ are the electric and magnetic field respectively, ε and μ are the original permittivity and permeability and $\Delta\varepsilon$ and $\Delta\mu$ are the change of material properties respectively [151]. The resonance shift can be utilized to detect the presence of the sample and also change in the material properties, e.g., due to defects. Moreover, SRRs resonate at much higher wavelengths than its physical dimensions ($\sim \lambda/16$), thus providing sub-wavelength detection of targets. A major advantage is the fact that the SRRs are excited inductively by $\mathbf{H}$ field, thus allowing integration of multiple unit cells on the same structure.

8.2.1 Parametric sweeps

Some of the most important parameters that can affect the performance of the sensor are the average ring radius r_0, ring thickness t, split gap g and the gap between the rings d (see Fig. 8.1 (b)). The effect of these parameters are studied in order to optimize the sensor, using Ansys HFSS simulation tool.

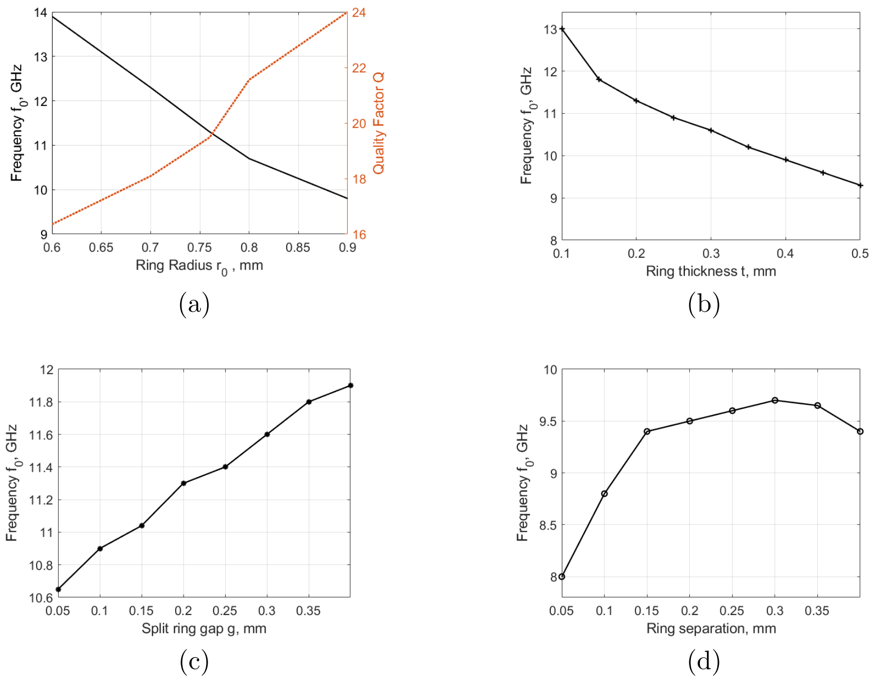

Figure 8.3: Parametric analysis of the sensor (a) Variation of f_0 and Q of the sensor with ring radius, (b) Variation of f_0 of the sensor with ring thickness, (c) Variation of f_0 of the sensor with split ring gap, (d) Variation of f_0 of the sensor with ring separation

8.2.1.1 Ring radius

The average radius of the ring r_0 is parametrically varied from 0.6 to 0.9 mm. Increasing the ring radius leads to an increase in the ring inductance as well as ring capacitance due to increased metal surface area, as described in [53]. This leads to lowering of the resonant frequency, as shown in Fig. 8.3(a). The resistance of the SRR is responsible for power dissipation and thus determines its Q factor. The Q factor can be expressed as $Q^{-1} = \delta/r_0$, where δ is the skin depth. Thus an increase in the ring radius leads to an increase of the quality factor as shown in Fig. 8.3(a). Another parameter that affects the Q factor is the thickness of the substrate. As the thickness of the substrate increases, the trace width needs to increase in order to maintain the effective impedance of the microstrip line as 50 Ω, thus increasing the Q factor of the sensor [152].

8.2.1.2 Ring thickness

The thickness of the ring t is varied from 0.1 to 0.5 mm. Increasing the thickness of the ring leads to an increase in the ring inductance due to increase in surface currents as well as ring capacitance due to an increase in surface area. This leads to a decrease in resonant frequency, as shown in Fig. 8.3(b).

8.2.1.3 Split gap

The gap of the split g is varied from 0.05 to 0.4 mm. Increasing the split gap of the ring leads to a decrease in the ring inductance due to decrease in surface area of the ring. Increasing the split gap also leads to a decrease in the ring capacitance due to an increase in the separation between the ends of the ring. This leads to an increase in resonant frequency, as shown in Fig. 8.3(c).

8.2.1.4 Ring separation

The ring separation, which is the gap between the inner and outer rings of the SRR g is varied from 0.05 to 0.4 mm. The inner ring, which is oriented in an opposite direction to the outer ring is responsible for concentrating the fields, thereby generating a large capacitance across the gap between the rings. An increase in the gap has a counterbalancing effect due to decrease in the mutual capacitance and inner ring inductance, as well as increase in outer ring inductance. If the gap is too small, the effect of the capacitance of inner ring is more pronounced, leading to an increase in resonant frequency. However, if the gap is too large, the effect of increase in outer ring inductance is more pronounced and leads to a decrease in resonant frequency. This effect is observed in Fig. 8.3(d).

8.3 Modified sensor

Prior research on using a general SRR sensor has demonstrated accurate sensing applications such as biomolecule, DNA and strain sensing [153]. However, in order to tailor fit the sensor for imaging and NDE applications, the sensor design needs to be modified. The sample is scanned from the edge of the sensor instead of the top for efficient scanning, improved detection and resolution. While one SRR ring (S) is placed on the scanning edge of the sensor, a second equivalent SRR cell (reference ring) is placed on the other side of the microstrip line. During the scanning process, the reference ring (R) does not interact with the sample and the resonant frequency of R (f_r) does not change as it is not loaded, while the resonant frequency for the S (f_s) changes due to close proximity of the sample. Thus the frequency shift of the sensing ring with respect to the reference ring can be calculated on the fly. Thus, this modification eliminates the need for calibration or a reference signal.

A second modification is introduced in the geometry of the SRR to extend the tip of S as shown in Fig. 8.4(a, b). The new design improves the resolution and enables better scanning accuracy. The fringing fields at the ring gap can detect local changes of permittivity due to the large capacitance of the SRR. The sample can be scanned along the x axis in two typical configurations as shown in Fig. 8.4 (c) and Fig. 8.4 (d). However, the resolution of imaging is limited to the dimensions of the unit cell ($\sim \lambda/16$) for 1st configuration. For a better imaging resolution, the sample needs to be inspected in the second configuration. In such a case, the fringing fields due to the split capacitance of the outer ring is primarily responsible for interrogation and inspection of the sample. Thus the resolution is dependent on the split gap ($\sim \lambda/100$), and is highly enhanced compared to first configuration. As shown in Figs. 8.4 (a,b), the tip of the sensing ring is extended outwards to guide the fringing fields

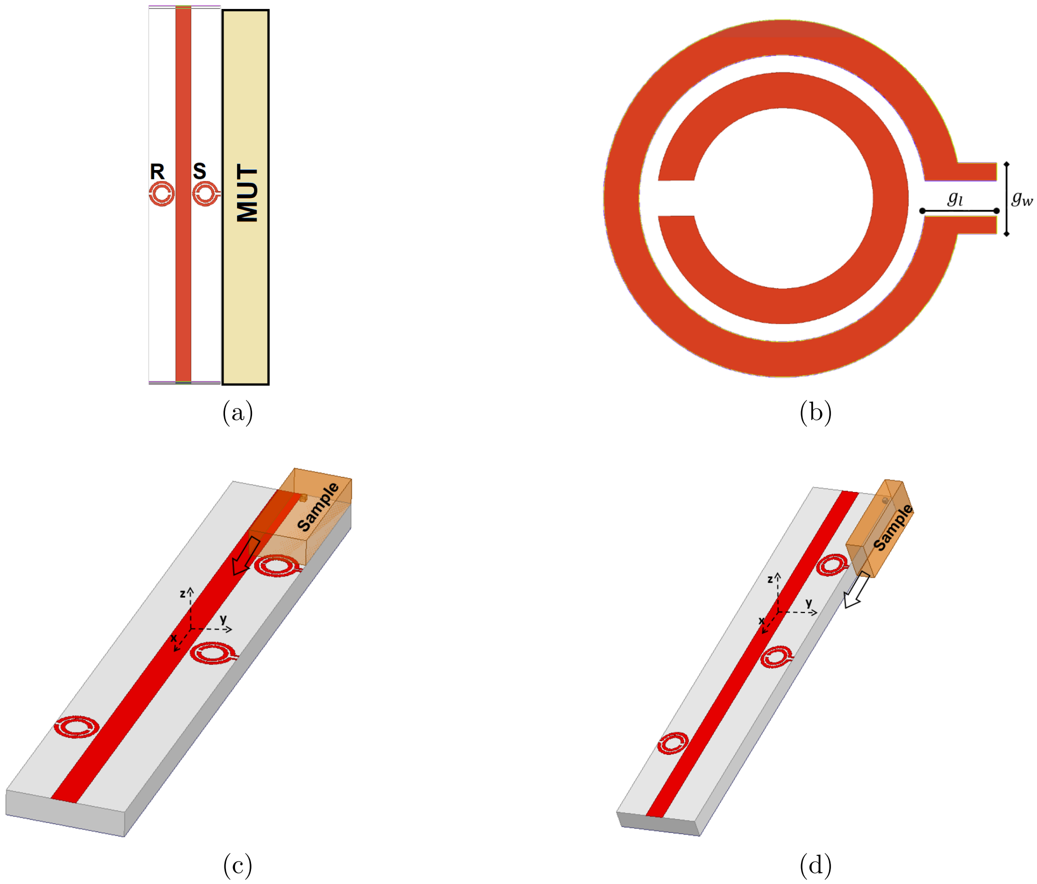

Figure 8.4: Extended tip sensor (a) Configuration 1: Sample placed parallel to surface of ring, (b) Configuration 2: Sample placed perpendicular to surface of ring, (c) Overall structure, (d) Extended ring

and make it more sensitive along the edge. The increased inductance and capacitance due to the additional metal and increase in plate area leads to a decrease in resonant frequency of S, relative to that of R, as is evident from Fig. 8.5 (a). As shown in Figs. 8.5 (c,d), the induced electric field plotted at the two frequencies show S and R excited at their corresponding resonances. It is observed that maximum induced fields are focused at the gap between the outer rings and are also guided along the tip extension of the sensing ring. Moreover, it is easier to scan large sample areas in the 2nd configuration than the 1st configuration, since the lift-off distance is minimal and the sample size is independent of the sensor. The fields from the extended sensor tip are also higher than that of a conventional SRR in the vicinity

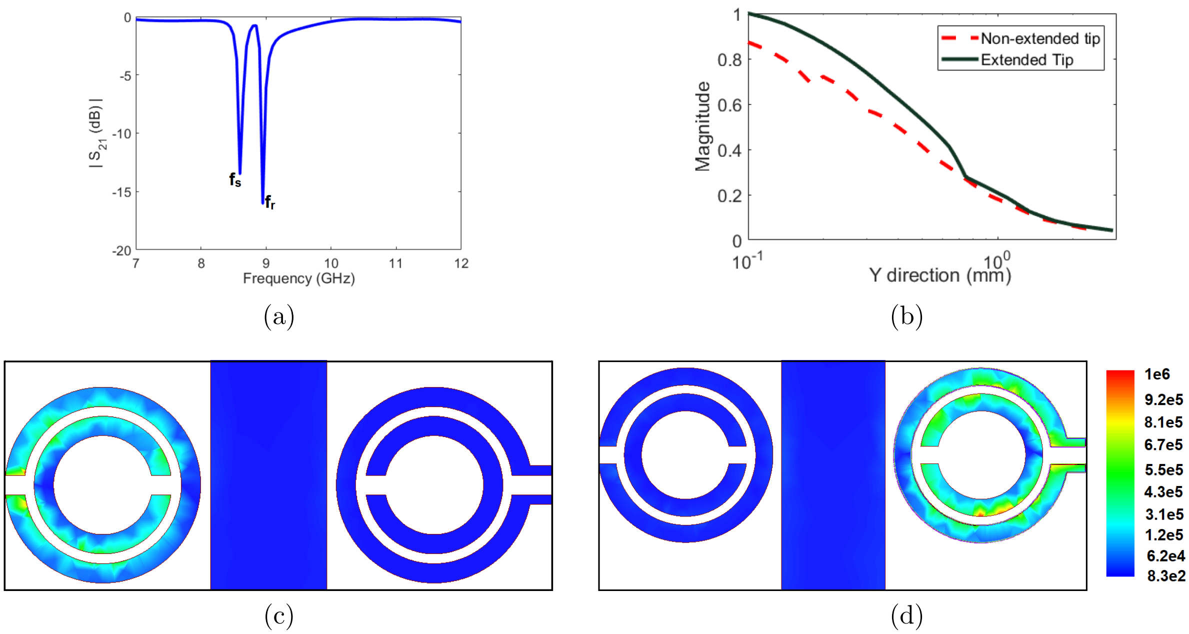

Figure 8.5: Insertion loss, field distribution and induced electric field of the extended tip sensor (a) Magnitude of Insertion loss, (b) Electric fields decay slower in the extended tip SRR sensor than the general SRR sensor, (c) Induced electric field: f_r, (d) Induced electric field: f_s

of the sensor as shown in Fig. 8.5 (b).

In order to demonstrate the advantage of the extended tip, two sets of test simulations are considered for detection of a teflon cuboid target of length, width and height of 1 mm. The two cases consider the target scanned in configurations 1 and 2 with and without the tip extension. The insertion loss for the two cases is shown in Fig. 8.6. Based on the resonance shifts of Fig. 8.6, it can be observed that without the extension, the sensor is capable of detecting the target in 1st configuration, while it is unable to detect the target in 2nd configuration. However, the extended tip sensor is capable of detecting the target both in 1st and 2nd configuration. Thus the extended tip sensor has better detection and higher resolution in 2nd configuration than the conventional SRR sensor, while keeping the fringing field distribution unhampered. Further modifications such as tapering of the tip closer to each other would increase the resolution of the sensor, but would lead to a faster decay of

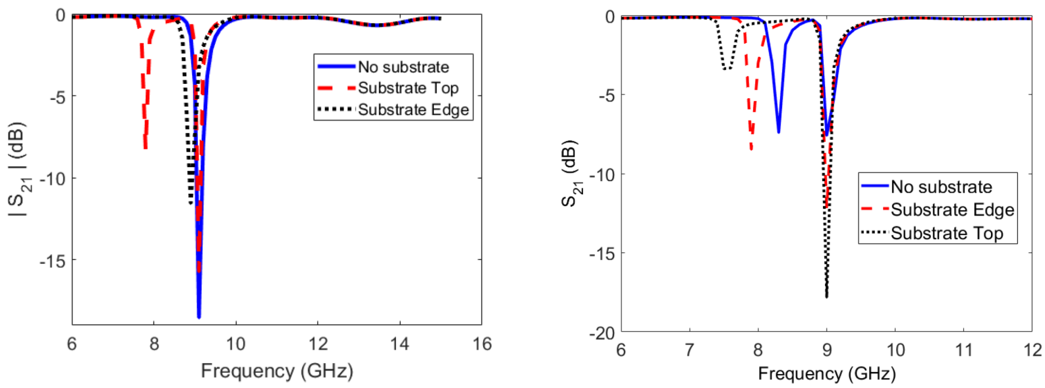

(a) (b)

Figure 8.6: Insertion loss magnitude of the sensors with and without extended tip for target detection (a) Insertion loss of sensor without tip extension in presence of target, (b) Insertion loss of sensor with tip extension in presence of target

Table 8.1: Sensor dimensions

Parameters	r_0	t	d	g_l	g_w
Dimensions (mm)	0.76	0.2	0.1	0.2	0.2, 0.1

the fringing fields, thus providing lower penetration [154].

Based on the above mentioned concepts, a final prototype design is chosen for simulations as shown in Fig. 8.7(a), with dimensions listed on Table 8.1. The band-stop structure allows integration of multiple SRR cells on the microstrip line, each resonating at different

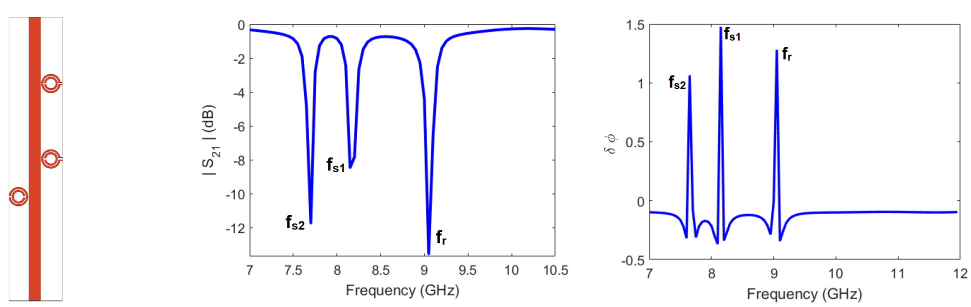

(a) (b) (c)

Figure 8.7: Final Sensor (a) Design, Resonant frequency obtained from Insertion loss (b) Magnitude, (c) Phase difference

frequencies. Thus two sensing rings (S1, S2) are placed on the same side of the microstrip line with different gap widths of 0.2 and 0.1 mm, along with R on the other side of the line. Additionally all the rings are separated by a distance of 8 mm ($\sim \lambda/4$) from each other so that there is no coupling between them. The gap width of S2 is smaller than that of the first sensing ring. As discussed in section II A, a lower gap width of S2 results in a capacitance increase, thus leading to a lower resonant frequency, as shown in Fig. 8.7(b). Hence S2 has a lower resonant frequency (f_{s2}) than that of S1 (f_{s1}). From simulation studies and parametric analysis, it is observed that both magnitude and phase information are sensitive to sample properties and thus can serve as candidates for determining the resonance shift. As shown in Fig. 8.7(c), the exact measure of the resonant frequency can be extracted from the local minima of the unwrapped phase, obtained by differentiating it with respect to frequency. The evolution of the proposed sensor along with corresponding results are presented in Fig. 8.8 (a), (b).

8.4 Simulation studies

8.4.1 Parametric analysis for imaging

Parametric studies are performed using HFSS to determine the limits and capability of the final sensor for defect detection and imaging. A dielectric sample is examined, with its dielectric constant and the lift-off distance between the sample and sensor tips varied. For each of these parameters, the shift of the resonant peak value is used as a measure of the resolution of the sensor.

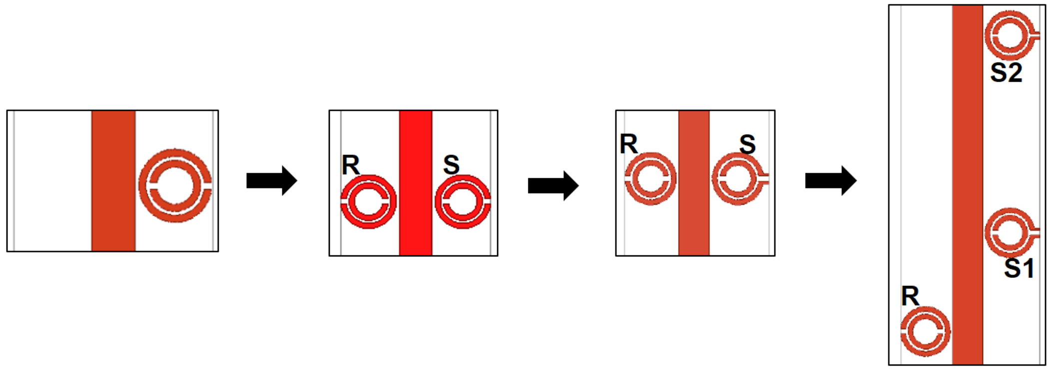

(a)

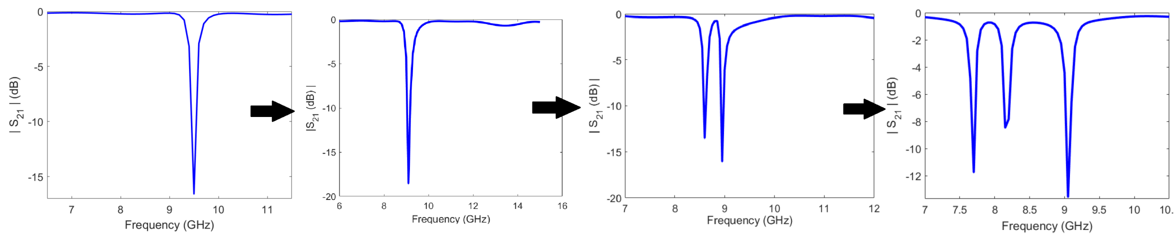

(b)

Figure 8.8: Evolution of the proposed sensor, (a) Design modifications, (b) Performance of the designs (Addition of equivalent reference ring shifts resonance to the left; Extension of tip of S results in two separate resonant frequencies for R and S; 3 resonant frequencies for R, S1 and S2)

8.4.1.1 Dielectric constant

The presence of a dielectric sample changes the capacitance of the overall structure due to dielectric loading, thus changing the resonant frequency of the unit cells, according to (8.2). Three dielectric materials having different dielectric constant (ε_r=1,3 & 9) are placed in configuration 2. As seen from Fig. 8.9 (a), f_r is constant for all the cases, while f_{s1} and f_{s2} shifts to the left due to the dielectric loading of the sample. The shift in the resonance frequency (δf) with respect to dielectric constant of the sample is studied by varying ε_r from 1 to 10, as shown in Fig. 8.9 (b). The slight discrepancy in Fig. 8.9 (b) is a result of the computational errors associated with the numerical simulations. The 2nd order polynomial fitted calibration plot can serve as a look up table to directly calculate the dielectric constant

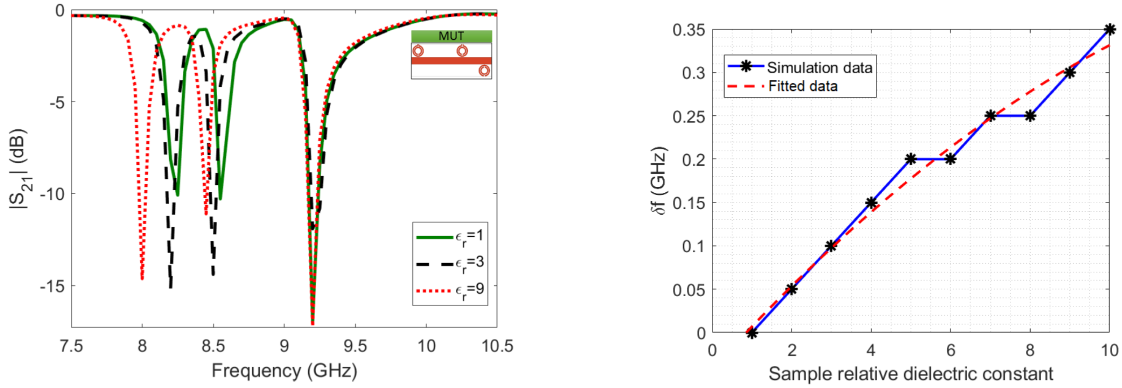

(a) (b)

Figure 8.9: Relationship of resonance with dielectric constant (a) Magnitude of insertion loss vs ε_r, (b) Resonant frequency shift vs ε_r

of an unknown sample from the resonance frequency shift of the sensor.

8.4.1.2 Sample lift-off

The fringing fields at the tip of the ring interacts with the dielectric sample resulting in a change of the effective capacitance and inductance of the sensor. As the sample is moved farther away from the sensor edge, this interaction is weaker. Hence the effect of lift-off and resonant frequency needs to be studied in order to determine the limits of detection. When the sample is placed at the edge of the sensor, both f_{s1} and f_{s2} shifts to the left, as seen in Fig. 8.10 (a). As the sample is moved farther away from the sensor, both f_{s1} and f_{s2} move closer to the actual resonant frequencies of the rings, due to less interaction of the fields with the sample. The shift in the resonance frequency (δf) is studied by varying the lift-off distance from 0 to 10 mm, as shown in Fig. 8.10 (b). Additionally, it is observed that S1 has a deeper field penetration than S2 due to its larger gap width, and thus might be more sensitive towards lift-off, as seen in Figs. 8.10 (a,b). This is evident from the the electric field distribution plot at the two ring resonances (Figs. 8.10 (c,d)), which shows that the fields

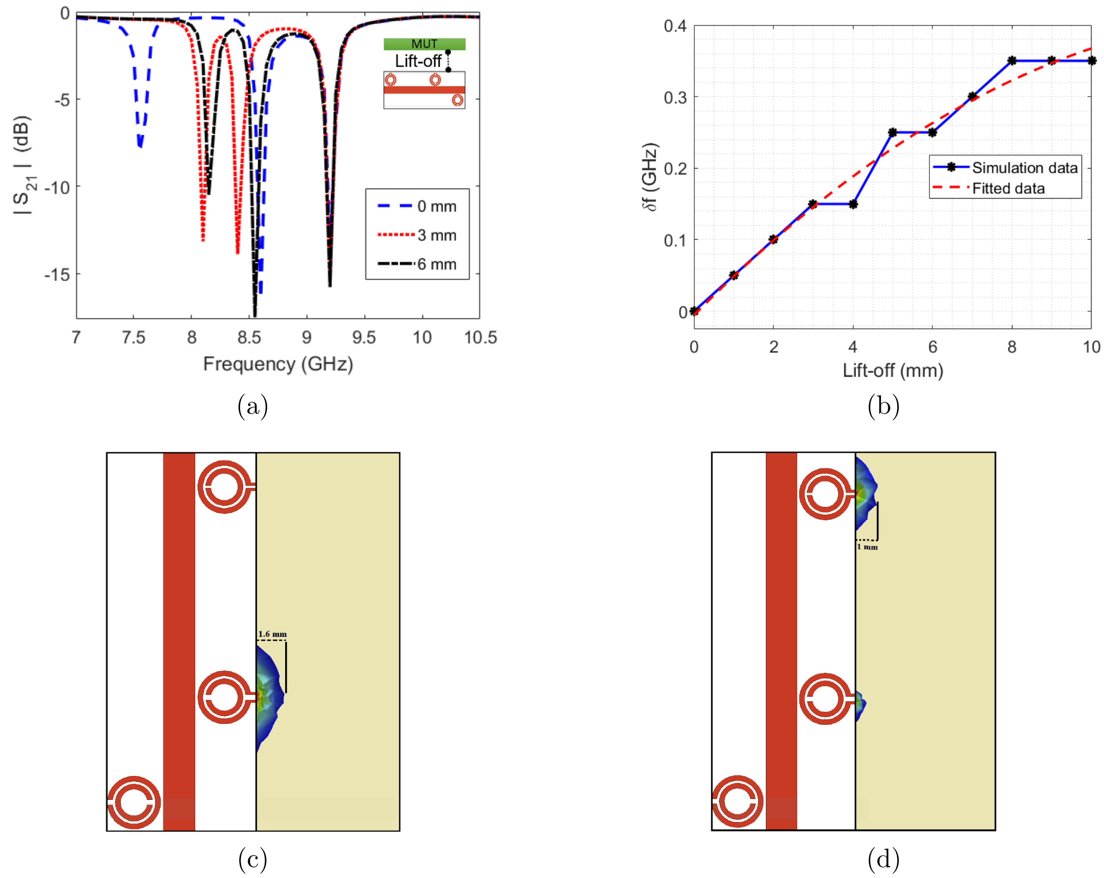

Figure 8.10: Relationship of resonance with lift-off (a) Magnitude of insertion loss vs lift-off, (b) Resonant frequency shift vs lift-off, (c) Electric field at f_{s1}, (d) Electric field at f_{s2}

decays to 5 % of its total magnitude in 1.6 mm for sensing ring 1 and 1.1 mm for sensing ring 2.

8.4.2 Imaging studies

HFSS simulations are performed to evaluate the proposed sensor in order to mimic imaging experiments. Fig. 8.11 shows the schematic of two geometries for detection of a target in air and a defect in a GFRP sample with dielectric constant 3.4.

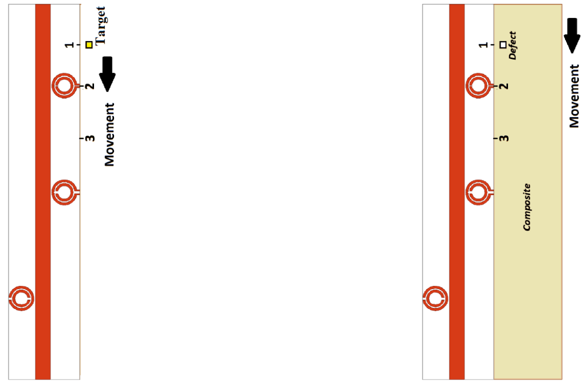

(a) (b)

Figure 8.11: Schematic of 2 simulation geometries (a) Target detection, (b) Defect detection

8.4.2.1 Target imaging

A dielectric square block with dimensions 0.4×0.4×0.4 mm^3 and ε_r=3 is moved along the edge of the sensor, as shown in Fig. 8.11(a). The insertion loss magnitude is plotted in Fig. 8.12(a) for positions 1, 2 and 3. From Fig. 8.12(a), it is observed that for positions 1 and 3, the resonant frequency for all rings is unchanged, since both positions correspond to no change in the dielectric properties. The resonant frequency of sensing ring 2 shifts to the left at position 2 when the fringing fields of SRR 2 interacts with the target, validating equation (2) in section 4(a). The phase change at the resonant frequencies is tracked along with the scan and plotted in Fig. 8.12(b). In the vicinity of the target, the phase at the resonant frequency of both sensing rings changes by 15°, while it remains constant at all other frequencies. The full width at half maxima (0.6 mm) of the phase change (Fig. 8.12(b)) can provide an estimate of the actual size of the target.

8.4.2.2 Defect detection

A GFRP composite sample, placed in close proximity of the sensor is moved along the edge, as shown in Fig. 8.11(b). The sample has a small air void (defect) of 0.5 mm diameter,

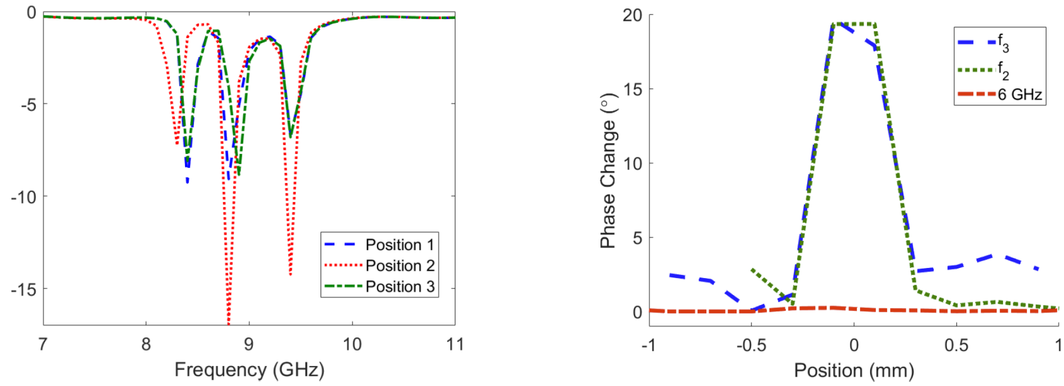

(a) (b)

Figure 8.12: Simulation results of target imaging (a) Insertion loss for 3 positions: S2 detects target at position 2, (b) Phase change at resonant frequencies provides an estimate of the target size

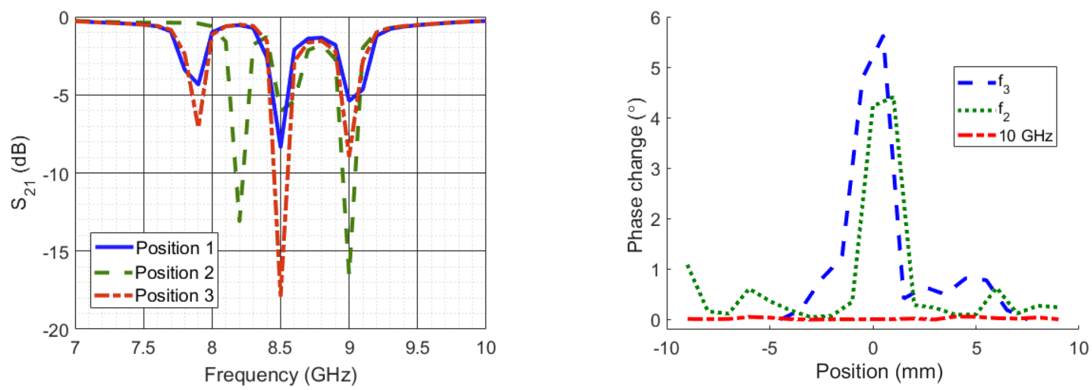

(a) (b)

Figure 8.13: Simulation results of defect imaging (a) Insertion loss for 3 positions: S2 detects defect at position 2, (b) Phase change at resonant frequencies provides an estimate of the defect size

placed 0.5 mm away from the edge of the sample. For the three different positions shown in the figure, the insertion loss magnitude is plotted and shown in Fig. 8.13(a). Similar to the previous case, it is observed that for positions 1 and 3, the resonant frequency for all rings are unchanged, since both positions correspond to no change in the dielectric properties. However, for position 2, the resonant frequency of sensing ring 2 shifts to the right. The loss of dielectric material is responsible for shifting the resonance to the right. The phase change

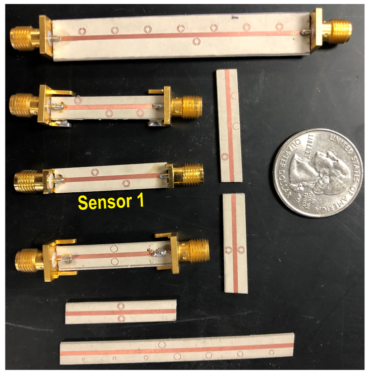

Figure 8.14: Different sensors fabricated (US quarter for size comparison)

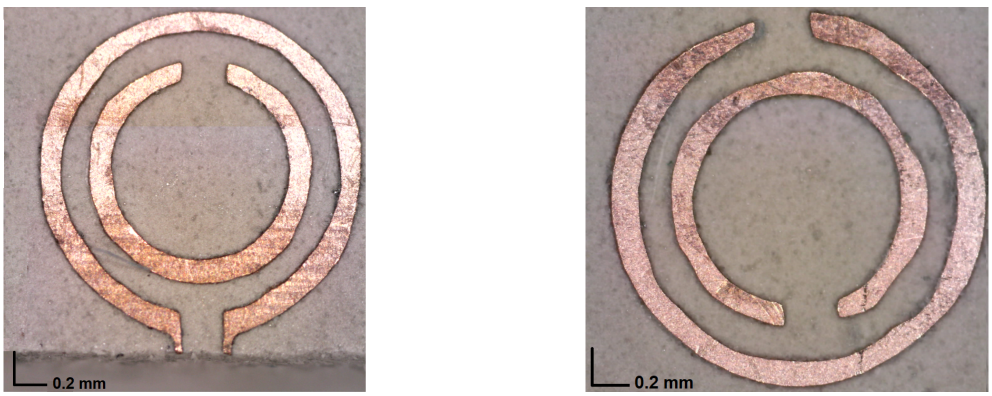

(a) (b)

Figure 8.15: Fabricated sensors: Microscope image of (a) extended tip sensing ring, (b) reference ring

at the resonant frequencies is tracked with respect to the scan and plotted in Fig. 8.13 (b). In the vicinity of the defect, the phase at the resonant frequency of both sensing rings changes by 6°, while it remains constant at all other frequencies. The full width at half maxima (1 mm) of the phase change (Fig. 8.13 (b)), can provide an estimate of the actual size of the defect.

8.5 Measurement results

Different variations of the proposed sensors are fabricated and shown in Fig. 8.15. The sensors were fabricated using conventional photolithography.

8.5.1 Performance of the sensor

The insertion loss of the sensor is measured using a E5070B Vector Network Analyzer (VNA). The performance of the sensor with a reference ring and a single sensing ring shows two resonant peaks. The first resonance at 6.2 GHz corresponds to the extended tip SRR, while the second resonance at 9.1 GHz corresponds to the reference SRR. The insertion loss is investigated in presence of different materials, placed near the tip and are shown in Fig. 8.16. It is clearly observed that the resonant frequency of the reference SRR is unchanged, while the resonant frequency of the extended tip SRR shifts in the presence of the materials. The resonance frequency shifts to the right in the presence of conductive materials such as aluminum ($\sigma = 10^6$ S/m) and CFRP ($\sigma = 5 \times 10^3$ S/m). The resonance frequency shifts to the left in the presence of dielectric materials such as plastic ($\varepsilon_r = 2$) and GFRP ($\varepsilon_r = 3.1$). When the sensor is positioned close to a 1 mm diameter through hole defect in the GFRP sample, the resonant frequency shifts to the right with respect to a healthy sample (Fig. 8.16) in accordance with (8.2) and Section IV A. Thus, the sensor is sensitive to dielectric as well as conductive changes of the test sample and shows potential for NDE applications.

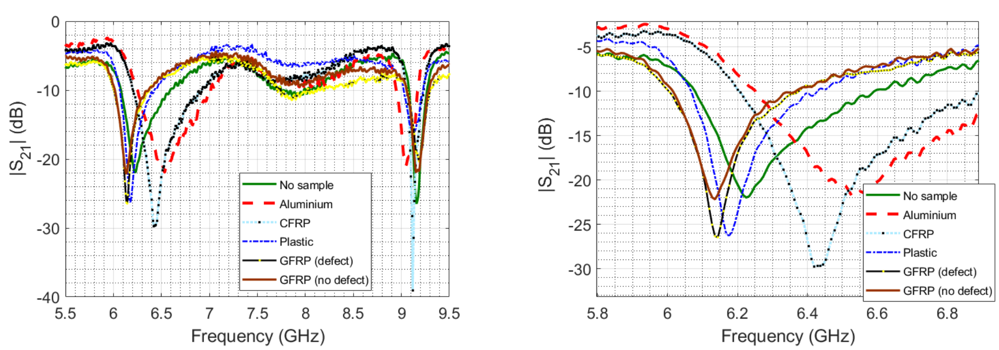

(a) (b)

Figure 8.16: Performance of the sensor (a) Measured Insertion loss, (b) Resonance shift

8.5.2 Microwave imaging experiments

8.5.2.1 Experimental setup

The imaging setup consists of the microstrip sensor directly connected to the VNA. The sensor is kept stationary, while moving the test samples using an X-Y raster scanning platform. The scanner is driven by Aerotech linear motor model MTC250, with fully control from A3200 software-based machine controller. An in-house C sharp software synthesizes the motion and data collection operation. The motion resolution is 0.1 mm in x, y and z directions. Ignoring the tilt angle and surface roughness, a nominal lift-off of 0.5 mm is used for performing all measurements in order to ensure that the sample does not touch the sensor. The experimental setup is shown in Fig. 8.17. The overall setup is initially utilized to detect a metallic target. Finally, the system is used to image sub-wavelength defects in additive manufactured metallic and composite samples.

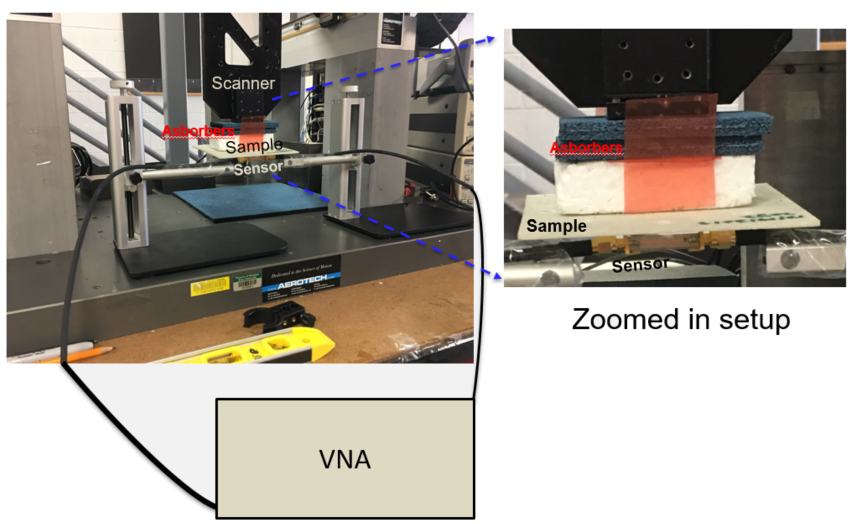

Figure 8.17: Experimental setup for imaging

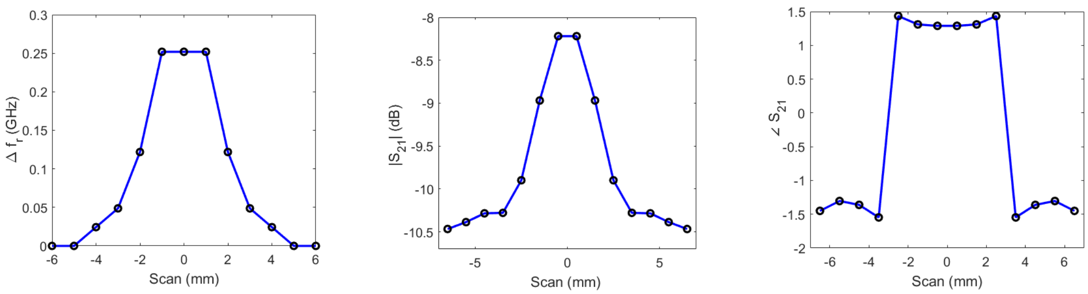

(a) (b) (c)

Figure 8.18: Detection of metal using sensor (a) Resonance shift, (b) Shift of S_{12} magnitude at resonance, (c) Shift of S_{12} phase at resonance

8.5.2.2 Metal detection

A one dimensional coarse scan (1 mm step size) of an aluminium sample of dimensions 6.5 mm × 10 mm × 10 mm is performed in presence of the sensor. Fig. 8.18 (a) shows that the resonant frequency is 6.2 GHz in the absence of the sample, it starts increasing and shifts by a maximum of 250 MHz when the sample is at the center of the ring. As the sensor starts leaving the sample, the resonant frequency starts decreasing again and goes back to 6.2 GHZ as the sample exits the sensor. Additionally, the insertion loss magnitude and phase is computed at the resonant frequency of the sensor and is plotted in Figs. 8.18 (b,c). The resonant frequency shifts to the right in the presence of the metal, thus leading to an increase of the magnitude and phase of the insertion loss at the resonant frequency in air.

8.5.2.3 NDE of additive manufactured metals

As discussed in the previous section, the sensor shows a high sensitivity towards detection of metals. Next, the sensor is used to image defects of various shapes and sizes in an additive manufactured metal (AMM) sample. During the additive manufacturing process, the production of some defects are unavoidable, such as surface roughness, fatigue and porosity [155, 156]. Hence a robust and reliant NDE system is required for inspection of

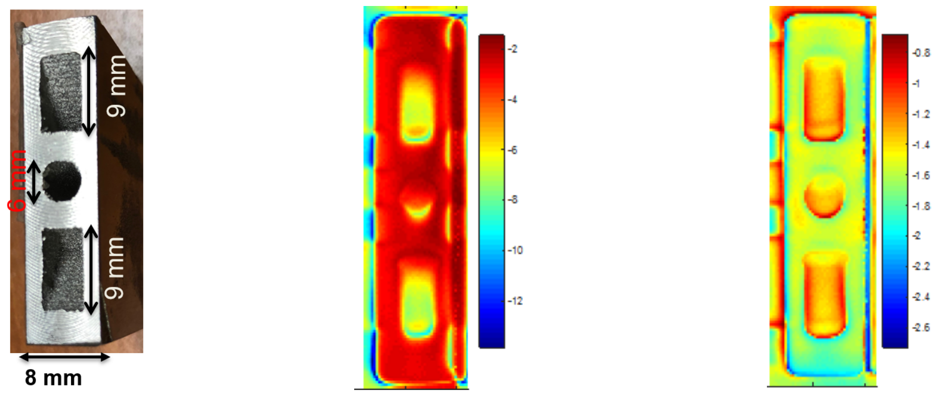

(a) (b) (c)

Figure 8.19: Imaging of different shaped defects in a AMM sample (a) Sample, (b) S_{12} magnitude at resonance, (c) S_{12} phase at resonance

such materials during manufacturing as well as in service conditions. The proposed sensor is utilized for imaging surface holes of an AMM sample. The sample is scanned with an x and y resolution of 0.25 mm.

A 35 mm × 50 mm × 8 mm SS316 sample is printed using a standard Binder Jet process. One surface of the sample consists of closely spaced circular and rectangular holes, as shown in Fig. 8.19 (a). The length and width of both rectangular holes are 9 mm × 4 mm, while the diameter of the circular hole is 6 mm. These surface holes serve as calibration defects in order to estime the accuracy of the sensor. During the scan, the raw magnitude and phase of the insertion loss is computed at the resonant frequency of the sensor and is plotted in Figs. 8.19 (b,c). The resonant frequency shifts to the right in the presence of the metal, thus leading to an increase of the magnitude and phase of the insertion loss. Both magnitude and phase values of the sensor is capable of imaging all the three holes with high precision and accuracy.

Another surface of the sample consists of 4 closely spaced sub-wavelength circular flat bottom holes D1, D2, D3 and D4 of diameter 0.7 mm ($\lambda/45$), 1.5 mm ($\lambda/20$), 1 mm ($\lambda/30$)

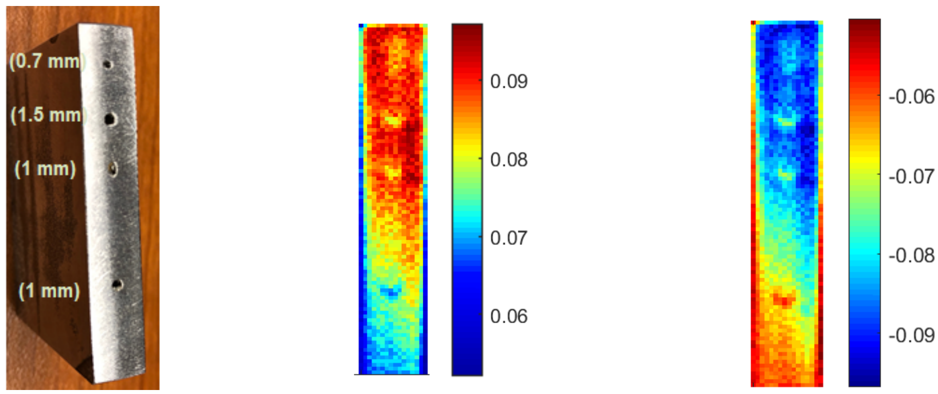

(a) (b) (c)

Figure 8.20: Imaging of different sized defects in a AMM sample (a) Sample, (b) S_{12} magnitude at resonance, (c) S_{12} phase at resonance

and 0.9 mm ($\lambda/33$) as shown in Fig. 8.20 (a). The raw magnitude and phase of the insertion loss is computed at the resonant frequency of the sensor and is plotted in Figs. 8.20 (b,c). The three bigger holes (D2, D3 and D4) are easily detected, while the smallest hole (D1) indication is relatively small, as shown in Fig. 8.20 (b, c). Thus the sensor demonstrates its capability for imaging defects in an AMM sample of different shapes and size, including sub-millimeter defects of size as small as 0.7 mm.

8.5.2.4 NDE of composites

Finally, the sensor is utilized for imaging of sub-wavelength defects in a GFRP composite sample. A vacuum assisted resin infusion technique was used to manufacture a glass fiber reinforced polymer (GFRP) laminate (fibers woven at 0 and 90 °) in house at the Composite Vehicle Research Center. A reinforcement of S2-glass plain weave fabric (Owens Corning Shield Strand S) with areal weight of 818 g/m^2. and a two part toughened epoxy SC-15 were used with areal weight of 818 g/m^2. The resin used was a two part toughened epoxy, namely SC-15 (Applied Poleramics Inc., CA). The laminates were cured in a convection oven

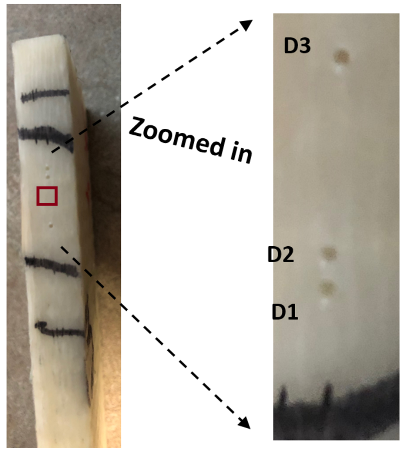

Figure 8.21: GFRP Sample with defects

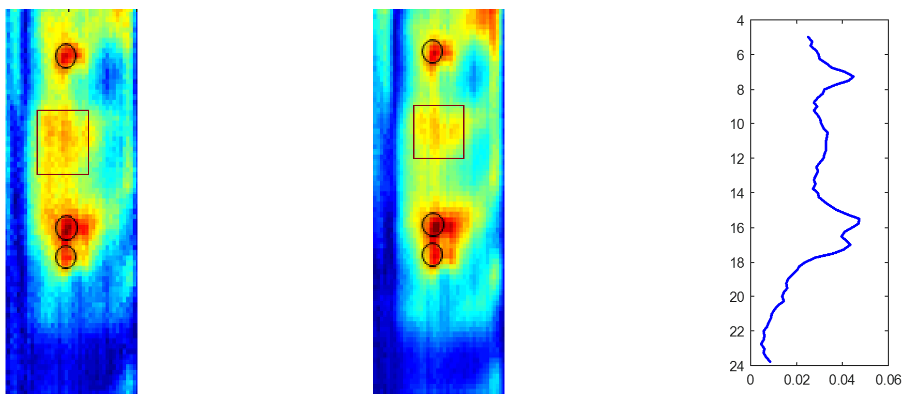

(a) (b) (c)

Figure 8.22: Imaging of different sized defects in a GFRP sample (red box indicates delamination area) (a) S_{12} magnitude at resonance, (b) S_{12} phase at resonance, (c) Line scan signal detects all defects

at 60°C for 2 h followed by a post cure of 4 h at 94°C. Three surface flat bottom holes (D5, D6 and D7) of diameter 0.7 mm ($\lambda/45$) are machined in the sample. D5 and D6 are closely positioned with a spacing of 0.7 mm, while D7 is situated at a distance of 1 cm ($\lambda/3$) away from D6. The depth of D6 and D7 is 1 mm ($\lambda/30$), while the depth of D5 is 0.4 mm ($\lambda/80$). Along with the holes, there is a fiber delamination around the area between D6 and D7, as indicated in Fig. 8.21. The GFRP sample along with the fabricated defects are shown in Fig. **??**. The sample is scanned with x and y resolution of 0.25 mm. The raw magnitude and phase of the insertion loss is computed at the resonant frequency of the sensor and is plotted in Figs. 8.22 (a,b). The three defects are easily detected, and the smallest defect (D5) barely detectable. Although it can be seen that there is some coupling between D5 and D6, a simple threshold enhances the image. Along with the defects, both amplitude and phase measurements show a region of the sample indicated by the box, which could be due to the delamination. As shown in Fig. 8.22 (c), a line scan of the energy image through the peak value indicates three peaks corresponding to three defects. The full width at half maxima of this signal can be used to determine the spatial dimensions of the defects. Further, it is interesting to note that the peak corresponding to the smallest defect D5 is smaller than that of D6 and D7. This shows that the sensor can also be potentially used for sub-surface depth imaging. Thus, the sensor demonstrates it capability for imaging sub-wavelength surface defects as well as fiber delaminations in composite materials.

8.6 Conclusion

A microstrip line coupled SRR sensor is designed for near field microwave imaging and NDE applications. The design of the unit cell is optimized by conducting robust, parametric sweeps of the important design parameters of the ring. The sensor is optimized for scanning samples in the 2nd configuration, rather than the 1st configuration (Fig. 8.4(a,b)) in order to improve the scanning efficiency and resolution. The efficiency of the sensor for NDE is studied using HFSS model based parametric study with respect to dielectric constants and lift-off distances. The fabricated sensors show great potential for use in a microwave imaging setup to detect sub-wavelength, surface defects of various shapes and sizes in metals and GFRP composites. High sensitivity and low detection error demonstrates the efficacy of the sensor for NDE of composites. The potential future applications and design strategies of the sensor lay the foundation for a robust, reliant NDE system for rapid inspection of large areas of composites. Future work involves studying the performance of the fabricated sensors for sub-surface 3D imaging, as well as design of the sensors in rigid-flex substrates in order to image complex structures.

Chapter 9

Conclusion

9.1 Key contributions

A novel hybrid electromagnetic imaging system is developed that combines the benefits of both far field and near field electromagnetic systems.

Key contributions of this research can be enlisted below:

- Design of a robust microwave TR imaging algorithm: A 2D FDTD numerical model is used for TR processing and imaging based on the concepts of TR is developed for simulation studies and parametric analysis. Time reversed electromagnetic fields are back-propagated using the numerical model to focus back at the primary or secondary source locations. Advanced localization techniques such as the minimum entropy and time integrated energy method are utilized to achieve spatio-temporal focusing.

- Configuration of a far field microwave system: A pulsed time domain experimental system is configured for performing far field TR imaging of targets in air and defects in composite samples.

- Design of a cheap, microstrip TR mirror: A microstrip time reversal mirror is developed for compact TR imaging and applied for detection and hyperthermia of tumors in multi-layered breast phantoms.

- Design of a metamaterial lens: The challenges associated with the diffraction limited resolution of far field imaging are investigated by the design of a MM lens in the measurement set up for achieving sub-wavelength resolution.

- Sub-millimeter near field prbe: Novel probes based on SRR sensors are investigated for high resolution, sub-wavelength near field imaging applications.

9.2 Future work

The current research conducted in TR paves way to a lot of possibilities of using it for further applications. Some of the interesting applications are as follows:

- MUSIC and DORT: A shortcoming of the basic TR technique is that it follows diffraction limits. From a mathematical point of view, the time reversed signals for two well resolved targets correspond to the linear combination of two non-null orthogonal eigenvectors. However, when the targets are not well separated, the eigenvectors are no longer orthogonal due to the cross-coupling between the targets. Thus, the image fields interfere with each other resulting in poor image quality. Moreover, iterative TR results in the fields converging to the strongest target. However, techniques such as MUSIC that utilize the rank-deficient nature of TR data and use subspace rather than signal space of TR data might be helpful in detection of closely spaced targets. Moreover, complicated TR selective focusing methods, such as the DORT can be employed to focus on individual targets selectively. The basic technique of TR-DORT is shown in Fig. 9.1. These algorithms are currently being investigated for application to detection of closely spaced targets. However, they are either time-consuming or expensive, since they require design of automated RF switching circuits for recording

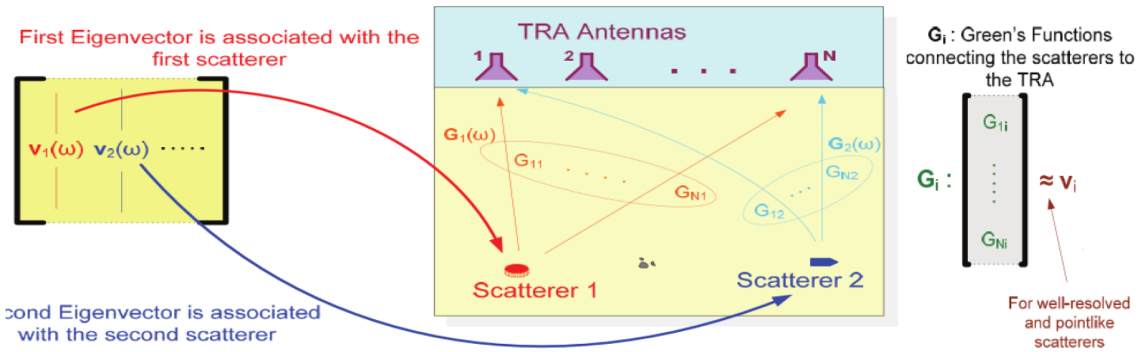

Figure 9.1: Full time domain DORT Technique for well resolved point-like scatterers

multiple projections of the antenna array system.

- Challenges in breast tumor imaging: Several future work on using TR for breast tissue imaging needs to be conducted in order to translate the method from lab into the clinical stage. They are as follows:
  - Experiments with this setup on more realistic breast phantoms with multiple, sub-wavelength sized tumors need to be performed.
  - A fully automated coherent antenna array experimental setup, coupled with a parallel supercomputer for the back-propagation simulations needs to be set up in order to use the method has potential for real time implementation.
  - A robust algorithm needs to be developed that is capable of extracting tumor contribution from total fields, thus eliminating the need for the healthy breast contribution.
  - A detailed tissue model along with clutter removal techniques is needed for validating the approach for further complicated and realistic scenarios.
  - The increase in breast tissue temperature needs to be calculated from the bio heat transfer equation.

  - Gelatin based phantoms for thermal therapy applications should also be investigated.
  - Finally, the recent development in the field of cheap and compact RF circuits for TR will be utilized to develop a physical TRI system that can use the similar hardware systems for imaging as well as thermal therapy applications.

- Design issues of metamaterial lens: Future work in the field of the metamaterial lens involves several tasks. They are as follows:

  - The analytical expressions and parametric studies for determining the focusing spread and shift for a lossy, imperfect metamaterial lens needs to be derived.
  - Although TR was successfully combined with the lens, all the simulations were performed in transmission mode. In several practical inspections, there is only single side access. Hence the performance of the metamaterial lens for NDE applications needs be reevaluated for reflection mode setup.
  - Another interesting future work lies in the optimizing of the shape or electrical properties of the lens in order for improving its down-range resolution.
  - Simulation studies need to be conducted in the future considering the physical, periodic structures, in order to match simulation studies with experiments and estimate the discrepancies between an ideal homogenized medium and practical periodic structures
  - Finally the lens needs to be fabricated and practical NDE experiments need to be performed to demonstrate the practical significance of the lens.

- Tailor SRR sensors for complex imaging scenarios: Future work in this research involves:

- studying the performance of the fabricated sensors for sub-surface 3D imaging. Based on prior simulation studies, the sensor is expected to have 2 mm of sub-surface penetration. Experiments for detecting sub-surface defects need to be performed.
- The design of the sensors in rigid-flex substrates needs to be investigated in order to perform imaging of complex structures such as dielectric tube defects and joints.
- The optimum design of the sensor allows array integration in a PCB layer stackup. This property needs to be utilized by designing a multiple switching circuit based sensor, which can be potentially utilized for rapid near field three dimensional imaging.

APPENDICES

Appendix A

Inverse scattering problem

The free space vector wave equation for electric field of a time harmonic wave incident on an isotropic arbitrarily shaped object is given by [13]:

$$\nabla^2 \overrightarrow{E} + \omega^2 \mu_0 \varepsilon(\overrightarrow{r}, \omega) \overrightarrow{E} = 0. \tag{A.1}$$

The corresponding scalar wave equation in order to solve individual components of the electric field is given by :

$$\nabla^2 \phi(\overrightarrow{r}) + \omega^2 \mu_0 \varepsilon(\overrightarrow{r}, \omega) \phi(\overrightarrow{r}) = 0, \tag{A.2}$$

where $\phi(\overrightarrow{r})$ can be $E_x(\overrightarrow{r}), E_y(\overrightarrow{r}), E_z(\overrightarrow{r})$. Adding and subtracting $\omega^2 \mu_0 \varepsilon_0$ from the above equation, we obtain [33]

$$\begin{aligned} \Big(\nabla^2 + \omega^2 \mu_0 \varepsilon(\overrightarrow{r}, \omega) + \omega^2 \mu_0 \varepsilon_0 - \omega^2 \mu_0 \varepsilon_0\Big) \phi(\overrightarrow{r}) &= 0 \\ \Big(\nabla^2 + k_0^2) \phi(\overrightarrow{r}\Big) &= -O(\overrightarrow{r}, \omega) \phi(\overrightarrow{r}) \end{aligned} \tag{A.3}$$

where $k_0^2 = \omega^2 \mu_0 \varepsilon_0 = (2\pi/\lambda)^2$, λ is the wavelength of the time harmonic field and $O(\overrightarrow{r}, \omega) = \omega^2 \mu_0 \varepsilon_0 (\varepsilon_r(\overrightarrow{r}, \omega) - 1)$. In the absence of any scatterer, since the incident field $\phi^{inc}(\overrightarrow{r})$ exists everywhere, the above equation is transformed to:

$$(\nabla^2 + k_0^2)\phi^{inc}(\overrightarrow{r}) = 0 \tag{A.4}$$

Substituting $\phi(\overrightarrow{r}) = \phi^{inc}(\overrightarrow{r}) + \phi^{sc}(\overrightarrow{r})$ in A.4, where $\phi^{sc}(\overrightarrow{r})$ is the scattered field, we obtain the free space Helmholtz wave equation for the scattered fields:

$$(\nabla^2 + k_0^2)\phi^{sc}(\overrightarrow{r}) = -O(\overrightarrow{r}, \omega)\phi(\overrightarrow{r}). \tag{A.5}$$

The solution to the above equation can be obtained using the scalar Greens function [14]. The unknown scattered field in A.5 can be expressed in terms of the free space scalar Greens function, $g(\overrightarrow{r}|r')$ which satisfies

$$(\nabla^2 + k_0^2)g(\overrightarrow{r}|r') = -\delta(\overrightarrow{r} - r'). \tag{A.6}$$

where r' is the location of the source. Thus, the field scattered by the dielectric scatterer is expressed as [33]

$$\phi^{sc}(\overrightarrow{r}) = \int_{V'} O(\overrightarrow{r}, \omega)\phi(\overrightarrow{r})g(\overrightarrow{r}|r')dr'. \tag{A.7}$$

The Born approximation linearizes A.7 for imaging weakly scattering dielectric objects. The first order Born approximation states [33]

$$\begin{aligned} \phi(\overrightarrow{r}) &= \phi^{inc}(\overrightarrow{r}) + \phi^{sc}(\overrightarrow{r}) \\ &\sim \phi^{inc}(\overrightarrow{r}), \end{aligned} \tag{A.8}$$

provided $0 < O(\overrightarrow{r'}, \omega) << 1$. In that case, A.7 is modified to

$$\phi^{sc}(\overrightarrow{r'}) = \int_{V'} O(\overrightarrow{r'}, \omega)\phi^{inc}(\overrightarrow{r'})g(\overrightarrow{r'}|r')dr'. \tag{A.9}$$

Appendix B

Far field experimental system and measurements

This appendix summarizes the reflectivity arch range based microwave time domain measurement system, used for performing far field imaging experiments. The details regarding the equipments used in the scattering system and the procedures used for obtaining measurements out of the system are explained in this section. The time domain system is shown in Fig. B.1. The equipments used in the time domain system are mentioned in Table B.1.

The reflectivity Arch was received from General Electric to be used in electromagnetics lab. The arch consists of two horizontal, three meter radius, 90 segments joined together

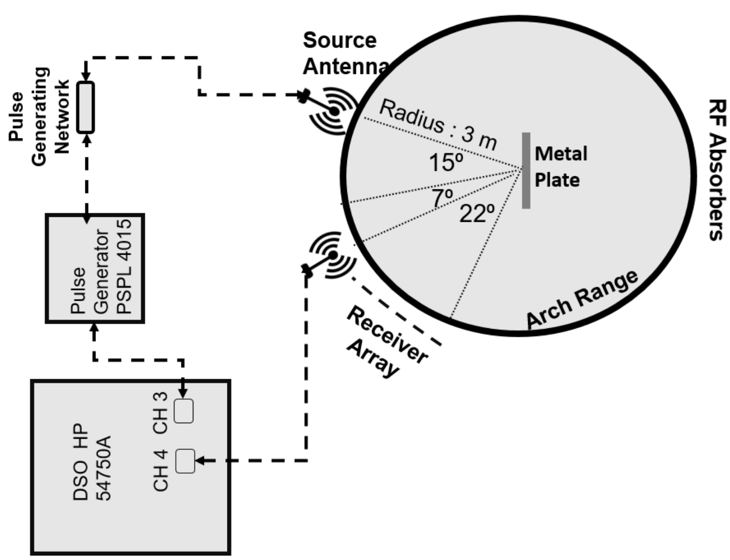

Figure B.1: Far field experimental setup

Table B.1: Equipment used for time domain measurements

Quantity	**Item**
1	Reflectivity arch (General Electric)
1	Hewlett Packard digital sampling oscilloscope model HP54750A
1	Picosecond Pulse Lab Pulse generator, model 4015B
1	PSPL 5208-DC pulse generating network
2	American Electronic Laboratories H-1498 TEM horn antennas
2	Polyethylene lens
1	Newstyle USB -3.5 External Floppy Disk Drive
-	RF Absorbers

to form a semicircular structure with two antenna carriers traveling along the top. A third 90°segment is located opposite the first two, providing a platform for the third antenna. Each segment has a 0.21 m aluminum channel rolled on a radius of three meters mounted atop a welded aluminum tubular space frame. The space frame base has provisions for leveling the structure and for bolting the structure to the ground. The arch, appears heavy enough to prevent accidental shifting, so it does not seem necessary to bolt it to the ground. The overall range diameter is 6.096 m, while the antennas and lenses are placed at a height of 1.219 m above the floor. The history and usage of the arch can be accurately described in an excerpt from Reflectivity Arch Measurement System, Final Technical Report, written by C.R. Jameson and A.H. MacDonald, Georgia Technological University, December 1988.

"The Reflectivity Arch is a facility which can be used to perform radar cross section (RCS) measurements, radar absorber evaluation, antenna pattern measurements, radar transmission studies, and material measurements. Material measurements can be made in both reflection and transmission mode. These tests can be performed in the frequency region 2-18 GHz in a continuous wave (CW) mode or, with additional software, the test data can be used to determine the pulse response of a target or antenna.

Table B.2: Beamwidth of the arch range system

Frequency (GHz)	**Beamwidth (mm)**
8-Row	225
8-Column	212
10-Row	200
10-Column	210
12-Row	177
12-Column	205

The development of the vertical reflectivity arch is credited to the Naval Research Laboratory who designed this dual-antenna facility to evaluate the broadband absorption capabilities of flat-panel radar absorbing materials. Since that time, the arch has been a standard method for radar cross section reduction (RCSR) measurements of absorbers and it is used in various forms by the U. S. Navy at its Dahlgren, Virginia facility, the Naval Research Laboratory and by absorber manufacturers such as Emerson and Cumming and Nippon Electric."

A table showing the beam-width at 8, 10, and 12 GHz along the row and column of the arch range is shown in Table B.2. The beam-width is determined to be greater than -3 dB of the maximum signal [157]. As observed from the table, an increase in frequency leads to a decrease of the beam-width. The details of the other instruments mentioned in are as follows:

- A Hewlett Packard digital sampling oscilloscope (DSO) model HP54750A is used to display and measure the back-scattered fields. It has a time-domain-reflectometer/time-domain-transmission (TDR/TDT) plug-in module, model HP54753A, which provides 20 GHz and 12.4 GHz channels for the oscilloscope.

- This TDR/TDT device has an integrated step generator, which sends steps from channel 3 with a rise time of 45 ps and an amplitude of 200 mV. This unit triggers a step generator made by Picosecond Pulse Labs (PSPL), model number 4015B.

- A remote pulse head (PSPL 4015RPH) follows the pulse generator and creates another step. The step signal is sent into a PSPL 5208-DC pulse generating network where a pseudo-Gaussian pulse signal is generated.

- The transmitting and receiving antennas are American Electronic Laboratories H-1498 TEM coaxially fed double ridged horns each with a bandwidth of 2 to 18 GHz. Orientation of each antenna may be rotated by 90, allowing measurement of horizontal, vertical, and cross polarization.

- Polyethylene lenses are mounted with variable distance in front of the horn antennas to collimate the antenna beam. Primary advantages of the lenses are minimization of edge effects by confining the incident energy to the vicinity of the sample and reduction of phase variation across the target.

Some of the advantages and disadvantages of the particular time domain system over an equivalent frequency domain system are mentioned in [48]. The measurements are taken using the following procedure:

- Absorbers are placed near any metal object close to the arch range in order to reduce high reflections from them.

- An X-Y leveling laser is used to ensure that both antennas and the target plane to be imaged are in the same plane, and the targets are placed relative to the center of the arch range, where the peak of the main beam of the transmitter antenna is located.

- Clutter is eliminated by measuring the background signal with no target present and, subsequently, subtracting it from the target signal.

- The time scale/ grid of the oscilloscope needs to be changed based on the desired time resolution. For the conducted measurements, a time grid of 512 ps was chosen.

- A time window of about 10 nsec is chosen in order to include the scattering from target, but eliminate the antenna coupling.

- A total of 1024 sampling points were chosen within this time window, in order to provide an alias-free bandwidth much greater than that of the antennas, obtained from the Nyquist criterion.

- An averaging of repeated measurements was used to reduce system noise. Measurements indicated that 256 averages using 1024 sample points were enough for clean experimental data.

- The voltage scale of the oscilloscope needs to be changed based on the desired SNR. A higher SNR ensures more power and stronger signals. However, if a significantly large voltage scale is chosen, the signals may saturate and are hence truncated. For the conducted measurements, a voltage scale of 1 V was chosen.

Appendix C

Breast phantoms

- Phantom 1: The normal breast tissue can be created using Soybean oil, which is cheap and has electrical properties quite close to fatty breast tissues. The tumor can be created using diluted 35 % Diacetin solution and distilled water (DIW). The skin region can be taken into account using FR-4 Glass epoxy material. A matching medium of Soybean oil can be used to immerse the antenna in order to reduce dispersion losses at the breast interface. Advantages of this phantom are:

  - The phantom is a liquid model and can be easily disposed.
  - The model is stable, and can be used multiple times.
  - The dielectric properties of the tumor can be tuned by varying the water content in the diacetin solution.
  - The dielectric contrast between soybean oil and diacetin is comparable with fatty breast tissues and malignant tissues.

  However some disadvantages of this phantom are :

  - Crude soybean oil and diacetin are not commercially available and needs to be arranged from chemical factories.
  - It is advisable to characterize the dielectric properties of the diacetin solution

throughout the frequency spectrum after adding DIW to the concentrated solution.

- Phantom 2: Details on the recipe of this solid phantom are as follows :
  - Products required : Polyethylene powder (PEP), agar, DIW , Bactine Spray, Para film
  - The procedure for making the normal breast tissue is as follows :
    * Pour DIW into a glass flask and put on a burner with a low flame or on a digital plate.
    * Heat the solution to 88 °C. High temperature is required as there cannot be any heat supply to the blender.
    * Add a few drops of a bactericide, such as Bactine spray.
    * Add the powder reagents, as a mixture of PEP and agar in the recipe. The powder mixture is added in tiny amounts to the liquid. The mixture is stirred continuously around 40 rpm to 60 RPM and gently to form a homogeneous solution with minimal bubbles.
    * Once the mixture is homogeneous and thick, pour into a suitable mould. Initially, the temperature is about 68 °C to 75 °C. Allow the phantom to cool down to room temperature then place it at 5 °C for solidification.
    * Use high quality plastic wraps, such as parafilm, to store the phantom after solidification to prevent dehydration.
  - The procedure for making the malignant tissue is as follows :
    * For gelatin-based tumor phantoms, gelatin powder is dissolved in hot saline

(about 60 °C) and set to solidify.

    * For alginate-based tumor phantoms, alginate is dissolved in cooled saline and immediately set in a mold, as alginate powder solidifies rapidly.

- Phantom 3: Details on the recipe of the solid dough based phantom are as follows:
  - Products required : Water, soy bean oil, peanut butter, corn our, wheat flour and Vaseline cream. The procedures for making the normal breast tissue is as follows :
  - Procedure 1:
    * Water mixed with corn our, in the ratio of 2:1 is heated for 20 minutes.
    * Add soy bean oil and petroleum jelly premixed, and stir to form a jelly like form.
  - Procedure 2:
    * Mix bean oil, wheat our, peanut butter.
    * Add to Vaseline cream in the ratio of 1:1.
    * The procedure for making the tumor is as follows :
    * Vaseline cream and wheat flour were slowly mixed in 2:1.
    * A ratio of 1:1 oil and corn flour were mixed and then the two preview samples were put together into one experimental bottle in which we added some water about 80 ml.
    * To control the dielectric constant of this sample due to the high water content, a temperature of about 90 °C was applied to the solution whereas a measurement is carried out every 5 minutes heat.

Table C.1: Properties of various phantoms

Phantom	**State**	**Type**	**Disposability**
Recipe 1	liquid	chemical products	stable, easily disposable
Recipe 2	solid	chemical products	unstable, not easily disposable
Recipe 3	solid	commercial products	unstable, disposable

* Add soy bean oil and petroleum jelly premixed, and stir to form a jelly like form.

A table representing the overall advantages and disadvantages of the three proposed phantom models is shown in Table C.1.

BIBLIOGRAPHY

BIBLIOGRAPHY

[1] Elise C Fear, J Bourqui, C Curtis, D Mew, B Docktor, and C Romano. Microwave breast imaging with a monostatic radar-based system: A study of application to patients. *IEEE transactions on microwave theory and techniques*, 61(5):2119–2128, 2013.

[2] James D Taylor. *Introduction to ultra-wideband radar systems*. CRC press, 1994.

[3] Z Su, S Ventre, L Udpa, and A Tamburrino. Monotonicity based imaging method for time-domain eddy current problems. *Inverse Problems*, 33(12):125007, 2017.

[4] Wolfgang-M Boerner, Hans Brand, Leonard A Cram, Dag T Gjessing, Arthur K Jordan, Wolfgang Keydel, Günther Schwierz, and Martin Vogel. *Inverse methods in electromagnetic imaging*, volume 143. Springer Science & Business Media, 2013.

[5] Nadine Joachimowicz, Christian Pichot, and Jean-Paul Hugonin. Inverse scattering: An iterative numerical method for electromagnetic imaging. *IEEE Transactions on Antennas and Propagation*, 39(12):1742–1753, 1991.

[6] Martin Brühl and Martin Hanke. Numerical implementation of two noniterative methods for locating inclusions by impedance tomography. *Inverse Problems*, 16(4):1029, 2000.

[7] Larry Yujiri, Merit Shoucri, and Philip Moffa. Passive millimeter wave imaging. *IEEE microwave magazine*, 4(3):39–50, 2003.

[8] AH Barrett, Ph C Myers, and NL Sadowsky. Detection of breast cancer by microwave radiometry. *Radio Science*, 12(6S):167–171, 1977.

[9] Paul M Meaney, Margaret W Fanning, Dun Li, Steven P Poplack, and Keith D Paulsen. A clinical prototype for active microwave imaging of the breast. *IEEE Transactions on Microwave Theory and Techniques*, 48(11):1841–1853, 2000.

[10] Saptarshi Mukherjee, Anders Rosell, Lalita Udpa, Satish Udpa, and Antonello Tamburrino. Differential geometry based model for eddy current inspection of u-bend sections in steam generator tubes. In *AIP Conference Proceedings*, volume 1806, page 110023. AIP Publishing, 2017.

[11] RA Fenner, EJ Rothwell, and LL Frasch. A comprehensive analysis of free-space and guided-wave techniques for extracting the permeability and permittivity of materials using reflection-only measurements. *Radio Science*, 47(1), 2012.

[12] David M Pozar. *Microwave engineering*. John Wiley & Sons, 2009.

[13] Constantine A Balanis. *Advanced engineering electromagnetics*. John Wiley & Sons, 2012.

[14] Edward J Rothwell and Michael J Cloud. *Electromagnetics*. CRC press, 2008.

[15] Weng Cho Chew. *Waves and fields in inhomogeneous media*, volume 522. IEEE press New York, 1995.

[16] Arthur S Agatston, Warren R Janowitz, Frank J Hildner, Noel R Zusmer, Manuel Viamonte, and Robert Detrano. Quantification of coronary artery calcium using ultrafast computed tomography. *Journal of the American College of Cardiology*, 15(4):827–832, 1990.

[17] Weng Cho Chew and Yi-Ming Wang. Reconstruction of two-dimensional permittivity distribution using the distorted born iterative method. *IEEE transactions on medical imaging*, 9(2):218–225, 1990.

[18] B Bogert. Demonstration of delay distortion correction by time-reversal techniques. *IRE Transactions on Communications Systems*, 5(3):2–7, 1957.

[19] KE Schreiner, HL Funk, and E Hopner. Automatic distortion correction for efficient pulse transmission. *IBM Journal of Research and Development*, 9(1):20–30, 1965.

[20] Mathias Fink. Time reversal of ultrasonic fields. i. basic principles. *IEEE Trans. Ultrason., Ferroelect., Freq. Control*, 39(5):555–566, 1992.

[21] Francois Wu, Jean-Louis Thomas, and Mathias Fink. Time reversal of ultrasonic fields. ii. experimental results. *IEEE Trans. Ultrason., Ferroelect., Freq. Control*, 39(5):567–578, 1992.

[22] Jean-Louis Thomas and M.A. Fink. Ultrasonic beam focusing through tissue inhomogeneities with a time reversal mirror: application to transskull therapy. *IEEE Trans. Ultrason., Ferroelect., Freq. Control*, 43(6):1122–1129, Nov 1996.

[23] Geoffroy Lerosey, J De Rosny, A Tourin, A Derode, G Montaldo, and M Fink. Time reversal of electromagnetic waves. *Phys. Rev. Lett.*, 92(19):193904, 2004.

[24] Julien De Rosny, Geoffroy Lerosey, and Mathias Fink. Theory of electromagnetic time-reversal mirrors. *IEEE Trans. Antennas Propag.*, 58(10):3139–3149, 2010.

[25] Benjamin E Henty and Daniel D Stancil. Multipath-enabled super-resolution for rf and microwave communication using phase-conjugate arrays. *Phys. Rev. Lett.*, 93(24):243904, 2004.

[26] Panagiotis Kosmas and Carey Rappaport. Use of the fdtd method for time reversal: Application to microwave breast cancer detection. In *Electronic Imaging 2004*, pages 1–9. International Society for Optics and Photonics, 2004.

[27] Saptarshi Mukherjee, Antonello Tamburrino, Lalita Udpa, and Satish Udpa. Nde of composite structures using microwave time reversal imaging. In *42nd Annual Review of Progress in Quantitative Nondestructive Evaluation*, volume 1706, page 100002. AIP Publishing, 2016.

[28] S Reyes-Rodríguez, N Lei, B Crowgey, L Udpa, and SS Udpa. Time reversal and microwave techniques for solving inverse problem in non-destructive evaluation. *NDT&E INTl*, 62:106–114, 2014.

[29] Mehmet E Yavuz and Fernando L Teixeira. Full time-domain dort for ultrawideband electromagnetic fields in dispersive, random inhomogeneous media. *IEEE Trans. Antennas Propag.*, 54(8):2305–2315, 2006.

[30] Yuanwei Jin, José MF Moura, and Nicholas O Donoughue. Time reversal in multiple-input multiple-output radar. *IEEE J. Sel. Topics Signal Process.*, 4(1):210–225, 2010.

[31] Robert C Qiu, Chenming Zhou, Nan Guo, and John Q Zhang. Time reversal with miso for ultrawideband communications: Experimental results. *IEEE Antennas Wireless Propag. Lett.*, 5(1):269–273, 2006.

[32] Antoni Broquetas, Jordi Romeu, Juan M Rius, Antonio R Elias-Fuste, Angel Cardama, and Luis Jofre. Cylindrical geometry: A further step in active microwave tomography. *IEEE Trans. Microw. Theory Techn.*, 39(5):836–844, 1991.

[33] Andrew F Peterson, Scott L Ray, Raj Mittra, Institute of Electrical, and Electronics Engineers. *Computational methods for electromagnetics*, volume 2. IEEE press New York, 1998.

[34] Kane Yee. Numerical solution of initial boundary value problems involving maxwell's equations in isotropic media. *IEEE Transactions on antennas and propagation*, 14(3):302–307, 1966.

[35] Gerrit Mur. Absorbing boundary conditions for the finite-difference approximation of the time-domain electromagnetic-field equations. *IEEE transactions on Electromagnetic Compatibility*, (4):377–382, 1981.

[36] Jean-Pierre Berenger. A perfectly matched layer for the absorption of electromagnetic waves. *Journal of computational physics*, 114(2):185–200, 1994.

[37] J Alan Roden and Stephen D Gedney. Efficient implementation of the uniaxial-based pml media in three-dimensional nonorthogonal coordinates with the use of the fdtd technique. *Microwave and Optical Technology Letters*, 14(2):71–75, 1997.

[38] J Alan Roden, Stephen D Gedney, et al. Convolutional pml (cpml): An efficient fdtd implementation of the cfs-pml for arbitrary media. *Microwave and optical technology letters*, 27(5):334–338, 2000.

[39] Matthew R Arnison, Kieran G Larkin, Colin JR Sheppard, Nicholas I Smith, and Carol J Cogswell. Linear phase imaging using differential interference contrast microscopy. *Journal of microscopy*, 214(1):7–12, 2004.

[40] Wenjun Zheng, Zhiqin Zhao, and Zai-Ping Nie. Application of trm in the uwb through wall radar. *Progress In Electromagnetics Research*, 87:279–296, 2008.

[41] Panagiotis Kosmas and Carey M Rappaport. Time reversal with the fdtd method for microwave breast cancer detection. *IEEE Transactions on Microwave Theory and Techniques*, 53(7):2317–2323, 2005.

[42] Xiaoyin Xu, Eric L Miller, and Carey M Rappaport. Minimum entropy regularization in frequency-wavenumber migration to localize subsurface objects. *IEEE Trans. Geosci. Remote Sens*, 41(8):1804–1812, 2003.

[43] Werner Gerum, P Malzahn, and K Schneider. 94-ghz twt for military radar applications. *IEEE Transactions on Electron Devices*, 48(1):72–73, 2001.

[44] Anthony Cresp, Ioannis Aliferis, MJ Yedlin, Ch Pichot, and J-Y Dauvignac. Investigation of time-reversal processing for surface-penetrating radar detection in a multiple-target configuration. In *Radar Conference, 2008. EuRAD 2008. European*, pages 144–147. IEEE, 2008.

[45] Liliana Borcea, George Papanicolaou, Chrysoula Tsogka, and James Berryman. Imaging and time reversal in random media. *Inverse Probl.*, 18(5):1247, 2002.

[46] Max Born and Emil Wolf. *Principles of optics: electromagnetic theory of propagation, interference and diffraction of light*. Elsevier, 1980.

[47] AJ Devaney. Time reversal imaging of obscured targets from multistatic data. *IEEE Trans. Antennas Propag.*, 53(5):1600–1610, 2005.

[48] Bradley T Perry, Edward J Rothwell, and Leo C Kempel. A comparison of the measured pulse response of layered materials using time-and frequency-domain systems [measurements corner]. *IEEE Trans. Antennas Propag.*, 49(5):117–123, 2007.

[49] Claire Prada and Mathias Fink. Eigenmodes of the time reversal operator: A solution to selective focusing in multiple-target media. *Wave motion*, 20(2):151–163, 1994.

[50] Ka-Sing Lim, Manimaran Nagalingam, and Chue-Poh Tan. Design and construction of microstrip uwb antenna with time domain analysis. *Progress In Electromagnetics Research M*, 3:153–164, 2008.

[51] Nadia Maaref, Patrick Millot, Xavier Ferrières, Christian Pichot, and Odile Picon. Electromagnetic imaging method based on time reversal processing applied to through-the-wall target localization. *Progress In Electromagnetics Research M*, 1:59–67, 2008.

[52] Benjamin R Crowgey, Edward J Rothwell, Leo C Kempel, and Eric L Mokole. Comparison of uwb short-pulse and stepped-frequency radar systems for imaging through barriers. *Prog Electromagn Res*, 110:403–419, 2010.

[53] P. Kosmas and C.M. Rappaport. Time reversal with the fdtd method for microwave breast cancer detection. *IEEE Trans. Microw. Theory Techn.*, 53(7):2317–2323, July 2005.

[54] PJ Gibson. The vivaldi aerial. In *Microwave Conference, 1979. 9th European*, pages 101–105. IEEE, 1979.

[55] Ehud Gazit. Improved design of the vivaldi antenna. In *IEE Proceedings H (Microwaves, Antennas and Propagation)*, volume 135, pages 89–92. IET, 1988.

[56] K Kota and L Shafai. Gain and radiation pattern enhancement of balanced antipodal vivaldi antenna. *Electronics Letters*, 47(5):303–304, 2011.

[57] Ping Wang, Haobin Zhang, Guangjun Wen, and Yuanhua Sun. Design of modified 6-18 ghz balanced antipodal vivaldi antenna. *Progress In Electromagnetics Research*, 25:271–285, 2012.

[58] Constantine A Balanis. *Modern antenna handbook*. John Wiley & Sons, 2011.

[59] A Balanis Constantine et al. Antenna theory: analysis and design. *MICROSTRIP ANTENNAS, third edition, John wiley & sons*, 2005.

[60] Marc C Greenberg, Kathleen L Virga, and Cynthia L Hammond. Performance characteristics of the dual exponentially tapered slot antenna (detsa) for wireless communications applications. *IEEE Transactions on Vehicular Technology*, 52(2):305–312, 2003.

[61] Amin M Abbosh and Marek E Bialkowski. Design of ultrawideband planar monopole antennas of circular and elliptical shape. *IEEE Transactions on Antennas and Propagation*, 56(1):17–23, 2008.

[62] Werner Wiesbeck, Grzegorz Adamiuk, and Christian Sturm. Basic properties and design principles of uwb antennas. *Proceedings of the IEEE*, 97(2):372–385, 2009.

[63] Saptarshi Mukherjee, Lalita Udpa, Satish Udpa, and Edward J Rothwell. Target localization using microwave time-reversal mirror in reflection mode. *IEEE Transactions on Antennas and Propagation*, 65(2):820–828, 2017.

[64] Lazio Tabar, A Gad, LH Holmberg, U Ljungquist, Kopparberg County Project Group, CJG Fagerberg, L Baldetorp, O Gröntoft, B Lundström, JC Månson, et al. Reduction in mortality from breast cancer after mass screening with mammography: randomised trial from the breast cancer screening working group of the swedish national board of health and welfare. *The Lancet*, 325(8433):829–832, 1985.

[65] Martha S Linet, Thomas L Slovis, Donald L Miller, Ruth Kleinerman, Choonsik Lee, Preetha Rajaraman, and Amy Berrington de Gonzalez. Cancer risks associated with external radiation from diagnostic imaging procedures. *CA: a cancer journal for clinicians*, 62(2):75–100, 2012.

[66] Mariya Lazebnik, Leah McCartney, Dijana Popovic, Cynthia B Watkins, Mary J Lindstrom, Josephine Harter, Sarah Sewall, Anthony Magliocco, John H Booske, Michal Okoniewski, et al. A large-scale study of the ultrawideband microwave dielectric properties of normal breast tissue obtained from reduction surgeries. *Physics in medicine and biology*, 52(10):2637, 2007.

[67] Essex J Bond, Xu Li, Susan C Hagness, and Barry D Van Veen. Microwave imaging via space-time beamforming for early detection of breast cancer. *IEEE Transactions on Antennas and Propagation*, 51(8):1690–1705, 2003.

[68] P Wust, B Hildebrandt, G Sreenivasa, B Rau, J Gellermann, H Riess, R Felix, and PM Schlag. Hyperthermia in combined treatment of cancer. *The lancet oncology*, 3(8):487–497, 2002.

[69] M Kowalski, Babak Behnia, Andrew G Webb, and Jian-Ming Jin. Optimization of electromagnetic phased-arrays for hyperthermia via magnetic resonance temperature estimation. *IEEE Transactions on Biomedical Engineering*, 49(11):1229–1241, 2002.

[70] Mark Converse, Essex J Bond, Susan C Hagness, and Barry D Van Veen. Ultrawideband microwave space-time beamforming for hyperthermia treatment of breast cancer: A computational feasibility study. *IEEE Transactions on microwave theory and techniques*, 52(8):1876–1889, 2004.

[71] Mark Converse, Essex J Bond, BD Veen, and C Hagness. A computational study of ultra-wideband versus narrowband microwave hyperthermia for breast cancer treatment. *IEEE transactions on microwave theory and techniques*, 54(5):2169–2180, 2006.

[72] Hernan I Vargas, William C Dooley, Robert A Gardner, Katherine D Gonzalez, Rose Venegas, Sylvia H Heywang-Kobrunner, and Alan J Fenn. Focused microwave phased array thermotherapy for ablation of early-stage breast cancer: results of thermal dose escalation. *Annals of surgical oncology*, 11(2):139–146, 2004.

[73] John Stang, Mark Haynes, Paul Carson, and Mahta Moghaddam. A preclinical system prototype for focused microwave thermal therapy of the breast. *IEEE Transactions on Biomedical Engineering*, 59(9):2431–2438, 2012.

[74] J-L Thomas and Mathias A Fink. Ultrasonic beam focusing through tissue inhomogeneities with a time reversal mirror: application to transskull therapy. *IEEE Transactions on Ultrasonics, Ferroelectrics, and Frequency Control*, 43(6):1122–1129, 1996.

[75] Panagiotis Kosmas and Carey M Rappaport. Fdtd-based time reversal for microwave breast cancer detection-localization in three dimensions. *IEEE Transactions on Microwave Theory and Techniques*, 54(4):1921–1927, 2006.

[76] Yuhua Cheng, Yiming Deng, Jing Cao, Xin Xiong, Libing Bai, and Zhaojun Li. Multiwave and hybrid imaging techniques: a new direction for nondestructive testing and structural health monitoring. *Sensors*, 13(12):16146–16190, 2013.

[77] Kenneth A Leopold, Mark Dewhirst, Thaddeus Samulski, John Harrelson, J Alan Tucker, Stephen L George, Richard K Dodge, Wendy Grant, Scott Clegg, Leonard R Prosnitz, et al. Relationships among tumor temperature, treatment time, and histopathological outcome using preoperative hyperthermia with radiation in soft tissue sarcomas. *International Journal of Radiation Oncology* Biology* Physics*, 22(5):989–998, 1992.

[78] Huiqing Zhai, Shaoshu Sha, Varun K Shenoy, Sungyong Jung, Mingyu Lu, Kyoungwon Min, Sungchul Lee, and Dong S Ha. An electronic circuit system for time-reversal of ultra-wideband short impulses based on frequency-domain approach. *IEEE Transactions on Microwave Theory and Techniques*, 58(1):74–86, 2010.

[79] Saptarshi Mukherjee, Lalita Udpa, Rothwell Edward J Udpa, Satish, and Yiming Deng. Microwave time-reversal mirror for imaging and hyperthermia of breast tumors. *IEEE Journal of Electromagnetics, RF and Microwaves in Medicine and Biology*, "forthcoming".

[80] Saptarshi Mukherjee, Lalita Udpa, Satish Udpa, Edward J Rothwell, and Yiming Deng. Time reversal mirror for microwave imaging of breast tissues. *IEEE Transactions on Microwave Theory and Techniques*, "forthcoming".

[81] Hervé Tortel, Gilles Micolau, and Marc Saillard. Decomposition of the time reversal operator for electromagnetic scattering. *Journal of Electromagnetic Waves and Applications*, 13(5):687–719, 1999.

[82] Claire Prada, Sebastien Manneville, Dimitri Spoliansky, and Mathias Fink. Decomposition of the time reversal operator: Detection and selective focusing on two scatterers. *The Journal of the Acoustical Society of America*, 99(4):2067–2076, 1996.

[83] SP Lynch, X Lei, M Chavez-MacGregor, L Hsu, F Meric-Bernstam, TA Buchholz, A Zhang, GN Hortobagyi, V Valero, and AM Gonzalez-Angulo. Multifocality and multicentricity in breast cancer and survival outcomes. *Annals of oncology*, 23(12):3063–3069, 2012.

[84] Laura J Esserman, Dulcy Wolverton, and Nola Hylton. Integration of breast imaging into cancer management. *Current oncology reports*, 2(6):572–581, 2000.

[85] Saptarshi Mukherjee, Lalita Udpa, Yiming Deng, Premjeet Chahal, and Edward J Rothwell. Design of a microwave time reversal mirror for imaging applications. *Progress In Electromagnetics Research C*, 77:155–165, 2017.

[86] Saptarshi Mukherjee, Yiming Deng, Lalita Udpa, Satish Udpa, Prem Chahal, and Edward Rothwell. Microwave time reversal mirror for breast tumor detection. In *Antennas and Propagation & USNC/URSI National Radio Science Meeting, 2017 IEEE International Symposium on*, pages 791–792. IEEE, 2017.

[87] WR Adey. Tissue interactions with nonionizing electromagnetic fields. *Physiological reviews*, 61(2):435–514, 1981.

[88] Mariya Lazebnik, Michal Okoniewski, John H Booske, and Susan C Hagness. Highly accurate debye models for normal and malignant breast tissue dielectric properties at microwave frequencies. *IEEE Microwave and Wireless Components Letters*, 17(12):822–824, 2007.

[89] Chung-Kwang Chou, Gang-Wu Chen, Arthur W Guy, and Kenneth H Luk. Formulas for preparing phantom muscle tissue at various radiofrequencies. *Bioelectromagnetics*, 5(4):435–441, 1984.

[90] Marco G Bini, Amleto Ignesti, Luigi Millanta, Roberto Olmi, Nicola Rubino, and Riccardo Vanni. The polyacrylamide as a phantom material for electromagnetic hyperthermia studies. *IEEE Transactions on Biomedical Engineering*, (3):317–322, 1984.

[91] JJW Lagendijk, P Hofman, and J Schipper. Perfusion analyses in advanced breast carcinoma during hyperthermia. *International Journal of Hyperthermia*, 4(5):479–495, 1988.

[92] MP Robinson, MJ Richardson, JL Green, and AW Preece. New materials for dielectric simulation of tissues. *Physics in Medicine & Biology*, 36(12):1565, 1991.

[93] A Surowiec, PN Shrivastava, M Astrahan, and Z Petrovich. Utilization of a multilayer polyacrylamide phantom for evaluation of hyperthermia applicators. *International journal of hyperthermia*, 8(6):795–807, 1992.

[94] Mariya Lazebnik, Ernest L Madsen, Gary R Frank, and Susan C Hagness. Tissue-mimicking phantom materials for narrowband and ultrawideband microwave applications. *Physics in medicine and biology*, 50(18):4245, 2005.

[95] John R Willis. Variational and related methods for the overall properties of composites. *Advances in applied mechanics*, 21:1–78, 1981.

[96] CC Chamis and JH Sinclair. Durability/life of fiber composites in hygrothermomechanical environments. In *Composite Materials: Testing and Design (6th Conference)*. ASTM International, 1982.

[97] Ole Gunneskov, Nicholas Dudley Barlow, Mark Hancock, and Tomas Vronsky. Wind turbine blade, April 3 2007. US Patent 7,198,471.

[98] Mark Wagner and Guy Norris. *Boeing 787 dreamliner*. Zenith Press, 2009.

[99] Don E Bray and Roderick K Stanley. *Nondestructive evaluation: a tool in design, manufacturing and service*. CRC press, 1996.

[100] Olin E Weiss, Grant L Davis, James L Hudson, and Harlan T Dowell. Composite tape laying apparatus including means for plural longitudinal and transverse cuts, September 29 1981. US Patent 4,292,108.

[101] RobertA Kline. *Nondestructive characterization of composite media*. Routledge, 2017.

[102] Bryan Harris. *Fatigue in composites: science and technology of the fatigue response of fibre-reinforced plastics*. Woodhead Publishing, 2003.

[103] Alan A Baker, LR Francis Rose, and Rhys Jones. *Advances in the bonded composite repair of metallic aircraft structure*. Elsevier, 2003.

[104] Oleksii Karpenko, Anton Khomenko, Ermias Koricho, Mahmoodul Haq, and Lalita Udpa. Monitoring of fatigue damage in composite lap-joints using guided waves and fbg sensors. In *AIP Conference Proceedings*, volume 1706, page 120005. AIP Publishing, 2016.

[105] Guang Yang, Antonello Tamburrino, Lalita Udpa, Satish S Udpa, Zhiwei Zeng, Yiming Deng, and Peiwen Que. Pulsed eddy-current based giant magnetoresistive system for

the inspection of aircraft structures. *IEEE transactions on magnetics*, 46(3):910–917, 2010.

[106] Sergey Kharkovsky and Reza Zoughi. Microwave and millimeter wave nondestructive testing and evaluation-overview and recent advances. *IEEE Instrumentation & Measurement Magazine*, 10(2):26–38, 2007.

[107] Sasan Bakhtiari, Nasser Qaddoumi, Stoyan I Ganchev, and Reza Zoughi. Microwave noncontact examination of disbond and thickness variation in stratified composite media. *IEEE Transactions on Microwave Theory and Techniques*, 42(3):389–395, 1994.

[108] Stoyan I Ganchev, Nasser Qaddoumi, Emarit Ranu, and Reza Zoughi. Microwave detection optimization of disbond in layered dielectrics with varying thickness. *IEEE Transactions on Instrumentation and Measurement*, 44(2):326–328, 1995.

[109] Sasan Bakhtiari, Stoyan I Ganchev, and Reza Zoughi. Analysis of radiation from an open-ended coaxial line into stratified dielectrics. *IEEE Transactions on Microwave Theory and Techniques*, 42(7):1261–1267, 1994.

[110] Reza Zoughi. *Microwave non-destructive testing and evaluation principles*, volume 4. Springer Science & Business Media, 2012.

[111] Sergey Kharkovsky, Joseph T Case, Mohamed Ahmed Abou-Khousa, Reza Zoughi, and Frank L Hepburn. Millimeter-wave detection of localized anomalies in the space shuttle external fuel tank insulating foam. *IEEE Transactions on Instrumentation and Measurement*, 55(4):1250–1257, 2006.

[112] Gary S Schajer and F Bahar Orhan. Measurement of wood grain angle, moisture content and density using microwaves. *Holz als Roh-und Werkstoff*, 64(6):483–490, 2006.

[113] ET Thostenson and T-W Chou. Microwave processing: fundamentals and applications. *Composites Part A: Applied Science and Manufacturing*, 30(9):1055–1071, 1999.

[114] Najet Chakroun, Mathias A Fink, and François Wu. Time reversal processing in ultrasonic nondestructive testing. *IEEE Transactions on Ultrasonics, Ferroelectrics, and Frequency Control*, 42(6):1087–1098, 1995.

[115] Najet Chakroun, Véronique Miette, Mathias Fink, François Wu, Gérard Mangenet, and Lionel Beffy. Ultrasonic inspection of titanium alloys with a time reversal mirror. In *Review of Progress in Quantitative Nondestructive Evaluation*, pages 2105–2112. Springer, 1995.

[116] Buli Xu and Victor Giurgiutiu. Single mode tuning effects on lamb wave time reversal with piezoelectric wafer active sensors for structural health monitoring. *Journal of Nondestructive Evaluation*, 26(2):123–134, 2007.

[117] AM Sutin, PA Johnson, Donald O Thompson, and Dale E Chimenti. Nonlinear elastic wave nde ii. nonlinear wave modulation spectroscopy and nonlinear time reversed acoustics. In *AIP Conference Proceedings*, volume 760, pages 385–392. AIP, 2005.

[118] Vistasp M Karbhari. *Non-destructive evaluation (NDE) of polymer matrix composites*. Elsevier, 2013.

[119] Michael Saybolt, Saptarshi Mukherjee, Lalita Udpa, and Prem Chahal. A low cost microwave imaging system using a 6-port reflectometer for nde of composites. In *Proceedings of the American Society for Composites: Thirty-First Technical Conference*, 2016.

[120] Edward J Rothwell and Michael J Cloud. *Electromagnetics*. CRC press, 2010.

[121] Saptarshi Mukherjee, Antonello Tamburrino, Mahmoodul Haq, Satish Udpa, and Lalita Udpa. Far field microwave nde of composite structures using time reversal mirror. *NDT & E International*, 93:7–17, 2018.

[122] Viktor G Veselago. The electrodynamics of substances with simultaneously negative values of and μ. *Soviet physics uspekhi*, 10(4):509, 1968.

[123] David R Smith, John B Pendry, and Mike CK Wiltshire. Metamaterials and negative refractive index. *Science*, 305(5685):788–792, 2004.

[124] John Brian Pendry. Negative refraction makes a perfect lens. *Physical review letters*, 85(18):3966, 2000.

[125] Yiming Deng and Xin Liu. Electromagnetic imaging methods for nondestructive evaluation applications. *Sensors*, 11(12):11774–11808, 2011.

[126] D Shreiber, M Gupta, and R Cravey. Comparative study of 1-d and 2-d metamaterial lens for microwave nondestructive evaluation of dielectric materials. *Sensors and Actuators A: Physical*, 165(2):256–260, 2011.

[127] Sam Hyeon Lee, Choon Mahn Park, Yong Mun Seo, and Chul Koo Kim. Reversed doppler effect in double negative metamaterials. *Physical Review B*, 81(24):241102, 2010.

[128] Ekaterina S Belonogaya, Sergey N Galyamin, and Andrey V Tyukhtin. Properties of vavilov-cherenkov radiation in an anisotropic medium with a resonant dispersion of permittivity. *JOSA B*, 28(12):2871–2878, 2011.

[129] Chiranjib Goswami, Saptarshi Mukherjee, Subrata Karmakar, Manimala Pal, and Rowdra Ghatak. Fdtd modeling of lorentzian dng metamaterials by auxiliary differential equation method. *Journal of Electromagnetic Analysis and Applications*, 6(05):106, 2014.

[130] Benedikt A Munk. *Metamaterials: critique and alternatives*. John Wiley & Sons, 2009.

[131] John B Pendry, Anthony J Holden, David J Robbins, and WJ Stewart. Magnetism from conductors and enhanced nonlinear phenomena. *IEEE transactions on microwave theory and techniques*, 47(11):2075–2084, 1999.

[132] Anthony Lai, Tatsuo Itoh, and Christope Caloz. Composite right/left-handed transmission line metamaterials. *IEEE microwave magazine*, 5(3):34–50, 2004.

[133] Nathan Kundtz and David R Smith. Extreme-angle broadband metamaterial lens. *Nature materials*, 9(2):129–132, 2010.

[134] Koray Aydin, Irfan Bulu, and Ekmel Ozbay. Subwavelength resolution with a negative-index metamaterial superlens. *Applied physics letters*, 90(25):254102, 2007.

[135] JB Pendry and S Anantha Ramakrishna. Refining the perfect lens. *Physica B: Condensed Matter*, 338(1-4):329–332, 2003.

[136] Mahmoodul Haq, Anton Khomenko, Lalita Udpa, and Satish Udpa. Fiber bragg-grating sensor array for health monitoring of bonded composite lap-joints. In *Experimental Mechanics of Composite, Hybrid, and Multifunctional Materials, Volume 6*, pages 189–195. Springer, 2014.

[137] Lucio Barbato, Carlo Petrarca, Guglielmo Rubinacci, Antonello Tamburrino, and Salvatore Ventre. Numerical models for composite materials in e-ndt. *Studies in Applied Electromagnetics and Mechanics*, 38:47–54, 2013.

[138] P Banerjee, S Safdarnejad, L Udpa, and SS Udpa. Ndt techniques: Signal and image processing. *Reference Module in Materials Science and Materials Engineering*, 2014.

[139] Portia Banerjee, Lalita Udpa, Satish Udpa, and James Benson. Confidence metric for signal classification in non destructive evaluation. *NDT & E International*, 91:88–96, 2017.

[140] Robi Polikar, Lalita Udpa, Satish Udpa, and Vasant Honavar. An incremental learning algorithm with confidence estimation for automated identification of nde signals. *ieee transactions on ultrasonics, ferroelectrics, and frequency control*, 51(8):990–1001, 2004.

[141] Portia Banerjee, Oleksii Karpenko, Lalita Udpa, Mahmood Haq, and Yiming Deng. Prediction of impact-damage growth in gfrp plates using particle filtering algorithm. *Composite Structures*, 2018.

[142] Douglas E Adams and Madhura Nataraju. A nonlinear dynamical systems framework for structural diagnosis and prognosis. *International Journal of Engineering Science*, 40(17):1919–1941, 2002.

[143] Dmitry Isakov, Chris J Stevens, Flynn Castles, and Patrick S Grant. A split ring resonator dielectric probe for near-field dielectric imaging. *Scientific reports*, 7(1):2038, 2017.

[144] Ali Karami Horestani, Christophe Fumeaux, Said F Al-Sarawi, and Derek Abbott. Displacement sensor based on diamond-shaped tapered split ring resonator. *IEEE Sensors Journal*, 13(4):1153–1160, 2013.

[145] Hee-Jo Lee and Jong-Gwan Yook. Biosensing using split-ring resonators at microwave regime. *Applied Physics Letters*, 92(25):254103, 2008.

[146] Nophadon Wiwatcharagoses, Kyoung Youl Park, and Premjeet Chahal. Metamaterial-inspired miniaturized microwave sensing probes. In *Electronic Components and Technology Conference (ECTC), 2012 IEEE 62nd*, pages 2106–2111. IEEE, 2012.

[147] M Shamonin, E Shamonina, V Kalinin, and L Solymar. Resonant frequencies of a split-ring resonator: Analytical solutions and numerical simulations. *Microwave and optical technology letters*, 44(2):133–136, 2005.

[148] Juan Domingo Baena, Jordi Bonache, Ferran Martin, R Marqués Sillero, Francisco Falcone, Txema Lopetegi, Miguel AG Laso, Joan Garcia-Garcia, Ignacio Gil, M Flores Portillo, et al. Equivalent-circuit models for split-ring resonators and complementary split-ring resonators coupled to planar transmission lines. *IEEE transactions on microwave theory and techniques*, 53(4):1451–1461, 2005.

[149] Koray Aydin, Irfan Bulu, Kaan Guven, Maria Kafesaki, Costas M Soukoulis, and Ekmel Ozbay. Investigation of magnetic resonances for different split-ring resonator parameters and designs. *New journal of physics*, 7(1):168, 2005.

[150] Martin Schueler, Christian Mandel, Margarita Puentes, and Rolf Jakoby. Metamaterial inspired microwave sensors. *IEEE Microwave Magazine*, 13(2):57–68, 2012.

[151] RA Waldron. Perturbation theory of resonant cavities. *Proceedings of the IEE-Part C: Monographs*, 107(12):272–274, 1960.

[152] E Hammerstad and O Jensen. Accurate models for microstrip computer-aided design. In *Microwave Symposium Digest, 1980 IEEE MTT-S International*, pages 407–409. IEEE, 1980.

[153] Rohat Melik, Emre Unal, Nihan Kosku Perkgoz, Christian Puttlitz, and Hilmi Volkan Demir. Metamaterial-based wireless strain sensors. *Applied Physics Letters*, 95(1):011106, 2009.

[154] Izyani Mat Rusni, Alyani Ismail, Adam Reda Hasan Alhawari, Mohd Nizar Hamidon, and Nor Azah Yusof. An aligned-gap and centered-gap rectangular multiple split ring resonator for dielectric sensing applications. *Sensors*, 14(7):13134–13148, 2014.

[155] Tim Sercombe, Noel Jones, Rob Day, and Alan Kop. Heat treatment of ti-6al-7nb components produced by selective laser melting. *Rapid Prototyping Journal*, 14(5):300–304, 2008.

[156] William E Frazier. Metal additive manufacturing: a review. *Journal of Materials Engineering and Performance*, 23(6):1917–1928, 2014.

[157] John Edwin Ross. *Application of transient electromagnetic fields to radar target discrimination*. PhD thesis, Michigan State University. Department of electrical Engineering, 1992.